Quantum-Fluctuation-Initiated Coherent Raman Comb in Hydrogen-Filled Hollow-Core Photonic Crystal Fibre

Yingying Wang

A thesis submitted for the degree of Doctor of Philosophy of

University of Bath

Department of Physics

June 2011

Abstract

This thesis explores the generation and the coherence properties of Raman frequency combs that are initiated from vacuum fluctuations using hydrogen-filled hollow-core photonic crystal fibre (HC-PCF). The motivation is to explore a novel route for generating attosecond pulses and waveform synthesis.

To this end, work has been undertaken in the design and fabrication of HC-PCF, in the generation of Raman comb with a compact set-up and finally in an experimental demonstration of the mutual coherence between the comb spectral components.

Here, the well-established photonic bandgap (PBG) HC-PCF is further developed. Surface mode spectral positions are controlled by chemical etching technique, and a single piece of fibre with two robust bandgaps is fabricated. Furthermore, the second established class of HC-PCF; namely large-pitch Kagome-lattice HC-PCF, has experienced challenging developments. This led to the fabrication of a hypocycloid-core seven-cell Kagome HC-PCF with comparable attenuation value to that of PBG HC-PCF while offering much larger bandwidth.

Using the fabricated HC-PCF, different Raman frequency comb systems are developed. In addition to the previously-generated multi-octave Raman frequency comb from a large 1064 nm Nd:YAG Q-switch laser, several more compact version of Raman comb sources have been developed, including one whose lines lay in the visible and UV for applications in forensics and biomedicine.

The Raman frequency comb generated inside a length of hydrogen-filled HC-PCF is further investigated by studying the coherence of the Raman lines. Despite of vacuum-fluctuation-initiation, it is demonstrated that the comb has self- and mutual-coherence properties within each single shot, bringing thus the possibility of generating attosecond pulses with non-classical properties.

Preface

Attosecond science and quantum optics have progressed following different paths, as they entail the use of light with seemingly opposite features. On one hand, synthesizing attosecond pulses (< 10^{-15} s) requires phase-locked optical frequencies that span a spectral width of the order of 1,000 THz or larger (e.g. from UV to mid-IR). The photons forming this light are coherent, and result primarily from a classical coherent interaction between the atoms and the exciting lasers. An example of a technique to create such an ultra-broad coherent comb is high harmonic generation (HHG), which is a well-developed solution in generating attosecond pulses in the soft X-ray spectral region. Another example is Stimulated Raman scattering (SRS), which - provided the coherence of the Raman medium is judiciously excited, has recently been identified as an alternative mechanism for generating broad frequency coherent comb. Among the successful Raman coherence excitation schemes, we count the molecular modulation technique whereby two high power and large-duration* pulsed lasers with frequency difference slightly detuned from the Raman transition frequency (adiabatic preparation), or a transform-limited pump laser whose bandwidth is larger than the Raman shift (impulsive regime). This coherent preparation of Raman medium modulates the fields to generate a coherent Raman frequency comb. It is noteworthy that in all the above approaches, the spontaneous emission from the quantum vacuum fluctuations plays no significant role in the dynamics of the laser-matter interaction. Instead the phase correlation between the generated spectral components is determined by the pumping lasers.

On the other hand, in several branches of quantum optics, the light emission of interest results from the coupling of an atom or a molecule with the electromagnetic vacuum. Consequently, spontaneous emission resulting from quantum vacuum fluctuations plays a central role, and the ensuing emitted photons, which form inherently

* By “large duration” we mean the laser pulse duration larger than 1ns.

incoherent light, can exhibit nonclassical features such as squeezing, photon antibunching or entanglement.

This seeming dichotomy between photons involved in the attosecond pulse generation and those from spontaneous emission, raises the question whether it is ever possible to create attosecond pulses from quantum noise. Surprisingly, preliminary results that use the well developed Photonic tools in the group led by F. Benabid, known as gas-phase photonics material group (GPPM), show that one could indeed trigger an ultra-broad Raman comb from spontaneous emission.

In the GPPM group, we combine the quantum optics with the ground breaking technology of HC-PCF. The basic principle consists of using HC-PCF as a host for the light-matter interaction whose initiation is from vacuum fluctuations, such as SRS generation with a single frequency pump laser. The unique feature of HC-PCF enabled the excitation of SRS in molecular hydrogen (H_2) from spontaneous emission to a degree that an optical frequency comb spanning over 1000 THz from UV to mid-IR has been generated. A combination of experimental indications and theoretical conjectures hint that the generated comb is coherent, that is its spectral components are phase-locked, which thus opens a new route in generating attosecond pulse and waveform synthesis.

This thesis is dedicated to explore experimentally this conjecture by developing tailored HC-PCF for the Raman comb generation and using a novel interferometeric method for cross-phase correlation measurements.

As an essential photonic tool used throughout my PhD project for the generation of optical frequency comb from quantum noise, HC-PCF is introduced in details in Chapter 1 by presenting its guidance mechanisms, which explain why it can act as a perfect host for light-matter interactions such as SRS. Previous achievements on SRS, which led to the Raman frequency comb generation, are also reviewed in Chapter 1.

The ever increasing applications in HC-PCF and their unusual guidance mechanisms make HC-PCF a popular research subject in its own right. The development of HC-PCF forms Part 1 of my thesis. This part comprises three chapters (chapters 2, 3 and 4). Chapter 2 deals with surface mode suppression in PBG HC-PCF. Surface

modes are HC-PCF guided modes that reside in the silica core-surround. The coupling of these modes with the core modes hinders the PBG HC-PCF from achieving a smooth guidance and extremely low loss. In this chapter I show how one could control these modes. I investigated the dependence of a surface mode to the core-surround thickness using a chemical etching technique. Moreover, several interesting core-surround patterns are explored.

Another disadvantage of PBG HC-PCF is its limited bandwidth. Chapter 3 covers the design and fabrication of a PBG HC-PCF which exhibits a double bandgap HC-PCF. This was achieved by fine tuning the strut thickness and apex size. A fibre with two robust bandgaps centred at 1064 nm and 1550 nm has been fabricated.

Chapter 4 covers the development of a new type of Kagome HC-PCF. Kagome HC-PCF represents the second class of HC-PCF and it differs from the PBG guiding HC-PCF by its broadband transmission window and the physical mechanism underlying the light guidance. Because of its broadband guidance, this fibre is widely used through the thesis for Raman frequency comb generation. Compared to PBG HC-PCF, however, the loss is still a limiting factor in this type of fibre and, although some efforts have been made to reduce it by design of the cladding, the loss was still in the range of 1 to 0.5 dB/m. Here, I present a different design approach whereby I control the core shape of the Kagome structure in order to reduce the loss. I found that a proper design of the core-surround structure can reduce the loss to ~40 dB/km, comparable to the loss of PBG HC-PCF.

The second main work of my PhD is to demonstrate the coherence properties of the quantum-initiated Raman frequency comb. This is covered in part 2, which comprises four chapters; from chapter 5 to chapter 8. In Chapter 5, I review the background and the previous achievements on Raman frequency comb generation in hydrogen-filled HC-PCF. I review the quantum theory of the first order Stokes amplification, and the basic principles that govern the generation of a Raman comb from vacuum noise (i.e. in the absence of any coherent injection).

In chapter 6, I present several “miniature” versions of the Raman comb laser source, and whose spectral outputs are tailored for forensics and biomedicine. Within this

context, the previously generated comb suffers from some major limitations. Firstly, the output power is shared with spectral lines in infrared which has little use in the targeted biomedical applications. Secondly, the pump laser used to generate the comb is a large and cumbersome Nd:YAG laser which doesn't qualify for application where compactness and portability is necessary. To that end, I generate several small compact multiline Raman laser systems, with a very high spectral visible lines.

Chapters 7 and 8 cover a set of experiments to investigate the coherence of the Raman comb. For many applications such as attosecond pulse generation, the mutual coherence of the components of its spectral content is a prerequisite. On the other hand the quantum noise nature of the onset of the above-mentioned Raman comb requires an experimental and unambiguous substantiation of the claim on the comb coherence. This is the scope of chapter 7 and 8 where I experimentally demonstrate the coherence of the Raman comb. In Chapter 7 I focus on the self-coherence of any arbitrary Raman components. For a better understanding of the "self-coherence", I introduce a modal picture and I demonstrate the photon statistics of the comb in several aspects.

As a further investigation on the coherence of the Raman comb, in Chapter 8, I investigate on mutual coherence between different comb components. I deduce the degree of correlation experimentally and theoretically. The results show that the spontaneously generated Raman frequency comb did have a high degree of coherence. This opens the potential for attoscience and optical waveform synthesis.

Finally in Chapter 9, I summarize the thesis and give a proposal for future work.

Acknowledgement

Foremost, I would like to thank Fetah Benabid for both offering me the opportunity to study here as a PhD student and being a great mentor during my PhD. He provides me an interesting PhD topic to study and gives me guidance, trust and support throughout these years. Without him, this thesis would simply not have been written.

The second person to thank is my love Wei Ding, who plays an important role in my life as a husband, and in my career as a private tutor. Whenever I have doubts and difficulties, he is there to help.

Thanks are given to the past and current members in the GPPM group. Firstly, I thank Francois Couny who gives invaluable inputs into my PhD project in many aspects. A lot of skills are learnt from him like fibre fabrication, alignments on optical bench, paper writing skills to mention a few. I would also like to thank Phil Light who gave me plenty of help during my first year and Natalie Wheeler with whom I worked together in these years. Thanks are given to all other members in GPPM: Tom Bradley, Meshaal Alharbi and a lot more.

I would also like to acknowledge our cooperators who helped in the theoretical part of the thesis: Michael Raymer, Chunbai Wu, and John Roberts.

Thanks to those others who helped for the thesis: Peter Mosley, Brian Mangan and Fei Yu. Especially to Peter Mosley who gives many useful suggestions.

Finally I would like to thank helpful technicians--Bob Draper, Wendy Lambson, Steven Renshaw and Alan George.

This thesis is dedicated to my husband and my parents who I thank for continuous support in my life.

Table of Contents

Publication List

Journal Papers

1. Y. Y. Wang, F. Couny, P. J. Roberts and F. Benabid. "Low loss broadband transmission in optimized core-shape Kagome Hollow-Core PCF", *Opt. Lett.* **36** 669-671 (2011).

2. W. Chunbai, M. G. Raymer, Y. Y. Wang and F. Benabid. "Quantum theory of phase correlations in optical frequency combs generated by stimulated Raman scattering", *Phys. Rev. A* **82**, 053834 (2010).

3. Y. Y. Wang, C. Wu, F. Couny, M. G. Raymer and F. Benabid. "Vacuum fluctuation-initiated coherence in multi-octave optical frequency Raman combs", *Phys. Rev. Letts.* **105**, 123603 (2010).

4. B. Beaudou, F. Couny, Y. Y. Wang, P. S. Light, N. V. Wheeler, F. Gérôme, and F. Benabid. "Matched cascade of bandgap-shift and frequency-conversion using stimulated Raman scattering in a tapered hollow-core photonic crystal fibre", *Opt. Express* **18**, 12381–12390 (2010).

5. Y. Y. Wang, F. Couny, P.S. Light, B.J. Mangan & F. Benabid. "Compact and portable multiline UV and visible Raman lasers in hydrogen-filled HC-PCF" *Opt. Lett.* **35,** 1127-1129 (2010). (Also published in the *Virtual Journal for Biomedical Optics* **5** 1127-1129 (2010)).

6. F. Benabid, F. Couny and Y. Y. Wang. "NOVEL LASERS: Photonic microcell unleashes the full potential of gas lasers" *Laser Focus World*. **46** May (2010).

7. P. S. Light, F. Couny, Y. Y. Wang, N. V. Wheeler, P. J. Roberts and F. Benabid. "Double photonic bandgap hollow-core photonic crystal fiber" *Opt. Express* **17,** 16238-16243 (2009). (Highlighted by *Nature Photonics* **3**, 606 - 607 (2009)).

8. Y. Y. Wang, P. S. Light and F. Benabid "Core-Surround Shaping of Hollow-Core Photonic Crystal Fiber Via HF Etching". *IEEE Photonics Technol. Lett.* **20** 1018-1020 (2008).

9. Yiquan Wang, Y. Y. Wang, Shuai Feng and Zhiyuan Li, "The effect of short-range and long-range orientational orders on the transmission properties of quasiperiodic photonic crystals" *Europhys. Lett.* **74**, 49–54 (2006).

Conference Papers

1. Y. Y. Wang, A. Husakou, B. Mangan and F. Benabid "Spatial and Temporal Dynamics of Raman Coherence in Hydrogen-filled HC-PCF" *The Conference on Lasers and Electro-Optics (CLEO) 2011*, QTuO4.

2. Y. Cheng, Y. Y. Wang and F. Benabid "Fabrication and Characterization of Ultra-large Core Size (>100μm) Kagome Fiber for Laser Power Handling" *The Conference on Lasers and Electro-Optics (CLEO) 2011*, CTuE1.

3. O. Heckl, C. Saraceno, C. Baer, T. Südmeyer, Y. Cheng, Y. Y. Wang and F. Benabid "Temporal Pulse Compression in a Xe-Filled Kagome-Type Hollow-Core Photonic Crystal Fiber at High Average Power." *The Conference on Lasers and Electro-Optics (CLEO) 2011*, CMJ1.

4. C. Wang, N. V. Wheeler, J. Lim, K. Knabe, M. Grogan, Y. Y. Wang, B. R. Washburn, F. Benabid and K. L. Corwin "Portable Acetylene Frequency References inside Sealed Hollow-core Kagome Photonic Crystal Fiber." *The Conference on Lasers and Electro-Optics (CLEO) 2011*, CFC1.

5. Y. Y. Wang, F. Gerome, G. Humbert, J.M. Blondy and F. Benabid, "Low loss and broadband hollow-core photonic crystal fibers" *SPIE Photonics West 2011*. **Invited Talk.**

6. N. V. Wheeler, Y. Y. Wang, M. D. W. Grogan, T. A. Birks and F. Benabid, "large core photonic microcells" *SPIE Photonics West 2011.* **Invited Talk.**

7. F. Benabid, Y. Y. Wang, "Quantum fluctuation initiated coherence in multi-octave Raman frequency comb" *Colloquium on Physics of Quantum Electronics 2011 (PQE)* **Invited Talk.**

8. Y. Y. Wang, F. Couny, P. J. Roberts and F. Benabid, "Low loss broadband transmission in optimized core-shape Kagome hollow-core PCF" *The Conference on Lasers and Electro-Optics (CLEO) 2010*, CPDB4, **Post-deadline Paper.**

9. Y. Y. Wang, F. Couny, P. S. Light, B. J. Mangan and F. Benabid, "Compact and portable multiline UV & visible Raman lasers in hydrogen-filled HC-PCF" *The Conference on Lasers and Electro-Optics (CLEO) 2010*, CTuM2.

10. Y. Y. Wang, F. Couny, B. J. Mangan and F. Benabid, "Ultra-long-lived molecular coherence in hydrogen filled hollow-core photonic crystal fiber", *The Conference on Lasers and Electro-Optics (CLEO) 2010*, QTuG1.

11. C. Wu, E. Mondloch, M. G. Raymer, Y. Y. Wang, F. Couny and F. Benabid, "spontaneous phase anti-correlations in Raman optical frequency comb generation", *The Conference on Lasers and Electro-Optics (CLEO) 2010*, QTuA5.

12. M. Katsuragawa, K. Raju, P. K. Shiraga, H. Aoki, F. Benabid, F. Couny, and Y. Y. Wang, "Efficient generation of broad Raman sidebands in a kagome-lattice-type photonic crystal fiber" *The Conference on Lasers and Electro-Optics (CLEO) 2010*, CTuT6.

13. Y. Y. Wang, F. Couny, P. S. Light and F. Benabid, "Compact and Portable Multiline UV & Visible Raman Laser in Hydrogen-filled HC-PCF" *European Conference on Optical Communication (ECOC) 2009*, **Post-deadline Paper.**

14. Y. Y. Wang, F. Couny, P. S. Light and F. Benabid. "Coherence Properties of Optical Frequency Comb Generated in Large Pitch HC-PCF Filled with H2." *The Conference on Lasers and Electro-Optics (CLEO) 2009*, CTuB4.

15. P. S. Light, F. Couny, Y. Y. Wang, N. V. Wheeler, P. J. Roberts and F. Benabid, "Double Photonic Bandgap Hollow-Core PCF." *The Conference on Lasers and Electro-Optics (CLEO) 2009*, CPDA7, **Post-deadline Paper.**

16. F. Couny, B. Beaudou, P. S. Light, Y. Y. Wang, N. V. Wheeler, F. Gerome and F. Benabid, "Modal and spectral evolution of Raman lines in a H2-filled hollow-core PCF taper" *The Conference on Lasers and Electro-Optics (CLEO) 2009*, JTuB4.

17. Y. Y. Wang, P. S. Light and F. Benabid, "Core-surround Shaping of Hollow Core Photonic Crystal Fiber via Fiber Etching." *The Conference on Lasers and Electro-Optics (CLEO) 2008*, JFE2.

18. G. Humbert, Y. Y. Wang, P. S. Light, F. Benabid, and P. J. Roberts, "Nonlinear effects in a silica-node of a hollow-core photonic crystal fiber within the photonic bandgap" *The Conference on Lasers and Electro-Optics (CLEO) 2008,* JTuA49.

19. B. Beaudou, F. Couny, Y. Y. Wang, P. S. Light and F. Benabid, "Tapered Hollow-Core Photonic Crystal fiber for Cascaded Stimulated-Raman-Scattering" *The Conference on Lasers and Electro-Optics (CLEO) 2008*, JFC5.

Abbreviations

AFF Air filling fraction

ARROW Anti-Resonant Reflective Optical Waveguides

AS1 1st order anti-Stokes

BOE Buffered oxide etchant

Cavity QED Cavity quantum electrodynamics

CEP Carrier-envelope phase

DOPS Density of photonic states

EIT Electromagnetically induced transparency

FOM Figure of merit

FWHM Full width at half maximum

FWM Four wave mixing

GPPM Gas phase photonics material group

H_2 Molecular hydrogen

HC-PCF Hollow-core photonic cystal fibre

HF Hydrofluoric acid

HHG High harmonic generation

IR Infrared

OSA Optical spectrum analyzer

PBG Photonic bandgap

PMC Photonic microcell

S/AS	Stokes and anti-Stokes
S1	1st order Stokes
SEM	Scanning electron microscope
SMF	Single mode fibre
SRS	Stimulated Raman Scattering
TIR	Total internal reflection

Chapter 1

Background and Introduction

In this opening chapter, we review the prior work that underlies the scope of the present thesis. The review includes the physics governing the light guidance mechanisms of the two main types of HC-PCF that emerged in the last decade. Furthermore, we discuss how these fibres make an ideal host for laser-gas interactions and the technique of gas loading inside the fibre core that this entails. Finally, we review the basic knowledge of SRS and the previous achievements made in SRS in H_2-filled HC-PCF.

1.1 Historical Overview of HC-PCF

The idea of photonic bandgap (PBG) and the subsequent photonic crystal materials were first proposed in 1987 by Yablonovitch [1] and John [2]. Photonic bandgap is a region in the wavevector-frequency space where an electromagnetic wave with a given wavelength and propagating at a given direction is forbidden to travel through. Similar to electronic bandgaps in solid state physics, photonic bandgap often arises in periodic structures. In 1991, Russell [3, 4] extended the PBG concept, which thus far was limited to the case of in-plane propagation, to out-of plane PBG. By in-plane propagation, we mean that the wave-vector of the electromagnetic wave is perpendicular to the periodicity plane of the photonic structure. Here, the photonic bandgaps of interest are those related to confined and guided optical modes along a direction which lies out-of-plane of the photonic structure periodicity. This breakthrough led to the first theoretical demonstration of the out-of-plane PBG in 1995 by Birks *et al*. [5] suggesting that a PBG could be observed in a structure such as the one shown in fig. 1.1a and that a new type of fibre (called PCF) could guide with no need for total internal reflection (TIR). The experimental demonstration of a PBG air-guiding fibre known as hollow-core photonic crystal fibre (HC-PCF) was then reported by Cregan *et al* in 1999 [6]. In addition to the interest of this newly introduced concept of out-of-plane PBG optical guidance, among the major driving motivations in investigating such a fibre was the development of an optical fibre for long-haul communication that could transmit light with much lower optical power loss that the state-of-the-art of conventional optical fibre. Propagation loss could be dramatically lower than that of silica, where the ultimate linear optical loss figure is set by the Rayleigh scattering, would be much reduced for an air-guiding fibre. Indeed, since HC-PCF guides light in a hollow core, it can potentially guide light with several orders of magnitude lower than the fundamental limit of ~0.16 dB/km achievable in silica based single mode fibre. Hitherto, however, the lowest loss obtained with this type of fibre is 1.2 dB/km, which is still one order of magnitude higher than conventional fibre. This is mainly due to the roughness of the air/glass interface [7] which is inherent to the fibre fabrication technique.

Another major concern of this PBG guided HC-PCF is its limited transmission bandwidth of ~ 70 THz due to its intrinsic guiding mechanism. This gives rise to the development of another type of HC-PCF which doesn't guide through a bandgap. It was first reported in 2002 in a fibre with Kagome lattice structure by Benabid *et al* [8] where an extended guidance over a broad frequency band is presented. However at that time, the guidance mechanism was not well understood. This hindered its further improvement to the fibre loss and transmission bandwidth. From 2006, the broadband guidance HC-PCF acquired a rapid development in both the experimental fabrication [9-11] and the physical understanding [11-13]. It was shown that this type of fibre favors a large pitch and guides via inhibited coupling between the core modes and the cladding modes. Compared to the PBG HC-PCF, the drawback is its relatively higher loss (>0.5 dB/m)*.

Despite the above mentioned higher attenuation of the two types of fibres compared to the conventional optical fibre, the fact that HC-PCF guides light in air instead of silica opens a great number of applications. For example, the ability to guide light in air or vacuum offers the possibility of transporting short and powerful laser pulses with little spectral or temporal distortion due to low optical nonlinearity [14]. Furthermore, by engineering the fibre chromatic dispersion, picosecond-duration laser-pulses were compressed to one hundred femtosecond duration [15]. Another important application, which is well developed in Benabid's group, is the enhanced gas-laser interaction. By filling the core of a HC-PCF with a particular gas and illuminating it with a laser, light and matter can interact in a diffractionless manner along several metres of fibre with very high efficiency thanks to the μm scale core size and the low intrinsic loss of the HC-PCF. Based on this enhanced interaction efficiency, subtle quantum effects become observable for the first time, for example in electromagnetically induced transparency (EIT) in molecular gas [16, 17]. Closer to the

* This figure has since been dramatically reduced by the author, see chapter 4.

subject of this thesis, non-linear light matter interaction can also occur, for example by introducing a Raman active medium such as H_2 gas into the hollow-core. As a matter of fact, a series of breakthroughs have been made in this area of nonlinear optics, that led for the first time to a million-fold reduction in the threshold for SRS generation compared to experiments performed in free space, allowing the use of a single, low average-power nanosecond pulsed laser [11] in the experimental setup. These results led to the generation of a Raman frequency comb in a H_2-filled HC-PCF, the main topic of this thesis.

In this chapter, we cover in more details our current understanding of how light is guided in the PBG-guidance small-pitch triangular-structure* HC-PCF (known as PBG HC-PCF for short) and inhibited-coupling guidance large-pitch typically Kagome-structure HC-PCF (known as Kagome HC-PCF for short)† described above (Section 1.2). Section 1.3 presents some of the evidence behind the rationale of using HC-PCF for gas-laser interaction, as well as some of the techniques for gas-loading into these intricate structures. The final section of the chapter will be concerned with the particular application of SRS in HC-PCF (Section 1.4). These sections provide fundamental basis for understanding the work presented throughout this thesis.

1.2 Light Guidance in HC-PCF

Photonic Crystal Fibre is a type of optical fibre where the cross section comprises a 2D photonic crystal structure with a core defect at its centre (fig. 1.1a&b). This core acts as the light guiding feature of the optical fibre. The propagating modes of that core defect are described by their propagation constant β, which is the component of the light

* The term "triangular-structure" is chosen for historical reasons, and refers to the triangular arrangement of the air-holes of the photonic structure. In some publications, it is called "honeycomb-structure" due to the arrangement of the apex.

† Here the Kagome HC-PCF is named by its structure and the PBG HC-PCF is named by its guidance mechanism. This is due to historical reasons.

wavevector k_0 along the propagation axis (fig. 1.1b). In order to identify the guiding properties of a particular structure, it is useful to study the dispersion diagram of the defectless infinite photonic crystal, which corresponds to an infinite cladding. This gives a diagram linking β (sometimes expressed as the effective index $n_{eff}=\beta/k_0$) to k_0 as shown schematically in fig. 1.1c [5]. Here, both quantities are normalized by multiplying by the cladding pitch Λ (the spacing between neighbouring rods, see fig. 1.1c). Thanks to the photonic structure of a PCF's cladding, the dispersion diagram contains more features than conventional optical fibre or total internal reflection waveguide, including bandgap "fingers" that can potentially cross the low index material. Here, we consider a PCF made up of two different materials, we use n_{high} and n_{low} to indicate the refractive indices of the high index material (usually silica) and the low index material (usually air) respectively. These indices are represented in the dispersion diagram by straight purple lines (material dispersion is ignored). In order to highlight the different guidance mechanisms that are possible with PCF, we introduce schematically in the diagram the index n_{clad} which represents the effective index of the fundamental and extended mode of the cladding photonic structure (curved purple line in fig. 1.1c). The three dispersion lines n_{high} and n_{low} and n_{clad} represent reference lines whereby below each line light is forbidden to propagate in that particular medium.

With the introduction of a core-defect in the photonic structure (we still limit to two materials in the structure), core-guided modes can exist, their effective index ($n_{eff}=\beta/k_0$) position within the dispersion diagram hints at the guidance mechanism involved. Indeed, depending on the index of the core defect relative to that of the cladding, light in PCF could either be guided by conventional TIR, by PBG guidance [5] or the most recently proposed inhibited coupling guidance [11]. If the core material support modes with effective indices such that $n_{eff}>n_{clad}$ (dark grey region in fig. 1.1c), light is guided by TIR. This is the typical case in solid core PCF. If the core is chosen such that $n_{eff}<n_{clad}$ (white and light grey regions in fig. 1.1c), light can't be guided by TIR. Instead, optical guidance could occur if the couple ($\beta\Lambda$, $k_0\Lambda$) falls into one of the photonic bandgap finger-shaped regions which are represented as blue zones in the dispersion diagram and corresponds to a combination ($\beta\Lambda$, $k_0\Lambda$) for which the cladding photonic structure doesn't support modes. From the diagram we see that these regions

do extend below n_{low}, which means PBG guidance is possible with a defect whose material index is lower than n_{low} (white region in fig. 1.1c). Consequently, if the low-index material is air, guidance in a hollow-core via PBG is possible over a bandwidth approximately given by the width of the light blue region along the air-line. Such bandgap guidance is experimentally observed in hollow core PCF [6] and in all solid PBG PCF [18]. The mechanism by which the PBG regions are formed is discussed in section 1.2.1.

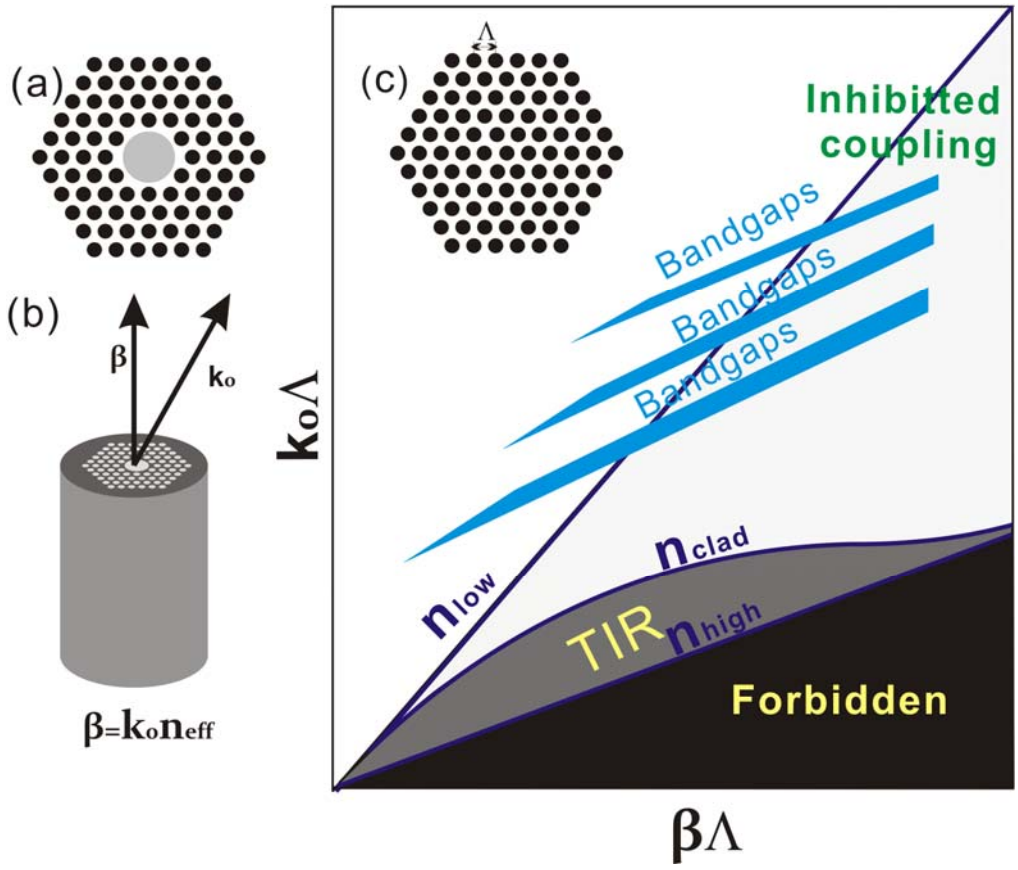

Fig. 1.1 (a) Typical cross section of a PCF; (b) Geometrical presentation of the wavector k_0 versus its component along propagation axis β; (c) Typical propagation/ band diagram of a defectless PCF (as shown in the insert of (c)) plotted by normalized wavevector $\beta\Lambda$ versus $k_0\Lambda$ showing different regions of light guidance. The three purple curves represents three reference lines n_{high} and n_{low} and n_{clad} and below each line light is forbidden to propagate in that particular medium. The blue regions are bandgaps.

In addition to PBG, it was recently demonstrated that guidance in the region of $n_{eff}<n_{low,}$ could be achieved via another guidance mechanism called inhibited coupling or Von Neumann Wigner optical guidance in a large pitch region [11, 19], details of which are discussed in section 1.2.2. The Kagome HC-PCF [9] is the typical example of

such guidance and it was recently demonstrated that in some solid core fibre, light can also be guided by inhibited coupling [20].

In the following sections, we will elaborate on the PBG and the inhibited-coupling guidance mechanisms and how these are implemented in HC-PCF. The TIR guidance of PCF will not be discussed here since it is well known in conventional optical fibres.

1.2.1 Photonic bandgap guidance

Conventionally, the design of PCF is usually undertaken by solving the full-vectorial Maxwell-Helmholtz equation and casting it as an eigenvalue problem using either the planar wave expansion or finite element methods [21]. The results of such a heavy numerical calculation give the density of the photonic state (DOPS) in the cladding structure for each (β, k_0), a more detailed version of the simplified schematic example of fig 1.1c. Despite their power in predicting the dispersion of each mode of the cladding, these calculations gave little insight on how PBG in PCF are formed. To gain a better understanding of the mechanism behind the guidance, a strong parallel between the formation of photonic bandgaps in optical fibres and the tight-binding model [22] in solid state physics has been drawn and experimentally demonstrated [23].

As a reminder, the tight binding model of solid state physics stipulates that the electronic allowed states, in a crystal for example, are formed as the results of "bringing closely together" the isolated and identical atoms constituting the crystal (fig. 1.2a). Let's consider a crystal formed by well separated individual atoms with well defined electronic energy levels and wavefunctions. As the atoms move closer together, the crystal's wavefunction (Bloch functions) becomes delocalized and the degeneracy of its energy levels is lifted, creating bands of electronic states which are a linear superposition of the isolated atomic wavefunctions. The electronic state with the highest energy (upper side of the band) is formed by an antisymmetric wavefunction, in which the sign of the wavefunction changes upon moving from a chosen site to a nearest neighbour. The lower energy level is symmetric, i.e. it shows no sign of oscillations, and is a more tightly-bounded state. It was suggested in [23] that a similar model can be constructed in the periodic structure of a photonic crystal (fig. 1.2b) simply by replacing the electrons around the atomic nucleus with photons guided in

high index waveguides (eg. silica rods). Other parameters are analogized accordingly as shown in fig. 1.2. The energy level is regarded as the effective indices of the guided mode. The difference however is that the electrons naturally sit in a low ground state energy level (potential well) while photons are guided in the highest refractive index material. Similar to the electronic band gaps formed between the ground and excited energy levels, the photonic bandgap is formed in the dispersion diagram between fundamental mode and high order modes of the high index waveguides.

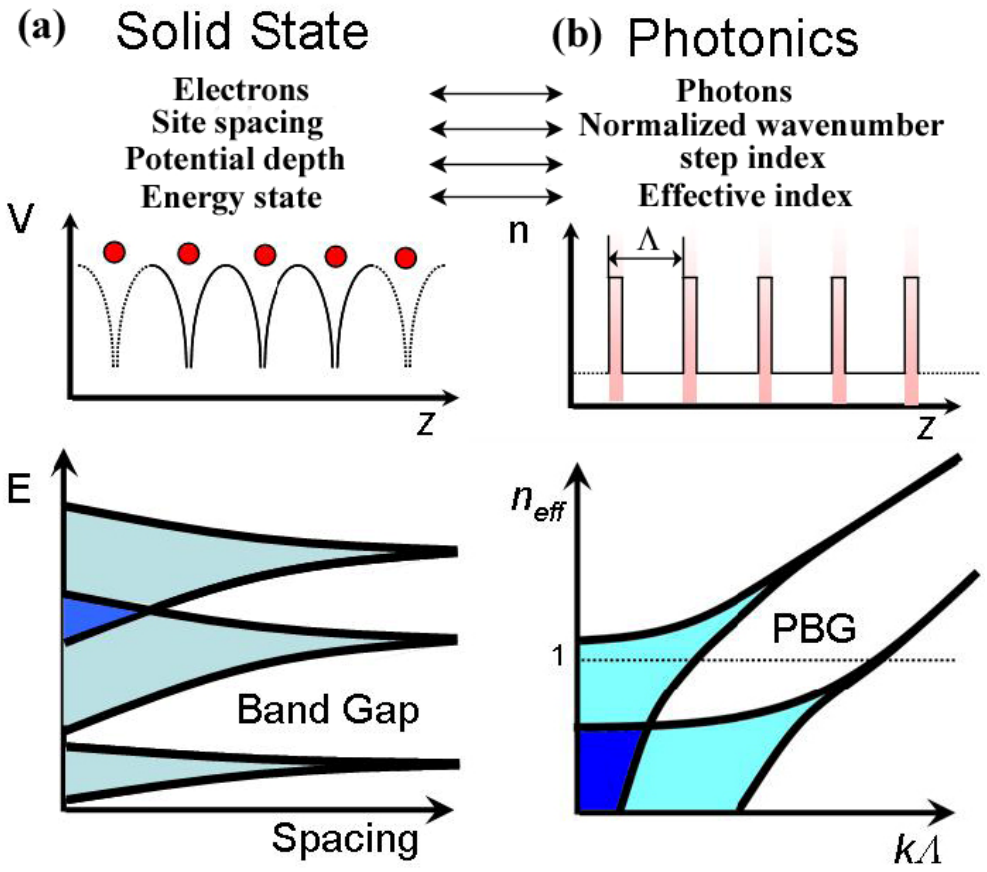

Fig. 1.2 Schematic illustration showing the analogy of photonic allowed bands & bandgap (b) to the atomic allowed bands & bandgap (a) [24] .

Now let's consider in more details how these photonic bandgaps are formed. Fig. 1.3a plots the dispersion curves of different modes (LP_{01} and LP_{11}) supported in a single silica rod. The dispersion curves for these modes follow the following analytical expression [25]:

$$\beta^2 = (n_{co}k)^2 - \frac{U_\infty^2}{\rho^2}\frac{k^2}{(k+\eta/\rho)^2} \tag{1.1}$$

where ρ is the radius of the rod, U_∞ is the modal constant equal to 2.405 for the fundamental mode and to 3.832 for the second order mode. η is a function of refractive index of the rod n_{co}. Here n_{co} is taken to 1.45 and η is 0.7. When a 1D array of rods is considered, the coupled mode theory which is similar to the tight binding description is applied. The rods are assumed to have a Gaussian transverse mode profile and only couple to the nearest-neighbour rods. The calculated curve for 1000 rods with diameter 0.45Λ, where Λ is the pitch of the array is shown in fig. 1.3b. One can find that the increased coupling between the rods (decreasing $k\Lambda$) broadens the allowed individual effective modal indices into allowed bands, leaving photonic bandgaps to form in between (fig. 1.3b). As the frequency decreases, the spread in effective index of the allowed photonic bands increases, shifting these photonic bandgaps toward lower effective indices. It can be seen in this example that for $k\Lambda<7$, the bandgap can exist in the region $n_{eff}<1$ (shaded green area). Practically, this means that if a hollow defect is inserted in this array of rods, light can be guided in the defect*. In analogy to the most tightly bound state of the tight-binding model in atomic physics, the mode of the photonic crystal with the highest effective index corresponds to the most strongly confined mode (tight-bounded mode).

* Here, we ignore the effect of the modes in air.

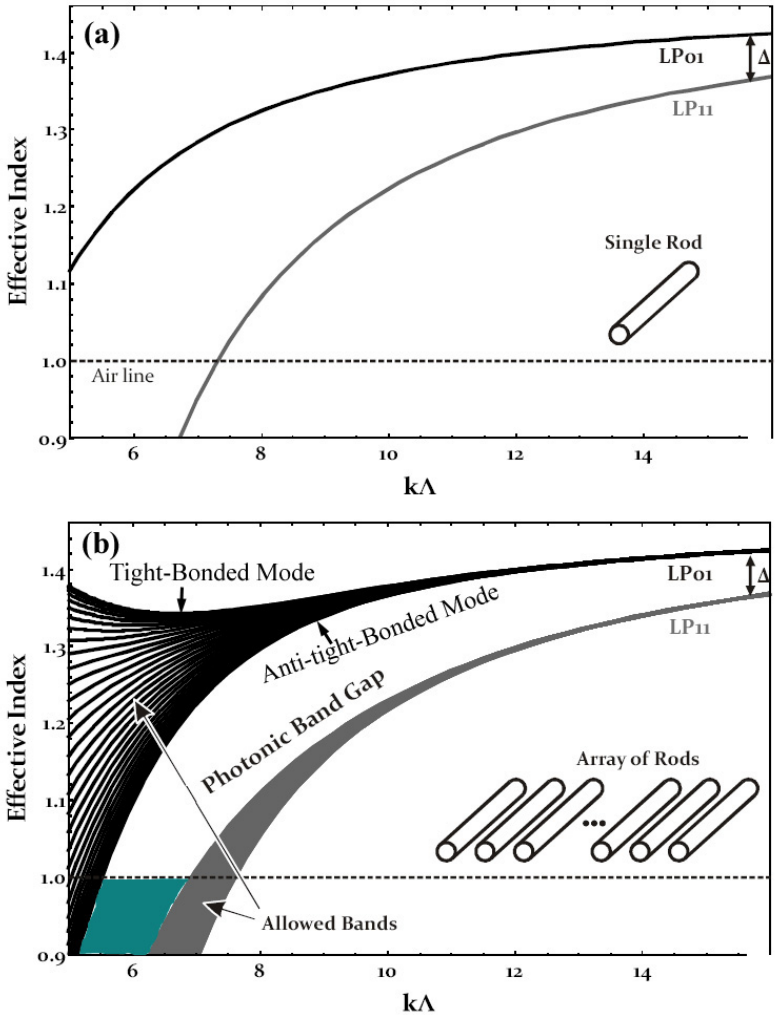

Fig. 1.3 Toy model for 1D periodic structure [24]. (a) Dispersion curves of a single rod and (b) dispersion curve of an array of rods.

This model is also valid for two dimensional photonic crystal structures (fig. 1.4a). For example, the all solid PBG fibre [18] where Ge-doped raised-index rods are distributed among low-index pure silica background (fig. 1.4b). It is worth mentioning that the first explanation of bandgap formation in the all solid PBG fibre was not given by the tight binding model but the "cellular method" [26] by Birks *et al.* [27] using a semi-analytical approach which models the out-of-plane mode structure of the fibre cladding. The model provides information on the width of the cladding pass-bands and gives better insights into the understanding of the formation of bandgaps in all-solid PBG PCFs than other explanations based on analogy to the Bragg fibre [28, 29] and the Anti-Resonant Reflective Optical Waveguides (ARROW) [30] model. However, the cellular method is of less use when considering HC-PCF. This is because the more

complicated structure in HC-PCF where the Ge-doped rods with pure silica background are replaced by pure silica rods (also called apexes) with air background and the apexes have to be connected by so-called silica struts (fig 1.4c). Because of this complex topological structure, the "cellular method" is not as comprehensive any more. Instead, Couny *et al*. [23] demonstrated that the tight binding model gives a broader insight into the guidance of HC-PCF by experimental identification of its structural features including apexes, struts and air holes.

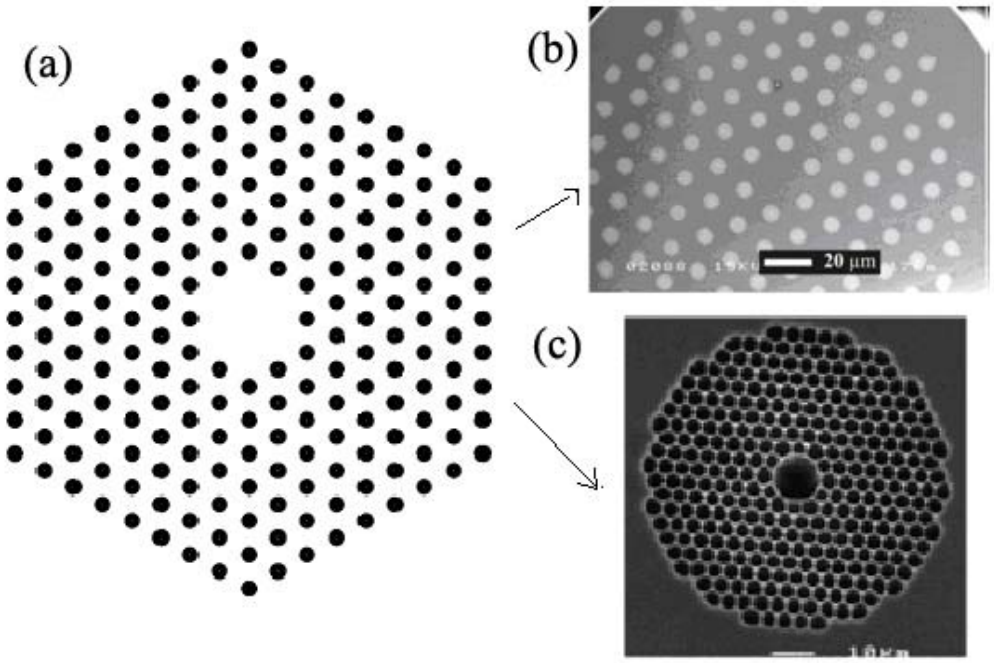

Fig. 1.4 (a). Model of a bandgap fibre structure. (b). realization in all solid bandgap fibre. (c).realization in HC-PCF.

Figure 1.5 shows the calculated DOPS diagram for PBG HC-PCF using the plane wave approach [31] for an infinite cladding structure (fig. 1.4c). The density of photonic states is, by definition, the number of allowed electromagnetic modes per unit frequency interval typically plotted against both normalized frequency ($k\Lambda$) and normalized wave-vector ($\beta\Lambda$) or effective refractive index (n_{eff}) of a given perfect photonic structure (i.e. with no core defect). It is a complied mapping of the solutions of the propagation equation and shows all modes supported in the periodic structure. It also indicates clearly the regions for which there are no solutions to the equation (i.e. no light can exist in any constituent of the structure). Compared to the dispersion

diagrams in fig. 1.1-fig. 1.3, the DOPS plot gains more insights into the PBG formation. In the DOPS map presented here, the DOPS is represented as a linear grey-scale ranging from dark for low allowed density of photonic states to white for a maximum DOPS. Black represents no solution to the propagation equation and therefore where photonic bandgap lies. For guidance to be achieved in a hollow core, the core modes need to lie within the black region of the PBG that is under the vacuum line (refractive index of the air) as plotted in dash-dotted white line in fig. 1.5. However, when the core mode arrives at the edge of the PBG, strong coupling is achieved between core and cladding mode, due to the very large overlap integral between them. This leads to energy transfer from core to cladding mode and ultimately increasing of the core mode loss at the edge of the bandgap. The bandwidth for PBG HC-PCF is thus limited. The coloured lines indicates the high symmetry modes, such as the tight bonded mode, including the modes that create the boundaries of the bandgaps. Calculated mode profiles for points A, B and C are shown in the right column of the fig. 1.5. One can clearly see that the bandgap edges are formed by the cladding modes with most of the lights from silica apexes (A), silica struts (B) and air holes (C). The experimental observation of these cladding modes has already been implemented with a scanning near-field optical microscope [23] which verifies this model.

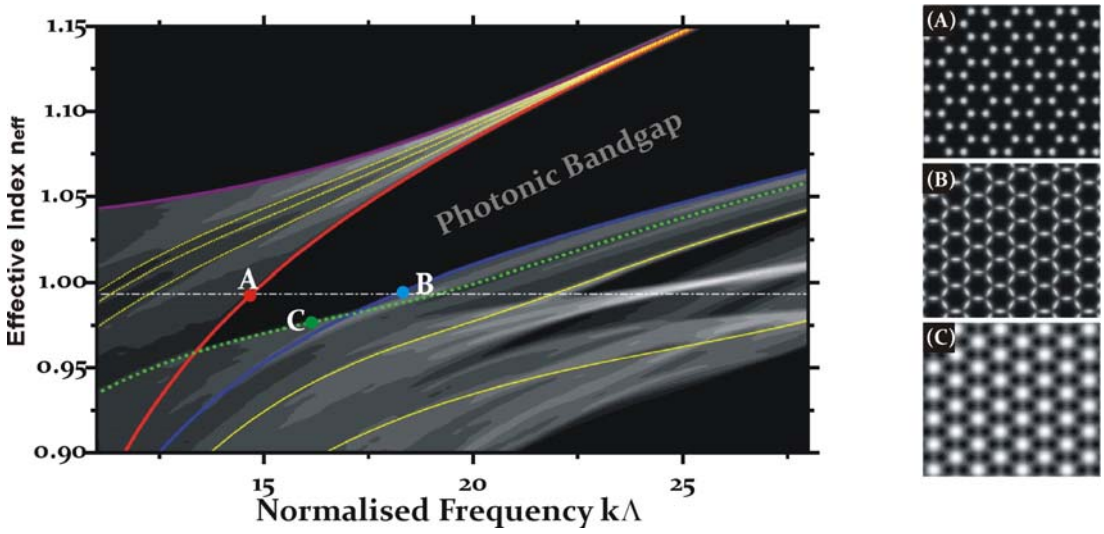

Fig. 1.5 Calculated DOPS diagram for a PBG HC-PCF cladding lattice [23]. A, B, C shows the cladding modes for the boundary of the bandgap below the air line. A: apex mode, B: strut mode, C: air mode.

The tight-binding model above not only provides us with a better understanding of out-of-plane PBG formation in HC-PCF but also offers routes to improve the optical attenuation and bandwidth of the fibre. For example, the most effective way to broaden the main bandgap shown in fig. 1.5 is to make the silica struts thinner and the apexes larger since the silica rods (apexes) are essential for forming bandgap structure while the struts are only a by-product of fabrication. Indeed, as shown in fig. 1.6, the width of the main bandgap increases dramatically with the increase of air filling fraction (AFF). However, the fabrication of large AFF fibre with a uniform structure is a challenge. The state-of-art fabrication shows an AFF=93% fibre with bandwidth of ~70THz and attenuation of 1.2dB/km at 1550nm [7]. It is also noteworthy that in fig. 1.5 at around $k\Lambda$=23, there is a second bandgap almost opening under the air line. This bandgap, however, favours a smaller apex. It will be shown in chapter 3 that by playing with the tight-binding model and carefully designing the three parameters: apex, strut thickness and air hole size (or pitch) the second bandgap can open for air guidance [32]. This leads to the fabrication of a single fibre with double bandgap and hence offers larger bandwidth for a number of applications.

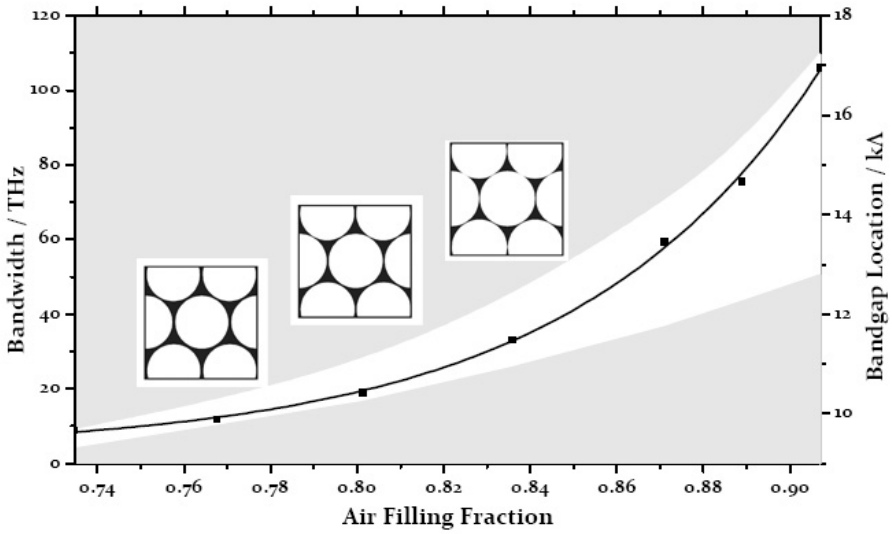

Fig. 1.6: Calculated bandgap width (solid line) and location of bandgap (white band) as a function of AFF for the structure formed by uniform circular holes (inserted) [23].

The above DOPS map is based on the cladding periodic and infinite structure with no defect considered and hence no modes inside the bandgap. When the core defect is introduced, a number of modes are allowed to form in the bandgap region. This

includes the fundamental and high order core modes guided in the air as well as surface modes residing in the inner side of the core-surround silica. These surface modes, by sharing the same frequency and the same propagation constant with the core modes, brings a phenomenon inside the bandgap called "anti-crossing". In chapter 2, we will focus on the properties of these modes where we show that by controlling the structure of the core shape, the mode properties can be tailored in the same way as the control of the cladding structure allows the shaping of the PBG itself.

1.2.2 Inhibited Coupling Guidance

In addition to the PBG HC-PCF, another type of HC-PCF exists. This class of HC-PCF doesn't rely on PBG for optical guidance, Kagome lattice HC-PCF is an example of such fibres. A salient feature of this type of HC-PCF is its broad transmission window compared to the PBG guiding HC-PCF. However, it exhibits a relatively higher loss figure (slightly less than 1 dB/m*).

Figure 1.7a shows a SEM of a typical 1-cell, 5-ring Kagome fibre†. As opposed to the triangular PBG HC-PCF (fig1.7c), the structure is formed by a tessellated "stars of David" pattern. Indeed, the word "Kagome" comes from the Japanese "bamboo basket". When observed under the microscope with a few centimetres of the fibre illuminated from below, one can see white light emerging from the Kagome fibre core indicating a broadband guidance (fig. 1.7b, at least in the visible region of the spectrum). The triangular PBG HC-PCF, on the other hand, guides only "one colour" (fig. 1.7c in the example green) hinting at a limited bandwidth.

* This figure, however, has been dramatically improved and reaching as 0.04 dB/m. Details of this are covered in chapter 4.

† By "N cell" we refer to a core defect which is formed by removing N cladding holes. Similarly, "M ring" corresponds to the number of layers of holes along a radial direction of the fibre cladding.

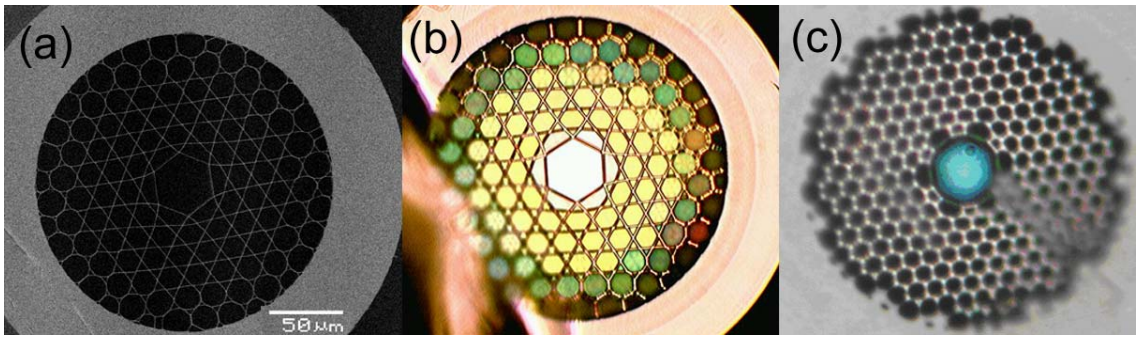

Fig. 1.7 (a) SEM of a Kagome fibre. (b) & (c) Comparison of the optical image under the microscope for (b) Kagome fibre and (c) triangular PBG fibre. (a) and (b) are the same fibre. (a) and (b) are scaled down to ~ 7 times smaller to have a comparison with (c).

Since the first demonstration of the fibre in 2002 the nature of the guidance mechanism of the Kagome fibre has attracted much attention, but it is only recently that the physics underlining the light guidance has been unveiled [11]. The DOPS of the Kagome cladding structure is shown in fig. 1.8. Here the DOPS diagram is in coloured form from red for high DOPS to blue for low DOPS and white for zero DOPS as indicated by the density legend in fig. 1.8. Also note that the Kagome fibre operates for much larger $k\Lambda$ ($k\Lambda$~100) compared to the PBG fibre ($k\Lambda$~15). In contrast to the triangular PBG cladding structure, the Kagome structure exhibits no bandgap but at the air line it passes through two low DOPS region I (for $k\Lambda$=20~60) and III (for $k\Lambda$=80~140) (fig. 1.8) with a higher DOPS region in between (for $k\Lambda$=60~80) [11]. At regions I and III, the resonance of the cladding holes are associated with the relatively flat deep red dispersion curves. One notices that these curves don't hybridize with those from the connected network of glass struts, which dispersion exhibits a steeper and less well pronounced blue-colored bands in region I and III or turquoise band in region II. This implicitly indicates the little symmetry overlap between the air-hole modes and the silica strut network modes which was corroborated later in [12].

In an attempt to explain the light confinement mechanism in Kagome fibre, Pearce *et al.* drew the analogy between the Kagome structure and the Bragg fibre [13]. However, the description does not provide a clear explanation as to why a leaky guided core-mode can cohabitate with cladding modes with seemingly perfect longitudinal phase matching (same propagation constant). A full explanation that likened the guidance mechanism to the Von-Neumann Wigner bound state in a

continuum from quantum physics was given in [11]. The existence of core modes (bound or quasi-bound states) within a continuum of cladding modes is explained by the fast oscillating transverse-field of the silica confined strut modes, which in turn results in a strong transverse wave-vector component mismatch with the core modes. In this way, the coupling between core and cladding modes is "inhibited" and light is guided in the air core with relatively low loss over the large spectral region of inhibition (I and III in fig. 1.8).

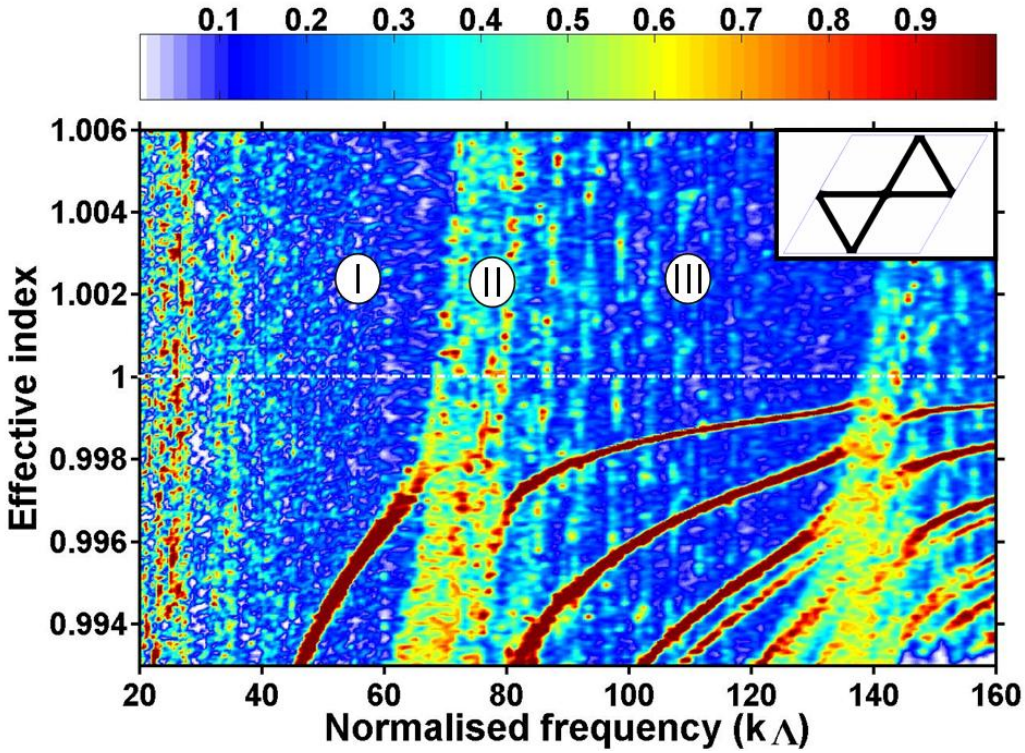

Fig. 1.8 DOPS map for Kagome lattice structure with a pitch of 12μm [11] (normalized wavevector up to 200, much larger than in PBG fibre). The white line indicates the air line which goes through the band I with low DOPS, band II with high DOPS and band III with low DOPS.

Figure 1.9 shows calculated core mode, cladding mode (based on a finite structure with a core defect) and unit-cell lattice mode (based on an infinite structure without core defect) at regions I, II and III of the DOPS map presented in fig. 1.8. For high transmission bands (regions I and III) and as predicted by the inhibited coupling theory, the core mode is strongly located in the air core with a slowly-varying phase distribution (i.e. HE_{11} like mode). The cladding modes with the same $k\Lambda$ and n_{eff} ($<10^{-5}$ difference with that of the core mode) are strongly localized in the silica struts with

rapid field decay into the air region. Moreover, the cladding modes in these regions exhibit fast phase oscillation of the field in glass, a manifestation of the large transverse wavevector components (i.e. higher order modes). This field distribution of the cladding mode is similar to that of whispering gallery modes [33] or high azimuthal number (m) modes in a thin ring waveguide [34]. Within this analogy, and approximating the thin silica web of a Kagome cladding structure to hexagonal rings [13], it is easy to link the supported mode azimuthal number to the perimeter length, l, and thickness, t, of the ring waveguide by $m = n_{eff}\left(l/\lambda\right)\left(1-\pi\left(t/l\right)\right)$ [34]. By virtue of the overlap integral definition, the power coupling between the slowly transverse phase-varying core modes and these fast-oscillating cladding modes decreases exponentially with the azimuthal number (fig. 1.10). One would then expect cladding modes with high m-number to couple less with the core modes than cladding modes with low m-number. As a matter of fact, these high azimuthal number modes could have very close propagation constant with a core guided mode (i.e. $\Delta\beta \sim 0$) without strongly interacting because the figure of merit of coupled waveguides $X = \Delta\beta/\kappa$ could remain much larger than one. Here κ is the overlap integral coefficient.

In region II of fig 1.8, core modes exhibit high loss, associated with glass strut modes on resonance with the cladding air hole modes. The lowest order resonance wavelength is estimated by $k\Lambda = \pi\left(\Lambda/t\right)\Big/\sqrt{n_{gl}^2-1}$, where t is the strut thickness and n_{gl} is the refractive index of the glass. For the thickness t=0.044Λ of the struts used in the calculation of fig. 1.8, this corresponds to $k\Lambda$=68, which coincides with normalised wavenumber values around which strong mode interaction is evident (fig. 1.9 II). The interaction increases the effective index of some of the air-dominated modes so that they may phase-match with the HE_{11}-like resonance of the core. This is similar to that of the anti-crossing modes in PBG HC-PCF mentioned in the previous section and to be discussed in chapter 2.

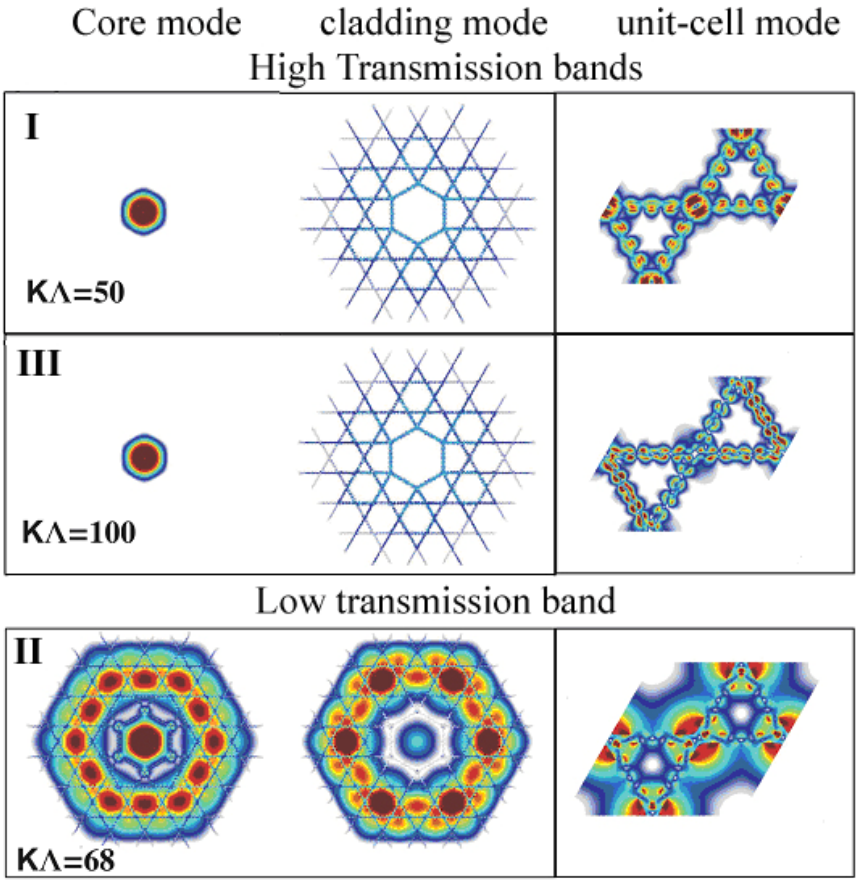

Fig. 1.9 Nature of the modes of the Kagome HC-PCF [11]. The first two columns show the core mode and a cladding mode with the same frequency and similar effective indices based on a finite structure with a core defect. The third column shows the mode of an infinite Kagome lattice structure without core defect. The three rows I, III and II correspond to the three bands shown in fig. 1.8.

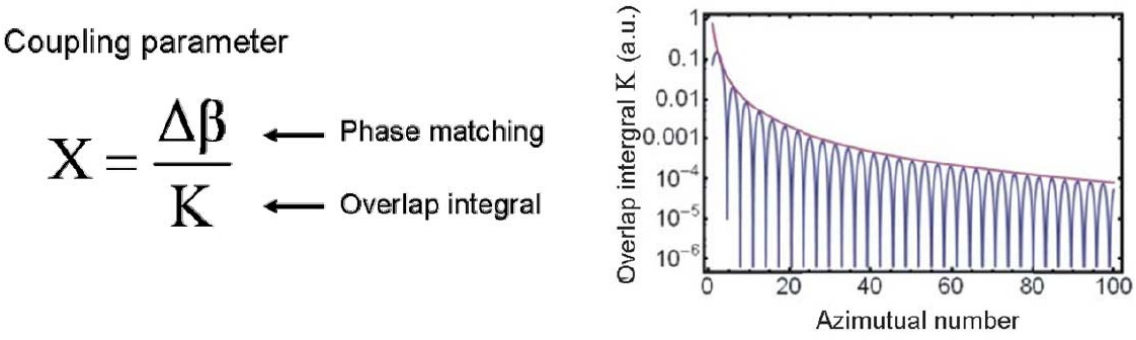

Fig. 1.10 The relationship between the coupling coefficient and the azimutual number derived from the coupled mode theory [34].

According to the expression of the azimuthal number, *m* is increased with the length of wave-guiding ring-like silica web relative to the guided wavelength and by

reducing the thickness of silica web relative to this length. Geometrically, this means that an ideal cladding structure topology for low loss and broadband guidance via inhibited coupling would require an elongated and thin silica web with no sharp bends or "nodes" so to increase the transverse mismatch via increasing the azimuthal-like number [11]. Figure 1.11 shows characteristics of three Kagome fibres fabricated with a view to optimizing the transmission bands. The thickness reduction obtained for fibres B and C compared to fibre A results in a dramatic enhancement of the transmission bandwidth accompanied by a shift of the bands to shorter wavelength.

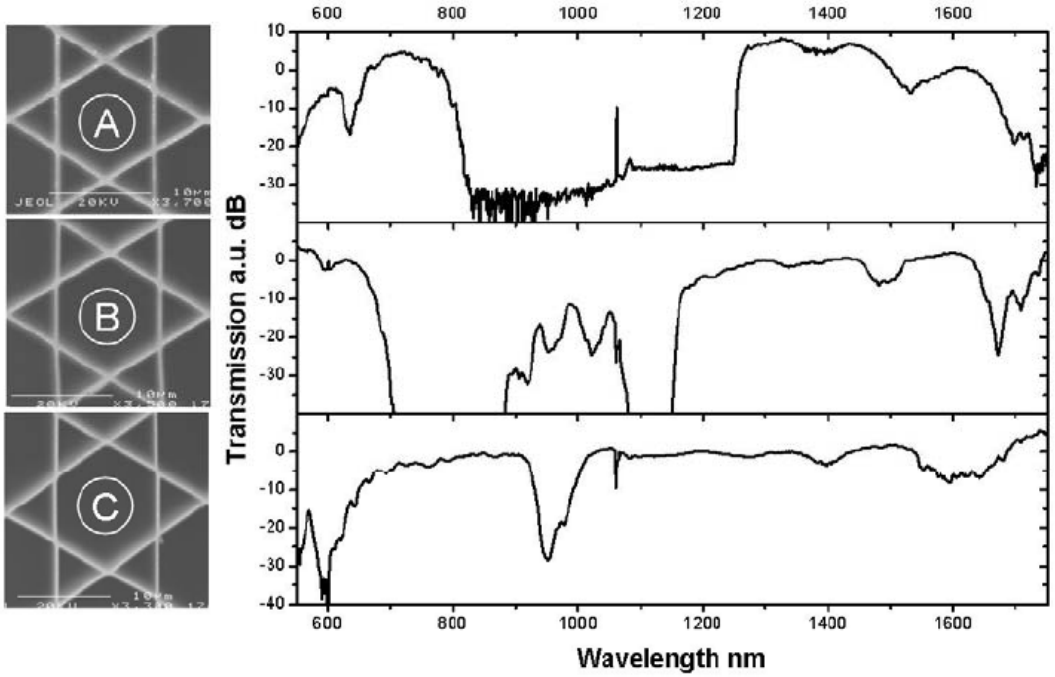

Fig. 1.11 SEM images of the cladding of a Kagome fibre fabricated at (A) 0 kPa, (B) 20 kPa and (C) 50 kPa gas pressure applied to both cladding and core [9]. For each fibre, an optical spectrum obtained using a supercontinuum source and an OSA, is attached alongside the corresponding SEM.

In a view to increase further the cladding strut length and diminish the number of nodes, another type of cladding topology: square lattice (fig. 1.12) was fabricated [10] with longer strut length and fewer nodes. It was theoretically predicted to have a considerably lower loss than the Kagome fibre though the experimental measurements shows similar properties as the Kagome. Furthermore, inhibited coupling was recently observed in solid core polymer fibre expanding the bandwidth to ~ 1 octave [20].

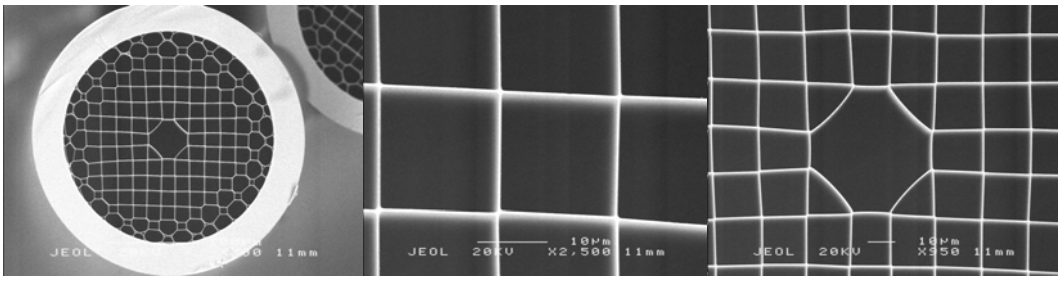

Fig. 1.12 Square-lattice HC-PCF with similar guiding mechanism and similar optical properties with Kagome-lattice HC-PCF [10].

Even though the cladding geometry has been optimized to the limit of the fabrication process, the optical attenuation figure over large bandwidth has stayed above 0.5 dB/m. Further improvement of the fibre relies on the core geometry optimization in a way that no distortion is introduced in the first ring of the cladding structure since most of the core-cladding field overlap occurs in this region. Indeed, as will be detailed demonstrated in chapter 4, we recently developed a hypocycloid core shape 7 cell Kagome HC-PCF that reduced the loss to ~0.04 dB/m. This is comparable to PBG fibre at some wavelengths with a much broader bandwidth.

1.3 HC-PCF for Gas-Laser Interactions

Advances in understanding of the guidance mechanism of HC-PCF highlighted above have been strongly driven by the development of the fabrication process of such fibres, as well as by their use in key photonic applications. One advantage of the hollow core fibre is that it can be filled with gas or liquid, hence making it an ideal host for matter-laser interactions. For example, some quantum effects, like EIT, that require stringent optical specifications in free space experiments or in those using glass capillaries, can be achieved in HC-PCF with much simpler optical designs and with a considerable reduction of optical requirements.

As I will introduce in section 1.4 (and show in more details in chapters 5 to 8), gas-filled HCPCF has now become a platform for rediscovering the SRS effect, and more especially for studying in depth the coherent properties of the generated Raman lines (called Stokes lines) in “low power, all-fibre” experimental setups. In this section, we will first present the rationale behind using these types of fibre to enhance the

interaction between the photons of the laser, propagating down the fibre, and the atoms and molecules of a gas or liquid, filling the hollow core. Then we will present the various techniques for filling gas into a HCPCF with as little impact as possible on the optical properties of the ensemble.

1.3.1 Figure-of-Merit

The driving force behind the use of HC-PCF for gas-laser interaction is their capability to enhance the effect by up to a millionfold. When considering interactions between photons and atoms (or molecule) inside a medium, the ideal optical parameters that influence the efficiency of these interactions would be (i) a diffraction-free propagation of light (ii) a low power loss and (iii) light confinement to very small area. This can be quantified by the following figure of merit (FOM):

$$FOM = \frac{L_{eff}}{A_{eff}} \times \lambda \tag{1.2}$$

where L_{eff} is the effective interaction length, A_{eff} is the effective area of interaction and λ is the wavelength of the laser. It can be easily seen that a small area of interaction over long distances is desirable to achieve a good interaction. Applying this definition to the specific cases of free space propagation, capillary guidance and comparing it to the results obtained for typical HC-PCF, one can build a picture of interaction enhancement of the HC-PCF compared to other techniques (fig. 1.13)

When propagating in free space (fig. 1.13a first row), the collimated beam will diverge after a given length. For a Gaussian beam, the interaction length is limited by the divergence of the focused laser beam expressed as twice the Rayleigh length: $L_{int}=2\pi w^2/\lambda$, where w is the beam waist radius and the effective area A_{eff} is approximately the beam waist area. This yields an FOM of ~2 (fig. 1.13b purple solid line). A common way to increase the FOM is to use a capillary (fig. 1.13a second row), also called "hollow waveguide". It can provide increased interaction length and smaller interaction area (by reducing the core size). However, this technique suffers from a fundamental limitation: it is a leaky waveguide with an exponential loss rate

inversely proportional to the core radius (fig. 1.13b green dash-dot curve). The FOM in this case is [8]:

$$FOM_{capillary} = \frac{6.8a\sqrt{n^2+1}}{\pi\lambda(n^2-1)} \tag{1.3}$$

where a is the diameter of the capillary and n is the refractive index. For a 10 μm radius glass capillary, the FOM is 10 times that of the free space.

On the other hand, the loss of HC-PCF is of the order of a few dB/km, whilst the interaction area is much reduced compared to the capillary technique (fig. 1.13a third row). The FOM of the HC-PCF can be written as [8]:

$$FOM_{HC-PCF} = \frac{\lambda}{\pi a^2 \alpha} \tag{1.4}$$

Here α is the loss of the fibre. The FOM of all types of HC-PCF, including both PBG and Kagome, falls into the shaded region in fig. 1.13b. The upper boundary (fig. 1.13b red dotted curve) shows the FOM of the PBG HC-PCF with the lowest loss of 2 dB/km [7]. In a 10 μm core HC-PCF, this yields a FOM of one million (10^6). When putting into applications where limited bandwidth is enough, this results in several orders of magnitude lower pump laser threshold. However, for some applications, high power delivery and broadband transmission is required and Kagome HC-PCF is a better candidate. Comparing fig. 1.13b cyan dashed curve (the lower boundary of shaded area, representing typical Kagome loss) and green dash-dotted curve (representing capillary) one can see that for large radius, the Kagome fibre exhibits no obvious superiority. This drives the motivation of developing low loss Kagome fibre, ideally comparable to PBG fibre, as will be presented in chapter 4.

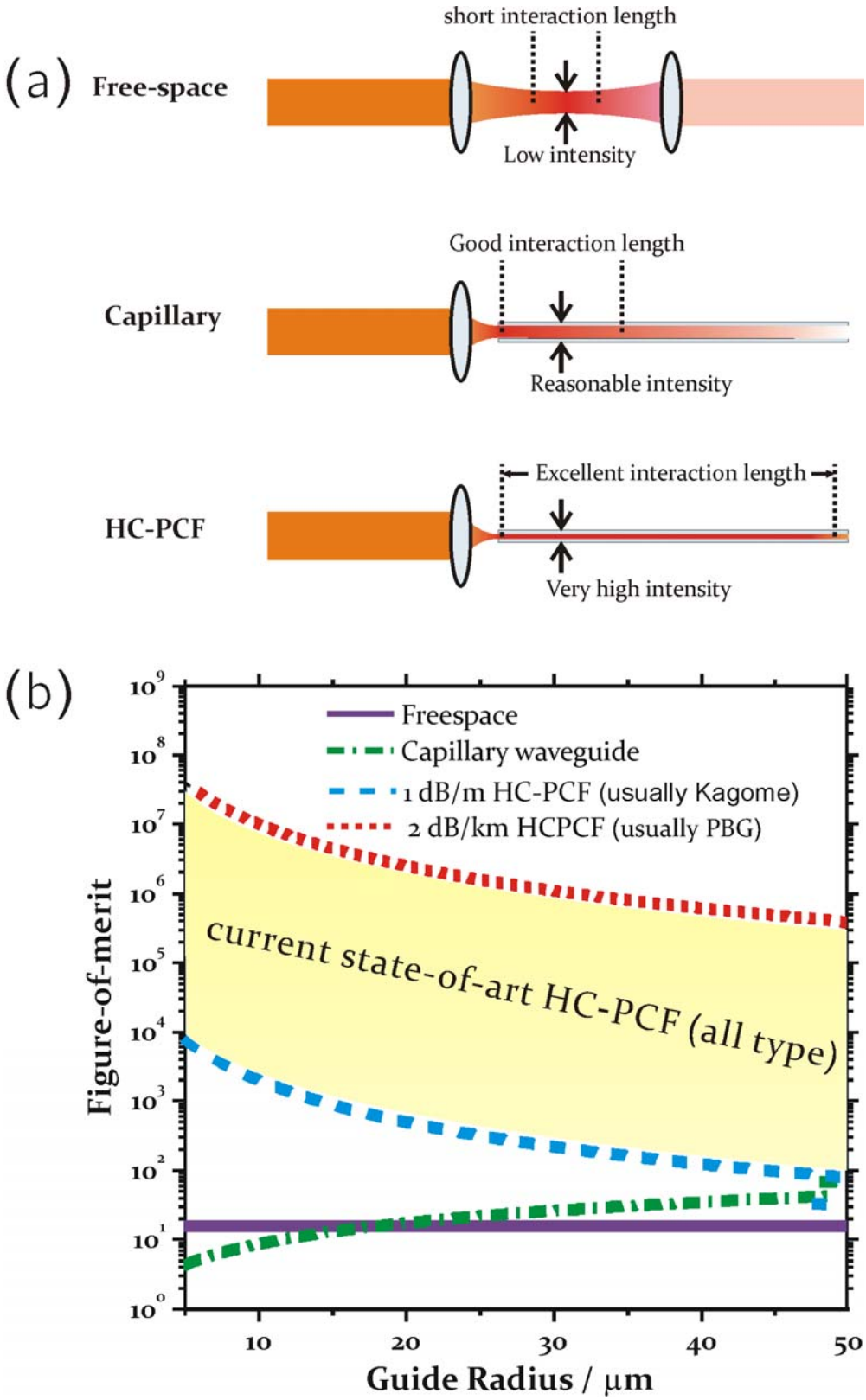

Fig. 1.13 (a) Comparison of gas-laser interaction efficiency with different host: free-space, capillary and HC-PCF. (b) FOM versus radius for different host: free-space (purple and solid), capillary (green and dot-dashed), HC-PCF with 1 dB/m loss usually for Kagome fibre (cyan and dashed) and HC-PCF with 2 dB/km loss usually for PBG fibre (red and dotted). Shaded area shows the region where current forms of all HC-PCF reside.

1.3.2 Gas loading and photonic microcell

Before HC-PCF can be used as an efficient host for nonlinear experiments, a number of challenges related to the loading of the gas into HC-PCF need to be tackled in order to realize an acceptable purity and pressure. The first demonstration of filling HC-PCF with gas was reported in 2002 [8]. The loading is based on applying a differential pressure between the two ends of the fibre. This is done by placing one end of the fibre into a custom-made chamber (fig. 1.14a) that can be evacuated or filled with the required gas. This gas control chamber is compact and contains a gas inlet face, a pressure gauge, a quartz window and a fibre holder. Besides, it can be mounted onto the translation stage, giving convenient coupling of light into the fibre. The fibre holder is specially designed to ensure a hermetic seal (fig. 1.14b) with compressed vacuum seals and rubber o rings. This system enables controllable and fast gas loading and the fibre can be easily cleaned by heating and flushing away unwanted gas and residues.

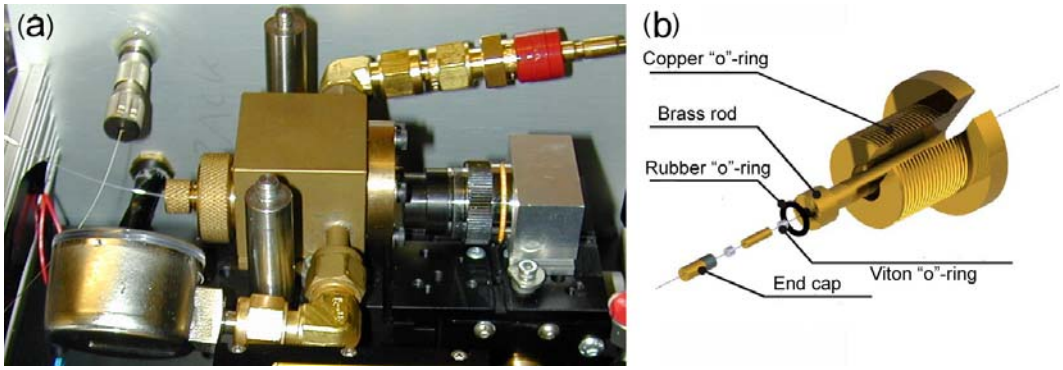

Fig. 1.14 (a) Photograph of a gas control chamber used for evacuating and filling HC-PCF. (b) shows the details of the fibre holder with hermetical seals by use of several rings.

The gas control chamber, though allowing easy pressure control, is not an ideal device since it takes too much space and one end is still not sealed. Once the required gas mixture pressure is achieved in the fibre, the stability and compactness of the device can be increased by hermetically splicing the HC-PCF to conventional solid core fibre. A photonic microcell (PMC) consists of a length of gas filled HC-PCF spliced at both ends to a solid core fibre with minimum splice loss. An example of the fabrication process for a simple high pressure gas PMC is shown in fig. 1.15. One end of the fibre is first spliced to a piece of solid core fibre (fig. 1.15a) using a filament fusion splicer.

The choice of the solid core fibre depends on the mode match with the HC-PCF and usually determines the fibre loss. The typical splice loss is 0.7 dB between a PBG 7 cell HC-PCF and a single mode fibre (SMF) (here corning SMF-28) coming from the mode mismatch of the two fibres, the core size mismatch and also the Fresnel reflection [35]. The other end is connected to a pressure control chamber and ~20 bar of gas is inserted into the system. When the pressure has stablilized, the fibre is cut at the chamber end (fig. 1.15b) and quickly spliced to another piece of solid core fibre (fig. 1.15c). As long as the timing of the splice is well controlled, the fibre can be filled with ~10 bar of gas inside. The finished PMC is an all fibre device, very compact (fig. 1.15d) with a lifetime tested to be several month, even years (depending on different gas). In the case of gases with high leakage through silica (such as H_2 and He), the limited lifetime imposed by this permeation can be extended by protecting the PMC inside a container full of a gas of the same composition or by coating the fibre with special materials that reduce the gas permeation. Several techniques to overcome this issue have been developed or are under investigation in Benabid's group.

Care must be taken to achieve each specific requirement. For example, if the gas can't be contaminated with air, the fibre needs to be cleaned by flushing with nitrogen and evacuated before loading the gas. If a very low pressure PMC is needed (<1 bar, for the laser metrology related applications), the fibre is usually loaded with high pressure helium gas as well as the low pressure required gas [36]. This avoids air going into the fibre during the cut since the total pressure is higher than 1 atm. Helium gas, with a low mass, can escape from the PMC from the side through silica afterwards, especially when the PMC is in a evacuated atmosphere. In this way, the low pressure gas is kept alone inside the gas cell. If the Fresnel reflection that happens at the interface between the solid core fibre and the HC-PCF needs to be avoided, an angle cleave is required. For example, in the case of a fibre laser, the Fresnel reflection can bring 4% of the incident laser power reflected back. If a Kagome fibre with a large core is in use, to avoid the mode mismatch with the conventional solid core fibre, a down tapering of the Kagome fibre or an up tapering of the solid core fibre is usually applied [37].

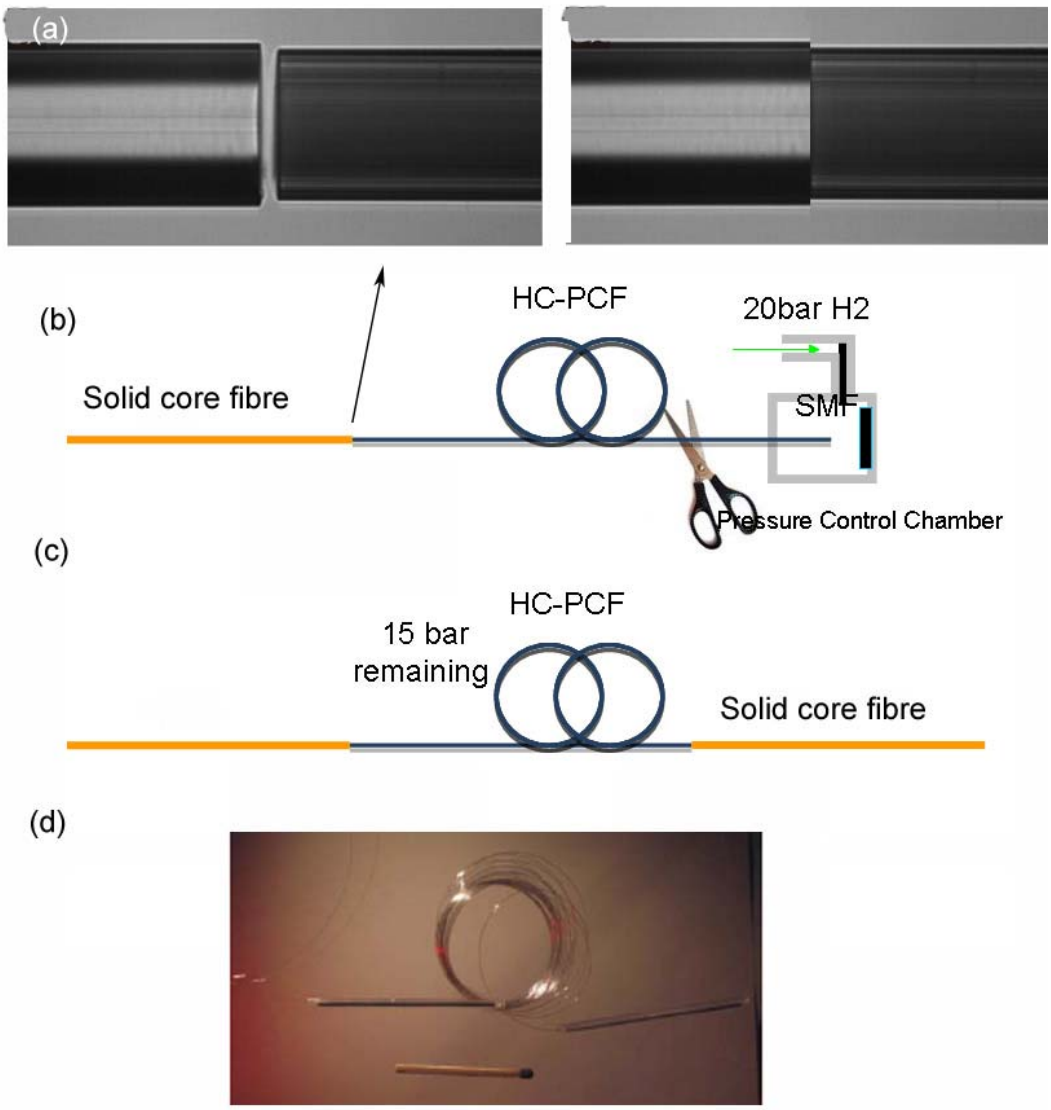

Fig. 1.15 Schematic Process of making a PMC. (a) shows the splice of a HC-PCF with a solid core fibre. (b and c) shows schematic process of filling the HC-PCF with gas, cut it and splice it with another piece of solid core fibre. (d) shows the completed PMC with the size compared to a match.

Combining the benefit of high FOM and the advances in gas loading, HC-PCF can now be treated as an ideal host for nonlinear interactions and quantum optics applications. This is why HC-PCF is used throughout the thesis for the investigation in Raman scattering and Raman comb generation.

1.4 Gas Raman Scattering inside HC-PCF

As discussed in section 1.3.1, the extraordinary way light is guided inside the hollow core of a HC-PCF makes it an excellent candidate for the detailed study of nonlinear

optical interactions in gaseous and liquid media. In this section, we concentrate the discussion on another main topic of the thesis, the study of SRS in H_2-filled HC-PCF. A brief introduction to the Raman effect is given here in order to help explain the previous results already obtained in generating, observing and analyzing SRS in H_2 filled HC-PCF.

1.4.1 Raman Scattering

The Raman effect is named after C. V. Raman who discovered it in 1928 [38]. Raman found that a sample of material scattering light from an intense, monochromatic source can produce scattered light at wavelengths other than that of the source. On the atomic level, the Raman scattering is an "inelastic scattering" whereby the frequency ω_0 of an incident laser fields get either downshifted (Stokes field of frequency ω_S) or up-shifted (anti-Stokes field of frequency ω_{AS}) by the interaction of the photons with the molecular system. From the energy conservation principle, this process can be written as $\omega_{S/AS} = \omega_P \mp \omega_R$ where ω_R is the Raman transition of the molecular system. The excess or loss of the energy between the incident field and the emitted one is therefore provided by the excitation (creation of an optical phonon at THz) or de-excitation of the medium respectively.

Depending on the type of excitation source, Raman scattering can be said to be spontaneous or stimulated Raman. Spontaneous Raman scattering is generally observed for low intensity incident radiation sources (i.e. the sun used in Raman's initial experiment). In this case, the scattering is multi-directional, non coherent and has a very low conversion efficiency to Stokes or anti-Stokes radiation. As a result, when a Raman-active medium is illuminated by a laser beam of relatively low intensity, the molecules may scatter light inelastically and hence independently and incoherently with one another. Above a certain incident pump power threshold, the intensity will be high enough, so that a large number of scattered photons will have the right phase to produce interference. They interfere with the incident wave and with the wave of the excited molecular motion in the medium. In this case, stimulated Raman Scattering is observed [39]. The Raman nonlinearity (Raman gain) of the medium offers the necessary coupling between those waves. Due to this interference,

there can be a rapid build-up of the radiation at the newly generated Raman-shifted frequencies at the expense of the incident beam power. The process can then be repeated for higher order Stokes and anti-Stokes (S/AS) generation in case when the power of the Stokes radiation goes above the threshold.

1.4.2 The special case of Hydrogen

For hydrogen, there are three types of Raman transitions: vibrational, rotational and their combination (ro-vibrational states). Figure 1.16 depicts the example of a diatomic molecule such as Hydrogen. Each vibrational state is denoted by the quantum number $\nu = 0, 1, 2, 3, \ldots$, with $\nu = 0$ the ground state. In Raman scattering, the selection rule for transitions between vibrational state is: $\Delta\nu = 0, \pm1, \pm2$. Each of these vibrational states have a fine structure of rotational states, denoted by the quantum number $J = 0, 1, 2, \ldots$ The selection rule for rotational Raman transitions is $\Delta J = 0, \pm2$.

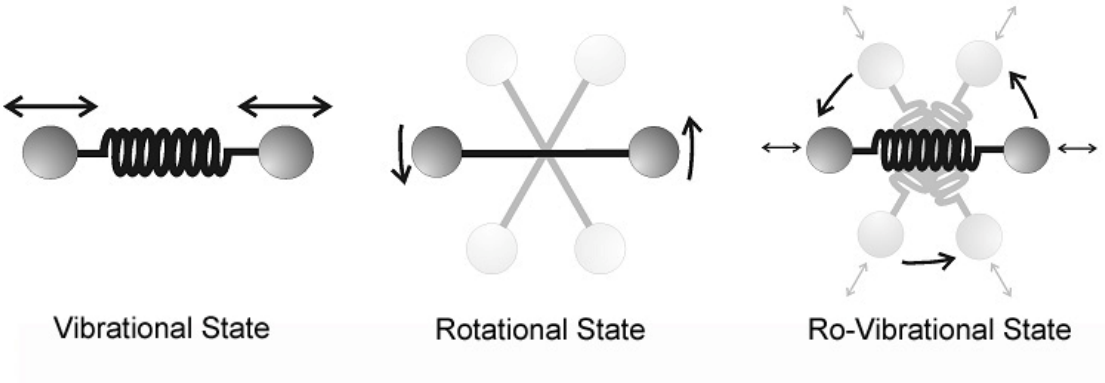

Fig. 1.16 Examples of different excited Raman states: vibrational, rotational and ro-vibrational.

At room temperature, molecular H_2 predominantly occupies the vibrational ground state $\nu = 0$; almost 75% of the molecules are in the rotational ground state $J=1$ (called ortho-H_2) due to the fact that the spin of both H_2 atoms of the S-state have the same direction. The remaining 25% of the molecules are in the rotational ground state with an angular momentum of $J=0$ (called para-H_2), where the spins of the two atoms are in opposite direction. However, when the temperature is lowered, as ortho-H_2 has a higher energy level than para-H_2, it becomes unstable and spontaneously changes into para-hydrogen. This can result in 99.95% of para-H_2 at 20K.

The Raman transition are usually written in the from $X\nu\nu_1(J)$, with X representing the branch of the transition, ν and ν_1 the initial and final vibrational states respectively and J the quantum number of the initial rotational state. The pure vibrational transition is represented by Q branch and the S branch represents the pure rotational transition. For example, in fig. 1.17, $Q_{01}(1)$ means the vibrational transition for ortho-hydrogen from ν=0 to ν_1=1. The Raman frequency of this transition is 4155 cm^{-1} (125 THz). $S_{00}(1)$ describes the purely rotational transition with $\Delta\nu$= 0 and from the initial rotational state J = 1 to the final rotational state $J1$ = 3 of ortho-hydrogen. The respective Raman frequencies is 587 cm^{-1} (17.6 THz). $S_{00}(0)$ is the rotational transition with $\Delta\nu$=0 and from J=0 to $J1$=2 of para-hydrogen with Raman frequency 353.3 cm^{-1} (10.6 THz).

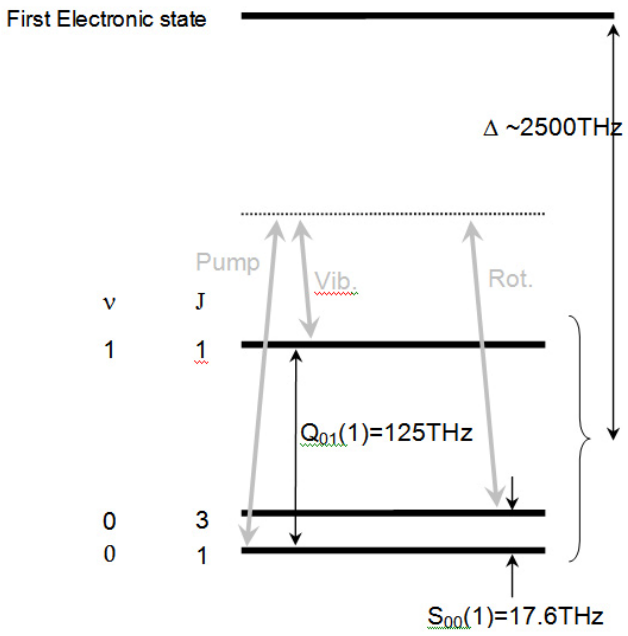

Fig. 1.17 Schematic representation of the energy level diagram for ortho-hydrogen showing the transition of $Q_{01}(1)$ and $S_{00}(1)$.

1.4.3 Raman scattering in HC-PCF

By filling the HC-PCF with H_2 gas, due to the high FOM of the HC-PCF, the threshold for SRS is extremely low. The first experiment of SRS in gas filled HC-PCF was reported by Benabid *et al* in 2002 [8] by coupling a Q-switched Nd:YAG laser at 532 nm to a Kagome type HC-PCF and observing Raman lines from the vibrational Raman resonance of H_2 (fig. 1.19a). The measured Raman power threshold was found to be 0.8

μJ (~133 W peak power) for the 1st order Stokes (S1) in a 1m long fibre, 100 times lower than any previously reported SRS observation. From then on, the main body of work in this area of non-linear photonics has been carried out by Benabid's group at Bath University.

Today's experimental setup for such Raman generation is very similar in principle to the 2002 experiment, with a relatively low intensity laser and polarization control at the input, a HC-PCF based gas cell as the Raman medium and a detection system such as an optical spectrum analyzer (OSA), oscilloscope or a camera in order to characterize the output (fig. 1.18). Although the setup is similar in some aspects, many different forms of Raman scattering have been observed. In 2004 [40], a PBG HC-PCF, allowing higher FOM (low loss, smaller core size) than the Kagome used in 2002 but limiting the number of Stokes generated (due to its narrow bandwidth), was used to almost completely convert a pump laser at 1064 nm to the S1* at 1134 nm (fig. 1.19b). The observed Raman threshold was as low as ~3 nJ (~3.9 W peak power) after 35 m of the fibre, 1 million times lower than in free space conditions and with a photon conversion reaching almost the quantum limit. In 2005, a small frequency comb based on rotational Raman in PBG fibre was reported [41] demonstrating that higher order Raman could also be obtained easily using HC-PCF (fig. 1.19c). In this particular case, the main contribution to the comb generation was the fact that the Raman conversion was done in the transient regime (see chapter 5), even though the laser power was only 150 nJ and the duration was as large as 14 ns. In 2007 [42], a CW Raman gas laser was achieved with again almost full conversion from the pump at 1064nm to the Stokes at 1134 nm indicating that applications requiring nearly 100% frequency conversion could be possible using the technique (fig. 1.19d). Later that year, an optical Raman frequency comb spanning over three-octave from 325 nm to 2300 nm was generated [11] with simply a single frequency Nd-YAG laser emitting 12 ns pulses at 1064 nm with a 50-Hz repetition rate and an average power of 200 mW and a 1m long Kagome

* In this thesis, as we mainly deals with rotational Raman resonance, the labels S/AS represent rotational Raman lines. Vibrational Raman lines are stated as vibrational S/AS.

type HC-PCF (much improved compared to the 2002 ones) filled with 15 bar H_2 (fig. 1.19e). It is worth mention that such high Raman conversion usually requires GW power and sub-ps pulse duration when HC-PCF is not applied [43].

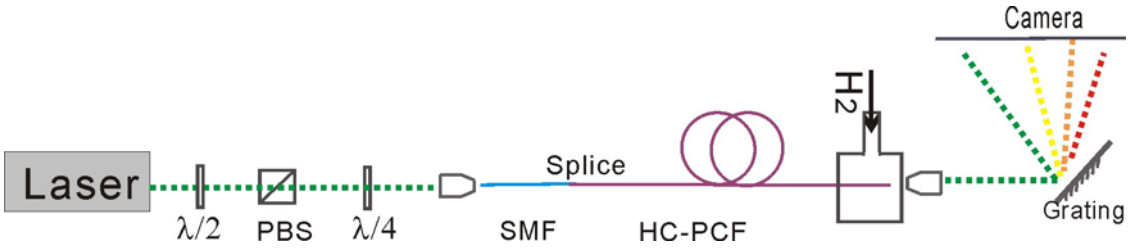

Fig. 1.18 typical setup for Raman generation in gas-filled HC-PCF. λ/2: half waveplate, PBS: polarizer; λ/4: quarter waveplate.

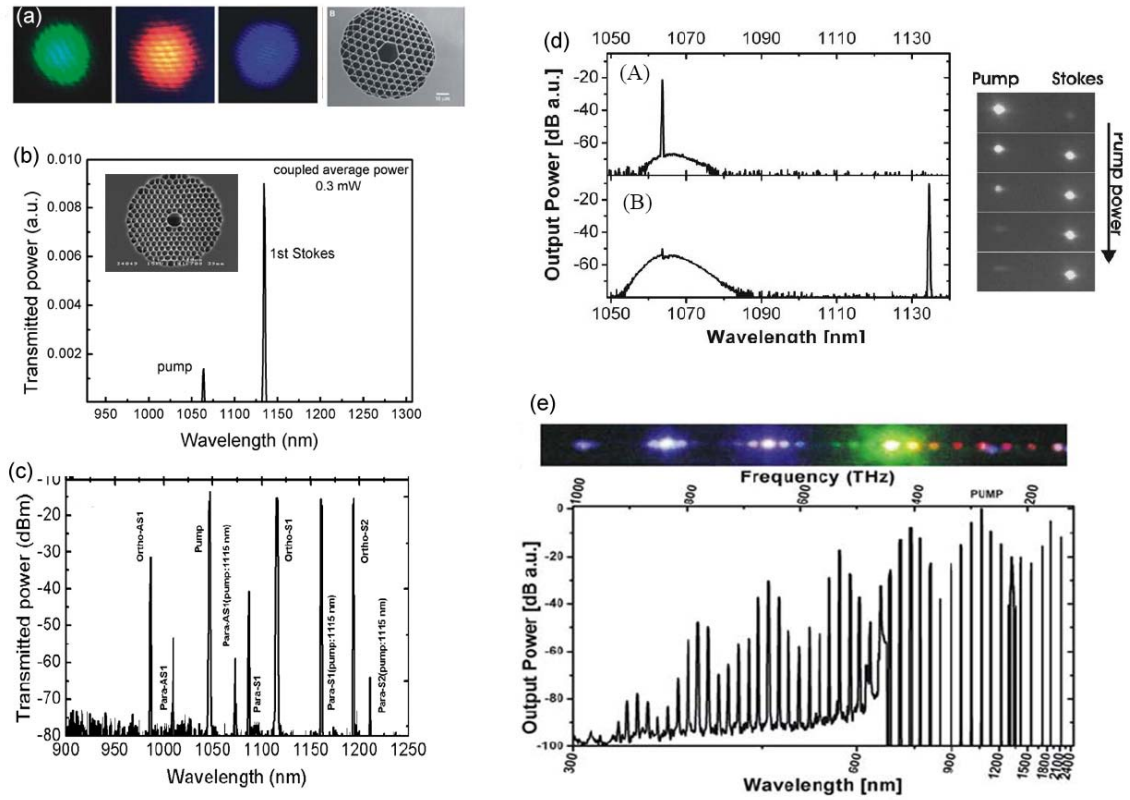

Fig. 1.19 Development of Raman generation from H_2 in HC-PCF. (a) the vibrational Stokes generarion in a Kagome fibre in 2002 [8]; (b) The full conversion of rotational Stokes in PBG fibre in 2004 [40]; (c) the small rotational Raman comb generated in 2005 [41]; (d) the first CW Raman laser in HC-PCF in 2007 [42] and (e) the Raman frequency comb spanning three octaves in 2007 [11].

In the light of these results, it appears that some unexpected conditions are fulfilled to achieve such high conversion efficiency, leading to some results that could,

at first, look difficult to explain, most noticeably in terms of the seemingly ultra-high coherence of the Raman medium achieved in HCPCF. Trying to answer some of these questions is the main topic of this thesis.

1.4 Thesis outline

Based on the above mentioned prior work, the present thesis covers a further study on both the HC-PCF characterization and on Raman frequency comb investigation. The thesis contains two parts.

Part 1 is the development of HC-PCF including three chapters.

In Chapter 2 we investigate the surface modes of PBG HC-PCF based on chemical etching. We show that by choosing the right core-wall thickness, one can optimize the optical guidance of the fibre. I did the majority of this work.

In Chapter 3 we show the fabrication and characterization of double bandgap HC-PCF, that is a single piece of HC-PCF with two optical bandgaps. The work is done together with my colleagues and the simulation results shown are carried out by Phil Light.

Chapter 4 is the fabrication of the newly-developed hypocycloid-core Kagome HC-PCF with a typical loss as low as 40 dB/km. This value is comparable to that of PBG HC-PCF while offering much larger bandwidth. The majority work has been done by myself and the simulation was carried out by F. Benabid and P. J. Roberts.

Part 2 is the Raman frequency comb generation by virtue of HC-PCF including four chapters.

Chapter 5 is the review of the Raman frequency comb generated in H_2-filled HC-PCF including the control of the Raman regimes, the frequency comb generated previously in the group and the predicted coherence properties.

Chapter 6 is the demonstration of compact and portable Raman frequency combs that can be used as multiline lasers for forensics and biomedicine applications. Most of the work was accomplished by myself with the help of F. Couny and P. S. Light.

Chapter 7 is the demonstration of the self coherence of the Raman frequency comb. A modal picture is introduced and we present the photon statistics of the comb to prove the single spatio-temporal modeness of the Raman lines. The experiment was performed mostly by myself.

In Chapter 8 we investigate the mutual coherence of the Raman frequency comb experimentally and theoretically. The experimental part is done by myself and the simulation is carried out in cooperation with Chunbai Wu and M. G. Raymer from University of Oregon.

Finally in Chapter 9, we summarize the thesis and give a proposal for future work.

Part 1

The development of HC-PCF has come to an age where the combination of low transmission loss and broad transmission bandwidth within a single fibre has become a determining factor in several applications [44]. As presented in chapter one, we count two classes of HC-PCF. Firstly, the commercially available PBG HC-PCF which can exhibit ultra-low attenuation, with typical figures of ~10 dB/km, ~70 dB/km and ~150 dB/km for optical guidance around 1550 nm, 1 μm and 800 nm respectively [7]. However these fibres have a narrow transmission bandwidth (~70 THz). Moreover, the performance of the fibre is disturbed by the existence of surface modes inside the transmission band. The second class of HC-PCF provides low loss guidance through inhibited coupling between core and cladding modes, analogous to Von Neumann Wigner bound-states in a continuum, such as large-pitch Kagome, square or triangular lattice HC-PCF [11]. Unlike PBG HC-PCF, these fibres provide ultra-broadband guidance at the expense of an increased attenuation (> 0.5 dB/m) compared to their PBG counterpart.

In this part, we present our recent improvements on these two types of fibre overcoming the above mentioned problems. For the PBG HC-PCF, we demonstrate, in chapter 2, the tailoring of the surface modes position with respect to that of the transmission band and in chapter 3 the fabrication of double bandgap HC-PCF offering more sufficient optical bandwidth. In chapter 4 we present the fabrication of hypocycloid core Kagome-lattice HC-PCF with much lower loss than conventional Kagome HC-PCF. All these developments in HC-PCF provide an outperforming platform for its applications and in particular for the Raman frequency comb generation which will be discussed in part 2.

Chapter 2

Tailoring the Surface Modes of PBG HC-PCF

*In this chapter, the dispersion properties of the surface modes in PBG HC-PCF are experimentally investigated by a novel technique based on chemical etching. The techniques allow the tailoring of the spectral position of the surface modes by reducing the core ring thickness. Using this technique, several intricate core structures, which are impossible to fabricate with the stack-and-draw technique, were fabricated.**

* This work has been published in:

Y. Y. Wang, P. S. Light and F. Benabid. "Core-Surround Shaping of Hollow-Core Photonic Crystal Fibre Via HF Etching" IEEE Photonics Technol. Lett. 20 1018-1020 (2008).

2.1 Introduction

In Chapter 1, we discussed the optical guidance mechanism of the triangular lattice PBG HC-PCF. We presented the DOPS map (fig. 1.5) of a uniform photonic crystal cladding structure without the core defect where one can see that a PBG region could extend below the airline (n_{eff}<1). In this chapter, we will consider the case when an air core defect is introduced. Within the PBG, the supported modes include, apart from the core modes, surface modes localized at the glass ring surrounding the hollow core [45, 46]. These surface modes limited the performance of the fibre transmission. Also, the beating of these modes with the core modes has a parasitic effect in applications such as those in laser metrology [47, 48] or quantum optics [16, 17]. On the other hand, the strong light confinement exhibited by HC-PCF surface modes makes them very valuable in applications such as nonlinear optics applications and sensing [19]. Consequently, it is of high interest to be able to control their spectral and modal properties such as their complete suppression from the transmission band or the tailoring of their modal shapes or spectral location within the photonic bandgap. Such control could be achieved via patterning the topology of the core-surround. In this chapter, we present a technique which enables a high degree of patterning capability on the core-surround of HC-PCF with length of ~20 cm. The technique is based on chemical etching of the inner-core of the HC-PCF with hydrofluoric acid (HF) solution. With this technique different core shapes were achieved and surface mode blue-shift was experimentally demonstrated as the thickness of the ring shaped core-surround was reduced.

2.2 Concept of Surface Modes in PBG HC-PCF

When a core defect is introduced in the photonic crystal cladding structure, the core shape accommodates modes within the PBG. The DOPS map calculated by plane wave method [31] using a fabricated 7- cell core fibre is shown in fig. 2.1. Inside the bandgap, there is the fundamental HE_{11} core mode close to the airline with a near-horizontal dispersion curve, indicating that most of the light travels in air. If the core is large, the high order modes can sometimes be supported as well with a lower effective index.

The dispersion curve is approximately flat. Alongside the core mode, there are several much steeper dispersion curves that exists within the PBG. The optical power of the associated modes resides in the silica core-surround of the hollow core. These modes are associated with the boundary of the air core and are called "surface modes".

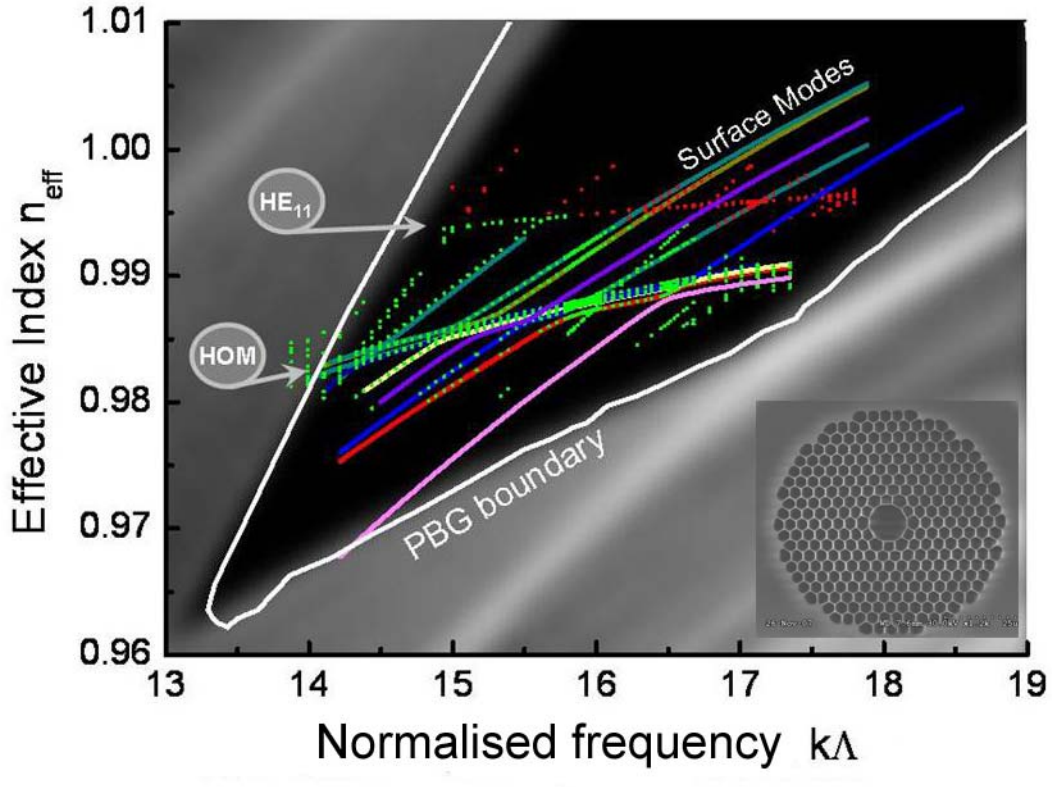

Fig. 2.1 DOPS diagram of the PBG falling below the vacuum line region [24]. Inside the PBG, air-guided fundamental mode (HE_{11}) and high order modes (HOM) as well as surface modes are shown. The fibre used for the modeling is shown in bottom right.

In contrast with the core mode where the confinement and guidance is due to PBG provided by the surrounding photonic structure of the cladding, the silica core-surround, which supports the surface mode, shows two structural sides. One side is formed by the cladding structured material, and the second side is air. Consequently, the confinement of the surface modes is provided by two mechanisms. At the interface between the air and the silica-core surround, the confinement is provided via TIR. On the other hand at the interface between the silica-core surround and the cladding, the guidance is provided by PBG because the effective index of the surface modes lay within the bandgap of the cladding [49]. Note that, since the surface mode overlaps

more with the silica structure than the core mode, it is more affected by the surface roughness and usually has higher loss than the core mode.

Due to the close proximity of the core-surround and the air-core, the core guided modes and the surface modes overlap spatially. Furthermore, under phase-matching conditions, i.e. when these two modes share the same frequency and same propagation constant, the modes hybridize and their dispersion exhibit anti-crossing as shown in fig. 2.2. Here, the steep slope curve (the green dashed line) and the near-horizontal curve (the black dotted line) correspond to the modes guided in the core-ring and in the air core respectively. Furthermore, fig. 2.2 shows the evolution of the intensity profiles of the hybridized modes (the red and the blue solid lines) near an anti-crossing. It is noteworthy recalling that in order for an anti-crossing to occur, the field distribution of the two modes, in addition to a spatial overlap, should bear a symmetry "overlap". Otherwise, the intrinsic orthogonality will prevent the mode hybridization, which is the case for the inhibited coupling of core mode and cladding modes in the Kagome HC-PCF.

The power distribution between the waveguiding features (i.e. hollow core and the core-surround) can be deduced using a simple model based on coupled waveguide theory. Due to the mode hybridization, the eigen-modes of the HC-PCF will no longer exhibit a profile of a core mode nor that of a surface mode. A method to model the eigenmodes is to approximate them to be the supermodes of the core mode (Ψ_1) and the surface mode (Ψ_2):

$$\begin{aligned} \Psi_+ &= \frac{1}{\sqrt{1+x^2}}(x\Psi_1 + \Psi_2) \\ \Psi_- &= \frac{1}{\sqrt{1+x^2}}(\Psi_1 - x\Psi_2) \end{aligned} \tag{2.1}$$

where x stands for the amplitude fraction in each mode and Ψ_+ and Ψ_- are orthogonal to each other. The mode evolutions of Ψ_+ and Ψ_- are shown in fig. 2.2. Before the anti-crossing point (small $k\Lambda$), Ψ_+ has the character of the core mode and Ψ_- the surface mode ($x=\infty$). Approaching the anti-crossing point, Ψ_+ and Ψ_- become mixtures of Ψ_1 and Ψ_2. In such a case, both eigenmodes will suffer high attenuation because they contain Ψ_2 features. On the right of the anti-crossing point (large $k\Lambda$), Ψ_+ is gradually

converted to a surface mode and Ψ_- the core mode (x=0). Generally speaking, the anti-crossing will create spectral windows where all the guided modes are highly attenuated. Therefore, several dips will appear in the overall transmission band of the HC-PCF.

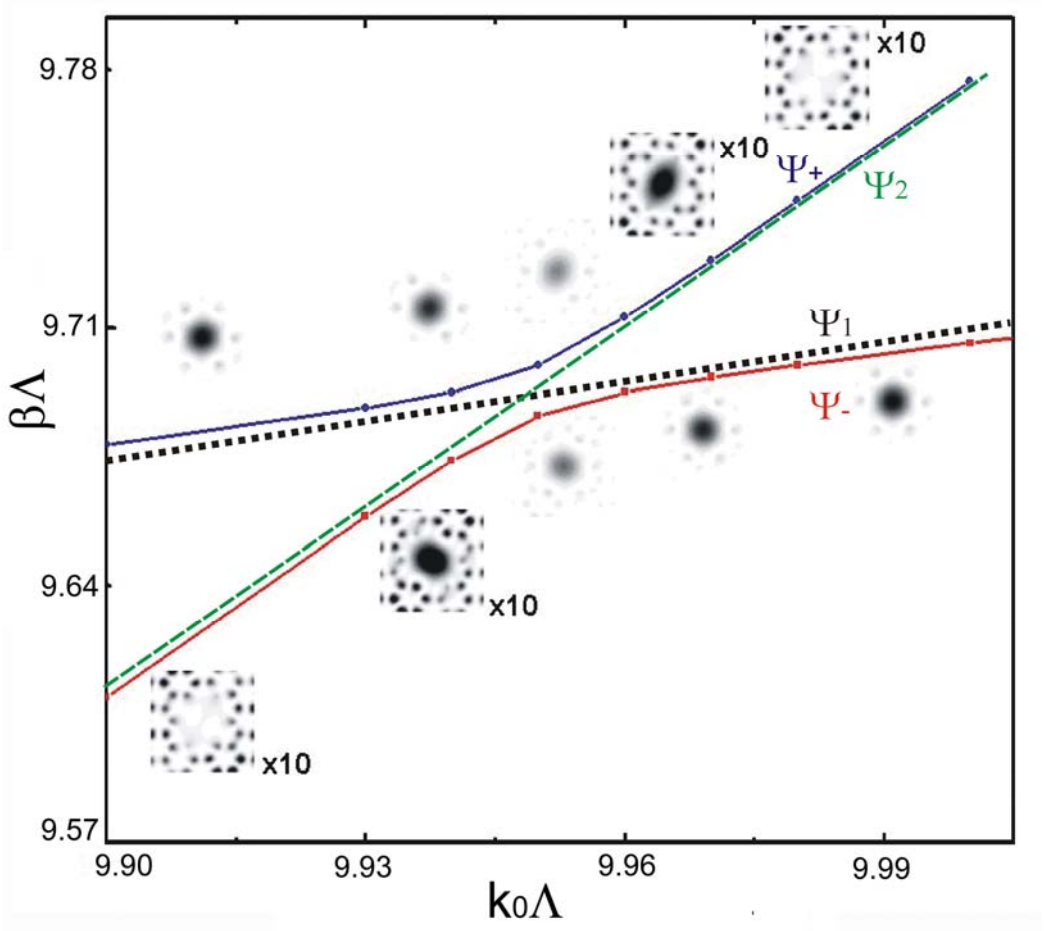

Fig. 2.2 Trajectories of the fundamental core mode and a surface mode at anti-crossing [50]. The intensity of the surface mode is magnified by 10. The core mode field (Ψ_1), the surface mode field (Ψ_2) and their superposed eigenmode (Ψ_+ and Ψ_-) are plotted as the black dotted line, the green dashed line and the red and blue solid lines respectively.

The core mode and surface modes can be experimentally observed. In fig. 2.3, the modal profiles from a 7-cell PBG HC-CPF with optical guidance centred at 1300 nm are shown. With different filters at different wavelengths, fundamental and higher order core modes, surface modes and modes at the anti-crossing can all be observed.

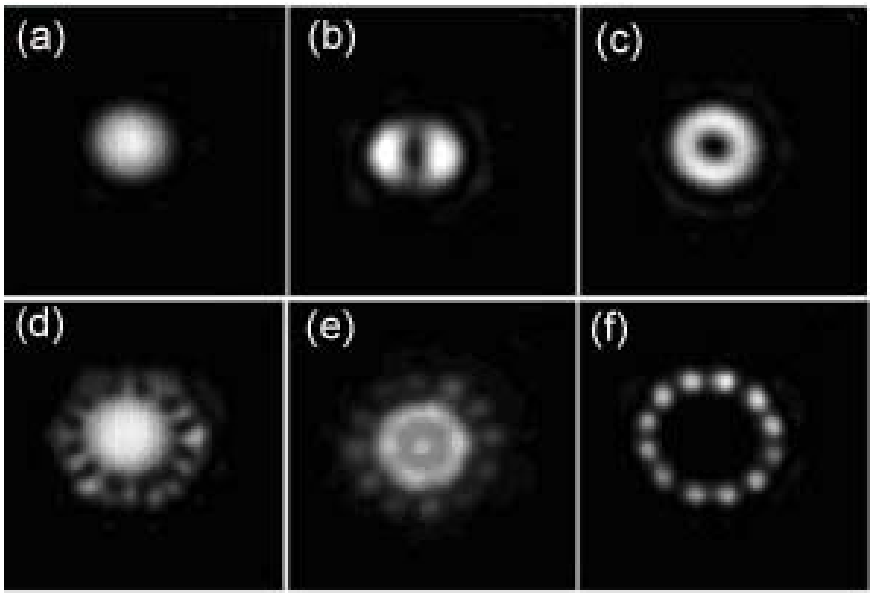

Fig. 2.3 Mode properties for a 7-cell PBG HC-PCF centred at 1300nm [24]. (a) is the fundamental core mode, (b) and (c) are the higher order core modes, (f) is the surface mode and (d) and (e) show an anti-crossing between the surface mode and the fundamental core mode and higher order core mode.

Numerical studies on surface modes

One straightforward way of reducing the loss caused by the silica surface is to adopt a large core, so that the overlap of the modal field with the silica surface is minimized. Indeed a minimum loss of 1.2 dB/km at ~1550 nm has been realized in a 19 cell HC-PCF [7]. However, in such a fibre, the low loss transmission band from 1510 nm to 1640 nm was still punctuated by three higher loss points of 25 dB/km at 1540, 1580 and 1605 nm which arise due to the anti-crossing events between the core guided mode and surface modes. Although the loss of the fibre is largely reduced, the influence of the surface modes have not been solved. Later, several groups proposed their respective models of eliminating surface modes by modifying the core structure. For example, in the structure in fig. 2.4a, making the core-surround "curvy" shifts the position of the surface modes to outside the bandgap [45, 50]. Another example is in fig. 2.4b where core termination is introduced to eliminate the effect of surface states [51]. However, the core shape of the proposed HC-PCF structure poses a real challenge in drawing such fibres.

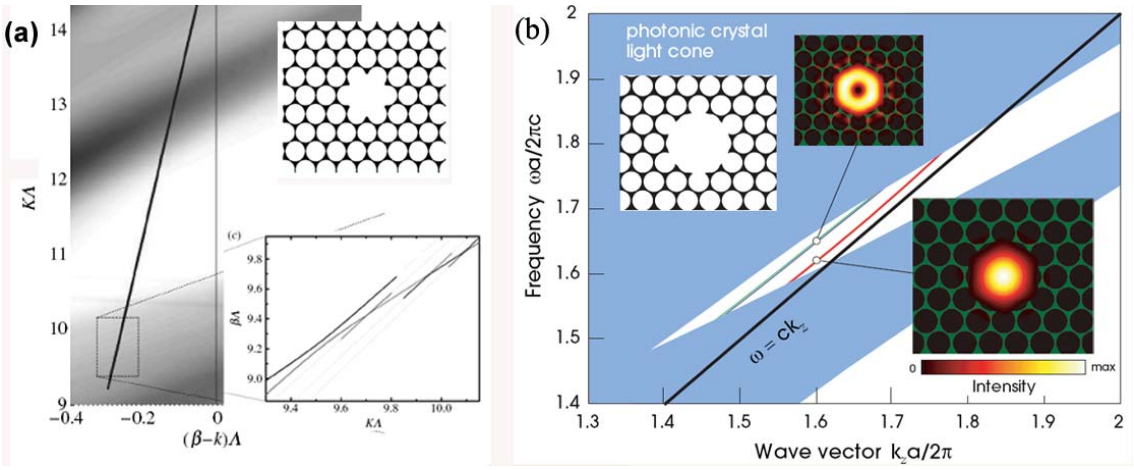

Fig. 2.4 Two ideal structures for HC-PCF free of surface mode. In the DOPS graph of (a), one can see the position of the surface modes has been shifted outside the bandgap [45, 50]. In (b), no surface modes are found [51].

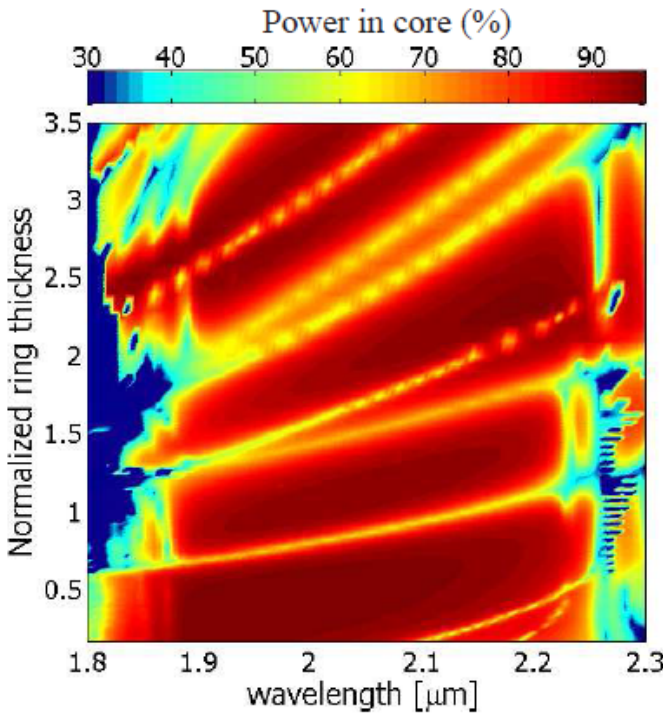

Fig2.5 Numerical study on the position of surface modes with core ring thickness by Correa *et al.* [52].

An extensive study of surface modes on a realistic fibre structure has been carried out by Correa *et al* in 2006 [52]. It shows that the position of the surface mode moves in accordance with the core ring thickness. Figure 2.5 presents the power in core fraction within the bandgap as a function of the ring thickness [52]. In the yellow regions, only

~60% of the power is confined in the core, representing the position of the modes anti-crossing. Here the normalized core ring thickness is defined by $t=t_r/(\Lambda-d)$, where t_r is the core ring thickness and $(\Lambda-d)$ represents the cladding strut thickness. From the plot we can see clearly that by reducing the normalized core ring thickness, the surface mode is blue-shifted. Meanwhile new surface modes emerge from the red end of the PBG. For that fibre design, when t=0.5, there is possibility that the surface modes are completely outside the bandgap. Later, a fibre was fabricated with core-ring thickness half of the cladding thickness in a larger pitch regime [53]. Claims of "no surface mode" is given [53] but no clear demonstration is provided since it is hard to reproduce from fibre to fibre.

2.3 Etching technique for surface mode tailoring

Although there are several investigations focusing on numerical modeling of surface mode behaviour, little experimental evidence has been presented to support them. In this section, we show experiments done by the author regarding the investigation of surface mode spectral location within the PBG using a chemical etching technique to manipulate the core surround shape and thickness.

2.3.1 Cane etching technique

The first attempt of achieving core structure similar to fig. 2.4 is to chemically etch an ordinary cane (fig. 2.6a). By heating up both ends of the 1 m long cane, the holes collapse in an order that smaller holes close before the large holes. A careful control of the heating can achieve an extent that the cladding holes are all closed and the core hole remain open. A diluted HF solution is then flushed into the cane to etch away the core ring. By carefully control the etching time, we managed to achieve a cane structure as shown in fig. 2.6b with no core ring thus similar to the one in fig. 2.4. The cane is then cleaned up by flushing with water, heating up and cleaving away the two collapsed ends. Unfortunately maintaining this structure during the fibre drawing proves difficult after several trials. The core structure tends to blow up to a degree that destroys the whole structure of photonic crystal cladding (fig. 2.6c).

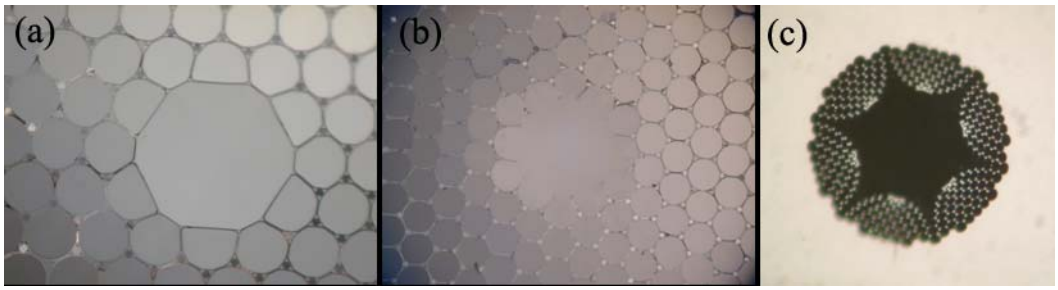

Fig. 2.6 Comparison of the unetched cane (a) and etched cane (b). (c) shows the fibre fabricated by the etched cane with no optical guidance.

2.3.2 Fibre etching technique

Though the etched-cane-to-fibre drawing is not sucessful, the chemical etching technique proves a useful tool for obtaining different structures. To that end, we initiate the idea of "fibre etching". This means no further drawing is needed after etching, though in terms of application, only short length of fibre can be processed because of high loss introduced during the etching. For research purposes, this technique allows the investigation of how the surface modes move with the strut thickness and what kind of core structures are possible to obtain.

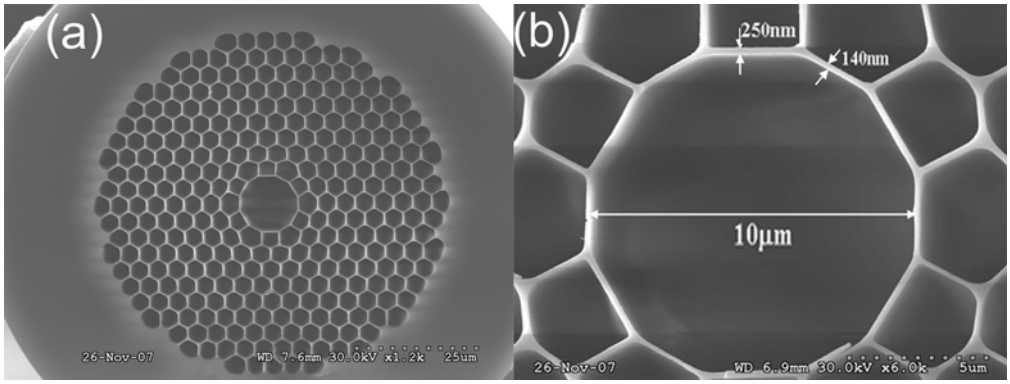

Fig. 2.7 (a). SEM of the cross section of the HC-PCF used via etching. (b). It has a core of 10um, core wall thickness of 250nm and 140nm.

Figure 2.7a shows the SEM images of a typical 7-cell HC-PCF which was used throughout this core-surround patterning process. The fibre has a core diameter of ~10 µm. The core ring contains six thin struts of 140 nm and six thicker struts of 250 nm (fig. 2.7b). The typical optical transmission of the fibre is centred at 1500 nm and exhibits a 3 dB bandwidth of ~300 nm (fig. 2.10a).

The modification to the cross section topology of the fibre core was achieved via etching the inner walls of the fibre-core with HF. Similar to the cane etching technique, in order to avoid HF solution entering the cladding, both ends of the fibre (fig. 2.8a) were heated with a filament splicer. This resulted in collapsed cladding holes with the core open (fig. 2.8b). In comparison with the micrographs in fig. 2.7a (by comparing the ratio of the core to the whole structure), the core diameter varied little after this collapsing process. The fibre-end was then mounted into a home-made pressure chamber (fig. 2.8c) and HF solution was pushed and flowed through the fibre core. Finally, after etching, the fibre was cleaned by flushing with water for several hours (fig. 2.8d) and dried by heating on a hot plate overnight (fig. 2.8e).

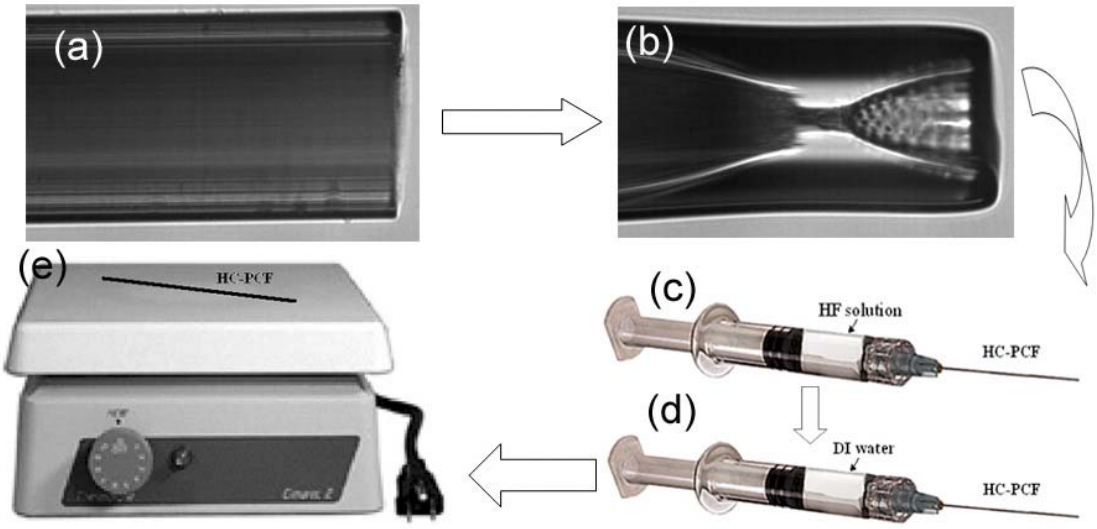

Fig. 2.8 Diagram of fibre etching process. (a) Optical micrographs of the fibre end before and (b) after collapsing process. (c) Schematic setup of the home-made pressure chamber to flush HF solution and (d) water. (e) Hotplate to dry the fibre overnight.

Choice of HF solution

In order to obtain a uniform etch, the acid density must be kept as constant as possible along the fibre length. This can be achieved by setting a high flow speed on one hand and using highly buffered HF solution on the other.

The etching of the silica ring causes a decrease of the initial acid density $D(0)$, and the acid density decays with time in the following manner:

$$D(t)/D(0) = \exp(-\alpha t) \tag{2.2}$$

where $D(t)$ is the acid density at specific time t. If the flow-through time (τ) is much less than the decay time $1/\alpha$, the variation of the etching along the fibre can be neglected. Note that the dilution of the acid is not helpful here since it only changes the initial acid density and does nothing to the decay time which is related to the core diameter.

In the case of non-buffered acid solution, the decay time is calculated to be 0.78 min according to the diameter of the fibre core (~10 μm) and the relationship between etching rate and acid density [54]. On the other hand, derived from the laminar-flow Poiseuille formula, which has been proven applicable in a ~10 micron scale tube [55], the flow-through time can be expressed to be:

$$\tau = \frac{32\mu_0}{d^2} \cdot \frac{L^2}{P} \tag{2.3}$$

where μ_0 is the viscosity, d is the core diameter, L is the length, and P the pressure difference. To reduce τ, a high pressure, thus a high flow speed, is of vital importance. In experiments, P was controlled via the differential pressure exerted between the chamber and the other end of the fibre and was set around 8 atm. If we aim at a flow-through time as small as 10% of the decay time for uniform etching, a fibre length of 11 cm is preferred. This length is a bit short for our optical measurement.

A longer fibre length, however, can be obtained when a buffered HF solution is used. This buffered etching solution compensates the depleted acid concentration via the buffering reaction [56]

$$NH_4F + H_2O \rightarrow NH_3 \cdot H_2O + HF \tag{2.4}$$

so lengthening the decay time. If the etching agent (NH_4F) is plentiful enough, the decay time, in principle, can be regarded as infinite. However, for practical reasons, we limit the fibre lengths to ~20 cm to ensure a maximum uniformity of the patterned core-surround.

In our experiment, a commercially available buffered oxide etchant (BOE) with volume rate of 100:1 (100 parts of 40% NH_4F solution plus 1 part of 49% HF solution) was used. The BOE solution was then diluted with water in a volume ratio of 1:30. The extremely low HF concentration reduces the etching rate to such a level that not only benefits the smoothness of the silica wall but also makes the control of etching time much easier. The etching rate for this diluted BOE solution, (HF concentration 0.017% in weight) was evaluated to be 0.2 nm/min according to the data sheet from General Chemical Corporation [54]. Measurements of the etching rate were also carried out by comparing average core-surround thicknesses of a fibre before (fig. 2.9a) and after (fig. 2.9b) a 160 min-long etching. The result is around 0.18 nm/min, which agrees well with the evaluated value.

Shift of surface modes

With this fibre-etching technique, different core-surround thicknesses were obtained depending on the etching time. Figure 2.9 shows the SEM of fibre samples before and after 160 min-long etching. The figure clearly illustrates the reduction of the core ring thickness.

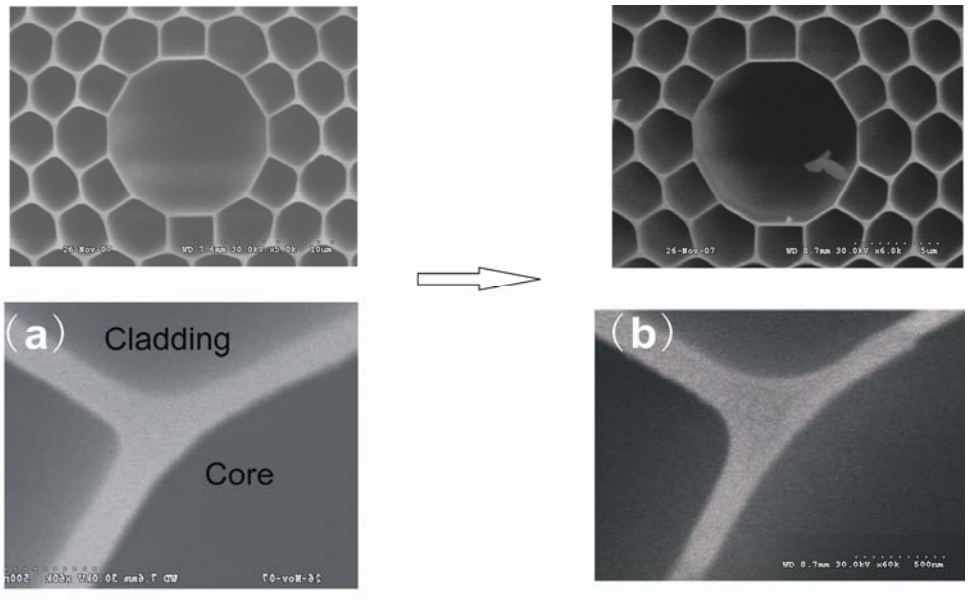

Fig. 2.9 SEM of the HC-PCF (a) un-etched fibre; (b) etching for 160 mins. We can see clearly that the cladding struts are not changed and the core-surround thickness is largely reduced.

To illustrate the effect of the core-ring thickness on the surface modes, we fabricated several ~20 cm long fibres with different core-ring thicknesses using the above technique. The transmission spectra of these samples were then measured and compared. In order to ensure that the measured spectra correspond to the core-guided light and not from the cladding, the output light was first imaged and then the central core part of the transmitted light profile was coupled into the OSA.

Figure 2.10 shows the evolution of the transmission spectrum for ~20 cm long fibre samples with different thicknesses of the core-ring. All the samples were produced from the same original fibre. Figure 2.10a shows the transmission of the first sample whose core-ring was kept un-etched. The transmission spectrum exhibits three dips at 1440 nm, 1455 nm and 1473 nm in a transmission band from 1400 to 1750 nm. The dips are the signature of a strong coupling of the core mode with surface modes. The spectra in fig. 2.10(b-g) show the transmission of six fibre samples that have gone through etching for different time durations which are 30, 55, 70, 90, 130 and 160 minutes respectively. This etching resulted in an estimated thickness reduction from the original fibre core-ring of 6 nm, 10 nm, 13 nm, 17 nm, 24 nm and 30 nm respectively.

The transmission spectra of these fibre samples show a clear blue shift of the initial absorption dips mentioned above. The shift increases with the thickness reduction (dashed line in fig. 2.10). Furthermore, the spectra of the etched fibres exhibit newly emerged dips on the red-side of the transmission band, indicative of a coupling with surface modes that are different from the initial ones. This behaviour was expected and agrees well with the numerical results in [52] (fig. 2.5).

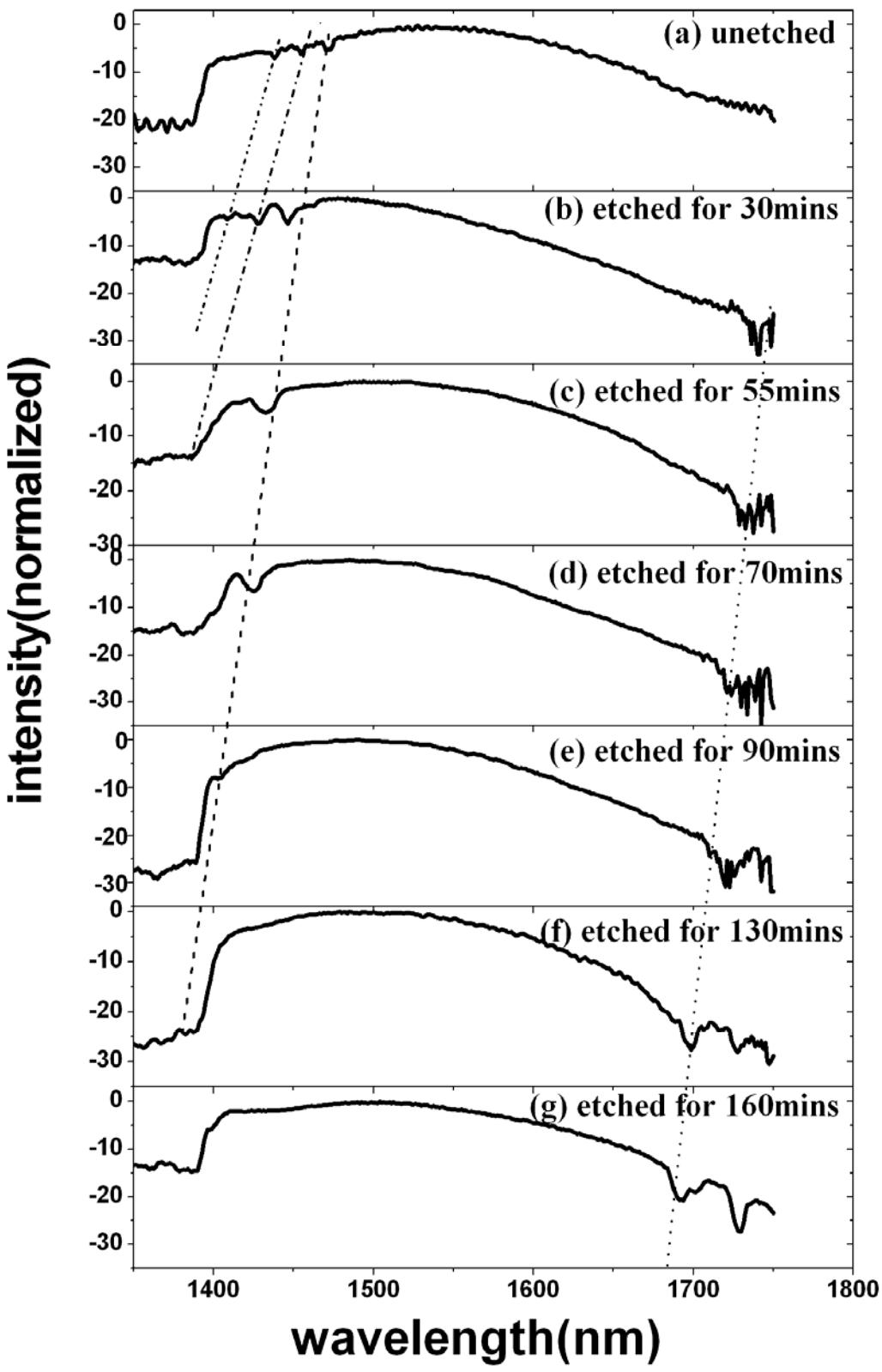

Fig. 2.10 Transmission spectrum of 7 samples, respectively un-etched, and etched for 30, 55, 70, 90, 130 and 160 minutes.

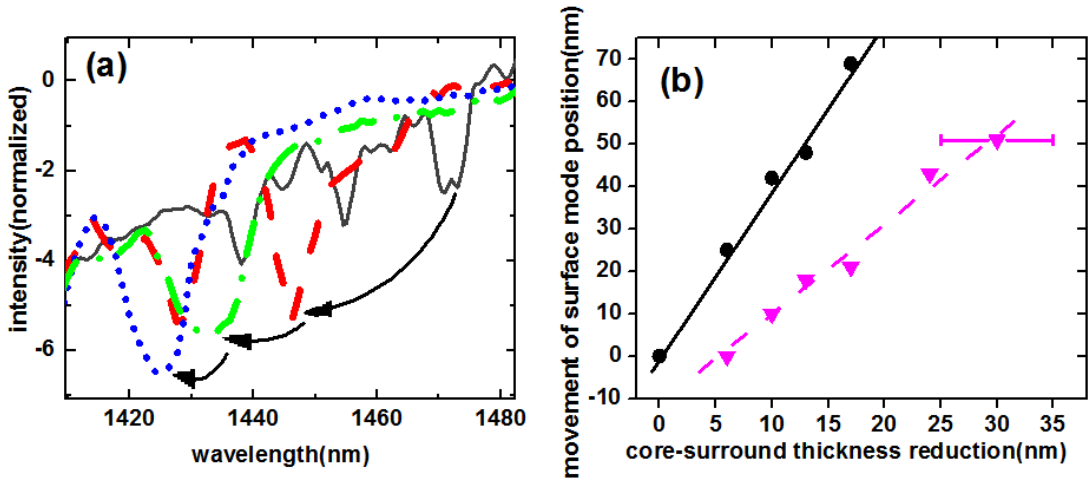

Fig. 2.11 (a) Zoom in of the blue-shift of the original surface mode dips. Solid black curve: original surface mode dips; dashed red curve: surface mode dips for fibre etched for 30 mins; dashed and dotted green curve: surface mode dips for fibre etched for 55 mins; dotted blue curve: surface mode dips for fibre etched for 70 mins. (b) Relationship between surface mode location and core-surround thickness. Circle black points: The original surface mode shift; Triangular pink points: The newly emerged surface mode shift. The black and pink lines are the fit of the points.

Figure 2.11a shows more resolved spectra for the shift of the initial dips. The plot clearly demonstrates the shift and then the disappearing of the absorption dip from the transmission band. A broadening of the initial dips is also observed here. This may be due to either the longitudinal non-uniformity or to the enhanced coupling of the surface modes with the cladding modes as they approach the band-edge.

As long as these dips are within the transmission band, their shift follows a linear trend with the thickness reduction. This is shown in fig. 2.11b where circle black points corresponds to the shift of third dip in the blue-side (dashed line in fig. 2.10) and the triangular pink points corresponds to the first dip (dotted line in fig. 2.10) in the red-side of the spectrum.

Various core-surround structures

It is noteworthy that some other core-surround structures are observed during the etching process. By etching the fibre for ~12 hours, the thin struts are completely etched away. This results in a core-surround structure shown in fig. 2.12a&b. It bears a strong similarity to the ideal model in fig. 2.4b and is potentially free of surface modes. 20 cm of fibre with this structure was obtained. However, no optical guidance can be

detected which may be because of the surface roughness at the edge of the remaining struts. Moreover, completely different patterns as shown in fig. 2.12c&d are also observed but only happen at the end of the fibre for a very short length (2mm). The reason why they appear is still unclear but may be explained by the abrupt pressure change when cutting the fibre. The topology of the fig. 2.12c is very similar to the one modelled in fig. 2.4a. We can see how different structures can be governed by our core-surround patterning technique.

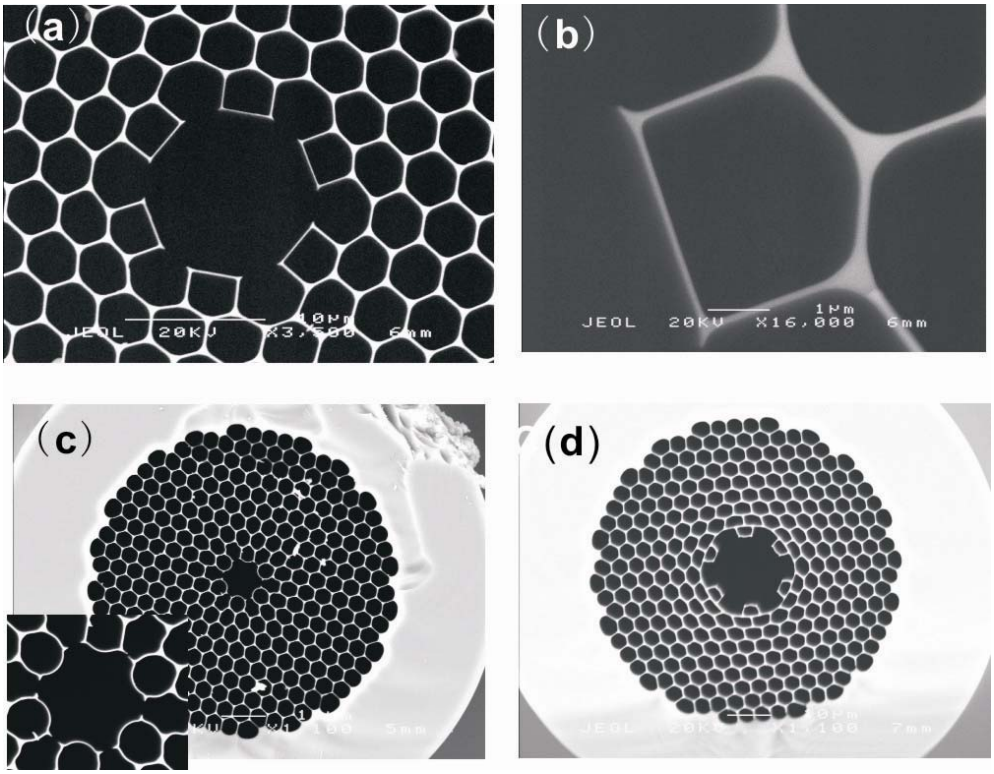

Fig. 2.12 SEM of the HC-PCF (a,b) after 12hours etching; (c,d) at the end of the etched fibre (see text for details).

2.4 Summary

By using the etching technique, we shift the surface mode to any desired position and various fibre structures can be obtained. This technique can be further improved in the future by using gaseous phase HF for a smoother surface and a longer length.

Chapter 3

Double Bandgap HC-PCF

*This chapter reports on the recent developments made on the design, fabrication and characterization of the triangular lattice PBG HC-PCF. Using insights gained from the photonic tight-binding model, we fabricated a double bandgap HC-PCF. The fabricated fibre exhibits two robust bandgaps centred at 1064 nm and 1550 nm. The design, fabrication and characterization of this fibre will be presented.**

* This work has been published in

P. S. Light, F. Couny, Y. Y. Wang, N. V. Wheeler, P. J. Roberts and F. Benabid. "Double photonic bandgap hollow-core photonic crystal fiber" Opt. Express 17 16238-16243 (2009).

3.1 Introduction

Advances in the design and fabrication of PBG HC-PCF have resulted in the advent of HC-PCF with optical attenuation as low as 1.2 dB/km at 1550 nm [7]. Efforts are now concentrating on speeding up the fibre fabrication process [53], tailoring the core for polarization maintaining purposes [57] and on the removal of unwanted surface modes from the bandgap [53, 58]. The latter aspect enables loss reduction together with an enhanced useable spectral bandwidth and lowered chromatic dispersion. Progress has also been made in finding PBG air-guidance in fibres with cladding structures other than the above-mentioned triangular-lattice [59]. Nevertheless, the narrow transmission bandwidth offered by PBG fibre has hindered the extension of its benefits to areas requiring the simultaneous guidance of optical frequencies spaced by more than 70 THz. For example, it would be desirable to bridge the wavelength ranges of Nd:YAG and Yb lasers at ~1 μm with that of the Ti:Sapphire (~800 nm) or Er-doped lasers used in telecommunications (~1.5 μm).

In this chapter we use the photonic tight-binding model framework to design and fabricate a single double PBG HC-PCF providing two spectral ranges of light guidance. The higher-order bandgap arises due to the extremely thin struts of the silica cladding and their fine-tuning relative to the apex size. The fibre is fabricated using novel techniques [53] without inserting the traditional interstitial rods between the capillaries in the stacking process and using a very thin core capillary. The fibre is demonstrated to guide light both at 1064 nm and 1550 nm with low chromatic dispersion, bridging thus telecommunications wavelengths with those of Nd:YAG and Yb fibre lasers.

3.2 Design of a Double Bandgap HC-PCF

In chapter 1, we used the tight-binding model to identify the resonators in PBG HC-PCF that are responsible for photonic band formation [23]. The calculated DOPS map in fig. 1.5 shows a fundamental bandgap centred around $k\Lambda = 15$. Intriguingly, there lies another bandgap at $\sim k\Lambda = 23$ but above the airline. Consequently, normal fibres exhibit almost no second bandgap. However, the presence of this second bandgap in the DOPS map raises the question of whether its spectral width and depth

can be increased sufficiently to achieve low-loss guidance through tailoring the resonator geometry. By virtue of the tight-binding model, changes to the resonator geometries alter their dispersion curves, and if done appropriately, the second PBG can open-up sufficiently below the air-line.

This idea was investigated numerically by making changes to the size of the struts and the apexes of a triangular-lattice that exhibits a very high AFF (~97%). Figure 3.1 shows the DOPS diagram simulated using a commercial finite-element method package (JCMwave)* [32]. The apex size is defined by its meniscus curvature *r* and the strut thickness is defined by its width *t* (fig. 3.1a). By comparing six structures with different apex size and strut thickness, the route to maximize the two bands can be investigated. Comparing the strut thickness in fig. 3.1(b-d) and apex radius in fig. 3.1(d&g), one can see that as expected the first bandgap favours large apexes and thin struts. The second bandgap edges, however, have a weak dependence on strut thickness (fig. 3.1c&f). From fig. 3.1(e-g), surprisingly, with the decrease of apex radius, the bandwidth of the second bandgap nearly doubled. Hence, to achieve two robust bandgaps, thin struts are favoured while a compromise on the apex size is unavoidable. In our case, the structure in fig. 3.1d with 0.15Λ apex size and 0.005Λ strut thickness was chosen for fabrication.

Another interesting point is the fact that the ratio between the central frequencies of the two bandgaps is independent of the strut and apex size. Set around 1.39, this ratio allows a good optical guidance for many interesting laser pairs such as telecoms/Nd:YAG (1310/1550 nm and 1064 nm), Nd:YAG/Ti:Sapph (1064 nm and 800 nm) and Ti:Sapph/HeNe (800 nm and 633 nm).

* The simulations were carried out by P.S. Light.

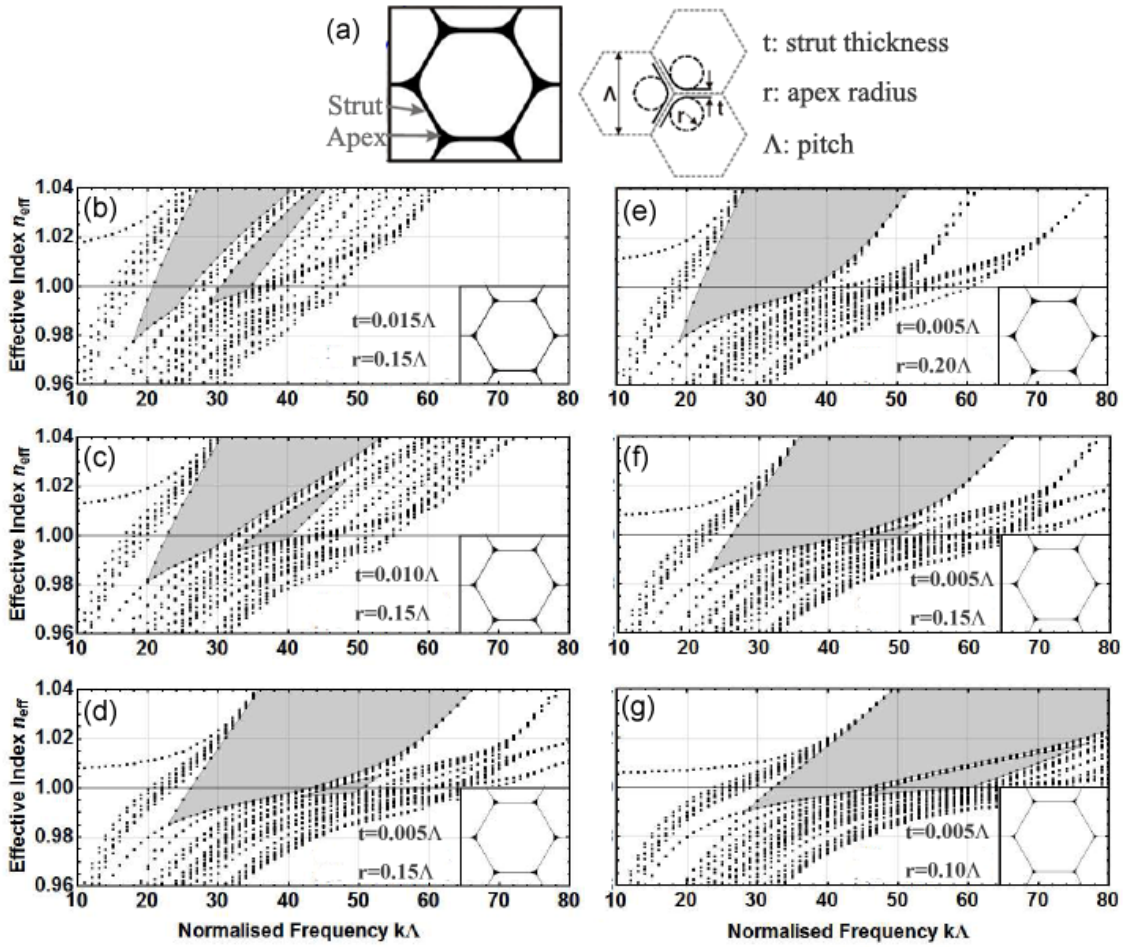

Fig. 3.1 Effective indices of cladding modes calculated at high symmetry points for six structures with different strut thickness and apex radius. (a) The strut thickness and apex radius is represented by t and r. (b)-(d) constant apex radius of $r = 0.15\Lambda$ and varying strut thickness of (b) $t = 0.015\Lambda$, (c) $t = 0.010\Lambda$ and (d) $t = 0.005\Lambda$; (e)-(g) constant strut thickness of $t = 0.005\Lambda$ and varying apex radius of (e) $r = 0.20\Lambda$, (f) $r = 0.15\Lambda$ and (g) $r = 0.10\Lambda$. The locations of bandgaps that cross the air-line are shaded. The horizontal line represents the air light line at $n_{eff} = 1$.

3.3 Fibre Fabrication

The stack-and-draw technique [60] for HC-PCF fabrication is well developed as illustrated in fig. 3.2. The main idea is to start with a large scale version of the structure and then stretch it to a final fibre. Dozens of capillaries (fig. 3.2a) drawn from the drawing tower are stacked one-by-one on a specially designed stacking rig to form a hexagonal structure. Several central capillaries are replaced by a large core capillary to form the core defect (fig. 3.2b). The stack is then inserted into a jacketing tube with some packings added to fill the gaps between the stack and the jacketing tube. The drawing of the stack to fibre is done in two stages: from stack to cane (fig. 3.2c) and

from cane to fibre (fig. 3.2d). This is because the overall draw-down ratio from the stack to the fibre is large therefore the process is difficult to control in one single step. The use of this intermediate stage also gives more opportunities in fibre design. When drawing fibres, different pressure may be applied to the core and cladding regions to control the air-filling fraction of the fibre and to ensure the structure is not deformed.

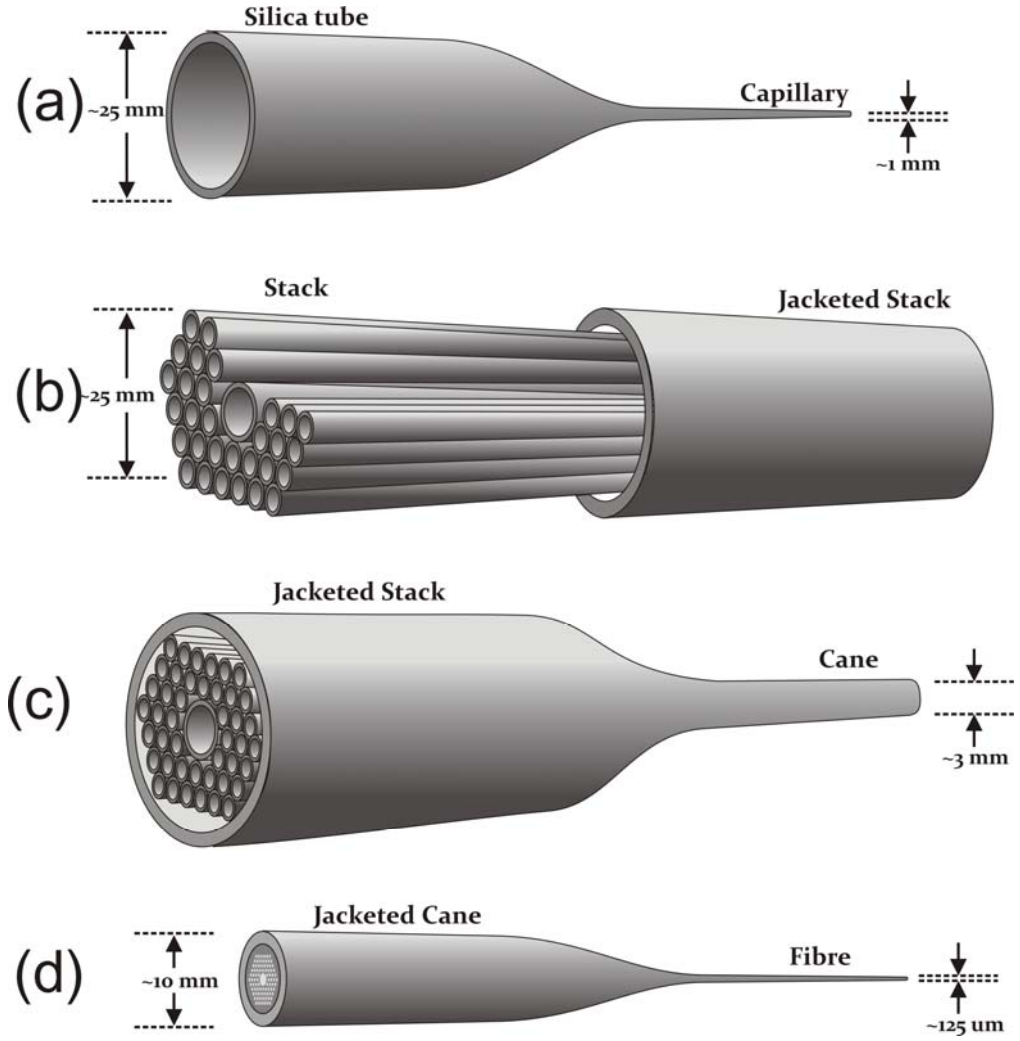

Fig. 3.2 An overview of the entire stack-and-draw technique. (a). drawing of capillaries; (b). capillaries are stacked and inserted into a larger tube; (c). the jacketed stack is drawn to smaller canes and (d) the jacketed canes is drawn into fibre.

Figure 3.2 only shows the main idea of fabricating HC-PCF. In the real fabrication process, slightly different techniques are applied for different type of fibre. For example, by removing different numbers of central capillaries, 1 cell, 7 cell or 19 cell fibre can be fabricated with different core size. During stack-to-cane process, for PBG fibre, interstitial holes between the capillaries need to be collapsed using a vacuum

while they are essential for Kagome fibre. Also here to avoid surface modes for the PBG fibre, the core capillary is pressurized to much greater degree than cladding capillaries during the initial capillary draw (fig. 3.2a).

Conventional fabrication technique of state-of-the-art PBG HC-PCF [7] involves the insertion of small rod between the capillaries in the stacking process. This is done so to increase the apexes size of the fabricated fibre since they are important to the fundamental bandgap. In our case however, the simulation results show the apex size needs to be reduced to maximize the high order bandgap. Thus we used a technique similar to the one reported in [53], where there are no interstitial rods being introduced. This is favoured because it allows a larger AFF. In the stacking process, thicker capillaries are used (fig. 3.3a). When drawing the fibre, very high pressure (>40kpa) is applied to inflate the capillaries. This results in the formation of very thin struts and relatively wide apexes (fig. 3.3c). The resulting fibre (fig. 3.3c), with a very high AFF (97%), has a bandgap with a similar central wavelength to the traditional PBG fibre (fig. 3.3d) but with a larger cladding pitch.

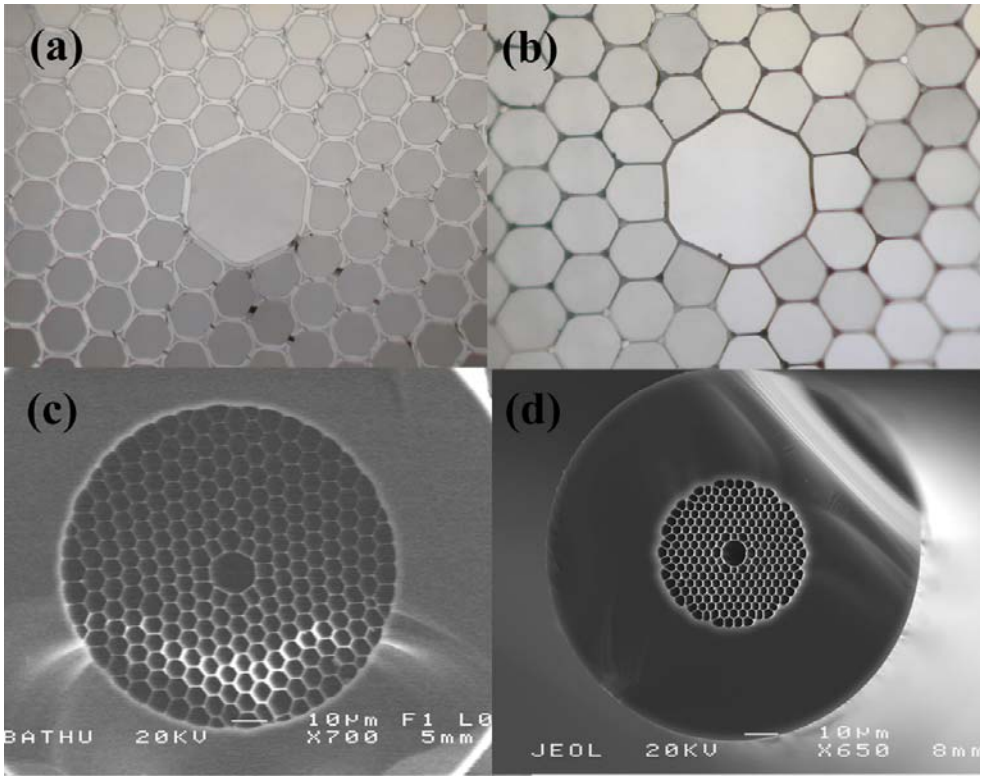

Fig. 3.3 Comparison of the PBG cane and fibre made by non-blobbied stack ((a) for cane and (c) for fibre) and blobbied stack ((b) for cane and (d) for fibre). With the same scale in the figure, the non-blobbied fibre shows a larger pitch then the blobbied fibre.

Based on the simulation results shown in section 3.2, several fibres were fabricated with different pitches. Figure 3.4 shows typical SEM images of the fibre cross-section (fig. 3.4a) with details of the core (fig. 3.4b), cladding (fig. 3.4c) and strut (fig. 3.4d). The pressurization during the fibre drawing allows the AFF to be 97% in the fibre cladding, with the strut thickness and apex curvature close to the simulation model in fig. 3.2. Due to the high pressure, the pitch has some variations across the cladding with an average of 6 μm (the pitch was usually ~2 μm for conventional ~93 % AFF PBG HC-PCF [7]). The core is around 18 μm and the cladding holes were blown up such that the strut thickness is ~100 nm.

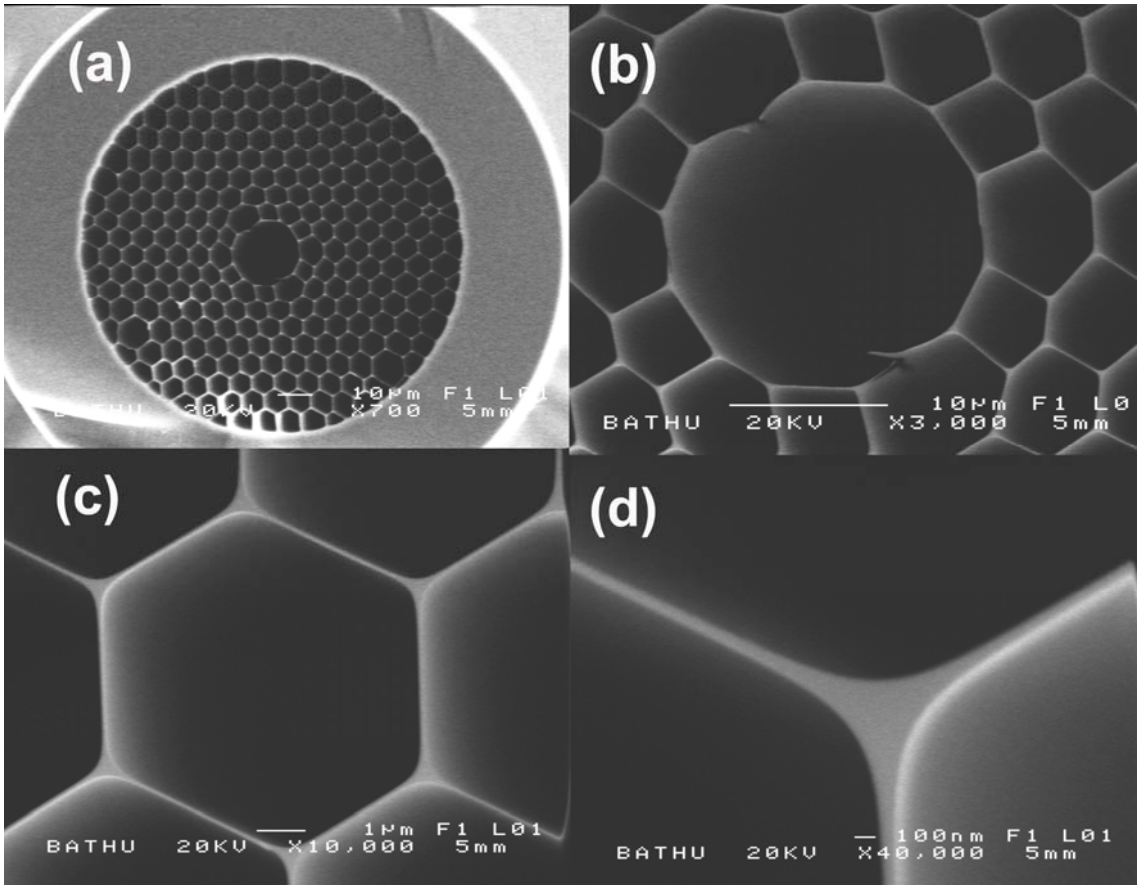

Fig. 3.4 SEM image of the fabricated fibre. (a) whole structure, (b) core, (c) cladding, (d) strut and apex.

3.4 Fibre characterization

3.4.1 Transmission and loss

Figure 3.5 shows the measured transmission and the attenuation spectrum of the fibre. The first bandgap centres at ~ 1515 nm and covers from 1335 nm to above 1750 nm (detection limit of the OSA). The second bandgap centres at ~ 1100 nm and covers from 1080 nm to 1140 nm. The optical bandwidths normalized to the central wavelength were found to be ~30% and 5.5% for the fundamental and 2nd order PBG respectively. Given the fact of the structure deformation, this matches reasonable well with the modelling results of central frequencies' ratio of 1.39 and spectral width of 32.7% and 13.3% for the fundamental and 2nd order PBG. From a cut back measurement from 25 m to 5 m, the first bandgap shows an attenuation of ~80 dB/km. This is relatively high compared to the conventional PBG fibre due to the non-uniformity of the cladding because of the high degree of structure expansion. The second bandgap shows a loss of ~500 dB/km. The increase in loss compared to the fundamental PBG, is due to partially the larger scattering loss at shorter wavelength [61] and the narrower bandwidth and "shallower" depth of the second order PBG, which would cause a higher confinement loss. Both of these loss figures can be significantly reduced by optimized control of pressurization during the fibre drawing process.

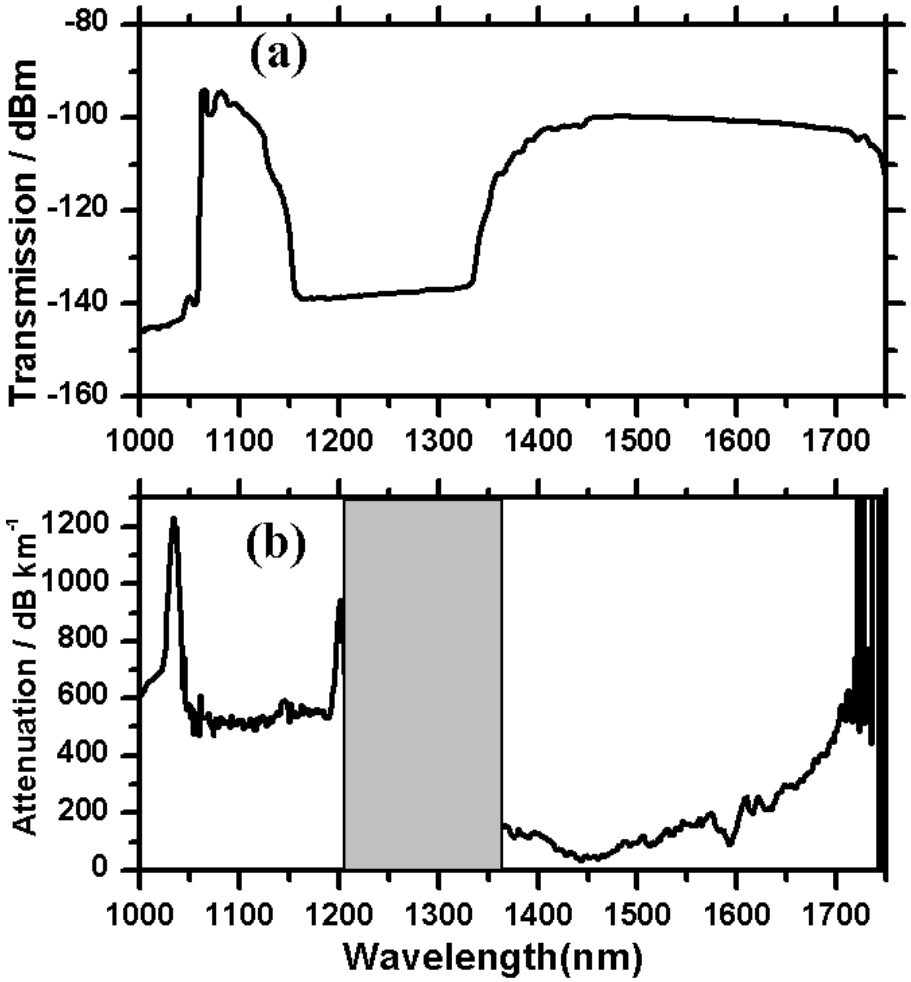

Fig. 3.5 (a) Transmission (b) attenuation spectrum of the fibre showing two bandgaps.

3.4.2 Dispersion

Apart from the transmission, another basic optical property of HC-PCF is its chromatic dispersion. It describes how the phase velocity $\upsilon(\omega)=\omega/\beta$ varies with wavelength throughout the transmission band of the fibre. For HC-PCF, the dispersion is normally fairly low since the light travels through air. This helps with efficient nonlinear processes such as Raman scattering of gas and pulse compression in HC-PCF. The exact dispersion can be tailored to a certain extent in the fibre design and fabrication process.

The dispersion is determined through measurements of group delay $D = \partial\beta_1 / \partial\lambda$, where β_1 is the group delay or inverse of group velocity. The group delay is measured using a Mach-Zehnder interferometer with controllable reference arm length [62] as

shown in fig.3.6. The supercontinuum source is split into two arms. One arm goes through the chopper wheel and is coupled to a 15-50 cm length of fibre. The other arm goes through exactly same components but without the fibre. A retro-reflector is positioned on a precision translation stage in this arm, and arm length is swept under computer control. The appearance of fringes with the sweep of the retro-reflector indicates the matched arm length.

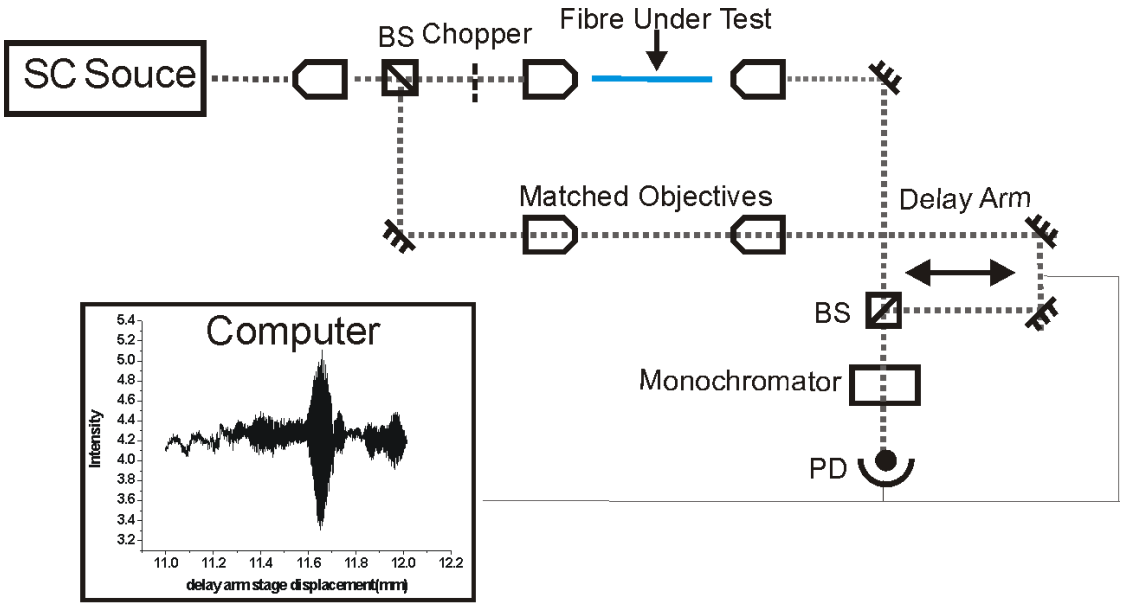

Fig. 3.6 Experimental setup for dispersion measurement based on a Mach-Zehnder interferometer. BS: beamsplitter PD: photodiode. On the computer shows the typical fringe by plotting the intensity at the photodiode as a function of retro-reflector dispalcement.

A 15 cm double PBG fibre was used by the author for the dispersion measurement. By selecting the wavelength (within the range of bandgap) of the monochromator, the measurement of the fringes was repeated at small wavelength intervals. The position of the fringe (retro-reflector displacement) determines the group delay $t_{gd}=2d_m/c$ where d_m is the displacement. A relationship of the group delay with wavelength can thus be plotted (fig. 3.7 square points). By fitting a polynomial curve to the group delay data (fig. 3.7 dashed grey curve), differentiating with respect to wavelength and dividing by the fibre length, the dispersion is obtained in ps nm^{-1} km^{-1} (fig. 3.7 solid black curve). The fibre shows a typical "S" shape dispersion curve with large normal dispersion near the short wavelength edge and large anomalous dispersion towards the long

wavelength edge. The magnitude of the dispersion toward the edges of the second bandgap is observed to be several times greater than that of the fundamental bandgap.

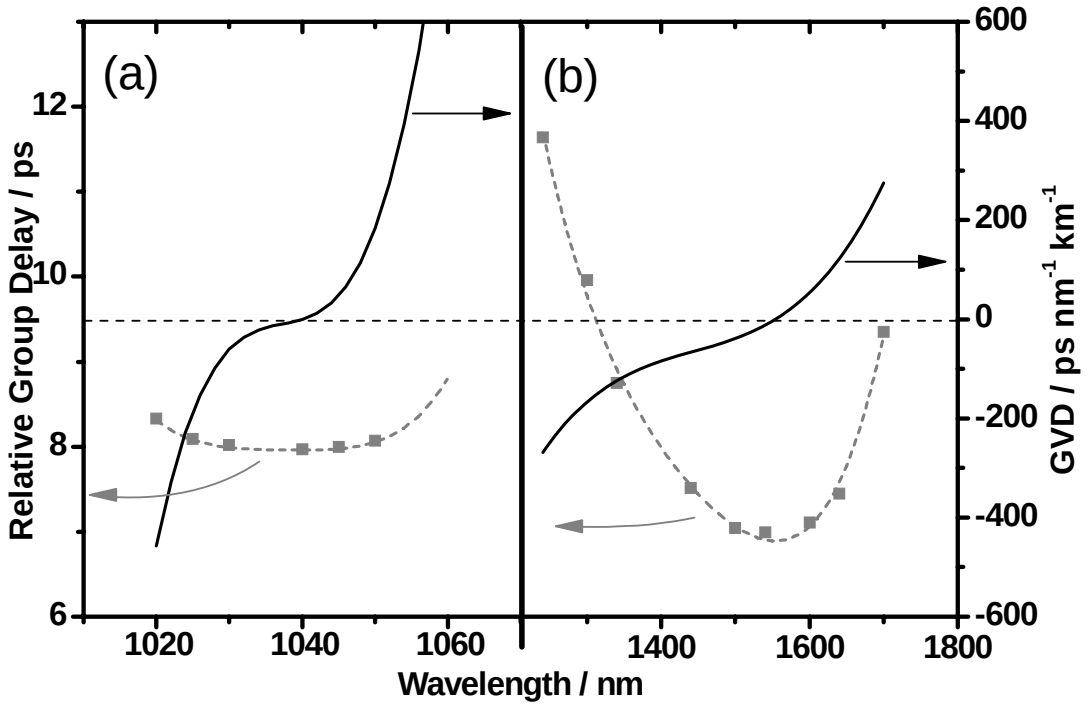

Fig. 3.7 Measured group delay (squares), and dispersion (solid lines) calculated based on fourth order polynomial fit to group delay data (dashed lines) at second bandgap (a) and first bandgap (b).

3.4.3 Tailoring the bandgaps

Several more fibres were fabricated and measured as shown in fig. 3.8. By reducing the pitch of the fibre from 6 μm to 5.3 μm, the first bandgap is blue shifted from 1550 nm to 1350 nm and the second bandgap from 1100 nm to 950 nm. Among them, fibre (c) guides both at 1064 nm and 1550 nm and hence is a very good candidate for transmission of both Nd:YAG/Yb radiation in a single fibre.

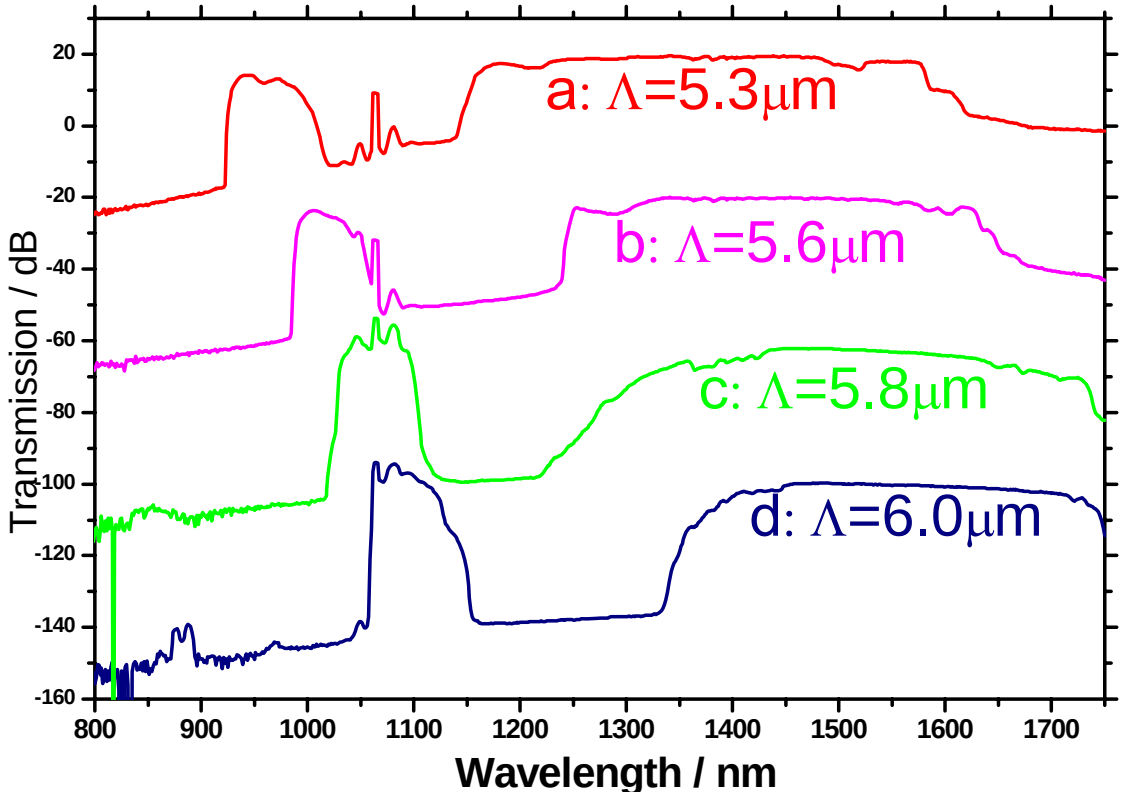

Fig3.8 Comparison of fibre transmission spectrum of 5m length for different pitches (offset vertically for clarity). (a). Λ=5.3 μm, (b). Λ=5.6 μm, (c). Λ=5.8 μm and (d). Λ=6.0 μm.

3.5 Summary

The advent of double bandgap fibre adds a competitive component into the PCF family. Simulations show that other than AFF, a more important parameter for the two bandgaps is the relative size of individual resonators in the fibre cladding. Experimentally, fabrication of fibre for dual-guidance of 1 μm and 800 nm light, or both 800 nm and 633 nm is in progress to add up to the double bandgap series, which currently only consist fibre with dual guidance at 1064 nm and 1550 nm. Work is also being carried out on the fine tuning of the parameters during the fibre draw to reduce the loss of the both bandgaps as they are still high for some of the applications. These fibres are promising for various applications such as delivery of laser pairs, which are often too separated in frequency to guide in a conventional HC-PCF.

Chapter 4

Core-Optimized Kagome HC-PCF Fabrication

This chapter reports on recent developments in Kagome HC-PCF fabrication. A seven-cell core and three-ring cladding large pitch Kagome lattice HC-PCF with a hypocycloid core shaped structure has been fabricated. The design of this core shape enhances the coupling inhibition between the core- and cladding modes. It offers a much lower optical attenuation than conventional circular core Kagome fibre (record loss figure of 40 dB/km) and more than two times larger optical bandwidth than the conventional PBG HC-PCF.[*]

---

* This work has been published in

1. Y. Y. Wang, N. V. Wheeler, F. Couny, P. J. Roberts and F. Benabid. "Low loss broadband transmission in optimized core-shape Kagome Hollow-Core PCF". Opt. Lett. 36 669-671 (2011).
2. Y. Y. Wang, F. Couny, P. J. Roberts and F. Benabid. CLEO/QELS 2010 Postdeadline section CPDB4.

4.1 Introduction

As described in the previous chapter, a double PBG HC-PCF was developed [32]; providing two spectral ranges of light guidance in a single fibre (eg. 1064 nm & 1550 nm). However, in terms of optical bandwidth, the spectral coverage of this fibre still remains much narrower than that of the large-pitch HC-PCF. Furthermore, unless using a material with a much lower index than silica, it is almost impossible to contemplate a significant increase in bandwidth for PBG HC-PCF because of the intrinsic properties of the dispersion of its silica cladding DOPS [23, 32]. On the other hand, due to the inhibited coupling mechanism of the large pitch broadband guiding HC-PCF, significantly decreasing further the optical loss of this type of HC-PCF poses a real challenge in both the cladding structure design and in the fibre fabrication. Geometrically, an ideal cladding structure topology for low loss and broadband guidance would require an elongated and thin silica web so to increase the transverse mismatch via increasing the azimuthal-like number [11]. This was experimentally attempted with Kagome-lattice and square-lattice HC-PCF by thinning the cladding glass web down to ~200 nm [11], and operating in the large pitch regime [9, 10]. However, even though the cladding geometry has been optimized to the limit of the fabrication process, the optical attenuation figure over large bandwidth has stayed above 0.5 dB/m due to the residual nodes at the intersections of the web-structure of the cladding. In this prior work, no particular attention has been given to the core structure. Due to fabrication process restrictions, the introduction of the core defect into the cladding structure results in a mismatch of geometrical symmetry between the core-surround and the cladding. Given the fact that most of the core-cladding field overlap occurs at the core-surround, the core-surround shape is thus of direct influence on the optical transmission of the fibre.

Here, and in line with the effort in fabricating low loss and broadband guidance HC-PCF, we explore a new avenue whereby we fabricated a Kagome-lattice HC-PCF with a hypocycloidal core-surround to enhance the coupling inhibition at the interface of the core and the cladding. We demonstrate experimentally and by numerical study that this core shape further reduces the coupling between the core modes and the cladding modes and therefore reduces the minimum achievable attenuation. The

fabricated fibres have an optimized seven-cell-core and three-ring-cladding structure with a typical optical transmission spanning from ~1100 nm to >1750 nm (limit of the OSA used) for the fundamental transmission band with a record attenuation baseline of ~40 dB/km. The development of this novel HC-PCF has potential for a number of applications where the combination of a large optical bandwidth and a low linear optical loss is a prerequisite.

4.2 Simulation Results

The impact of the core-surround is firstly investigated by numerical simulations carried out using the finite element method (JCMwave). The calculated loss spectra are shown in fig. 4.1. Figure 4.1(a) compares a loss spectrum for a three-ring Kagome generic cladding HC-PCF with a circular core (curve (1), blue) and hypocycloid core (curve (2), grey) respectively. In addition to exhibiting a similarly structured loss spectra due to resonances from the bends and web-intersections [11], the two fibres show distinctive differences for wavelengths longer than ~1.3 μm where the hypocycloid core fibre exhibits loss figures that are almost one order of magnitude less than that of the circular core. This can be partially explained by the fact that the hypocycloid core shape, in contrast to a circular core, doesn't cause distortions in the cladding structure. Furthermore, it was found out that the hypocycloid profile does provide less spatial overlap between the core modes and that of the silica struts.

In order to investigate the respective role of the cladding and the core-shape in the confinement loss, we calculate the loss spectra for a single circular ring, a single hypocycloid ring, a 1-ring and 3-ring Kagome HC-PCF with hypocycloid core (see fig. 4.1(b)). Here, the thickness of silica forming the different structures is taken to be 330 nm. A comparison between the loss spectra of the hypocycloid ring alone (curve (2), red), with the 1-ring cladding (curve (3), blue) and with 3-rings of Kagome cladding structure (curve (4), grey) shows clearly the confining role of the cladding. We particularly notice that by adding one ring (structure (3), blue) to the hypocycloid core (structure (2), red), most of the loss resonances are dramatically decreased. Adding two more rings (structure (4), grey) helps to further reduce some of the resonances but to a lesser extent than the addition of the 1st ring. The loss figure for the three-ring

curve shows a minimum of 46 dB/km at 1.8 μm. It is noteworthy, however, and unlike the PBG fibres, that the loss figures are not continuously reduced with increasing the number of rings. This is due to the guidance mechanism of this type of HC-PCF, where there is always a residual coupling between the continuum cladding modes and the core ones. Furthermore, the comparison between the circular ring (curve (1), pink) and hypocycloid ring (curve (2), red) in fig. 4.1(b) shows rather intriguing results. Except for the absorption peaks which are due to the small structural features (eg. intersection nodes), the hypocycloid ring exhibits a loss figure which is half that of the circular core. This fact is not anticipated, however, we could speculate that because of the longer perimeter of the hypocycloid relative to the circular surround, the silica-ring modes at frequencies away from the absorption peak exhibit faster transverse oscillations (i.e. higher azimuthal numbers), and hence lower transmission-loss by virtue of lower symmetry overlap with core modes. Furthermore, for wavelengths shorter than 660 nm, which corresponds to the glass thickness resonance [11], the hypocycloid ring or the extra cladding rings provide no significant reduction in loss compared to the anti-resonant single circular ring; indicating thus that inhibited coupling plays a lesser role in the confinement in this spectral range. We believe this is partly due to a stronger scattering at the shorter wavelength from the small cladding features such as the bends and the intersection nodes. However, in order to elucidate this, further work is required; particularly investigating the respective contribution of anti-resonance and inhibited coupling in the confinement loss.

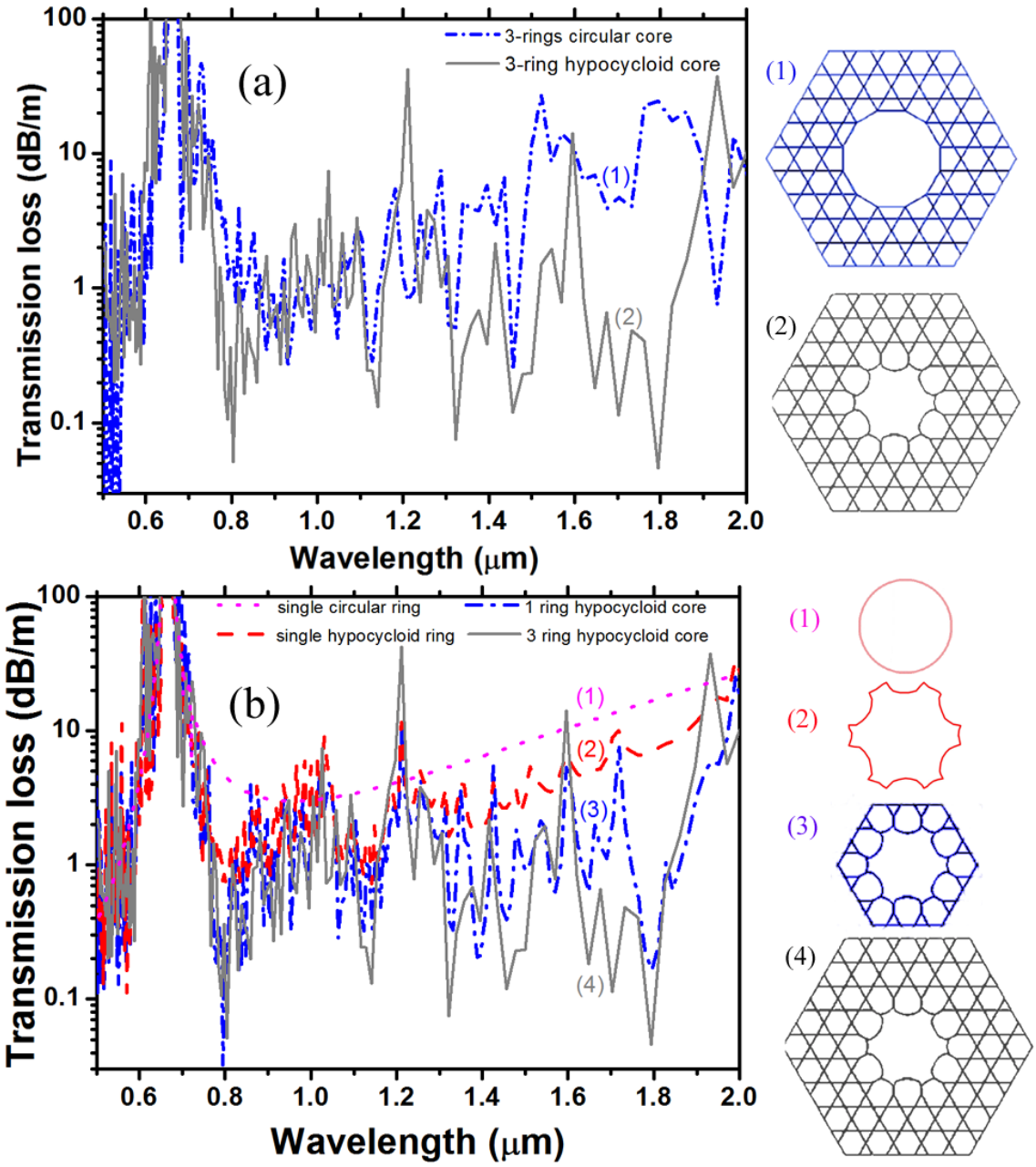

Fig. 4.1. (a) Calculated loss spectra for 7-cell core and 3-ring Kagome cladding HC-PCF with circular core ((1), blue and dotted) and hypocycloid core ((2), grey and solid). The corresponding structure used in the calculation is shown on the right. (b) Calculated loss spectra for a single circular ring ((1), pink and dotted), a single hypocycloid ring ((2), red and dashed), a 1-ring ((3), blue and dash-dotted) and 3-ring ((4), grey and solid) Kagome HC-PCF with hypocycloid core. The corresponding structure used in the calculation is shown on the right.

4.3 Experimental Demonstration

4.3.1 Fabrication Method

The hypocycloid-core Kagome fibre is fabricated using stack-and-draw technique as shown in chapter 3 section 3.3. To experimentally fabricate the hypocycloid core shape fibre, a "coreless" stack is used. When making the "coreless" stack, two core capillaries of the half length are inserted in the two ends, leaving a gap in between (fig. 4.2). The gap forms the "coreless" stack while the rest with the core capillaries supports the stack. The length of the gap is usually chosen to be <30 cm to avoid the cladding capillaries bending or falling into the gap area. To make efficient use of a 1m stack, a flame is introduced to heat the coreless area. This fuses the coreless part of the stack. While moving the flame through one direction, one end of the core capillary can be moved out gradually (fig. 4.2). This can be easily realized on the tower and a stack with up to 80 cm coreless area can be utilized.

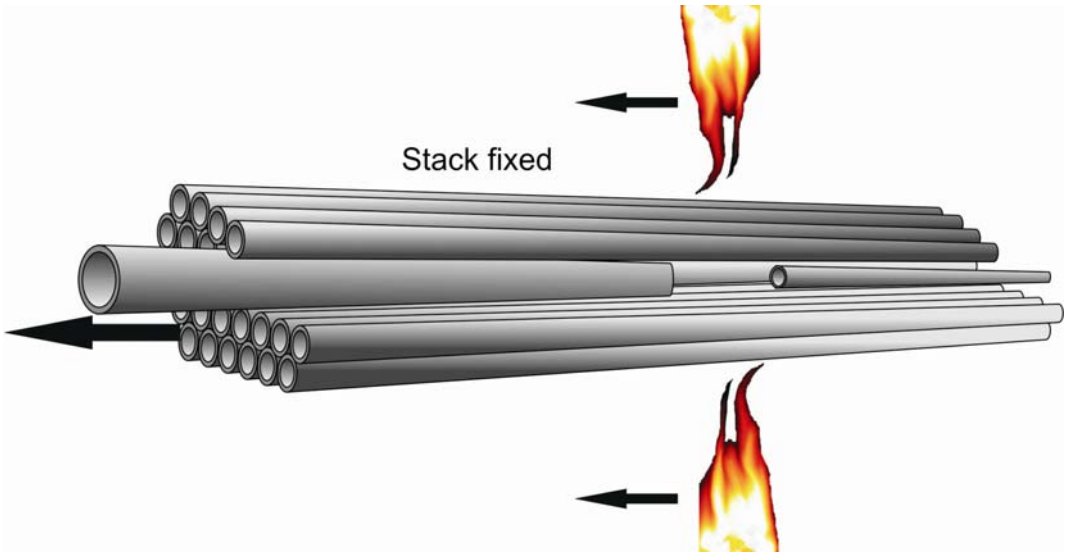

Fig. 4.2 Technique of making "coreless" stack. Two half core capillaries is used with a ~20 cm gap. After the stack is finished, heat is applied to the gap area. By moving one of the core capillary and the heat, up to 80 cm coreless stack can be formed.

4.3.2 Comparison of hypocycloid core and circular core

With the "coreless" stack technique, a seven-cell core, three ring Kagome-lattice cladding cane with a hypocycloid core shape was fabricated (fig. 4.3a). To illustrate the impact of the core-surround, two Kagome fibre were fabricated from the same cane. The two fibres exhibit identical cladding structures (18 μm pitch and ~ 330 nm strut thickness) but with different core-surround shape (fig. 4.3b&c). This was achieved by setting the pressure in the cladding to be the same during the draw of both fibres whilst applying a varying pressure in the core. The first fibre has a conventional circular core with a diameter of 75 μm. The second fibre, however, exhibits a 6-cusp hypocycloid core-shape with an inner diameter of 63 μm.

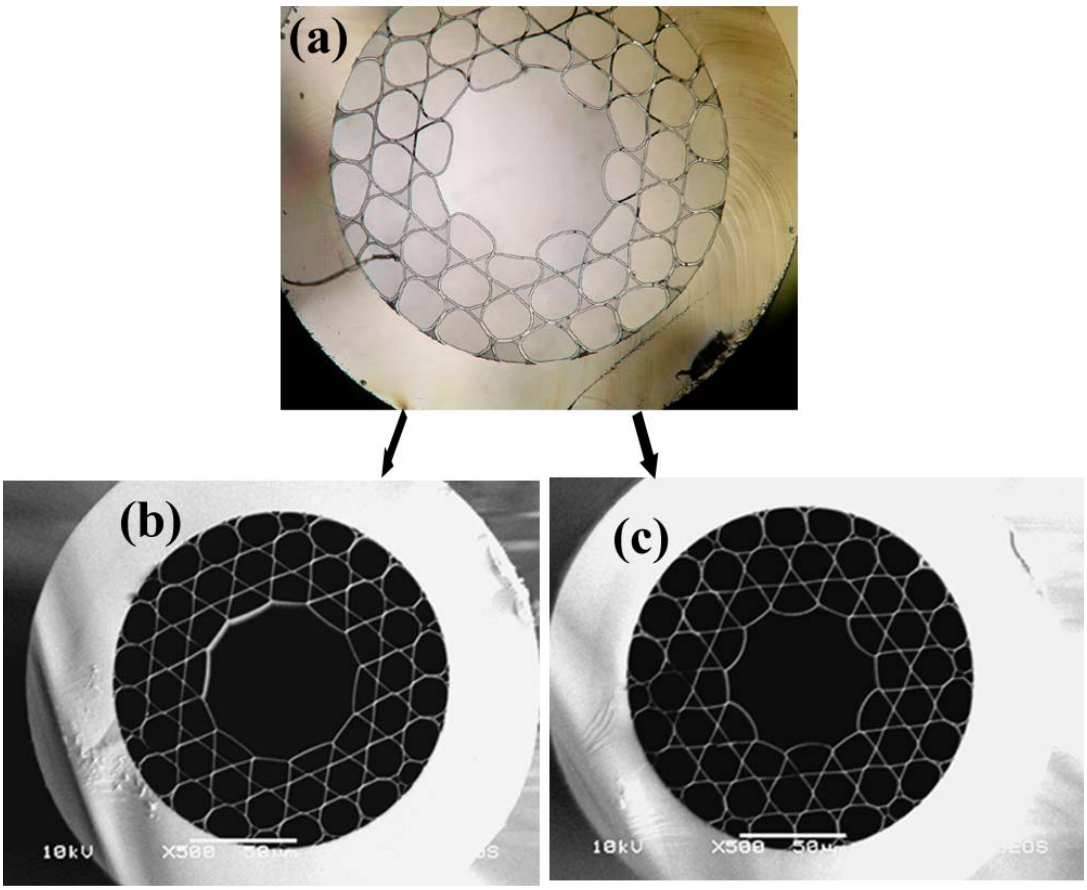

Fig4.3 Two Kagome fibre with circular (b) and hypocycloid (c) core shape fabricated from the same cane (a).

The optical attenuation of the two fibres was measured using a supercontinuum source and by a cut back measurement from 10 m length to 2 m length. The

attenuation spectra are shown in fig. 4.4. The circular core shape fibre exhibits a typical transmission spectrum with an average loss figure of 1.4 dB/m (fig. 4.4a), which is similar to previously reported Kagome HC-PCF [9]. The hypocycloid core shape fibre however, despite having the same cladding structure as the first fibre, exhibits a much lower attenuation with an average loss of 0.4 dB/m over a transmission band from 1050 nm to >1750 nm (fig. 4.4b). This agrees with the simulation results above (fig. 4.1a).

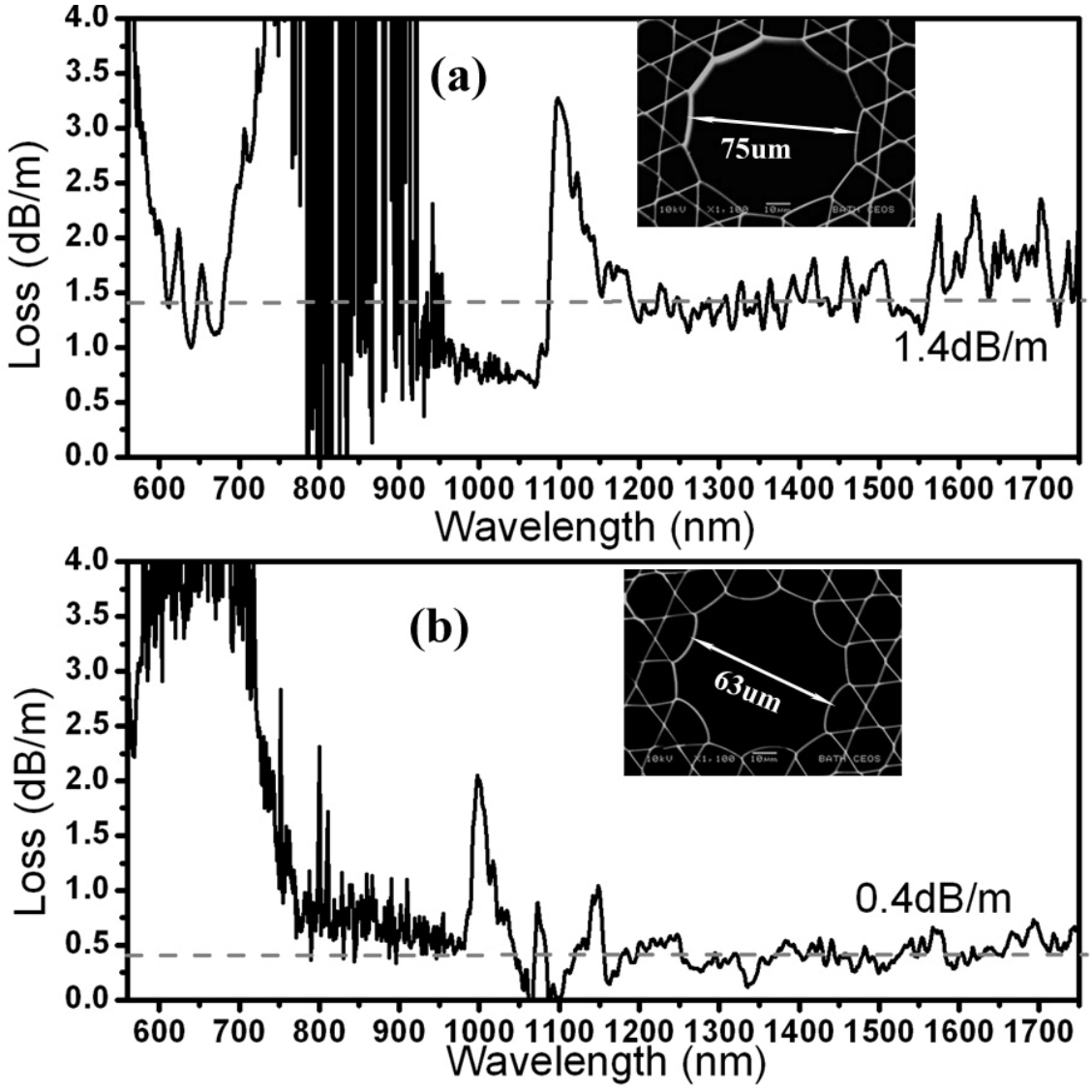

Fig4.4 Measured optical attenuation of the circular core shape (a) and the hypocycloid core shape (b) Kagome fibre.

4.3.3 A Kagome Fibre with state-of-art Loss figure (40 dB/km)

We then fabricated several fibres with further optimized hypocycloid cores and thinning the glass webs by controlling the relative pressure between the core and cladding during the fibre draw. In fig. 4.5, we show the SEM of the up-to-date best optimized fibre with an outer diameter of 300 μm, a pitch of 23 μm, and a strut thickness of 350 nm. The hypocycloid core has a perfect symmetric shape with an inner core diameter of 66 μm and an outer core diameter of 79 μm (fig. 4.5b), introducing no distortion to the 1st cladding ring.

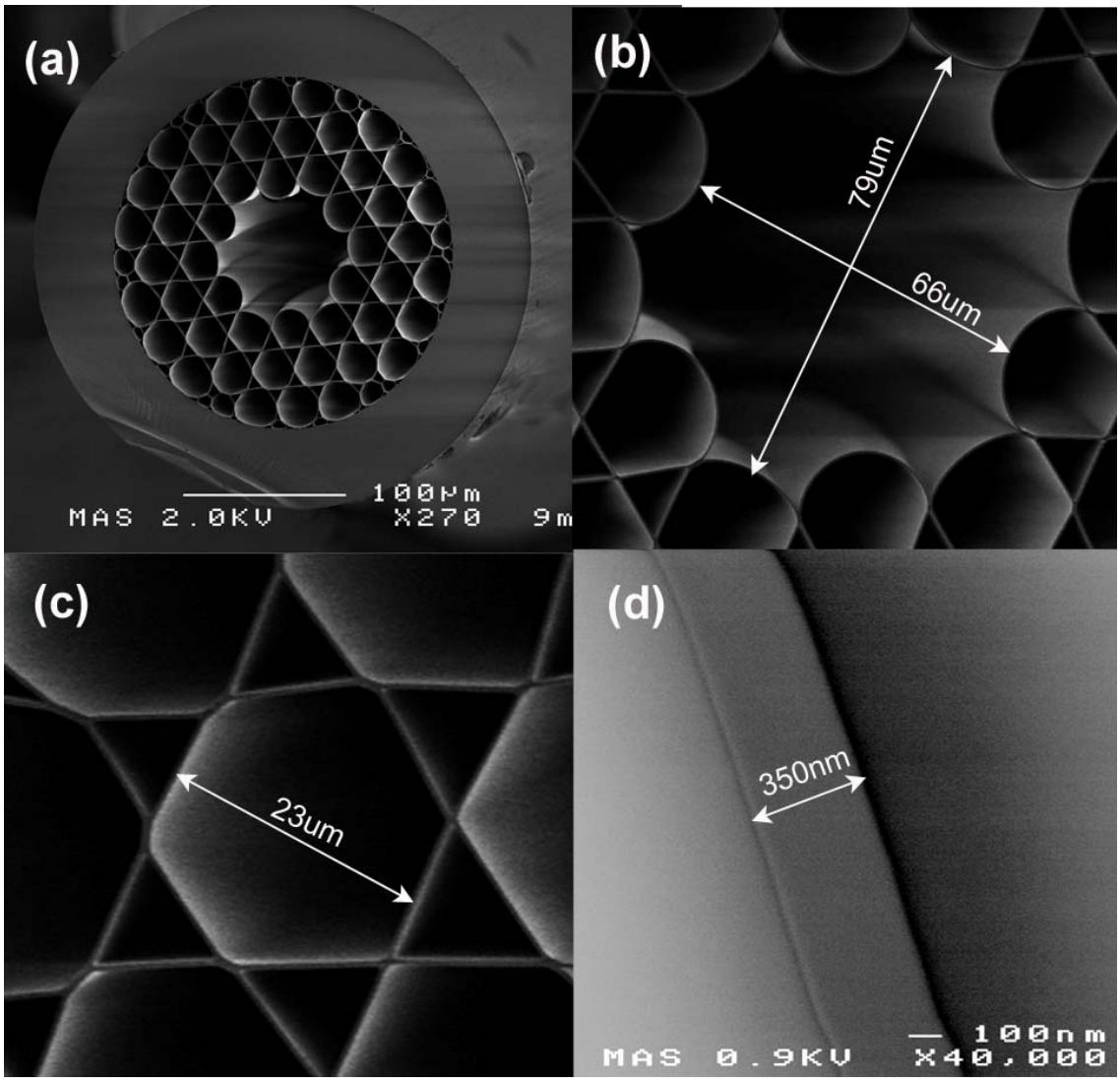

Fig4.5 SEM of the fabricated hypocycloid core shape fibre. (a) whole structure; (b) 66-79 μm core; (c) 23 μm pitch and (d) 350 nm strut thickness.

In fig. 4.6 we show the optical properties of this fibre. Figure 4.6a shows the transmission spectra of a 55 m and 5 m length of this fibre recorded using a white light source. One can see two bands with 5 m fibre, one from 600-750 nm and the other one in the near IR region. The visible band suffers a very high loss and disappears after 55 m. The loss spectrum for the IR band (fig. 4.6b) is obtained by cut-back measurement and shows a record baseline of 40 dB/km over a bandwidth spanning from 1100 nm to >1750 nm (limit of OSA) (bandwidth >100 THz) and reaching a minimum of 33 dB/km at 1440 nm and 1490 nm. This beats the PBG HC-PCF in terms of bandwidth (<70 THz for PBG) and demonstrates a comparable loss figure. This loss figure was confirmed by another cutback measurement using a supercontinuum source. It is noteworthy that the peaks in the attenuation spectrum correspond to the resonances of the different small cladding features such as bends and intersection nodes and are often barely visible for a transmission spectrum over a short length of fibre (fig. 4.6a for 5 m of transmission length) but are easily distinguished after a long transmission length (fig. 4.6a for 55 m transmission lengths, should be easier to see if 100 m is used) since they are the main cause of the loss. Because of the large core size of the fibre, high order modes can be supported in the core. However, by a judicious choice of the launching condition, matching the input light NA to the fibre NA (measured to be 0.023), it is possible to guide light in a fundamental core mode (fig. 4.6b insert).

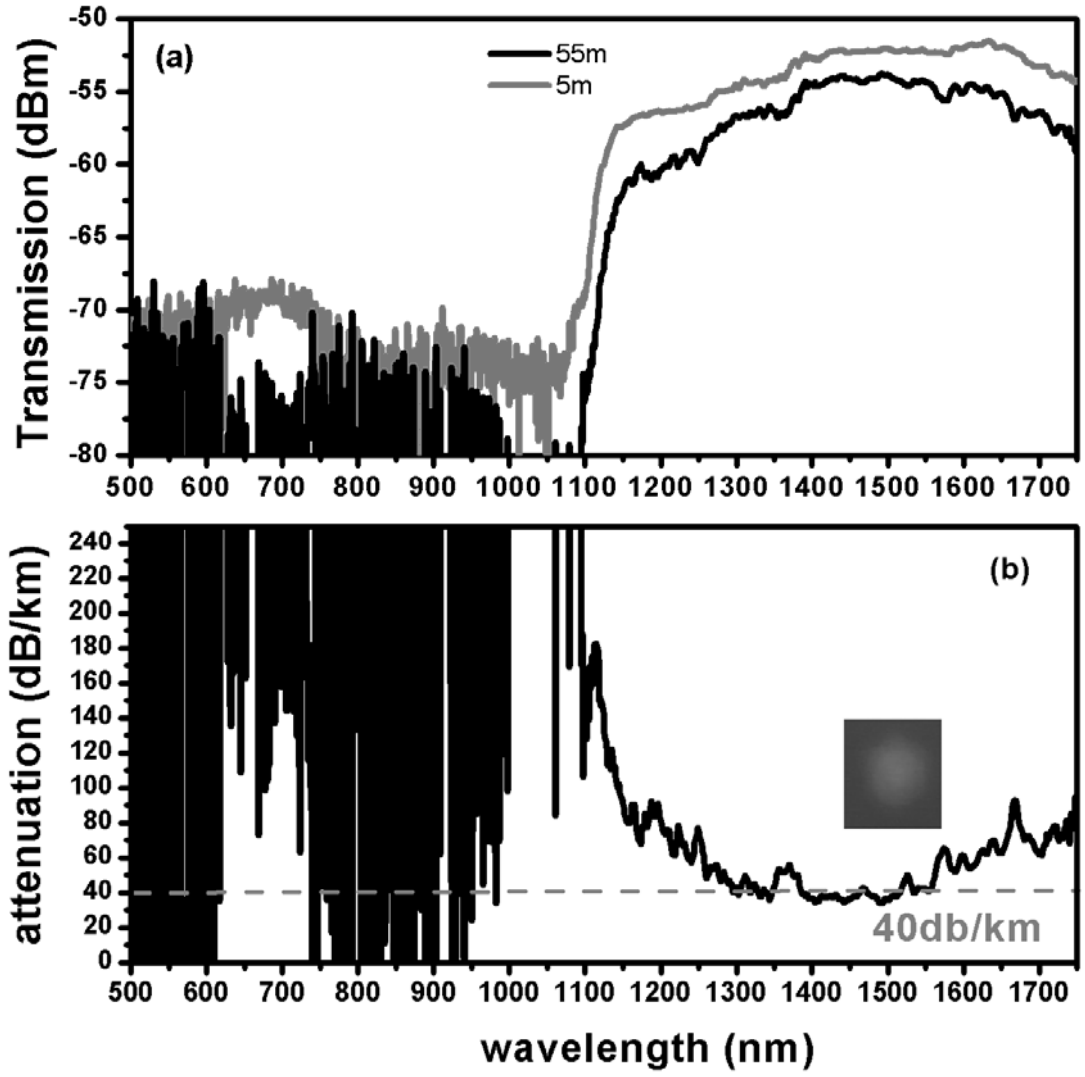

Fig4.6 Transmission (a) and attenuation (b) spectra of this fibre measured by the whitelight source with a cutback measurement from 55 m to 5 m fibre length. Insert shows the mode in the core by carefully selection of the launching conditions.

During the measurements, it was found that the fibre is very sensitive to bending. The bending loss is hereby measured. By launching the whitelight source to a 5 m long fibre with different bending radius (R) of 15 cm, 12.5 cm, 8 cm, 6.5 cm and 5 cm respectively, each with different turns, and comparing them with un-bended fibre (or fibre with large radius, eg. R>50 cm), the fibre bending loss can be estimated as shown in fig. 4.7a. At shorter wavelength near the edge of the band, the banding loss is extremely high with a value of ~2 dB/m for R=15 cm. This value is quickly decreased at longer wavelength. For >1300 nm, the bending loss stays <1 dB/m @ R=15 cm. However, when further bending the fibre, the bending loss is linearly increased with reciprocal of R as shown in fig. 4.7b where the bending loss is plotted against $1/R$ at

1550 nm. The reason for such high bending loss is believed to be because of the stronger overlap with silica while bent. Adding more cladding rings might solve this problem.

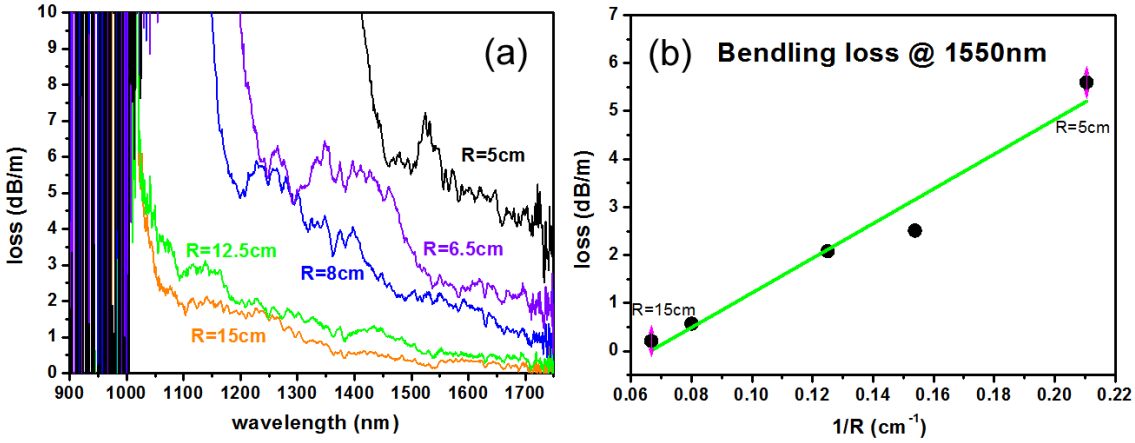

Fig. 4.7 (a) Bending loss of the hypocycloid core Kagome fibre with different bending radius, orange: 15 cm, green: 12.5 cm, blue: 8 cm, purple: 6.5 cm and black: 5 cm. (b) plotting the bending loss versus reciprocal of bending radius at a fixed wavelength of 1550 nm. The black solid points are the measured one and the green solid line is the linear fit.

4.3.4 Tailoring the fibre to shorter wavelength

As one can expect, tailoring the diameter of the fibre to smaller scale may allow guidance at shorter and more interesting wavelength. By gradually reducing the outer diameter, we achieved several fibres with their optical spectrum blue-shifted. Figure 4.8a shows a fibre with core diameter of 56 µm, pitch of 20 µm and strut thickness of 300 µm. The optical transmission spans from ~900 to >1750 nm (limit of OSA) (>160 THz) with attenuation baseline of 180 dB/km. In fig. 4.8b the fibre has a core diameter of 36 µm, a pitch of 16 µm and a strut thickness of 300 µm exhibiting a low loss band from 830 nm to 1350 nm (~140 THz) with attenuation baseline of 200 dB/km. Further reducing the diameter brought distortions to the core structure (fig. 4.8c). Nevertheless the fibre with a core diameter of ~30 µm, a pitch of 14 µm and a strut thckness of 230 µm still has a low loss band from 800 nm to 1350 nm (~150 THz). The attenuation baseline is 150 dB/km. The reason that this attenuation value is smaller than that of fig. 4.8b and the bandwidth is wider is because of the thinner struts. This series of fibres with different guiding band and different core sizes make it flexible for different

applications. For example, for high power delivery, large core size is favoured while for host of Raman scattering, smaller core size is preferred to achieve a higher FOM.

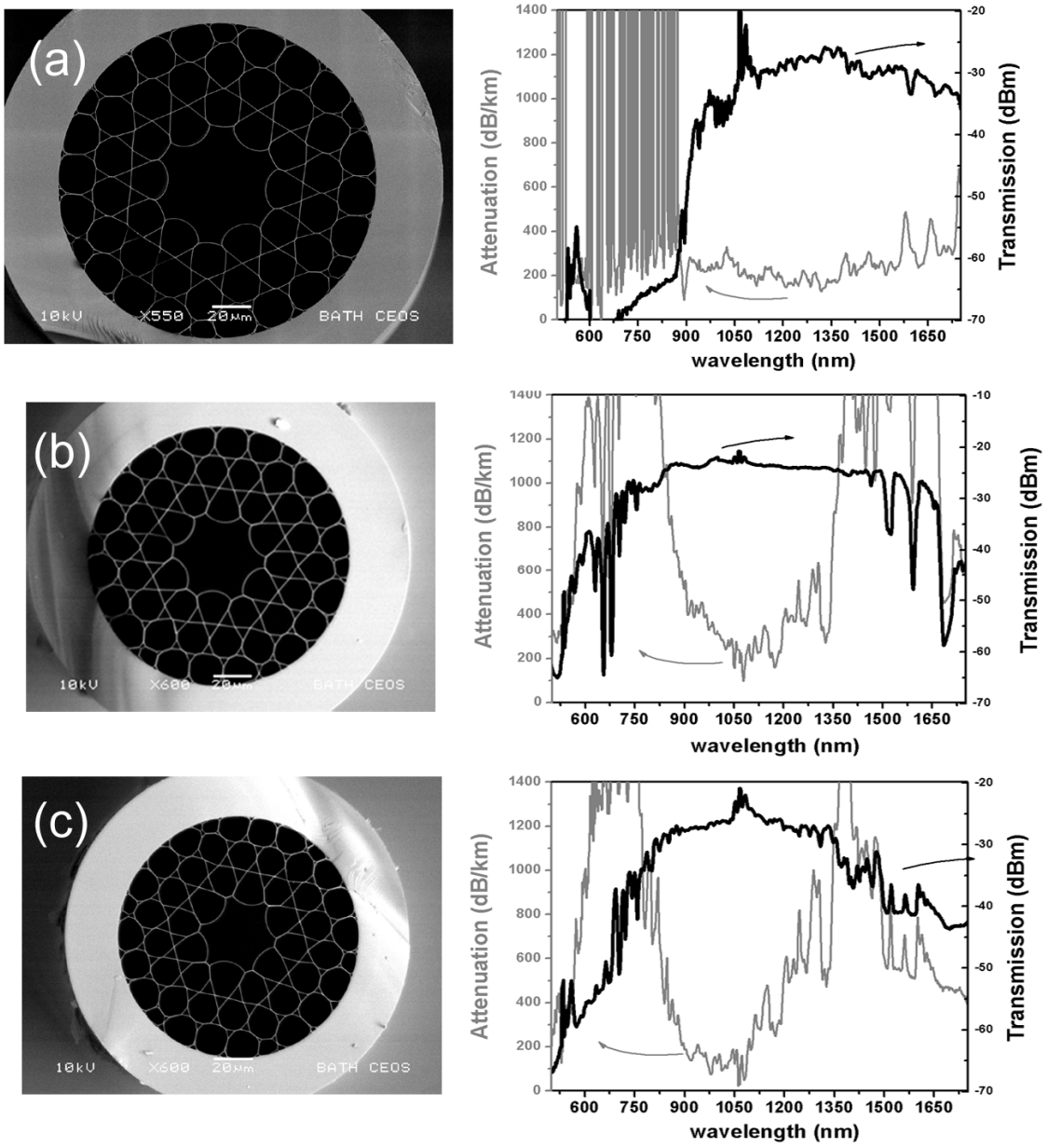

Fig4.8 Several hypocycloid core fibres with different core size and pitch. (a). core size of 56 μm, pitch of 20 μm and strut thickness of 300 nm with transmission of 5 m fibre (black) and loss (grey) spectrum. (b). core size of 36 μm, pitch of 16 μm and strut thickness of 300 nm with transmission of 2 m fibre (black) and loss (grey) spectrum. (c). core size of 30 μm, pitch of 14 μm and strut thickness of 230 nm with transmission of 5 m fibre (black) and loss (grey) spectrum.

Theoretically, by reducing the cladding pitch, one could shift the transmission band to the visible and even UV. However, this is difficult in the real fabrication process. Experiments show that with the decrease of the whole structure, the core is

more and more distorted (fig. 4.9a). Also, thinner struts are required at short wavelength region for a comparable bandwidth. One way to achieve a symmetric structure is to blow up the core to circular. Figure 4.9b shows a circular core fibre with a pitch of 12 μm. It exhibits a high attenuation of 1.5 dB/m due to the core structure. The optimization of the fibre is still in progress.

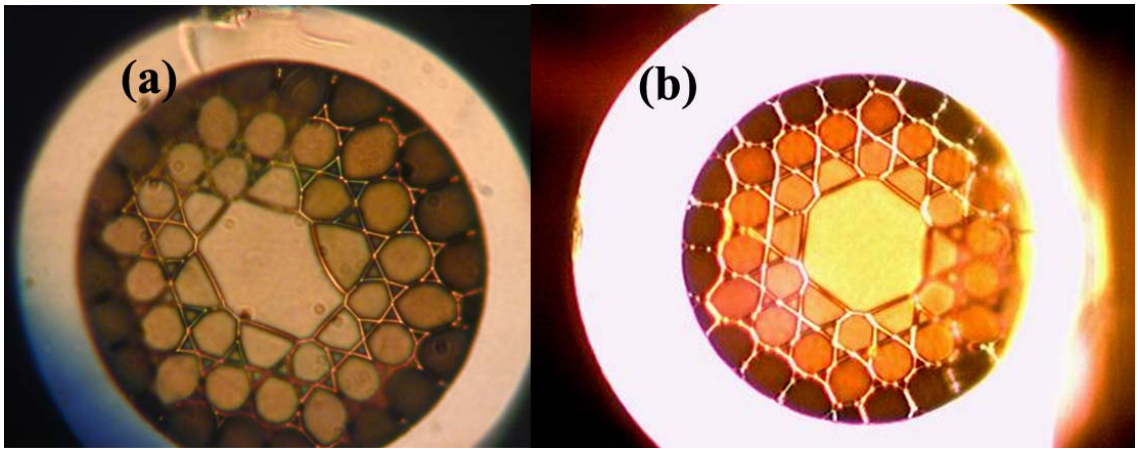

Fig4.9 fibre with 12 μm pitch (a) core distorted with no optical guidance; (b) core circular with high attenuation of 1.5 dB/km.

4.4 Summary

In conclusion, we have fabricated Kagome HC-PCF with a core-shape optimized for a record optical attenuation over a large spectral window, opening new prospects in designing and fabricating HC-PCFs that combine both large transmission bandwidth and ultra-low loss. Furthermore, a finer control in the fabrication process to reduce the glass thickness and to manage the core-shape is expected to improve the transmission performance to <40 dB/km and broaden the transmission window. The theoretical simulations showed that both the core-shape and the numbers of cladding rings play a role in the core mode confinement. Further studies are however needed to unravel the nature of the small cladding features and their effect on both the loss resonances and the core mode confinement.

Part 2

This part of the thesis discusses a body of work related to the generation of optical frequency comb based on the process of SRS. Thanks to the advent and the rapid development of HC-PCF over the years, efficient non-linear interactions between active gas and intense laser field becomes possible. Here the HC-PCF acts as a host for both light and gas to interact over several metres length and within micron-scale modal areas. This has been demonstrated throughout a number of reported experiments, and the scope of this part, which includes four chapters, represents a continuation of this and includes several new developments. In chapter 5, we review the physical background and the salient prior results in the generation of SRS in gas-filled HC-PCF, in particular the work which led to the generation of multi-octave Raman frequency comb spanning from the near-IR to the near-UV using a single pump laser pulse. In chapter 6 we report on the development of a compact version of SRS optical frequency comb using different and tailored HC-PCF filled with different gas and liquid phase materials. Of interest to the emerging bio-photonic applications, we demonstrate a Raman comb with several much-sought laser lines in the UV & visible spectral range. Chapters 7 and 8 deal with fundamental properties of the Raman comb. Here we show experimentally and theoretically, that despite the comb is generated through spontaneously emitted Stokes, all the spectral lines of the comb exhibit strong self-coherence and are mutually coherent (phase-locked) within each single shot. These results are of importance to attoscience and quantum optics.

Chapter 5

Review of Raman Comb Generation in H2-filled HC-PCF

This opening chapter of part 2 discusses the generation and the coherence proprieties of an ultra-broad (multi-octave) optical frequency comb based on "unseeded" SRS. Here, we review the theory of the amplification regimes of SRS, the control of SRS regimes in HC-PCF underpinning the coherent Raman generation, the Raman frequency comb generated previously and the prediction of its coherent properties.

5.1 Introduction

During the past decade, SRS [38, 63] has been identified as an alternative mechanism to HHG for creating attosecond pulses. Here, the Raman medium is optically excited in such a way that a coherence is built up [64] to a sufficient level to generate a broad optical comb comprising higher-order Stokes and and anti-Stokes components [65-70]. The most successful technique for the generation of such combs is the so-called molecular modulation [65-67]. In this technique, the medium Raman coherence is optically and adiabatically excited by two pump laser pulses with their frequency difference tuned near the Raman transition, to generate Raman lines that are mutually coherent and thus Fourier-synthesizable. In such a scheme the medium acts like a phase modulator with a modulation frequency equal to that of the Raman resonance. Another technique for optical frequency Raman comb generation is the use of a pump with a bandwidth larger than the Raman shift (known as the impulsive regime) [68-70]. In all these cases, Raman medium molecular excitation is coherently driven by the beating of the two exciting laser fields. This coherent build-up of the molecular excitation (or coherence) in turn modulates the fields to generate higher order Raman lines. Furthermore, the generation of coherent Raman combs requires very powerful transform-limited pulses whose duration is either very short (<10 fs) so its bandwidth is larger than the Raman transition frequency for the case of impulsive excitation or two nanosecond laser pulses whose frequency is slightly detuned from the Raman transition so to adiabatically excite the Raman coherence to a high value [65].

The above configurations contrast with single pump laser SRS whereby the Stokes is initiated from the spontaneous scattering, and thus the Stokes and the pump do not necessarily share a phase relationship. It is this mutual incoherence that drove researchers to devise schemes such as the ones mentioned above to avoid the quantum noise induced spontaneous emission adding to the laser pump noise [71].

A further possible technique to generate higher order Raman lines is to excite the Raman medium in the transient regime. This means driving the medium with only a single pump laser that emits a Megawatt of power (high gain regime) and whose pulse duration is much shorter than dephasing time T_2 of the Raman medium [43, 72, 73].

This is experimentally implemented by using transform limited sub-picosecond laser pulses, which raises the suggestion that the excitation is similar to the impulsive one.

In parallel to the above mentioned work, and subsequent to the development of HC-PCF, it has been shown that the transient regime of SRS (see section 5.2.2) could be achieved with much longer pulses (compared with the dephasing time T_2) and with very low powers [41]. This new configuration has led to ~70 THz wide Raman comb generation using PBG HC-PCF [41] and then a comb with a three-octave from 325 nm to 2300 nm, using Kagome HC-PCF [11]. Furthermore, this Raman excitation configuration raises the question of the mutual coherence of the Raman spectral lines as the process is initiated from the quantum noise induced spontaneous emission. We address this question experimentally and theoretically in chapters 7 and 8, and the present chapter aims to set the physical background and the prior art of the generation of Raman comb in HC-PCF.

In the following sections, we review the basic quantum theory behind SRS. We then highlight the different Stokes amplifications regimes. Finally, we show the generation of an ultra-broad Raman comb by virtue of H_2-filled HC-PCF and the predictions on the coherence of the comb.

5.2 Quantum theory and Regimes of SRS

Since its first prediction, theory of SRS has been undertaken using different approaches. The major ones include the photon rate-equation theory [74, 75], the semi-classical propagation theory [39, 76, 77] and the quantum-field propagation theory [78, 79]. The photon rate-equation theory deals with the average rate of photon flow and, thus, can not treat the coherent interaction between field and molecules. In the semi-classical theory, the electromagnetic field is treated as a classical quantity and the molecules are treated quantum mechanically. Although this approach has been extremely successful, the quantum fluctuation of the vacuum field is not included. It is noteworthy to state though that this method is often sufficient to simulate all aspect of SRS where the gain is sufficiently high. The inadequacy of this semi-classical approach is noticeable in the case of investigation of photon statistics or quantum information applications [80] where spontaneous emission and the properties of its temporal and spatial modes are

of importance. In the quantum-field propagation theory, the electromagnetic field is also quantized. Here, the spontaneously scattered Stokes is rigorously taken into account. Hence, the quantum theory is more comprehensive in predicting observable manifestations of the quantum initiation of SRS and will be applied in our studies. Furthermore, the quantum theory treatment gives unique insight into the nature of the physical mechanisms underpinning the onset of SRS.

5.2.1 Coupled-wave equation

We first consider a simplified case which has been studied by Raymer *et al*. [78]: a single pump laser pulse (pulse duration τ_0) with a narrow bandwidth (no impulsive excitation) is injected into a Raman active gas which is confined in a pencil-shaped medium (one-dimensional propagation) and spontaneously generates the 1st Stokes field (high order Raman lines are ignored) from a given far off-resonance Raman transition following $\omega_0 = \omega_S + \omega_R$ (fig. 5.1). In the case of un-depleted ground state and pump field throughout the Raman generation, the coupled wave equation which links the evolution of the Stokes field to that of the pump and the excitation of the Raman medium and under the slowly varying-envelope approximation, are reduced to:

$$\frac{\partial}{\partial z}\hat{E}_S^{(-)}(z,\tau) = -i\kappa_2\hat{Q}^{\dagger}(z,\tau)E_0(\tau) \tag{5.1.1}$$

$$\frac{\partial}{\partial \tau}\hat{Q}^{\dagger}(z,\tau) = -\Gamma\hat{Q}^{\dagger}(z,\tau) + i\kappa_1\hat{E}_S^{(-)}(z,\tau)E_0{}^{*}(\tau) + \hat{F}^{\dagger}(z,\tau) \tag{5.1.2}$$

Here, $\tau = t - z/\upsilon_s$ is the retarded time with υ_s being the group velocity of the Stokes wave. $E_0(z,\tau) \equiv E_0(\tau)$ is the un-depleted pump field which is treated classically. The complex coupling coefficients κ_1 and κ_2 are the nonlinear response terms of the coherence medium and are assumed to be instantaneous. The Stokes field operator $\hat{E}_S^{(-)}$ and $\hat{E}_S^{(+)}$ are related to the photon creation $\hat{a}^{\dagger}$ and annihilation operators $\hat{a}$. $\hat{Q}$ is the collective molecular-excitation operator at location $z \in [0, L]$. They are defined as

$$\hat{E}_S^{(-)}(z,\tau) = i\sqrt{2\pi\hbar\omega_S / AL}\,\hat{a}^{\dagger}(z,\tau) \tag{5.2.1}$$

$$\hat{E}_S^{(+)}(z,\tau) = i\sqrt{2\pi\hbar\omega_S / AL}\;\hat{a}(z,\tau) \tag{5.2.2}$$

$$\hat{Q}(z,\tau) = 1/(NA)\sum_{\{m\}_z}\hat{\sigma}_{31}^{m}(\tau) \tag{5.2.3}$$

where $\hat{\sigma}_{31}^{m}(\tau)$ is the raising operator for the m-th molecule located within a volume cell at position z, describing the excitation of the molecule from ground state $|1\rangle$ to vibrational state $|3\rangle$ (fig. 5.1). ω_0 and ω_s are the pump and the Stokes frequency and $\omega_R=\omega_0-\omega_s$ is the Raman-shift frequency (as shown in fig. 5.1). N is the molecular number density [81], A is the interaction area and L is the interaction length. In Eq. 5.1.2, terms $\Gamma\hat{Q}$ and $\hat{F}$ are the added terms representing the damping of the molecular oscillations due to the collisions at the dephasing rate Γ, and the quantum statistical Langevin operator describing the collision-induced fluctuation [78] respectively.

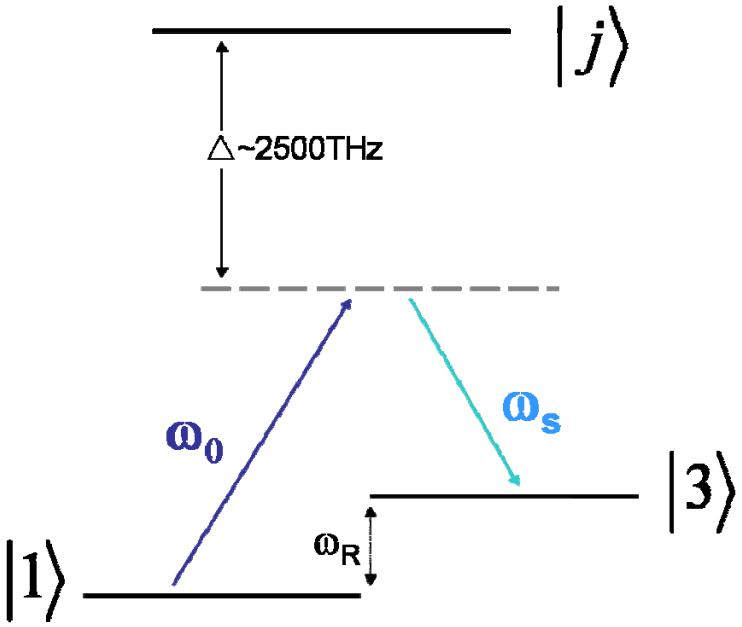

Fig.5.1 Schematic representation of the energy level diagram. A pump photon with frequency ω_0 drives the molecular/atom from the ground state $|1\rangle$ to the rotational state $|3\rangle$ and it emits a Stokes photon at ω_s.

The Maxwell-Bloch equation (5.1) indicates that the electric fields and the molecular motion are coupled together via the nonlinear term of the medium polarisability κ_1 and κ_2. The interference between the molecular motion field $\hat{Q}$ and the pump electric field E_0 drives the electric field $\hat{E}_S$ at the Stokes frequency. In turn, the interference between the different electric fields also drives the molecular motion. The comprehensive spatial and temporal buildup of the S/AS fields can be obtained from its solutions.

To solve the coupled mode equation (5.1), the initial conditions for the operators must be included, which are [78]:

$$\left\langle \hat{Q}^{\dagger}(z,0)\hat{Q}(z',0)\right\rangle = (1/AN)\delta(z-z') \tag{5.3.1}$$

$$\left\langle \hat{Q}(z,0)\hat{Q}^{\dagger}(z',0)\right\rangle = 0 \tag{5.3.2}$$

$$\left\langle \hat{E}_S^{(+)}(0,\tau')\hat{E}_S^{(-)}(0,\tau)\right\rangle = (2\pi\hbar\omega_s/AL)\cdot\delta(\tau-\tau') \tag{5.3.3}$$

$$\left\langle \hat{E}_S^{(-)}(0,\tau)\hat{E}_S^{(+)}(0,\tau')\right\rangle = 0 \tag{5.3.4}$$

These initial conditions describe the zero-point quantum fluctuations which represents white noise in time and space and the un-correlation of the molecules temporally and spatially. Equation (5.3.1) and (5.3.2) describes the quantum mechanical zero-point motion of the oscillator and Eq. (5.3.3) and (5.3.4) describes the free-field operator. In addition to the initial conditions, $\hat{F}$ continually reintroduces quantum fluctuation to the system otherwise the damping of $\hat{Q}$ in Eq. (5.1.2) would cause the zero-point fluctuations to decay exponentially.

5.2.2 Regimes of SRS

The expression of the Stokes intensity has been derived by Raymer and Mostowski [78] by adapting the initial conditions (5.3) to the coupled mode equation (5.1). The Stokes intensity output is related to the Stokes field by $I_S(L,\tau_0) = \frac{\nu_S}{2\pi}\left\langle \hat{E}_S^{(-)}(L,\tau_0)\hat{E}_S^{(+)}(L,\tau_0)\right\rangle$. The unit of the intensity (in W/cm^2) is set as the power transmitted through the end facet of the excited region of the Raman medium into the solid angle A/L^2 defined by the geometry of the region. Assuming the laser has a constant intensity I_P and

square-shaped pulse temporal profile $\tau \in [0, \tau_0]$, the deduced amplified Stokes intensity $I_S(L, \tau_0)$ takes the form [78]:

$$I_s(L,\tau_0) = \frac{\hbar\omega_s \Gamma g L}{2A}(e^{-2\Gamma\tau_0}[I_0^2(\sqrt{2gL\Gamma\tau_0}) - I_1^2(\sqrt{2gL\Gamma\tau_0})]) + \Gamma^2 gL(\int_0^{\tau_0} d\tau' e^{-2\Gamma\tau'}[I_0^2(\sqrt{2gL\Gamma\tau'}) - I_1^2(\sqrt{2gL\Gamma\tau'})]) \quad (5.4)$$

where I_0 and I_1 are modified Bessel functions. g is the steady-state gain coefficient $g = 2\kappa_1\kappa_2 |E_0|^2 / \Gamma$ and can be written as $g=g_{ss}I_P$ where g_{ss} is the Raman gain of the medium in cm/GW. A numerical evaluation of normalized Stokes intensity growth from Eq. 5.4 is presented in fig. 5.2 as a function of the normalized interaction time $\tau_0\Gamma$ for various values of the net gain gL. From this calculation, three regimes of Raman amplification can be defined.

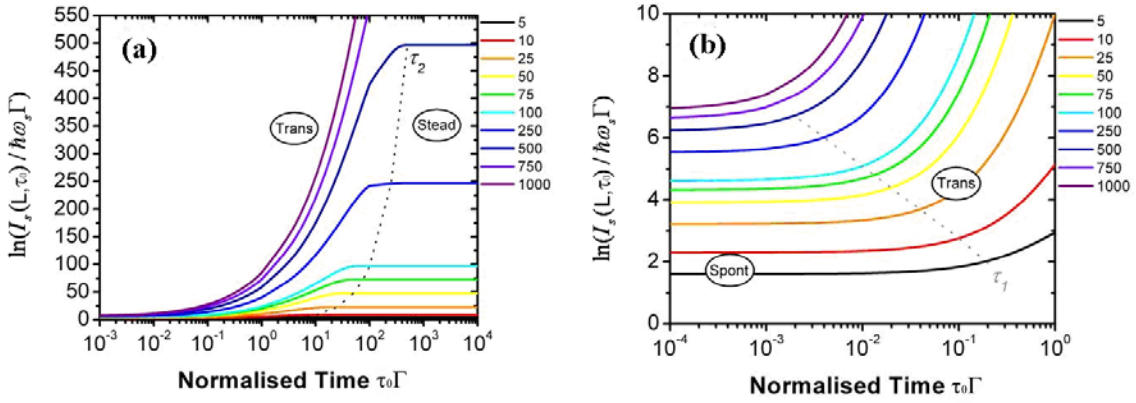

Fig. 5.2 Normalised Stokes intensity growth from quantum noise fluctuation as a function of normalised pump laser pulse width $\tau_0\Gamma$ for different values of gL using Eq. 5.4 [78, 82] (here A is set to 1 cm^2) for (a) high values and (b) low values of $\ln(I_s(L,\tau_0)/\hbar\omega_s\Gamma)$ showing the three regimes of Raman amplification. The passage times τ_1 and τ_2 are identified as dotted lines in (a) and (b) respectively.

For laser pulse duration τ_0 shorter than the characteristic time $\tau_1=1/gL\Gamma$ (i.e. in the excitation regime with small gain or short pump pulse regime), spontaneous Raman scattering is dominant. This regime is shown in fig. 5.2b below the dashed line τ_1. In this regime, the Stokes amplification is very low and is independent of the pulse duration τ_0. The expression of the Stokes intensity can be simplified to:

$$I_s^{SP}(L,\tau_0) = \frac{\hbar\omega_s \Gamma g L}{2A} \tag{5.5}$$

which indicates that the Stokes amplification follows the laser intensity in an algebraic fashion and represents an amplification of the spontaneous emission.

For pump laser pulse duration τ_0 longer than the characteristic passage time $\tau_2 = gL/\Gamma$, i.e. in the small gain or long pump pulse regime, the steady state regime is reached. In this regime, only the second term of Eq. (5.4) contributes to the amplification and could be reduced to the following expression:

$$I_s^{ss}(L,\tau_0) = \frac{\hbar\omega_s \Gamma e^{gL}}{2A\sqrt{\pi g L}} \tag{5.6}$$

Similar to the spontaneous regime, the Stokes intensity is also independent of the pulse duration τ_0 (see fig. 5.2a), though the achievable Raman amplification can be much higher since it follows an exponential build-up of gL ($I_S \propto e^{gL}$). This result also verifies that g is properly identified as the steady-state gain coefficient. Furthermore, it is noteworthy that in this regime, the photons contained in the generated Stokes pulse are not necessary correlated since the Stokes pulse generation time is sufficiently long for several molecular dephasings and excitations to occur.

For pulse duration τ_0 staying between the two characteristic passage times τ_1 and τ_2 ($1/gL\Gamma < \tau_0 < gL/\Gamma$), i.e. in the high gain or short pump pulse regime, the Stokes line strongly depends on the pump laser pulse duration τ_0 (fig. 5.2). This amplification regime is called transient. Only the first term in Eq. (5.4) contributes and can be approximated to:

$$I_s^{tr}(L,\tau_0) \approx \hbar\omega_s \frac{e^{2\sqrt{2gL\Gamma\tau_0}}}{8\pi A\tau_0} \tag{5.7}$$

In this regime, the Stokes intensity gain is related to the square root of gL. The pump pulse duration is long enough ($\tau_0 > \tau_1$) that the number of pump photon is large and triggers SRS but short enough ($\tau_0 < \tau_2$) that the collisional dephasing rate Γ has little effect on the stimulated Stokes since the Stokes duration $\tau_S = \sqrt{\tau_0 / 16gL\Gamma}$ is smaller

than T_2 [78] and independent of T_2 (note that g is inversely proportional to Γ hence $gL\Gamma$ is independent of T_2). Consequently, the phase of the Stokes field (within one pulse duration) is directly related to that of the pump and the molecular excitation (coherence). This implies that the generated Stokes maintains a certain degree of molecular coherence during the Raman interaction. A more detailed discussion about why the transient regime can result in coherent Raman will be given in chapter 7 section 7.2 where a modal picture is introduced showing that the Stokes photons are excited with a dominant spatial temporal mode.

The above study established the existence of three regimes of amplification for systems pumped by pulsed lasers distinguished by characteristic times $\tau_1=1/gL\Gamma$ and $\tau_2=gL/\Gamma$. In most experiments (i.e. free space or capillaries), the effective interaction length is limited by the Rayleigh range of the focused laser beam (for a single-pass configuration). In such conditions, the net gain remains small, and will become high (>100) only at very large pump peak powers (MW level). Thus the transient regime only appears with a MW-power transform limited sub-picosecond laser pulse. With the advent of HC-PCF, the above context changes dramatically. An effective interaction length of hundreds of metres has become possible and the Raman gain gz can be extremely large even with a mW average power laser (see section 5.3.2). Consequently, one could extend the transient regime to longer pulses and low power lasers.

5.2.3 Control of Raman regimes in H_2-filled HC-PCF

Benabid *et al*. [41], explored experimentally the dependence of Stokes amplification on pump pulse duration in the case of a Raman medium in a piece of HC-PCF. Among the salient results is that through the use of HC-PCF and by a simple choice of the fibre length one could obtain transient SRS even with a pulse duration several times larger than the dephasing time of the medium. This contrasts with previous results whereby the transient regime is often limited to transform-limited sub-picosecond laser pulses. To experimentally identify the Raman amplification regimes in HC-PCF, they investigated the evolution of the pump energy threshold E_P^{th} required to generate 1st Stokes line versus pump pulse duration. The Raman threshold net gain is defined to be

$G^{th} = \ln(I_s(L,\tau_0)/\hbar\omega_s\Gamma)$ (A is set to 1 cm²). This represents a conveniently chosen triggering point of the stimulated and corresponds to G^{th} being a number between 15 and 30. That means the Stokes intensity should be increased up to 10^{13} times compared to the initial noise (I_S^{noise} is defined as $\hbar\omega_s\Gamma/2$). Applying the above analytical approximations of the Stokes evolution in steady-state regime and transient regime (eqs 5.6 &5.7), we have

$$E_{P,SS}^{th}(\tau_0) = G^{th}\tilde{P}\tau_0 + E_{0SS} \tag{5.8.1}$$

$$E_{P,tr}^{th}(\tau_0) = (\tilde{P}/8\Gamma)[G^{th} + \ln(4\pi) + \ln(\Gamma\tau_0) + 2\Gamma\tau_0]^2 \tag{5.8.2}$$

for steady-state and transient energy threshold respectively. Here $\tilde{P} = A/g_{ss}L$ and has the unit of power. E_{0SS} is an offset given by $(G^{th})^2\tilde{P}\Gamma^{-1}$. When fibre loss is taken into account, L is written as $L = \int_0^{L_0} e^{-\alpha z}dz = (1-\exp(-\alpha L_0))/\alpha$ where L_0 is the actual fibre length, α is the intensity attenuation coefficient (in m^{-1}). The threshold gain also needs to be modified to $G^{th'} = G^{th} + \alpha z$.

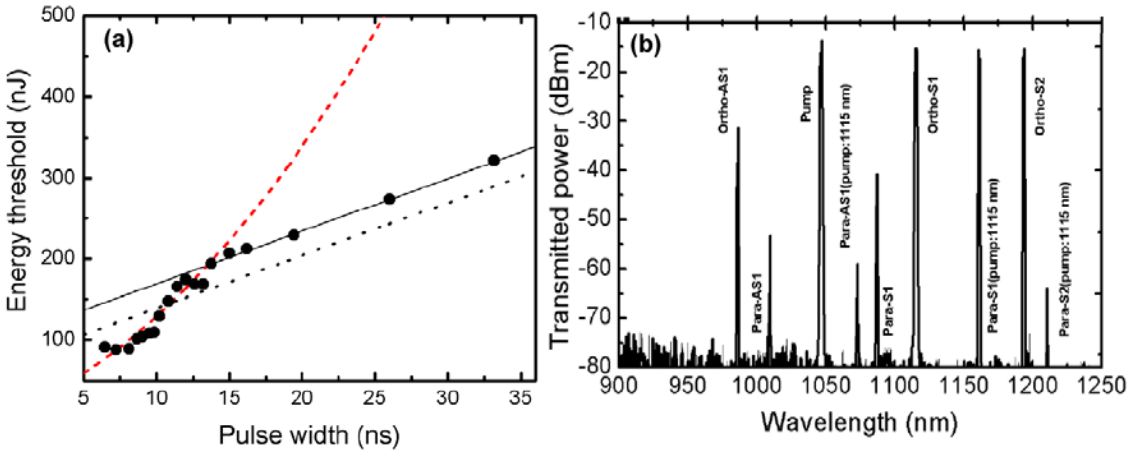

Fig. 5.3 (a) Energy threshold of the pump for the generation of the S1 line as a function of the pump pulse width [41]. The solid circles represent the experimental data. The red dashed and black dotted lines show the theoretical threshold for the transient and the steady-state regimes respectively. The black solid line is a linear fit for the data with pulse width greater than 14ns. (b) The SRS spectrum [41] generated by 11m of HC-PCF filled with H_2 at 10bar and pumped with 13ns pulses and less than 4μm pump energy.

The control of Raman regimes via pump pulse width was evaluated experimentally by coupling a Q-switched Nd:YVO_4 laser at 1047 nm with a pulse width varying from 6 to 45 ns, a linewidth of 260 GHz and energy of 100-300 nJ in to an 11m long PBG HC-PCF (A_{eff}=50 μm^2) filled with H_2 at 10 bar [41]. The pump peak power threshold was measured at the power meter when the S1 (1115 nm) was detected, corresponding to a G_{th}~20. The energy threshold was then deduced from this peak power measurement. The dephasing time was 200 ps taken from [83] and the Raman gain ~1 cm/GW taken from [84]. The experimental data is plotted in fig. 5.3a together with the theoretical threshold deduced from (5.8.1) and (5.8.2). From Eq. (5.8.1), in the steady-state regime, the threshold power is linear with the pulse width τ (fig. 5.3a black dotted line). This agrees well with the experimental data for pulse widths larger than 14 ns (fig. 5.3a solid circles) (by adding an offset in E_{0SS}). In the transient regime, Eq. (5.8.2) shows a quadratic evolution of the energy threshold with the pump pulse width (fig. 5.3a red dashed line), agreeing well with the experimental data for pulse widths shorter than 14 ns (fig. 5.3a solid circles).

The above investigation shows that, in contrast to the normal requirement of GW laser power and sub-picosecond pulse width for transient regime SRS generation, by the virtue of HC-PCF, the transient regime can happen for a pulse width of 14 ns at threshold energy of less than 150 nJ.

5.3 Raman Comb Generation in H_2-filled HC-PCF

After the generation of the S1, four wave mixing (FWM) will induce the 1st anti-Stokes (AS1) line $\omega_{AS}=2\omega_p-\omega_S$. Moreover, if the power is high enough, cascaded Raman will lead to the generation of higher order S/AS. As the spacing between the lines is fixed to that of the Raman conversion frequency Ω_R ($S_{00}(1)$), when a number of Raman lines are generated, they form a Raman frequency comb. If operating in the transient regime where the Raman lines can be coherent, this Raman frequency comb could be interesting for pulse shaping and waveform synthesis.

5.3.1 Experimental realization of Raman comb generation

In [41], by operating in the transient regime with 13 ns pulse duration and less than 4 μJ pump energy and using ~11 m PBG HC-PCF filled with 10 bar of H_2, a small rotational comb with 9 lines has been generated (fig. 5.3b), arising from both ortho-hydrogen and para-hydrogen. The generation of a several octave Raman frequency comb was realized in 2007 by Couny *et al* [11]. The comb was generated by a moderate power (400 kW) single Nd-YAG laser emitting 12 ns, nearly transform-limited pulses at 1064 nm with a 50 Hz repetition rate (fig. 5.4a). The HC-PCF used was a 70 cm large-pitch single-cell Kagome fibre with a 30 μm hollow core (fig. 5.4b). The fibre dominantly guides a polarization-degenerate HE_{11}-like mode confined in the core over a broadband range with a typical loss of 1 dB/m (fig. 5.4c). The setup of the comb generation is similar to that in fig. 1.17 except that no splice is applied. A typical output spectrum is shown in fig. 5.5. The spectral comb spans from below 400 nm in the UV to above 1750 nm in the IR with totally 45 emitted lines. The spectral components consist of S/AS lines spaced by ~125 THz for those raised from the vibrational $Q_{01}(1)$ transition and each vibrational line (and the pump line) generated its own rotational components separated by ~18 THz raised from the rotational $S_{00}(1)$.

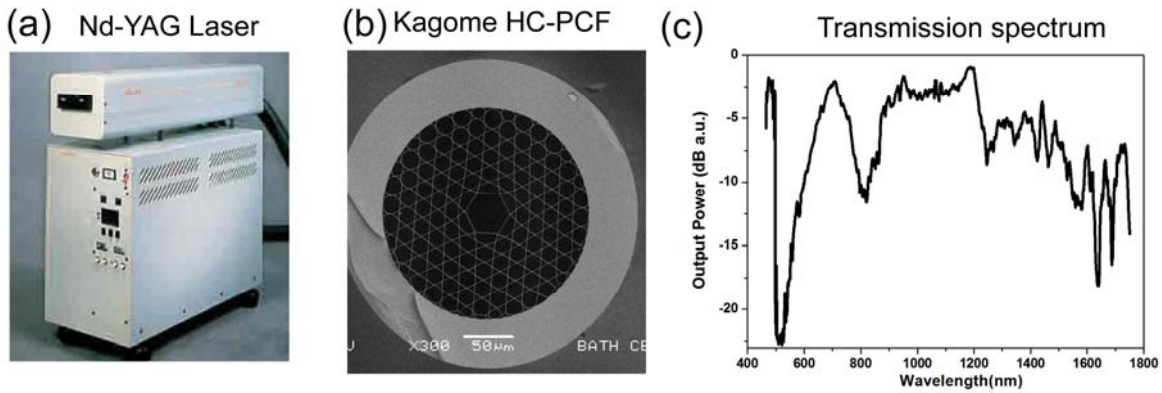

Fig. 5.4 Laser and fibre used for comb generation. (a) Nd-YAG laser; (b) SEM of the Kagome fibre used (c) Optical spectrum showing the broadband guidance of the fibre.

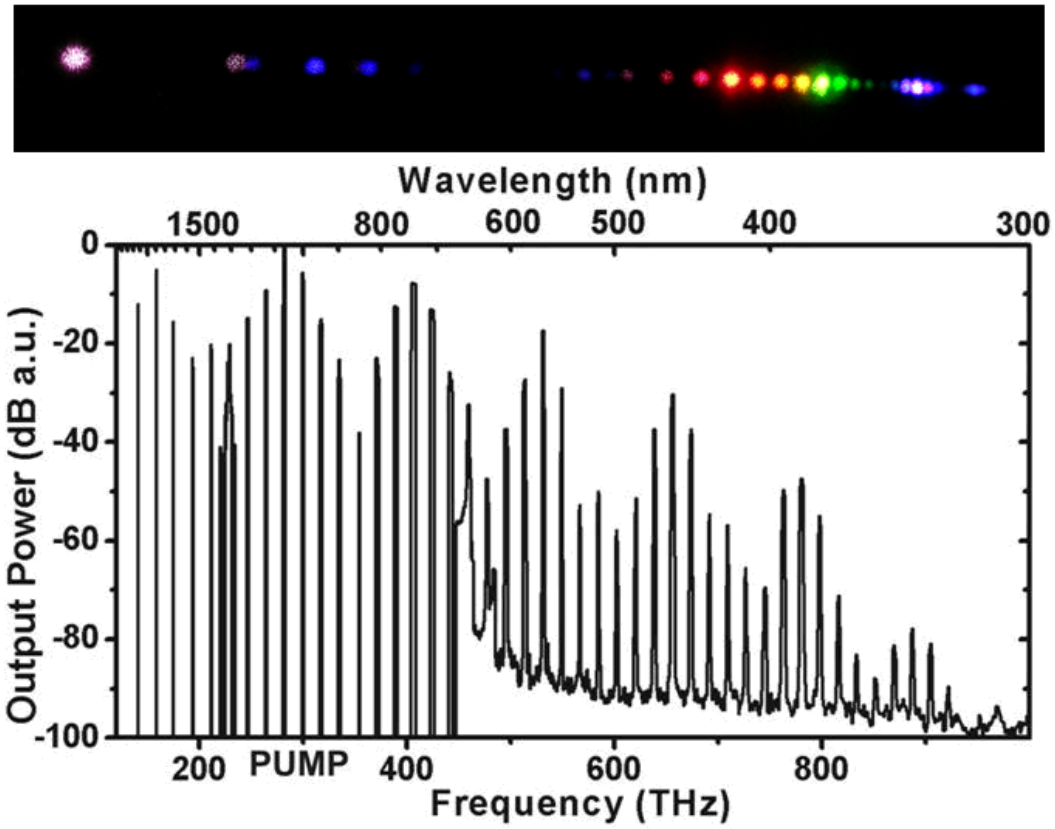

Fig5.5 Output spectrum of Raman comb [11] generated using the laser and the Kagome fibre system shown in fig.5.4 measured by an OSA (bottom) and displayed on a paper (top).

Though a large Raman frequency comb has been generated, the big infrared laser hindered some of its applications when compatibility is required. In chapter 6, we successfully achieve Raman frequency comb generations with a portable microchip laser, so that widens its applications in practical environments.

5.3.2 Predictions of coherence properties

As we stressed, the novelty of this comb generation is its origination from spontaneous Raman scattering or quantum noise. This raises the question of whether each comb component is self-coherent (i.e. its spectral content is that of a transform-limited pulse) and whether it is phase-locked to other components (mutual-coherence). A detailed investigation on the coherence properties of the comb will be given in chapter 7 & 8. However, one could give some qualitative predictions based on prior knowledge.

Self-coherence

It has been theoretically demonstrated that, under the transient and the high gain regime, the amplified 1st Stokes pulse is transform limited [78]. In the typical case of SRS in H_2-filled HC-PCF, the transient and high gain conditions are readily fulfilled. Indeed, even for a pump peak power of 50 KW from a pulse of τ_0=12 ns, the net gain is $gL=g_{ss}I_pL\approx140$ for a fibre length L=70 cm and core size of 30 μm. This gives $\tau_1 = 1/gL\Gamma = 7\times10^{-3}\,\text{ns}$ and $\tau_2 = gL/\Gamma = 140\,\text{ns}$, which in turn fulfills the transiency condition $\tau_1 << \tau_0 << \tau_2$. Furthermore, because of the quasi-single mode guidance of the fibre, we could speculate that the amplified Stokes is a single spatio-temporal mode (see Chapter 7). In conclusion, the first Stokes of the comb is generated in transient regime where coherence within each line is expected to be fulfilled. In turn, and by virtue of the parametric nature of the generation of the higher order Raman lines, it is expected to have all the component being self-coherent. Obviously, this simple calculation is far from enough for coherence demonstrations. A direct experimental observation of the coherence will be presented in chapter 7.

Mutual-coherence

A qualitative analysis of the mutual coherence of the Raman frequency comb has been made under the absence of any dephasing mechanism and based on iterative approximation [11]. This is based on extending the coupled wave equation (5.1.1) and 5.1.2 to higher order S/AS. The frequency of each comb component obeys the following relation owing to the energy conservation: $\omega_n = \omega_0 + n\,\omega_R$, where n denotes the n-th sideband (n > 0 for anti-Stokes, n = 0 for pump and n < 0 for Stokes). The Maxwell-Bloch equations of motion for the electric-field operators $\hat{E}_n$ of each individual comb line and the collective molecular vibration raising operator $\hat{Q}$ is:

$$\partial_z \hat{E}_n^{(-)}(z,\tau) = -i\kappa_{2,n+1}\hat{E}_{n+1}^{(-)}\exp(-i\Delta\beta_{n+1}z)\hat{Q}^{\dagger} - i\kappa_{2,n}^{*}\hat{E}_{n-1}^{(-)}\exp(i\Delta\beta_n z)\hat{Q} \tag{5.11.1}$$

$$\partial_\tau \hat{Q}^{\dagger}(z,t) = i\sum_{n=-N}^{N}\kappa_{1,n}\hat{E}_n^{(+)}\hat{E}_{n-1}^{(-)}\exp(i\Delta\beta_n z) - \Gamma\hat{Q}^{\dagger} + \hat{F} \tag{5.11.2}$$

$\Delta\beta_n \equiv \beta_n - \beta_{n-1}$. Eq. (5.11) is consistent with Eq. (5.1) in which phase mismatch or multi-lines were omitted [78, 85]. The solution to this equation will be given in chapter 8.

Furthermore, we can use classical theory to simplify the coupled wave equation (5.11) and draw an insight on how the comb is generated. Here, we treat the spontaneous field generations as classical random processes and defining the electric field and the molecular coherence with the real amplitude and phase:

$$E_n = \left|E_n\right| e^{-i\varphi_n}; Q = \left|Q\right| e^{-i\varphi_{QF}} \tag{5.12}$$

where φ_{QF} is a random additional phase of the collective, coherent state of the molecular excitations, determined by amplification of quantum fluctuations [86], which is nearly constant throughout a single pulse, $\varphi_{QF}(z) \approx \varphi_{QF}$ in transient regime. The evolution of the molecular coherence can be written as:

$$i\left|Q\right|\partial_\tau \varphi_{QF} + \partial_\tau \left|Q\right| = \sum_{n=-N}^{N} \left|\kappa_{1,n}\right|\left|E_n\right|\left|E_{n-1}^*\right| e^{i\left(\varphi_n - \varphi_{n-1} - \varphi_{QF} - \delta'\right)} \tag{5.12}$$

where $i\kappa_{1,n} = \left|\kappa_{1,n}\right| exp(-i\delta')$. Splitting the above equation to its real and imaginary parts gives rise to:

$$\begin{aligned} \partial_\tau \left|Q\right| &= \sum_{n=-N}^{N} \left|\kappa_{1,n}\right|\left|E_n\right|\left|E_{n-1}^*\right| \cos\left(\varphi_n - \varphi_{n-1} - \varphi_{QF} - \delta'\right) \\ \partial_\tau \varphi_{QF} &= \frac{1}{\left|Q\right|} \sum_{n=-N}^{N} \left|\kappa_{1,n}\right|\left|E_n\right|\left|E_{n-1}^*\right| \sin\left(\varphi_n - \varphi_{n-1} - \varphi_{QF} - \delta'\right) \end{aligned} \tag{5.13}$$

The first one implies that the molecular polarization grows at a maximal positive rate if $\varphi_n - \varphi_{n-1} - \varphi_{QF} - \delta' = 0$ .In such a situation, the second equation states that the random phase φ_{QF} of the molecular coherence will be time-independent, since the sine function will go to zero. Therefore, once the molecular coherence is built up, the random additional phase φ_{QF} is preferred to be independent to z and τ within each single pulse.

This analytical result is consistent with the concept of high-gain temporal filtering [87]. The idea is that the spontaneously generated comb lines arise from any initial phase, but the value that appears in the output will be that corresponding to the highest overall gain, as indicated by the highest growth rate of $|Q|$. Moreover, this high-gain temporal filtering mechanism also leads to time-independent phase-locking among different frequency combs with particular relations between them. This relation can be written as

$$\varphi_n - \varphi_{n-1} = \varphi_{QF} \tag{5.14}$$

where $\varphi_{QF} \equiv \varphi_{QF} + \delta'$ absorbs the constant δ' into the random phase initiation φ_{QF}. The random variable φ_{QF} has a uniform distribution between 0 and 2π. Including a deterministic phase offset (eg. pump phase) δ, we can self-consistently solve for the phases of all comb lines from Eq. (5.14):

$$\varphi_n = n\varphi_{QF} + \delta \tag{5.15}$$

This simple relation is a useful guide in understanding the global behavior of the Raman comb system.

Combining the ideal relation (5.15) with the frequency relations $\omega_n = \omega_0 + n\omega_R$, we find that the generated comb spontaneously satisfies the required relations for Fourier synthesis to create a periodic waveform. In order to see that, we express the synthesized waveform as:

$$E^*(t) = \sum_n \left| E_n^*(t) \right| e^{i[(\omega_0 + n\omega_R)t + n\varphi_{QF} + \delta]} = e^{i\omega_0 t + i\delta} \sum_n \left| E_n^*(t) \right| e^{in(\omega_R t + \varphi_{QF})} \tag{5.16}$$

The intensity will be determined by the summation term, which is invariant with period $T = 2\pi / \omega_R$ under the assumption that E_n is a slowly changing envelope compared to that period.

However, the carrier-envelope phase (CEP) of the synthesized waveform is changing, as we can see from Eq. (5.16), in which the term $e^{i\omega_0 t}$ is generally not

invariant over period T. If the pump is tuned and stabilized to a multiple of the molecular resonance frequency, i.e., $\omega_0 = m\,\omega_R$ (m is an integer), then one set (train) of periodic pulses with constant CEP will be created within one pump pulse. On the other hand, because the quantum phase φ_{QF} changes from shot to shot, the pulse trains within successive laser shots will not have the same waveform and will not be comprised of isolated short pulses. Further locking mechanisms, such as coherent injection of molecular coherence, have been used to overcome this limitation, and stable ultrashort pulse trains were created, with the cost of added experimental complexity [88].

The calculation in the transient regime and the qualitative prediction of phase correlation are obviously far from enough for coherence demonstration. Especially when early work on the statistical properties of SRS showed that if a spontaneously emitted Stokes field is excited by a quasi-monochromatic single driving laser pulse, a Stokes pulse is produced carrying with it signatures of its underlying quantum initiation, even though the Stokes pulse may contain macroscopic amounts of energy (e.g., 10^{16} photons) [80, 89]. Since our comb is triggered by spontaneous Raman scattering as well, the question of whether the generation of a coherent ultra-broad optical comb could be possible with such a random triggering process remains. Answering this question is of importance to attoscience, as it could provide novel coherent attosecond pulses with non-classical features [66, 90, 91], and to quantum optics by providing a possible solution to one of the most challenging tasks in quantum information; namely the generation of multipartite entangled optical states [92, 93]. In chapter 7 and chapter 8, the self- and mutual- coherence properties will be investigated.

Chapter 6

Compact Multiline Raman Lasers

*In this chapter, we report on one of the applications of Raman frequency comb generation in HC-PCF. These are compact multiline Raman lasers based on Kagome and PBG HC-PCF. The high Raman efficiency achieved through these fibres allows these compact, portable Raman laser systems to be used as pumps, making it an ideal candidate for forensics and biomedical applications.**

* This work has been published in

1. Y. Y. Wang, F. Couny, P.S. Light, B.J. Mangan and F. Benabid. "Compact and portable multiline UV and visible Raman lasers in hydrogen-filled HC-PCF". Opt. Lett. 35 1127-1129 (2010).

2. Fetah Benabid, Francois Couny and Yingying Wang. "NOVEL LASERS: Photonic microcell unleashes the full potential of gas lasers"Laser Focus World. 46 May (2010).

6.1 Introduction

High-specification visible and UV laser sources have become increasingly important in biological and environmental applications such as forensic science, bio-imaging, DNA sequencing and atmospheric monitoring. In these areas of expertise, a compact multi-lines laser system that would offer a large spectral coverage with a spectral purity similar to a single line laser would be of great interest. Additionally, because these sources are intended for non laser-specialised end-users, the simplicity of the laser design is also a prime concern. The current laser systems available for detection of for example the dyes in the family of Alexa Fluor (fig. 6.1) rely either on bulky, free-space apparatus delivering a single laser line, sometimes with no spectral tunability, or on a supercontinuum source, generated by a smaller and more portable pump laser, but limited to low spectral power-density and poor spectral resolution. Furthermore, these sources have an intrinsically restricted bandwidth that does not extend in the UV spectral range limited by the high dispersion and attenuation of solid core silica fibres and damaging effects such as photodarkening. For example, even with highly UV-tailored fibre, the shortest wavelength available is ~320 nm [94]. The advent of gas-filled HC-PCF technology and the development of the PMC hold the potential to lift these restrictions with the possibility of generating wavelengths further into the UV and create a new breed of photonic materials.

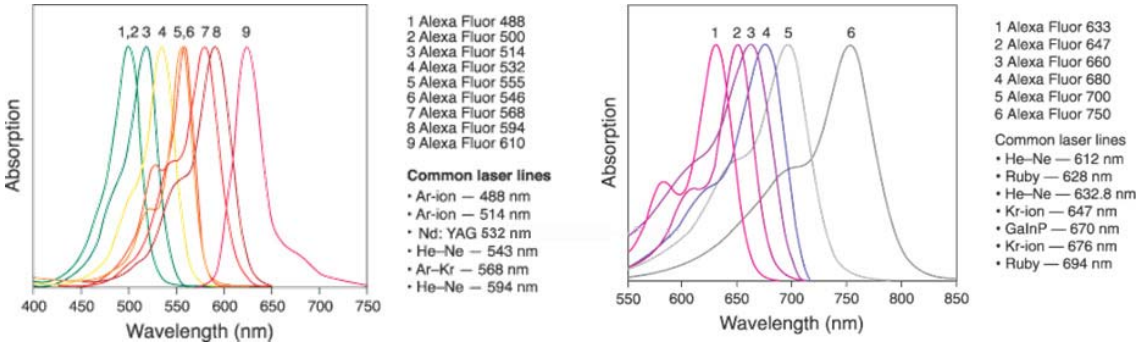

Fig. 6.1 Absorption spectrum of Alexa Fluor dyes [95]. Different dyes need different lasers for detection.

Both Kagome and bandgap HC-PCF have been demonstrated to be excellent hosts for Raman amplification when the fibre is filled with a Raman active gas [96]. As

mentioned in the previous chapter, through the use of large-pitch Kagome-lattice HC-PCF filled with H_2, an optical frequency comb spanning several octaves from UV to mid IR for almost 1000 THz has been demonstrated [11]. The novelty of the method consisted in the generation of the optical comb using a 1064 nm Nd-YAG laser with 12 ns pulse duration, 400 mW average power and 40 kW peak power, as opposed the GW power, transform-limited subpicosecond pulsed laser usually required [73] for coherent higher-order SRS (HSRS) generation. Thanks to the high laser intensity I_p achieved via the small effective area of the fibre core, its long interaction length z and the strong optical confinement of HC-PCF, the Raman amplification satisfies the transient regime condition $\Gamma \tau_p < g_0 I_p z$ for pump pulse duration τ_0 much longer than the dephasing time $T_2 = 1/\Gamma$ [41]. Although the resulting 45 spectral lines covered a spectral range spanning from the UV to the IR, the conversion efficiency to the visible and UV regions of the spectrum was low. Additionally, the system included a cumbersome laser and gas control chambers attached to the HC-PCF, therefore limiting its usefulness when portability is a requirement.

In this chapter, we present several Raman lasers with compact design and spectral lines concentrating in the UV, visible and near IR. The first one, with Kagome fibre and pumped at 532 nm, offers a broad spectral coverage from near-IR through to the much sought after yellow, deep blue and UV. The second one, based on PBG fibre and also pumped at 532 nm, presents a pump conversion concentrated in the visible region. The third one, with a hypocycloid core Kagome fibre and a pump laser at 1064nm, offers laser line options in the near infrared. And finally, we show that the Raman medium can also be replaced with ethylene gas or liquid ethanol for various purposes.

6.2 A multiline UV & Vis laser based on Kagome HC-PCF

To break the limitations on the existing large system of Raman frequency comb generation, a new multiline laser system is developed by changing the bulky 1064 nm laser (fig. 6.2a) with a head size already occupying 150x180x800 mm to a microchip laser (fig. 6.2b) centred at 532 nm with a laser head 30x40x120 mm. Besides, the laser can be battery powered in a similar manner to a laptop and is much cheaper in price. The compact 532 nm (Q-switched doubled Nd:YAG) diode pumped solid-state

microchip laser with repetition rate of 7 kHz provides pump pulses with 550 ps duration at an average output power of 25 mW and a peak power of 6 kW compared to the 40 kW and 12 ns bulky 1064 nm laser.

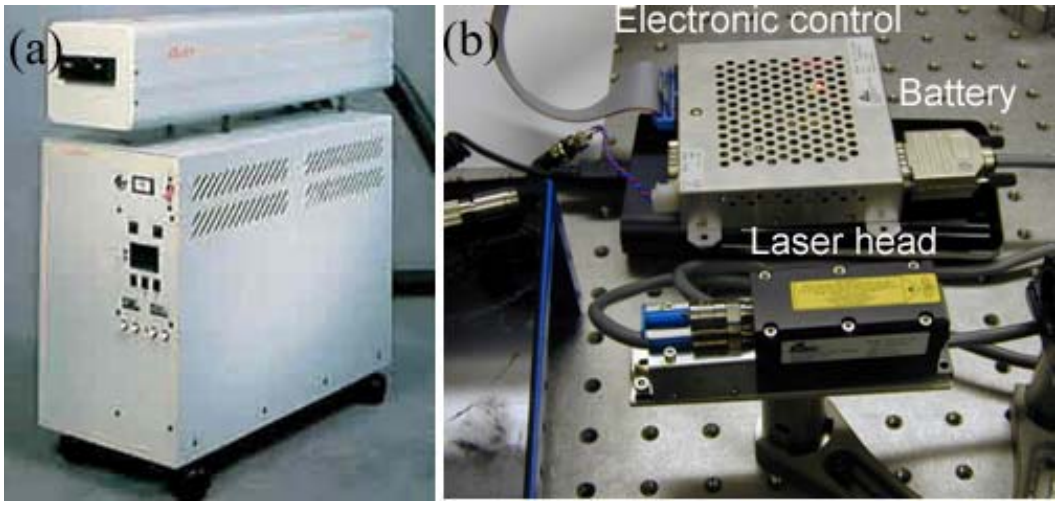

Fig. 6.2 Comparison of the size of the lasers. (a) is the 1064 nm Nd-YAG laser with a head dimension of 150x180x800 mm (b) is the microchip laser with a head of 30x40x120 mm and is battery powered.

As a consequence of the laser change, the fibre was also replaced. Although the fibre in [11] guides most of the light in the infrared, it is poor in the visible. A specially designed fibre was fabricated as shown in fig. 6.3a. The fibre had a hollow core of 30 μm surrounded by a photonic crystal cladding consisting of three rings of holes with a pitch of 12 μm. The limited number of rings of the fibre did not introduce more loss while it kept a smaller outer diameter of 130 μm, small enough to be spliced to conventional multimode fibre. The large pitch of the fibre gave a broadband guidance (fig. 6.3b) from the UV to the far infrared with a loss figure of ~1.5 dB/m in the visible and UV region. Furthermore, the higher loss region is set to be from 660 nm to 900 nm. This high loss region coincides with the wavelength of the vibrational S1 for H_2 and hence diminishes the vibrational SRS generation (125 THz Raman shift) and enhances the rotational Raman emission (~18 THz Raman shift) in the low-loss optical range of the fibre.

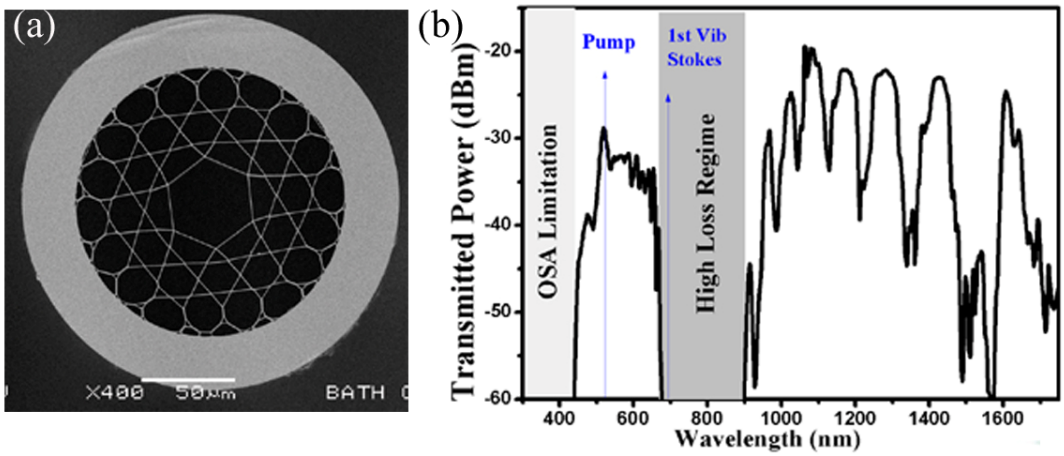

Fig. 6.3 (a) SEM and (b) transmission spectrum of the fibre measured by a supercontinum source and an OSA.

Figure 6.4 shows a picture of the experimental setup. The input end of the 2 m Kagome fibre is sealed in a compact gas chamber with 20 bar H_2 while the output end is spliced to a multimode fibre. The power coupled into the fibre is approximately 15 mW (peak power 3.6 kW). The input coupling into the HC-PCF is carried out using free-space coupling instead of the use of splicing technique [47]. This is motivated by the high mismatch in numerical aperture between this Kagome HC-PCF and the SMF fibre, whose subsequent high splice loss renders the PMC form less attractive than free-space coupling. However, these can be overcome by down-tapering the Kagome fibre in the future work [37]. At that pressure and wavelength, the rotational Raman linewidth of ortho-H_2 $S_{00}(1)$ is Γ~1GHz and the Raman gain coefficient g_{ss} is 1.5 cm/GW. The calculated Raman net steady state gain is $g_{ss}I_pz$ ~300, well within the transient regime condition $\Gamma\tau << g_{ss}I_pz$ for the coherent Raman generation. This means that the generated Raman lines are transform limited pulses with a gain-narrowed linewidth of less than 100 MHz [41, 42, 80].

The output spectrum for these systems is recorded by an OSA and also by imaging the output beam on a screen by dispersing it with a grating. Figure 6.5 summarize the results of these measurements for the Kagome-based system. The spectrum spans over 450 THz and contains 23 lines extending down to the hitherto poorly covered UV-visible range. In addition to 9 rotational Raman sidebands of the initial pump from the $S_{00}(1)$ of ortho-H_2, the spectrum counts one vibrational Stokes component and two vibrational anti-Stokes component from the $Q_{01}(1)$ transition of H_2 (125 THz); each

giving rise to a number of rotational sidebands, resulting in a comb-like spectrum extending from 712 nm in the near infra-red, to 353 nm in the UV. All the measured Raman components appear single mode, as shown for example in fig. 6.6 for the yellow line at 567 nm where both far field and near field exhibit a Gaussian profile.

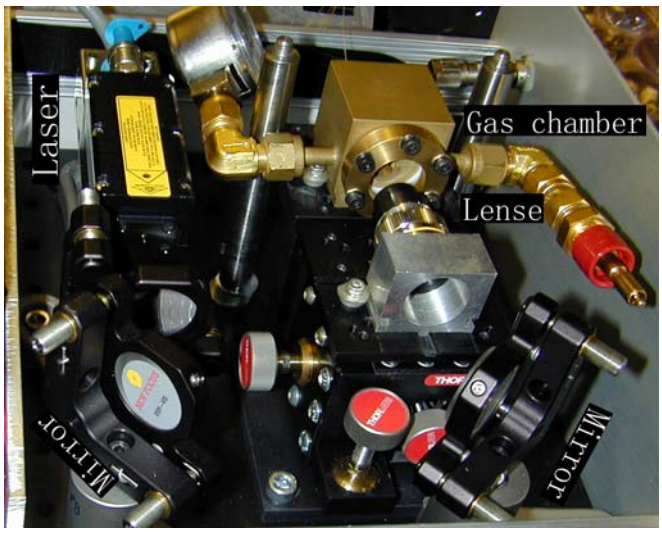

Fig. 6.4 A picture of the setup for multiline laser generation. The microchip laser goes through two mirrors, a lens and enters the fibre that is mounted in the gas chamber with 20bar H_2. The other end of the fibre is spliced with a multimode fibre.

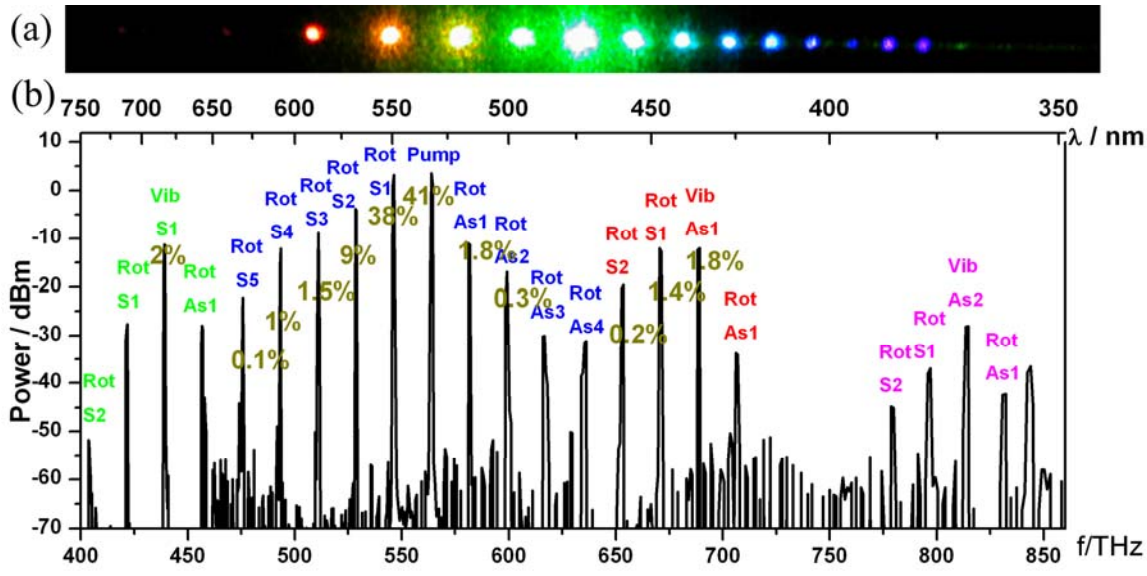

Fig. 6.5 Dispersed output spectrum for the Kagome fibre (a) displayed on a piece of paper, (b) measured with an OSA. The pump generates 9 rotational Stokes (labeled in blue) and three vibrational Stokes. Each of the vibrational Stokes generates its own rotational Stokes series (labeled in green, red and pink respectively). Numbers in dark yellow indicates the percentage of power for each line.

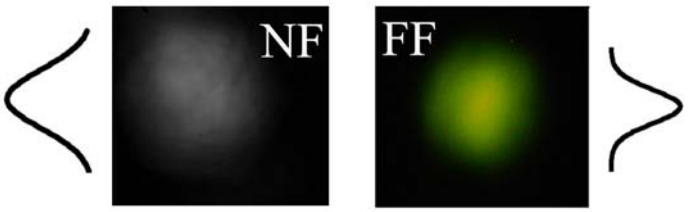

Fig. 6.6 Mode properties of the laser line at 567nm. Both the near field and the far field shows a single mode profile.

The efficiency of the process is illustrated by the fraction of the output power contained in each line, whereby 60% of the optical power is converted from the pump line to the rest of the spectral components. It is noteworthy that above threshold, the total power throughput drops significantly (~1 mW). We believe this is caused by the generation of Raman lines lying in the high loss region of the transmission spectrum of the fibre, yet another indication of the highly efficient conversion process that occur inside the fibre. Optimizing the transmission of the fibre and using higher power pump lasers would overcome this limitation. Nonetheless, based on the estimated upper limit of the linewidth of the different spectral lines of 100 MHz, the average spectral power density ranges from 130 mW/nm (or 0.2 mW/GHz with Vibrational S1) for the visible components to 7 mW/nm (or 3 μW/GHz with Vibrational AS2) for the UV components. In order to compare these figures with those of supercontinum sources, it is noteworthy that the largest reported average spectral power density is ~3 mW/nm for the spectral region around ~1 μm and with pump power of 5 W [97] or 2 mW/nm with pump power of 3.6 W in the blue region [98]. For the visible/UV range and a comparable pumping power level, this figure is only ~ 20 μW/nm [94] which is several orders of magnitude less than the present results. In addition to this high power spectral density, and as important, the spectrum exhibits spectral components with wavelengths not obtainable with other laser sources and that are highly sought after for applications such as the biomedical field. To illustrate this, fig. 6.7 shows the Kagome-based Raman gas laser spectrum superimposed with absorption peaks of 17 representative dyes from the family of Alexa Fluor [95], widely used as biological markers for the detection of the fluorescent dyes in DNA sequencing for example. One can see the overlap or near overlap of these absorption bands (note that the actual absorption lines are fairly wide, see fig.6.1, allowing “nearly overlap” to work) with

the laser lines generated through the Kagome-based system. For example, the absorption peak for Alexa Fluor 594, which lies at 590 nm is very close to the rotational S3 lines (588 nm), making the latter a very good candidate for efficient fluorescence with this marker. Besides, in the future, with a tunable pump laser or an alternative Raman gas and by tailoring the hollow core fibre optical transmission properties accurately, it is possible for the laser source demonstrated above to cover a much larger range of frequencies.

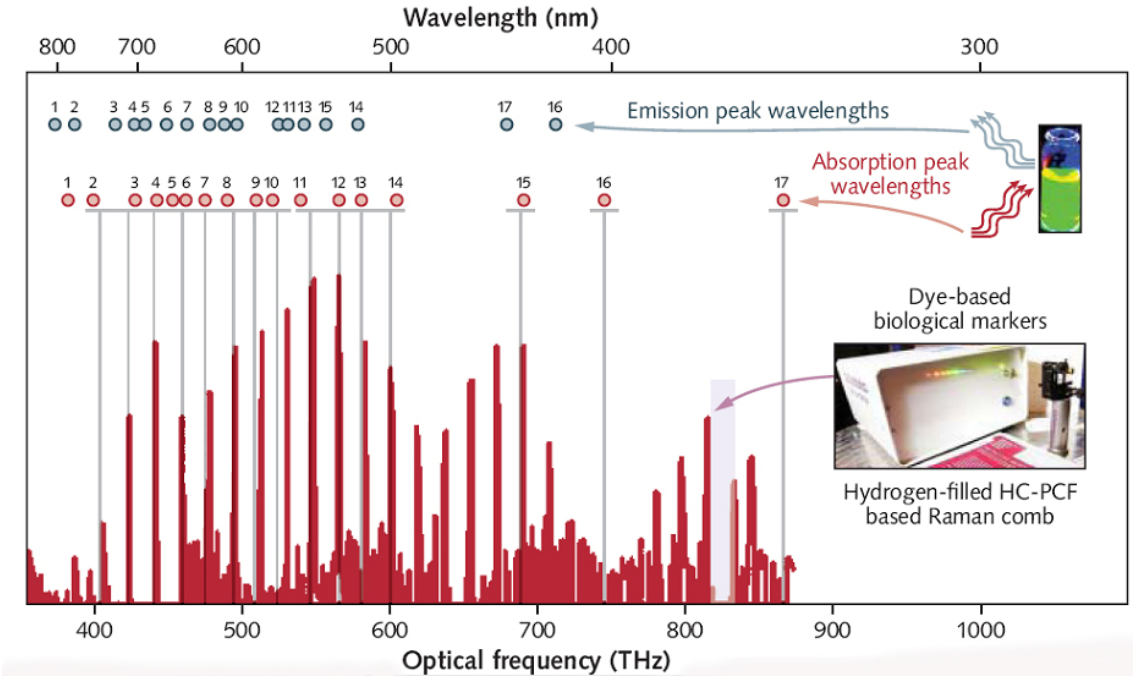

Fig. 6.7 Match of the single laser source with the absorption wavelengths of the Alexa Fluor family [95] of dye biological markers.

6.3 A multiline UV &Vis laser based on PBG HC-PCF

Although the Kagome fibre exhibits a broader transmission bandwidth than PBG fibre, allowing more lines to be generated, there are limitations on the power conversion efficiency because of the bigger core size and larger attenuation, hence smaller gain. By changing the Kagome fibre to PBG fibre, another multiline laser system with better performance at some of the lines has been developed.

Figure 6.8 shows a comparison of the PBG fibre with the Kagome fibre. The PBG fibre has a core of 5.4 μm surrounded by eight effective rings with a pitch of 1.4 μm

and an outer diameter of 81.3 μm (fig. 6.8c). This core size matches that of commercially available SMF for the visible (4 μm) therefore reduces the splice loss. The black curve in fig. 6.8a shows a flat bandgap optical guidance from 500 nm to 650 nm (~140 THz) with a measured loss ~1.1 dB/m. While this reduced bandwidth restricts the number of generated Stokes lines, it offers a higher power density than with Kagome fibre. Furthermore, because of the six-fold reduction in core diameter compared to that of Kagome fibre, the Raman net gain is ten times larger (i.e. $g_0 I_p z$ ~3000) for an input coupled average power of 10 mW. This fulfills thus the coherent Raman generation condition and the expected linewidth of the emitted lines is of the order of a few tens of MHz. Finally, figure 6.9 shows the experimental setup for the Raman fibre gas laser and illustrates the compactness and portability of the system which consists mainly of a 2-m PMC coupled to a battery powered pump laser.

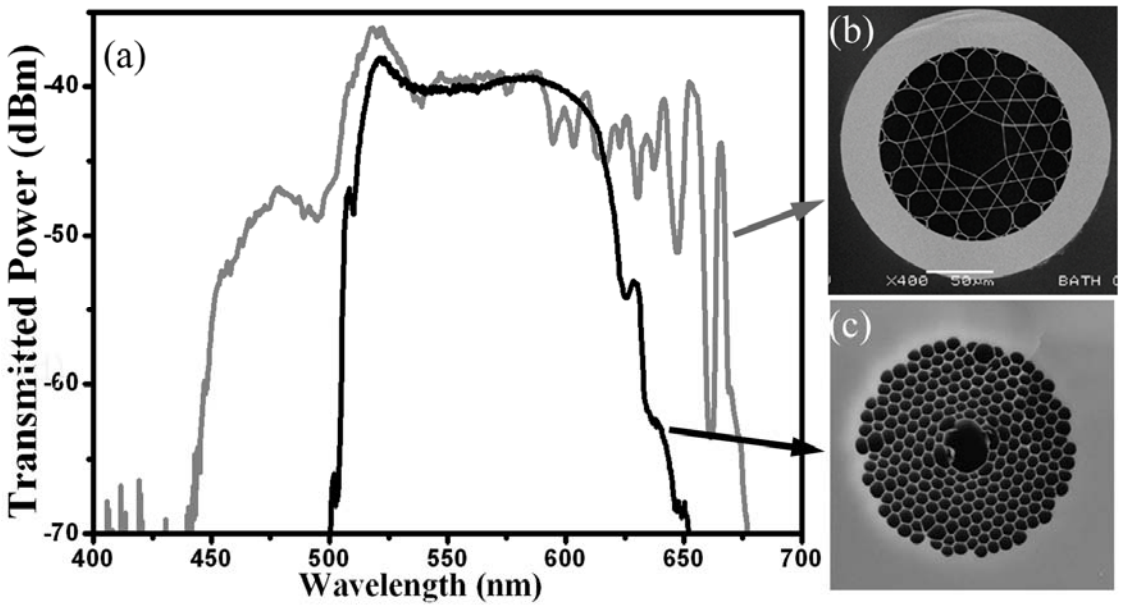

Fig. 6.8 Comparison of the PBG fibre with that of the Kagome fibre in (a) optical transmission spectrum, the black curve is the spectrum for PBG fibre and the grey curve is that for Kagome fibre; (b) SEM image, the top is the Kagome fibre and the bottom is the PBG fibre.

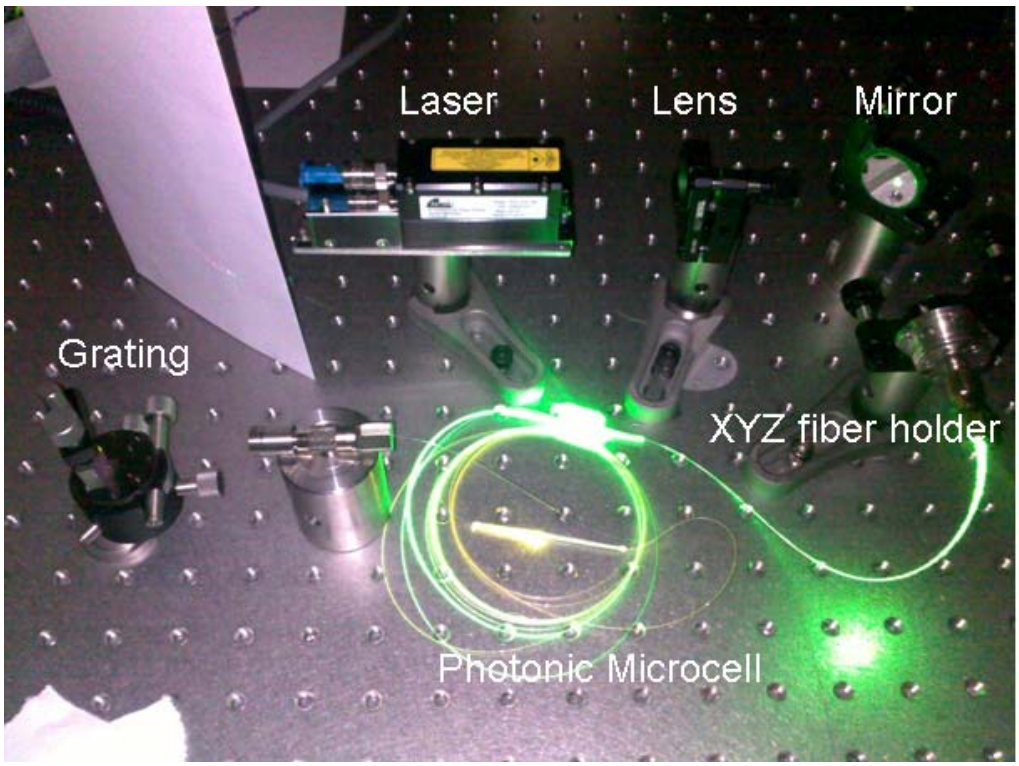

Fig. 6.9 Photograph of the setup for the PBG fibre system where a PMC is applied.

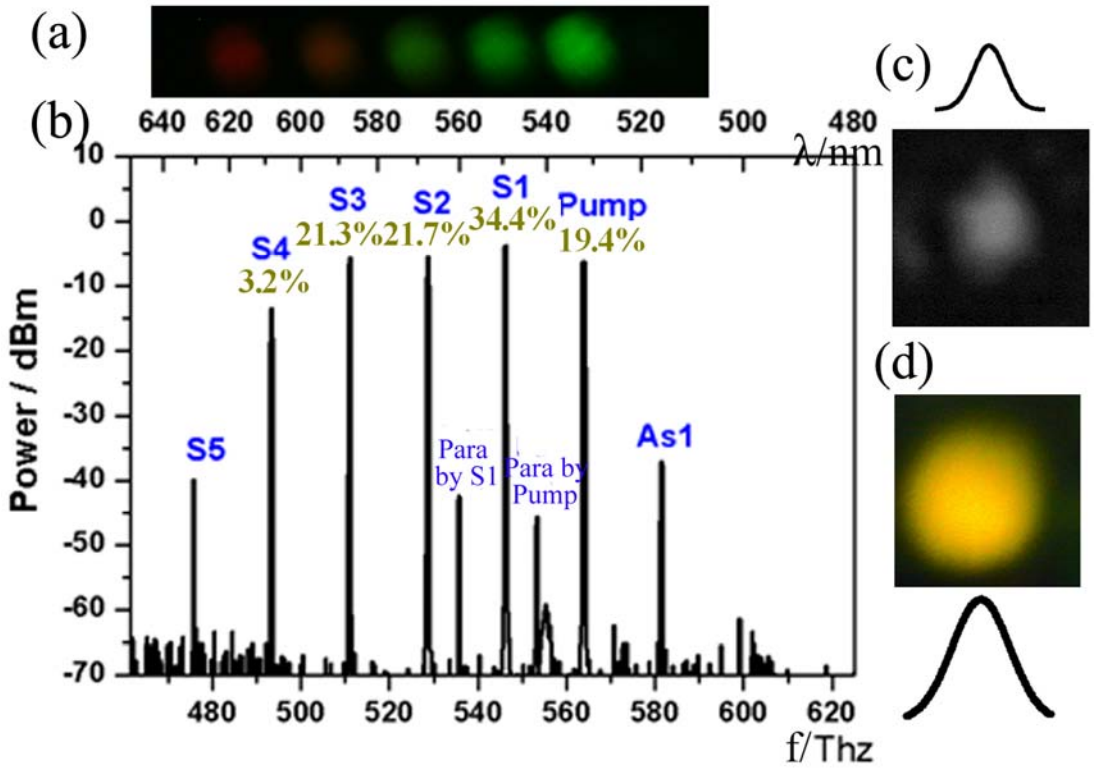

Fig. 6.10 Dispersed output spectrum for the PBG fibre (a) displayed on a piece of paper, (b) measured with an OSA. (c) and (d) shows the near and far field pattern for the line at 567 nm.

Figure 6.10a&b shows output for the PBG fibre-based PMC. Similarly to the Kagome-fibre, all the spectral components generated in PBG-fibre exhibit a single-modal behavior (fig. 6.10c&d). Furthermore, and as expected from its narrower bandwidth, the Raman spectrum generated from the PBG fibre-based PMC has a smaller number of high-order Raman components. Nonetheless, the conversion efficiency into these lines reaches 80% and is equally distributed between the pump and the three first Stokes orders. Two additional sidebands are also observed on either side of the S1 and can be identified as the rotational Stokes lines of the para-H_2 that make up 25% of normal H_2 at room temperature. Considering a linewidth of <50 MHz for the Stokes lines [41, 42, 80], the S1-S4 lines all have spectral density in excess of 400 mW/nm and even the para-H_2 lines can have a spectral density of 1 mW/nm.

It is noteworthy that the Raman lines have in some ways similar coherence properties as a laser (limit to single shot). Figure 6.11 shows the interference patterns of different Raman lines created by beating the same spectral component from each of two separate multiline systems of in a Mach-Zehnder interferometer. Much more detailed discussions about the coherence will be demonstrated in chapter 7 and chapter 8.

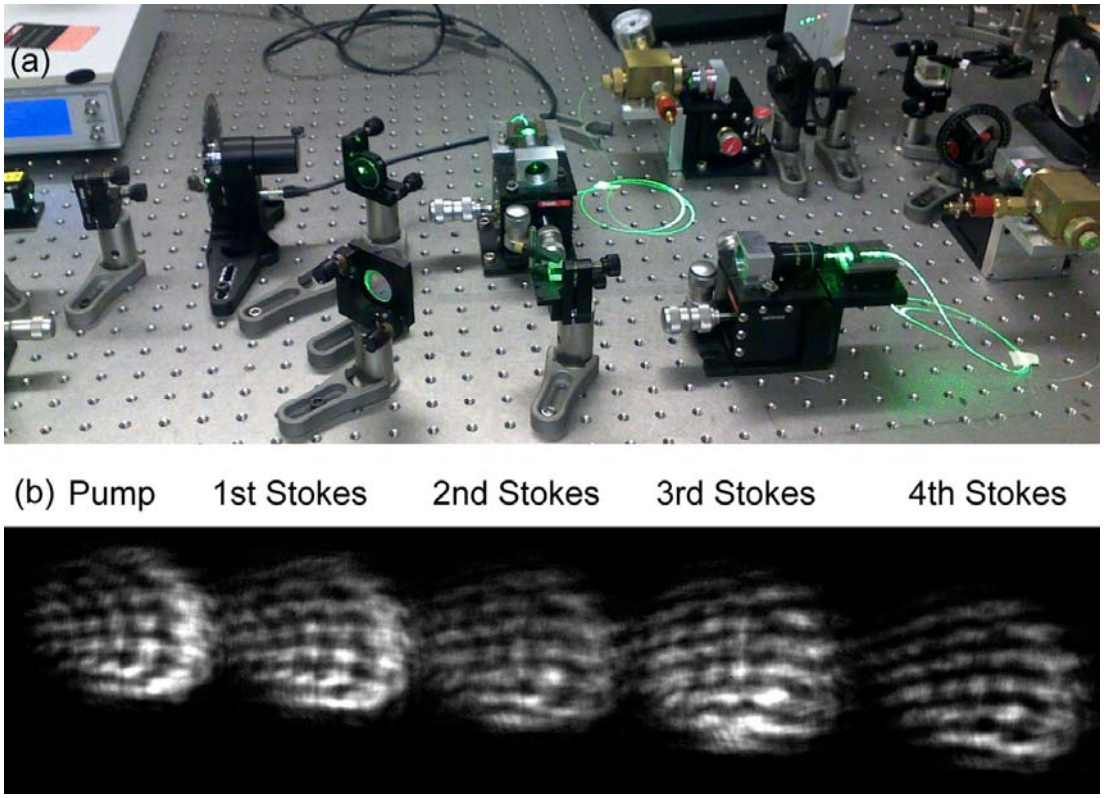

Fig. 6.11 (a) Mach-Zehnder interferometer with two PBG fibre based multiline lasers in the two arms. (b) Interference patterns created by the Raman lines from the two lasers.

6.4 A multiline infrared laser based on hypocycloid-core Kagome HC-PCF

To extend the series of compact multiline Raman lasers to the near IR region, we replace the 532 nm microchip pump laser source with a similar Q-switched Nd:YAG microchip laser but operating at 1064nm with average output power of 50 mW, repetition rate of 9 kHz and pulse duration 700 ps. Compared to the previous g_{ss}=1.5 cm/GW at 532 nm, the steady-state Raman gain coefficient is 4 times smaller at 1064 nm; g_{ss}=0.32 [99]. This means that the Raman energy threshold is much higher. However, thanks to the newly-developed hypocycloid-core 7 cell Kagome fibre whose transmission loss figures are comparable to the PBG fibre and 20 times less than the conventional high loss one-cell Kagome fibre, an infrared Raman comb can be generated with the microchip laser. Figure 6.12a shows the 7 cell Kagome fibre with a core size of ~36 μm used for this experiment. It exhibits a main optical transmission window from ~800 nm to ~1700 nm with an attenuation of ~100 dB/km and a

narrower high order transmission band from ~530 nm to ~580 nm with higher loss of 1 dB/m (fig. 6.12b).

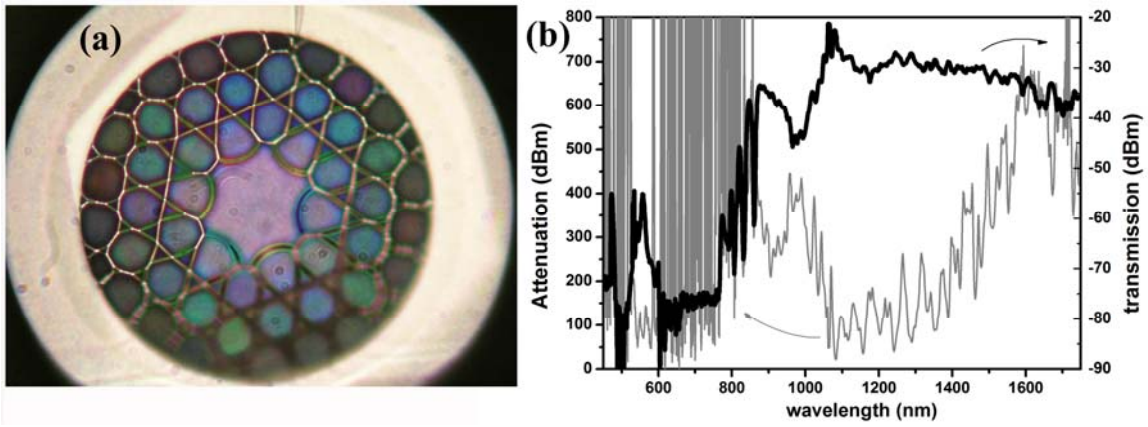

Fig. 6.12 (a) optical micrograph of the hypocycloid-core 7 cell Kagome fibre with a 36 μm core size; (b) optical transmission of 5 m fibre (black) and attenuation measured by a supercontinuum source by a cut back from 78m to 5m. The loss of the fibre at 532nm is confirmed to be 1 dB/m by using a 532 nm microchip laser.

The low loss of the fibre allows a longer fibre to be used. The results are shown in fig. 6.13 in a similar experimental configuration to the previous 532 nm Kagome system (fig. 6.4). When 2 m of fibre is used (fig. 6.13a), ~ 13 lines are generated. This includes 5 rotational components from the pump (labeled in blue), vibrational AS1 and its 4 more rotational Stokes (labeled in red) and 2nd vibrational anti-Stokes (labeled in pink). Besides, the pump laser has some residual at 532 nm, which generates 2 more rotational lines (labeled in green). With the increase of the fibre length to 5 m (fig. 6.13b), Stokes components at longer wavelengths are enhanced while lines around the high loss region (mainly vibrational AS1 and its sidebands) are largely reduced in intensity. When the fibre length reaches 13 m (fig. 6.13c), 10 Raman components remain, overlapping accordingly with the low attenuation window in the infrared and visible. Although fewer lines are generated, the intensity of the 5 Stokes lines from 1136 nm to 1553 nm is comparable to that of the pump indicating the high conversion efficiency in this case. Hence, different fibre lengths can be used for different application requirements. The low attenuation of the fibre also benefits the total output power of the system. The output/input power ratio (12 mW/ 50 mW) in the 1064 nm laser system is much higher than the previous 532 nm laser system (1 mW/ 15 mW).

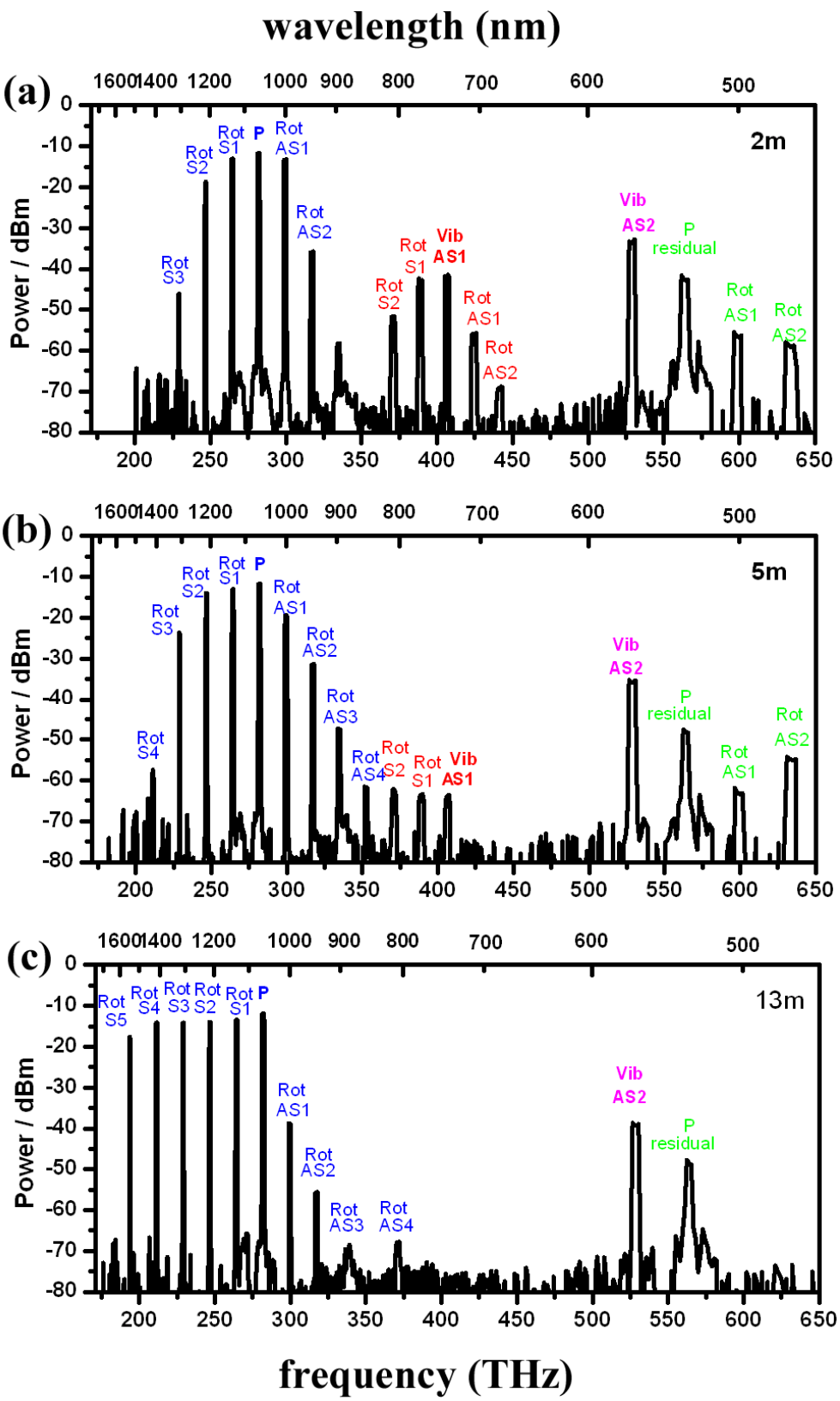

Fig. 6.13 Output spectrum of the infrared multiline system measured by an OSA with different fibre length (a) 2 m; (b) 5 m and (c) 13 m. The gas pressure is fixed at 20 bar.

6.5 Lasers with other Raman active material than H_2

The above lasers, all based on hydrogen, display lines with frequency differences of 18 THz. However, if spectral lines other than these are required, or the spectral power density is not high enough, an alternative Raman medium may be favoured. These Raman media, with larger Raman shift frequencies, generate fewer lines within the transmission bandwidth of the fibre but at higher spectral power density. Below, we explore two media. Firstly a gas phase ethylene and the second is a liquid ethanol.

Ethylene gas

Ethylene (C_2H_4) has chemical bonds of C=C and C-H, both Raman active. C=C has a Raman shift of 40 THz and C-H 90 THz [100]. By filling a PBG fibre with 20 bar of ethylene gas and pumping it using the 532 nm laser (fig. 6.14, gas chamber used at the output) as in the previous configurations, SRS was achieved. The colour of the fibre changed from green at the input to red at the output, indicating very high Raman conversion. The output spectrum was taken by an OSA and shown in fig. 6.15. This illustrates two strong Raman lines at 573 nm and 620 nm, corresponding to the 1st and 2nd order Raman conversion of the C=C bond. Due to the high loss at 630 nm, the C-H bond Raman is not observed nor are any anti-Stokes lines. Similar to the high conversion of H_2 in PBG fibre (80%), 83% of the pump power is converted to the Raman lines with the S1 containing 78%. The very high spectral density (1.5 W/nm) at 573 nm (523 THz) is interesting for some special dyes (e.g. Alexa Fluor 568) in biomedical science. Tailoring the fibre transmission to longer wavelength would allow better guidance at 620 nm (2nd Stokes for C=C) and 630 nm (1st Stokes for C-H). Also tailoring to shorter wavelength can avoid any 2nd Stokes so that the Raman transition at 573 nm is even stronger.

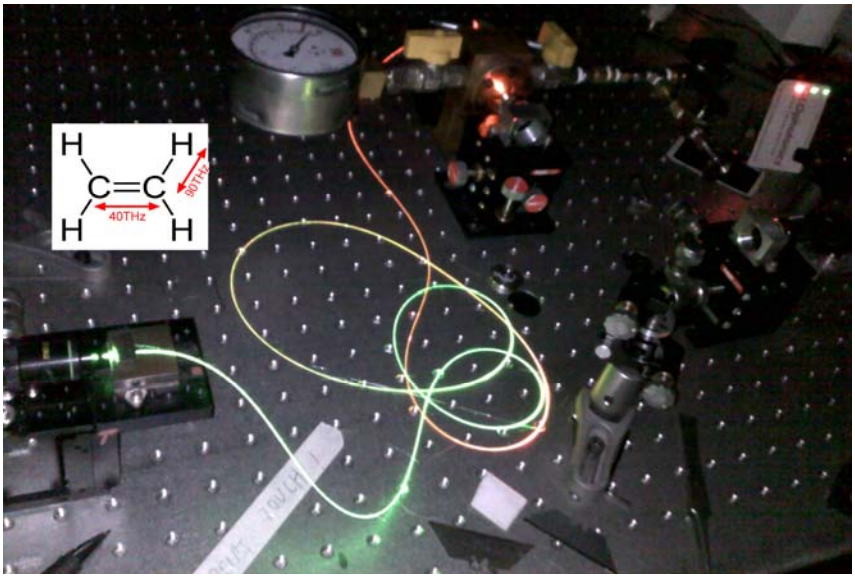

Fig. 6.14 Photograph of the PBG fibre system filled with ethylene by a gas chamber. Inserted shows the chemical bonds of ethylene with Raman shift written.

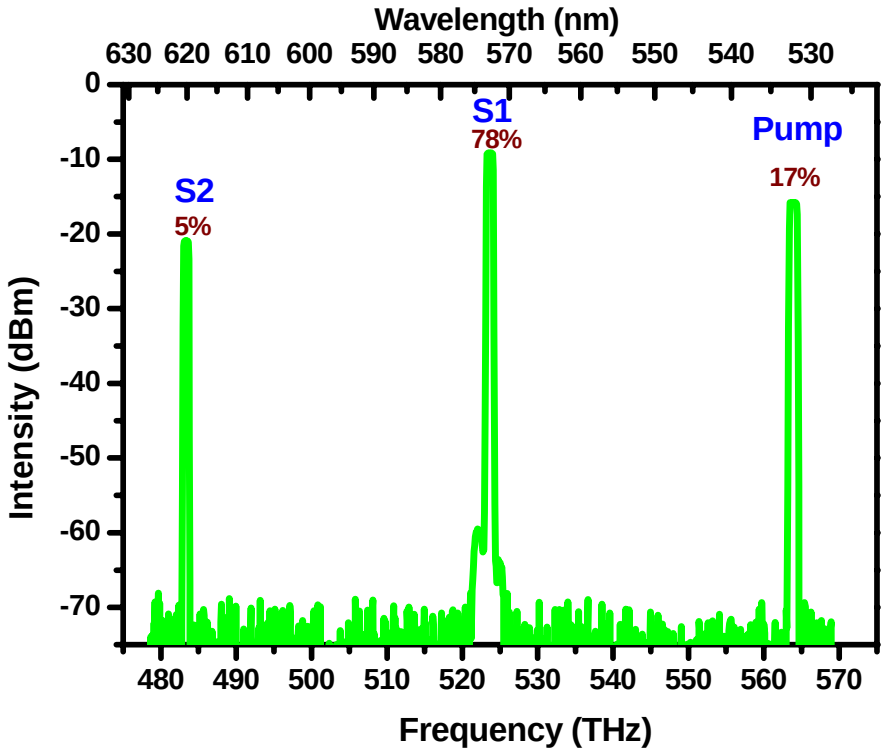

Fig. 6.15 Output optical spectrum for the PBG fibre filled with ethylene gas measured with an OSA.

Liquid ethanol

Not only gas can be used as a Raman medium, liquid (which could have a higher Raman gain than its gas phase) is also interesting. In our experiment ethanol (C_2H_5OH)

is chosen since it is Raman active and straightforward to work with. The Raman spectrum of ethanol inside HC-PCF has already been investigated [101, 102]. Liquid ethanol has a refractive index of 1.36, much higher than gas/air. When the whole structure (both the core and cladding) is loaded with ethanol, the position of the bandgap is blue-shifted [103]. When ethanol is loaded only in the core, the guidance is changed from bandgap guiding to TIR guiding. Here the latter is used, as TIR guiding is less sensitive to cladding defects. Figure 6.16 shows the transmission spectrum before (green curve) and after (red curve) filling with ethanol, where one can see how the guidance changes. Initially, the fibre has a bandgap centred at 1064 nm. When ethanol is loaded into the core, it guides over the whole spectral range of the OSA except for the absorption bands of ethanol (fig. 6.16 blue line shows the ethanol spectrum from [104]).

The first stage is to prepare an ethanol core PCF. In [101] tanks were used at both ends of the fibre to fill the core with ethanol using capillary force and were not removed in their optical experiments. Here we show simpler method that does not rely on tanks or chambers. The filling of ethanol is performed in the same way as the filling of HF described in Chapter 2. A 2 m long 7 cell HC-PCF with a bandgap centred at 1064nm is used. Firstly, the two ends are collapsed to close the cladding only and leave the core open. Secondly, ethanol is pushed into the core with a syringe. Finally, the two collapsed ends are cut off to avoid loss at the collapsing point. The resulting fibre has a core filled with ethanol and a cladding open to the air.

After the ethanol-core fibre is made, it is illuminated by the 532 nm laser directly with the two ends open to the air. Figure 6.17 shows the output Raman spectrum taken by the OSA. The Raman line of ethanol is created by the C-H bond with a Raman shift of 90 THz. A Raman line at 630 nm is observed with ~50% of the pump converted. No other line is detected due to the absorption of ethanol. This line is interesting for Alexa Fluor 633. The near field mode pattern shows a fundamental mode (inserted in fig. 6.17).

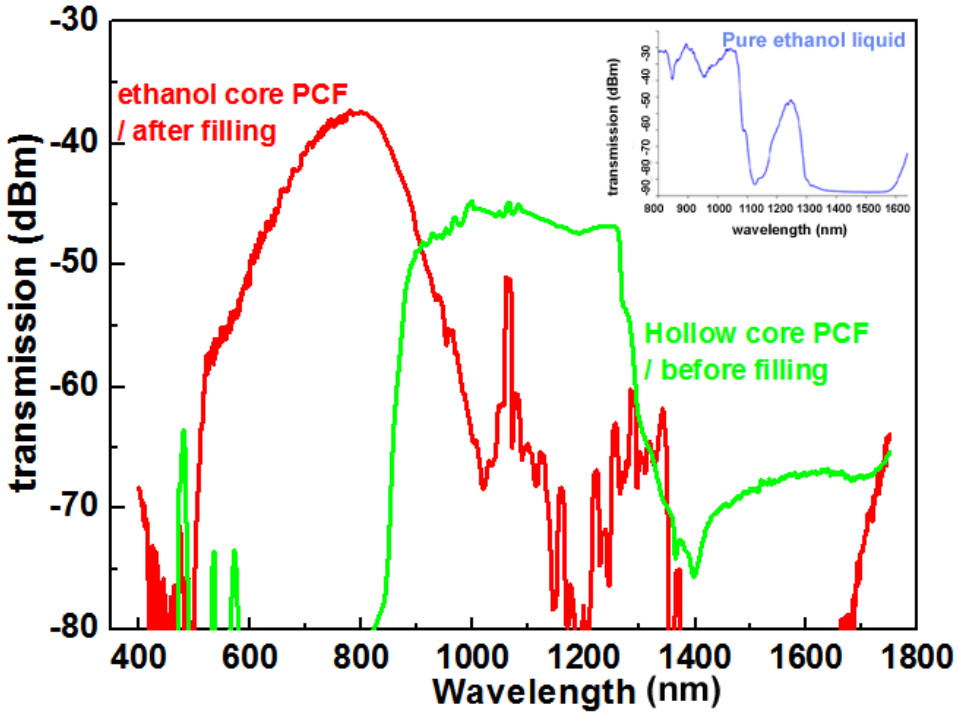

Fig. 6.16 Transmission spectrums for air filling HC-PCF (green curve); ethanol core PCF (red curve) and pure ethanol (inserted, blue curve) [104].

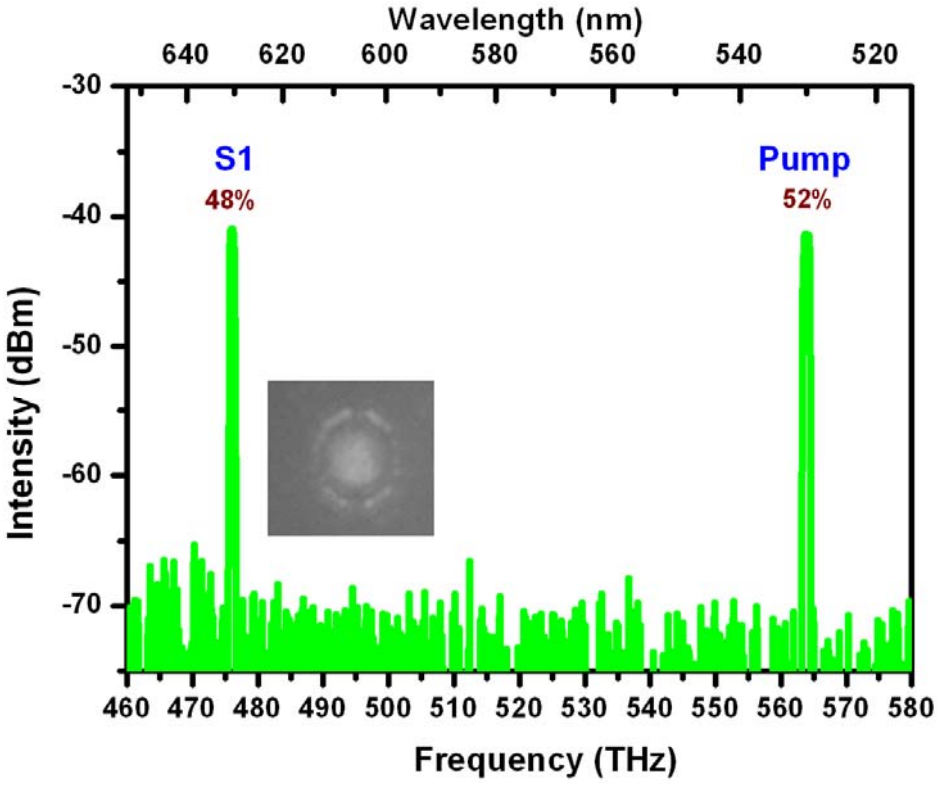

Fig. 6.17 Output optical spectrum for the PBG fibre filled with ethanol, measured with an OSA. Inserted shows the mode pattern of the S1 line.

6.6 Summary

In this chapter, several compact, portable multi-line Raman lasers were developed using a gas filled HC-PCF pumped with a diode pumped solid state laser at 532 nm. The first system was based on a Kagome lattice HC-PCF filled with H_2 and generated a large number of Raman lines (up to 23 emission lines), covering a broad spectral range from the near-IR to the UV, including the much sought-after yellow emission. The second system is a compact and easily integrable PMC device based on a PBG HC-PCF filled with H_2 that is hermetically spliced to SMF that emits only 7 Raman lines but with a much stronger power spectral density than the first multiline laser. The third laser system offers high spectral lines in the infrared region also with a compact design. Finally, the fourth and the fifth systems were based on PBG HC-PCF filled with ethylene and ethanol that exhibit only one or two lines but with very high power spectral density. All laser sources exhibit a high spatial beam quality and a spectral density that is orders of magnitude larger than supercontinuum sources. The exotic wavelengths generated by the system hold the potential to address unexplored environmental and biological applications.

All the above systems can be integrated into a compact and portable device with a size of 140x250x300 mm (fig. 6.18 with Kagome fibre and a gas chamber inside). The device can be further reduced in size by the use of a fibre-pigtailed laser, removing the need for coupling optics by splicing directly to the microcell, resulting in an extremely compact all-fibre multi-line Raman laser. The portability of the laser and the compactness of the PMC allows for this new laser system to be packaged as a small device that requires limited maintenance or alignment. This Raman laser has applications in areas such as forensics and drug recognition using fluorescence, where relatively high power density is required at a number of discrete wavelengths.

Fig. 6.18 Photograph of our multiline UV and visible Raman laser system.

Chapter 7

Photon Statistics of Raman Comb: Self-coherence

In this chapter, we experimentally explore the coherence of each spectral line of a multi-octave frequency comb spontaneously created by SRS in an H_2-filled HC-PCF. The results show that all the spectral components of the comb exhibit strong self-coherence within each single shot while maintaining the underlying quantum fluctuation nature from shot to shot. By introducing a modal picture of the onset of the Stokes field from the vacuum fluctuations and analysing the measured visibility of each of the spectral line interferograms, the results indicate that the macroscopic Raman amplification of the spontaneous Stokes field is limited to a single spatio-temporal mode. Furthermore, the degree of self-coherence and the photon statistics of a single Raman line are investigated under different experimental conditions. [*]

---

* This work has been published in:

Y. Y. Wang, C. Wu, F. Couny, M. G. Raymer and F. Benabid. "Vacuum fluctuation-initiated coherence in multi-octave optical frequency Raman combs". Phys. Rev. Letts. 105, 123603 (2010).

7.1 Introduction

In optical physics, the boundary between the quantum and classical realms is often delineated by the strength of the interaction of an atom or molecule with the vacuum electromagnetic field compared to that with the field from an exciting laser. In quantum optics the atom-vacuum interaction is non-negligible and spontaneous emission of photons plays a central role. Experimentally, this regime of light-matter interaction is encountered, for example, in cavity quantum electro-dynamics (QED) [105] or in spontaneous parametric down-conversion [106], wherein the photon statistics exhibit non-classical features [107]. On the other side of the quantum-classical boundary lies the predominantly classical regime of lasers and nonlinear optics. This regime applies for example to the field of attoscience, which entails the production of extremely short optical-pulses [108] resulting from a multi-octave optical comb of mutually coherent spectral lines. This is technically based either on HHG in noble gases [91] or HSRS in hydrogen or deuterium [66, 90]. In both processes, the regime of light-matter interaction is classical and the medium coherence is driven so quantum vacuum-fluctuations play no direct role in the comb-generation. For example, in the case of SRS, whose comb consists of frequency down-converted spectral lines (Stokes) and up-converted ones (anti-Stokes) and all spaced by the Raman transition frequency, the Raman medium is excited by a judicious choice of multiple pumping lasers or ultra-short pulsed lasers so that the medium excitation is coherently driven; thus overpowering any spontaneous emission [66, 90].

On the other hand, we have seen in chapter 5, that a multi-octave Raman frequency comb was generated from quantum noise in a H_2-filled HC-PCF with a single moderate-power long-pulse laser [11]. The single-pump-laser technique contrasts with those Raman excitation configurations, which rely on classically exciting the medium coherence by using multiple pump lasers or ultra-short pulsed lasers [66, 69, 90]. However, through a qualitative theoretical model and preliminary experimental observations it was hinted that the comb could be coherent (i.e. phase-locked). In the present and the following chapter we investigate this conjecture through a detailed experimental and theoretical study of the coherence and photon statistics within an arbitrary selected Raman line or between several Raman lines. Here,

we focus on the single-shot temporal and spatial coherence of each spectral line of the comb. It is noteworthy that early work on SRS has already reported on the coherence and quantum fluctuation when only one Stokes line [80, 81, 87, 89, 109] is generated. Also, the phase relation between the S1/AS1 is theoretically treated for the condition of the amplification of vacuum fluctuations [110]. However, what has not been observed before is compelling evidence of quantum initiation of an ultra-wide multi-line comb-like Raman spectrum by a quasi-monochromatic driving field and their coherence (self and mutual) properties.

Here we investigate the self-coherence of all the lines from a Raman comb. In section 7.2, we introduce the modal picture and the concept of a spatio-temporal mode within the context SRS generation [78]. In section 7.3, we present the experimental demonstration of the single-shot interference and shot-to-shot fluctuation of phase, visibility and power. We use a set-up consisting of an interferometer with a H_2-filled HC-PCF in each arm.

7.2 Modal picture

Early works on SRS show that the SRS entails a spontaneously emitted Stokes via quantum fluctuation, which acts as a seed for the resultant 1st Stokes field. The electric field of this seed can be represented as a linear superposition of several modes whose temporal and spatial characteristics are uncorrelated [81]. The results show that the dynamics of the Stokes amplification and subsequently the spectral and modal properties of the propagating output Stokes field strongly depend on the spectral and temporal characteristics of the pumping laser on one hand, and on the gas-laser interaction "configuration" on the other. This physical modal picture is detailed and explained below.

Modal expansion

Here, we first consider a general case [81] (fig. 7.1) when a pump pulse with a duration τ_0 interacts with a Raman medium with a dephasing rate Γ. The pump-medium volume interaction is taken to be cylindrically shaped with radius a (cross section area

A) and length *L* and the effects of pump diffraction and spatial incoherence as well as temporal incoherence are neglected.

The Raman process also contains a Stokes field that is spontaneously emitted with a thermal-like distribution of independent spatio-temporal modes or equivalently the collective molecular excitation has a thermal-like distribution of spatio-temporal modes [78, 87, 111]. The Stokes field at the output of the interaction volume $E_S(\rho, L, \tau)$ can thus be written as a Karhunen-Loeve expansion [112] of a set of individual coherent modes or wavepackets. The photons associated with the Stokes field could occupy one or several of these modes with no correlation. The Stokes field is written as follows:

$$E_S(\rho, L, \tau) = (2\pi\hbar\omega_s / A\nu_s)^{1/2} \sum_n \Phi_n(\rho) \left[\sum_k b_k^* \Psi_k^*(\tau) \right]. \tag{7.1}$$

with

$$\begin{aligned} &\int_A d^2\rho \Phi_n(\rho)\Phi_m^*(\rho) = \delta_{nm} \\ &\int \Psi_k(\tau)\Psi_l^*(\tau) d_\tau = \delta_{kl} \end{aligned} . \tag{7.2}$$

Here ρ indicates the transverse coordinates of the spatial modes of the field, and τ indicates the time coordinates and could span from $-\infty$ to $+\infty$. In this picture, the Stokes field at the output of the medium can be regarded as a multimode product of the spontaneous Stokes field that was emitted at an uncorrelated time with uncorrelated propagating spatial modes. Each of these emitted Stokes fields can be indexed by their spatial mode and their time-phase. Within this context, $\Phi_n(\rho)$ relates to the spatial profile of the mode and $\Psi_k(\tau)$ is its temporal component. Here, $\{\Phi_n(\rho)\}$ can be regarded as "a basis" for the spatial mode of the field, and primarily determined by the spatial profile properties of the pump and the geometry of the Raman medium. On the other hand, $\{\Psi_k(\tau)\}$ corresponds to a basis over whose elements the temporal component of the field is expanded and are chiefly determined by the SRS generation time [78, 113], as we will see below.

The number of these spatio-temporal modes has been the subject of previous work where quantifiable expressions have been deduced for the case of free space propagation [81, 114, 115]. Particularly, it has been shown that under a judicious choice of the pump-pulse temporal duration and the net Raman gain, one could amplify to a macroscopic level where only one single temporal mode from the multi spatio-temporal modes compose the Stokes fields. Similarly, if the generated Stokes field propagates with a Fresnel number (see below) smaller than unity along the interaction length, then the amplified Stokes field exhibits a single spatial mode. Below, we review the salient results of this work [81] and how these apply to the case of SRS in HC-PCF filled with a Raman active gas.

Number of Temporal modes

The number of Stokes temporal modes that are amplified depends on the pump duration and the Raman net gain [78] (see chapter 5). This is schematically shown in fig. 7.1. For the case where the pump pulse duration τ is less than $1/gz\Gamma$, the scattering process remains spontaneous and stimulated amplification is not reached. Consequently, the output is an amplified spontaneous emission whereby the Stokes amplification is low and the photons comprising its pulse are mutually uncorrelated in time and in wave-vector.

In the case of larger pump duration so $\tau \geq gz/\Gamma$, the Raman process falls in the steady-state regime. Due to the relatively high gain and the long pulse duration, most of the initiated temporal modes $\Psi_k(\tau)$ are amplified, resulting in a Stokes pulse whose overall phase is uncorrelated with that of the pump (fig. 7.1 second row). When $1/gz\Gamma \leqslant \tau \leqslant gz/\Gamma$, remarkably and crucially, the initial phase noise represented by the possibly large number of temporal modes $\Psi_k(\tau)$ is heavily filtered out under the high-gain transient conditions. This is explained by the fact that the generation time for the Stokes is smaller than the dephasing time of the Raman medium T_2. Subsequently, only the dominant temporal modes (i.e. those with the largest Raman gain) are amplified. This filtering process provides feedback to the amplification, allowing only a limited number of temporal modes to be amplified. If the Raman gain is extremely

high, the net outcome of this filtering can be a Stokes field that is determined solely by a single temporal mode $\Psi(\tau)$ (i.e. single phase) (fig. 7.1 third row) [41, 81].

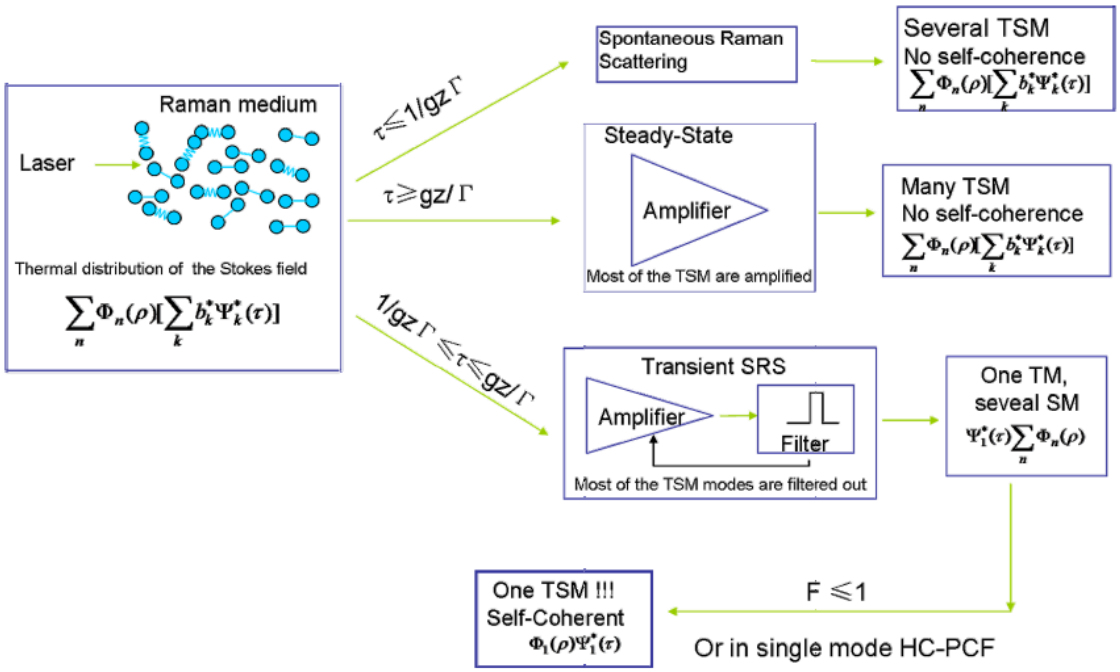

Fig.7.1 Description of the modal picture showing the self-coherence of different regimes of SRS.

In practice, the SRS transient regime has been limited to sub-pico (for hydrgen) pump pulse with gigawatt power level for the case of free-space configuration. However, as shown in chapter 5, when the Raman process takes place in the 30 μm core Kagome HC-PCF, even with a 12 ns duration pump (see section 5.3.1 and 5.3.2), the transient regime requirement can be easily fulfilled with a high Raman gain (gz=140) [11, 41]. This means only one dominant temporal mode is filtered out and amplified.

Number of Spatial modes

It is noteworthy that even if the Raman amplification takes place in the transient regime, the output Stokes pulse may still contains multimode spatio-temporal modes. This is due to the fact that to a single-phase temporal mode, we may associate several spatial propagating modes. In free-space configuration, the number of spatial modes is related to the Fresnel number (F) during the pump-medium interaction:

$$F = \frac{A}{\lambda_S L} \tag{7.3}$$

where λ_S is the Stokes wavelength. When F>1, as many as ~ F^2 spatial modes can pass through the output face [81, 115], giving an incoherent output. When F≤1 (but not <<1), the diffraction-limited angular divergence angle (~$\lambda_S / \sqrt{A}$) is of the order of the geometrical angle subtended by the cylinder ($\sqrt{A} / L$), and therefore only a very limited number of transverse spatial mode contributes strongly to emission along the pencil axis [81]. In other words, diffraction washes out any initial spatial incoherence associated with spontaneous emission (fig. 7.1 fourth row). Though it was argued later that even for F=1, the Stokes field may not be fully spatially coherent [115].

In case of HC-PCF, the number of spatial modes is no longer determined by the Fresnel number, but the number of supported guided modes. As seen in previous chapters (chapter 2&4), our Kagome fibre guides light mainly in a fundamental core mode along with a quartet of degenerate high order modes. These high order modes can be avoided by a judicious choice of launching conditions especially for longer wavelenghs. Moreover, the high order modes exhibit a higher transmission loss than the fundamental modes. Thus, for longer propagations, it is reasonable to assume our Kagome HC-PCF acts as a single mode fibre.

Based on the above analysis, the HC-PCF provides thus an excellent platform for Stokes amplification of a single spatio-temporal mode (i.e. a pure quantum state with a single spatial mode). This situation could provide an answer to the generation of the ultra-broad Raman frequency comb with H_2-filled HC-PCF. Below, we show that the experimental results corroborate this conjecture of the single spatio-temporal mode excitation and we analyze the photon statistics in our Raman frequency comb.

7.3 Experimental demonstration of self-coherence and photon statistics

Under the conditions of high gain transient regime and single mode propagation mentioned above, the Raman frequency comb generated involves only a single spatio-temporal mode for every pump laser shot. This means that the output of the Stokes field will have the form of a transform-limited wave packet with a well-defined single overall phase, shape and mode, i.e. it is an amplified version of a pure quantum state of the spontaneously emitted Stokes field [111]*. This wave packet mode corresponds to the Stokes spatio-temporal mode with the highest Raman gain and is reproducibly created on each laser shot. Finally, it is noteworthy that while the phase of this spatio-temporal mode is deterministic for each laser shot, it does vary randomly from shot to shot [113]. Consequently, as far as we are dealing with only one pump laser shot, the Raman comb generation is similar to those generated by coherent preparation. The difference though, is for different laser shots, the phase of the wave packet is different and random, as one would expect from the random nature of spontaneous emission. Consequently, a Raman line (at least the first Stokes) from any random shot can interference with a counterpart that was generated at the same frequency from any other random shots with strong interference patterns. We then say that the Raman line is "self-coherent". By "self-coherence" we mean the pulse associated with the Raman line exhibit a single temporal and spatial mode within each shot. In other words the pulse is transform limited. The interference pattern generated can give an idea of the degree of "self-coherence" and we can hence indicate whether the Stokes is a single spatio-temporal mode.

To demonstrate this, we experimentally build a Mach-Zehnder interferometer. We explore several routes to identify experimentally the statistics of the Raman lines: by

* It is noteworthy that the actual onset of the comb is in fact due to a spontaneously emitted and correlated pair of Stokes and anti-Stokes (see Chapter 8).

measuring the visibility of the Raman line-pairs and investigating their statistical properties from shot to shot on one hand and extracting the fluctuation of phase on the other hand.

7.3.1 Mach-Zehnder Interferometer

Figure 7.2 shows the interferometric set-up. This is used through chapter 7 and chapter 8 for the measurement of both self- and mutual- coherence and photon statistics of the comb components. Two 70-cm pieces of identical HC-PCF filled with 15 bar of H_2 were excited with equal optical power of 30 mW from a single-frequency Nd-YAG laser to independently generate identical Raman combs. The laser emits 12 ns, nearly transform-limited pulses at 1064 nm with a 50-Hz repetition rate. The long separation between the pulses (20 ms) ensured that the spatio-temporal mode excited by each successive pump pulse was uncorrelated. The HC-PCF used was a large-pitch single-cell Kagome fibre with a 30 μm hollow core. Both the laser and the fibre were the same as in [11] and are shown in fig. 5.3. The fibre dominantly guided a polarization-degenerate HE_{11}-like mode confined in the core. The practically single-modedness of the fibre and the long propagation length ensured that only one spatial mode was amplified. The output of the two combs is shown in fig. 7.3 when the two fibres were excited by ~30 mW average power in each arm, ensuring the transient regime conditions where one dominant temporal mode is excited. At the output, they were combined on a 50/50 beamsplitter and passed through a polarizer. A grating was then used to separate the Raman spectral pairs of the combined beam, and representative spectral pairs were sent to a CCD camera where they were recorded simultaneously on a single-shot basis. Care was taken so that one CCD frame of the camera corresponded to a single shot from the pump laser. Furthermore, to ensure a good spatial overlap between the two beams forming the spectral line pairs, an "endlessly single-mode" PCF [116] was placed at the output of each HC-PCF to act as a spatial mode filter.

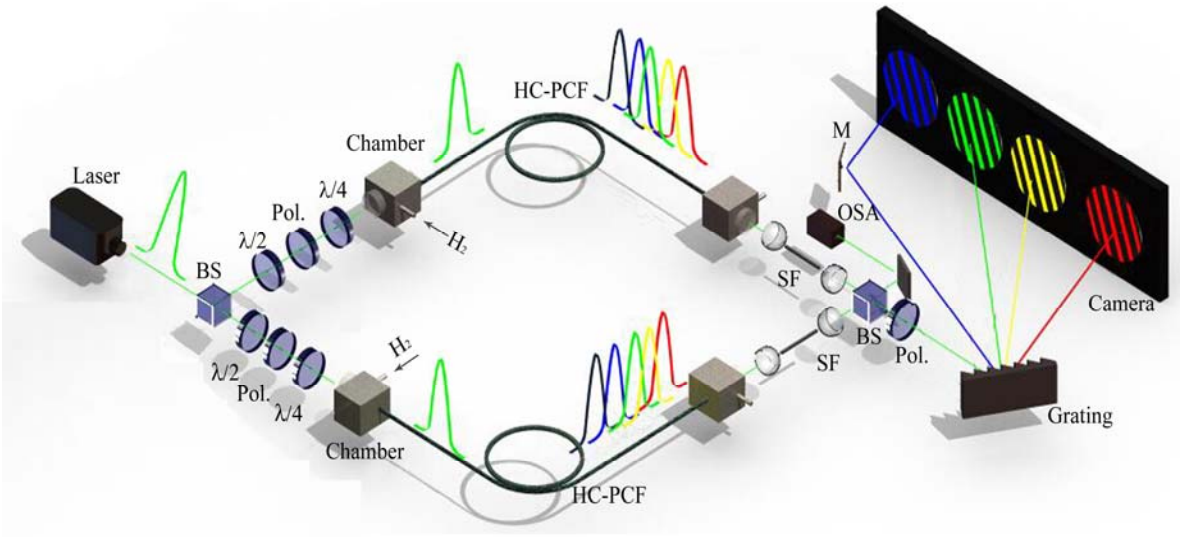

Fig. 7.2. Experimental interferometer for coherence demonstration. In the two arms are the two identical combs generated by a Nd-YAG laser through a H_2-filled HC-PCF. SF: spatial filter, BS: beam splitter, Pol: polarizer, λ/2: half-wave plate, λ/4: quarter-wave plate, M: mirror.

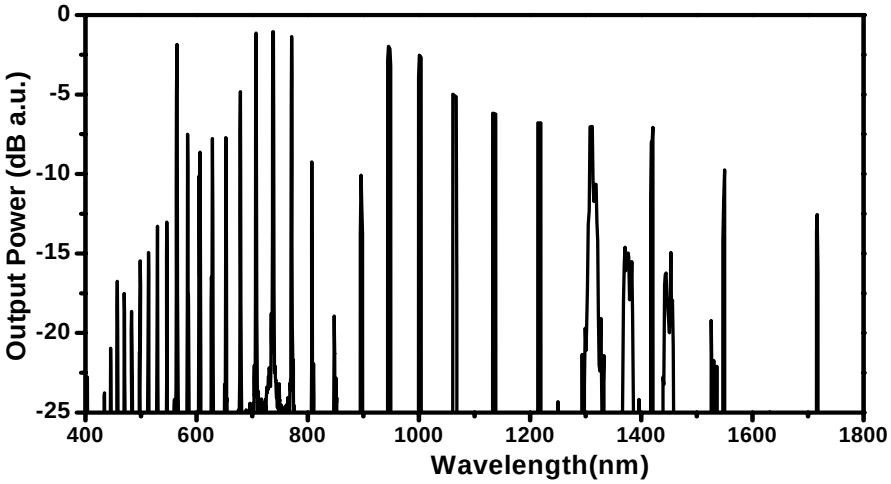

Fig. 7.3 Output spectrum for one of the Kagome fibre measured by an OSA.

7.3.2 Stokes Visibility Evolution

At the output on the camera the interference patterns for different wavelengths were obtained. Figure 7.4 shows single-shot profiles of the interferograms from the pump pair at 1064 nm and of four degenerate spectral pairs from the two fibres at wavelengths 740 nm (vibriational AS1), 770 nm (rotational Stokes generated by vibriational AS1), 1003 nm (rotational anti-Stokes generated by pump (AS1)), and 1134 nm (rotational Stokes generated by pump (S1)). The comb-line spatial-interferograms

exhibit high-visibility interference fringes, indicating strong "self-coherence" of each Raman line. Such interference occurs for every pair of comb components. These indicate strongly that the Raman amplification is triggered from a well defined mode of the spontaneously emitted Stokes seed. This bears resemblance to cavity-QED, wherein a single molecular excitation is strongly coupled to a single cavity mode [117]. However, the difference in the present configuration is that spontaneous emission is not strongly modified as in the case of cavity-QED, but instead, and owing to the optical guiding property of the fibre and the high-gain and highly transient regime of the Raman amplification, only a single spatio-temporal (a coherent pulse) is selected from the multimode vacuum field.

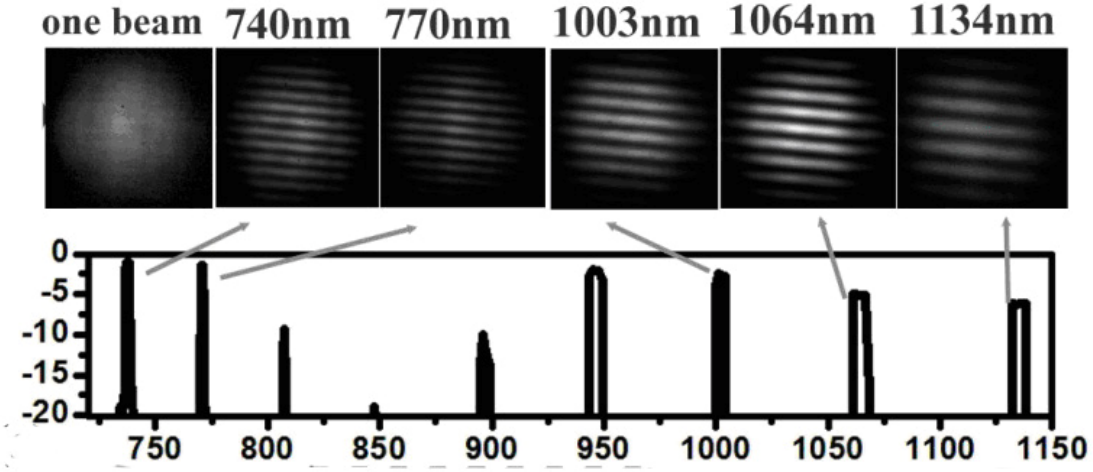

Fig. 7.4 Fringes at 740nm, 770nm, 1003nm, 1064nm and 1134nm.

To have a qualitative study, the degree of the self-coherence is investigated by measuring the visibility of the fringes from shot to shot. The visibility is the ratio of the intensity of the coherence part to the overall intensity [87]

$$V = \frac{2\sqrt{I_{C1}I_{C2}}}{I_1 + I_2} = \frac{I_{\max} - I_{\min}}{I_{\max} + I_{\min}} \tag{7.4}$$

where V is the visibility, I_{C1} and I_{C2} are the coherent parts in each arm of the generated one Stokes. I_1 and I_2 are the total intensity in each arm of one Stokes line. Experimentally, we measure the maximum and minimum intensity of the interference

pattern (I_{max} and I_{min}) and the visibility is deduced, representing the degree of the coherence part of the beams.

The visibility of the fringes from each of the frequency degenerate Raman lines is measured over more than 150 frames. These were selected from a larger number of frames and correspond to input laser average power fluctuating within 1% of 30 mW. This is necessary to minimize the pump laser pulse noise as it affects strongly the statistical outcome [109]. The visibility is extracted using the following procedure (fig. 7.5). Firstly, each single shot interferogram is captured and saved in a computer. Secondly, a one dimensional trace is extracted by applying a reference cross-line vertical to the fringe on the interferogram (fig. 7.5a). The obtained oscillatory trace is then normalized and fitted with a Gaussian-shape envelope (fig. 7.5b). The result of this is fitted to a sine oscillation (fig. 7.5c):

$$y = y_0 + A\sin(2\pi(x - x_0)/\lambda_0) \tag{7.5}$$

y_0, A, x_0 and λ_0 are amplitude offset, envelope amplitude, position offset and period of the sine function as drawn in fig. 7.5c. The fitting gives the visibility $V=A/y_0$ and the shot-to-shot relative phase $\varphi = 2\pi x_0/\lambda_0$. The measured relative uncertainty of the visibility was estimated to be about 5%. Furthermore, for limited sensitivity of the CCD camera, the visibilities under 0.1 cannot be distinguished and are here considered to be 0.1.

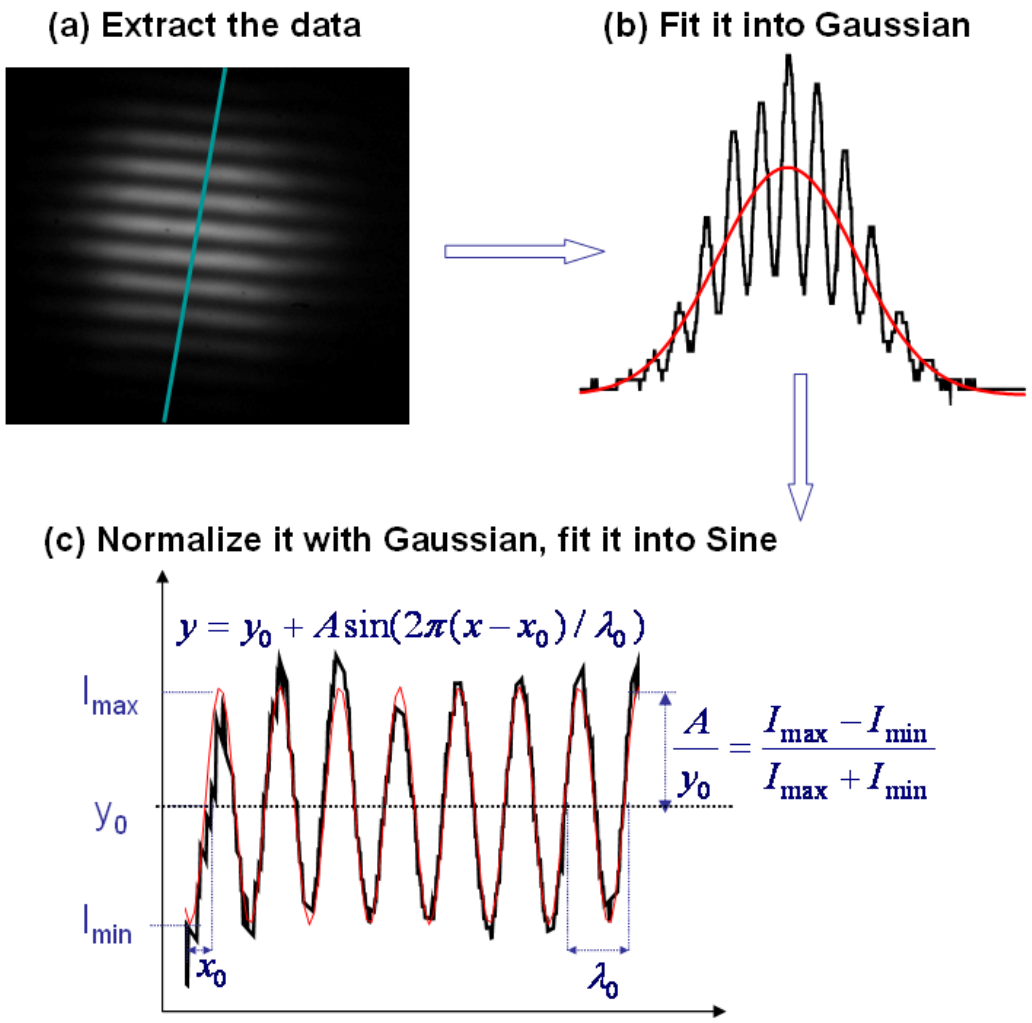

Fig. 7.5 Process of retrieving visibility and phase information from the interference pattern. (a) a reference pixel line is drawn in the fringe; (b) Gaussian (red) fits to the data (black) to normalize; (c) sine function (red) fits to the normalized data (black) with the equation shown holding visibility and phase informations.

For reference purposes, we first measure the visibility of the pump. The input pump exhibits an average visibility of 0.96 (fig. 7.6a) and is slightly degraded to 0.94 (fig. 7.6b) after propagation along the HC-PCF when no nonlinearity takes place i.e. without H_2 or with low power. We believe that this degradation is due to either the laser beam jitter which alters the slightly different coupling in the fibre in each arm of the interferometer, or to the thermal noise induced fluctuation in the effective index of the guided mode, which in turn create phase noise in the transmitted laser beam. In both cases, the standard deviation is small (0.020 and 0.023). When the comb was generated at 30 mW, the transmitted pump exhibits an average visibility of 0.85 (fig. 7.6c) with a higher standard deviation of 0.082. Notwithstanding that this is obviously

due to the presence of nonlinearity (i.e. SRS and FWM), it was impossible to assert whether the degradation in visibility was induced by a phase noise or amplitude noise in the pump. However, it is well known that the amplified Stokes in SRS exhibits strong amplitude fluctuations, which could thus affect the pump field via four wave-mixing.

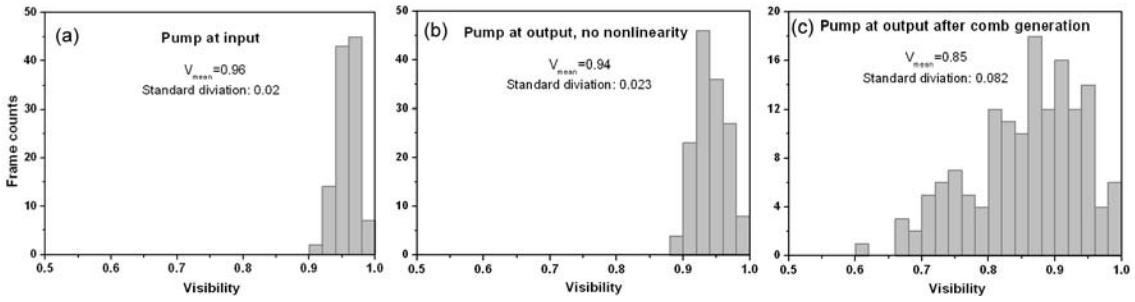

Fig. 7.6 Visibility distribution histogram for the pump (a) at the input; (b) at the output when no nonlinearity is involved. (c) at the output when the comb is generated. Note that the x axis starts from 0.5, and in fig.7.7 and fig.7.8 starts from 0.

In contrast to the pump whose visibility exhibits the common distribution of a coherent laser, the Raman lines, despite exhibiting strong single-shot self-coherence, show a strongly fluctuating visibility. Figure 7.7 plots the visibility distribution histogram of the S1/AS1 pair at 1134 nm and 1003 nm. The insert, which shows visibility against the frame number, clearly indicates the large and random fluctuations of the visibility from shot to shot. The maximum visibility goes to as high as 0.89 and 0.94, which is comparable to the pump, and their minimum goes down as low as the limit of our detection. Both two visibilities have a standard deviation of 0.17, which is much higher than that of the pump. Given the limited pump power fluctuation for the dataset considered here, such a large dynamic range in visibility is a strong indication of the vacuum fluctuation of a macroscopically amplified single mode quantum state. Finally, the average visibility has a value of 0.56, which is still high given the fact it is initiated from noise.

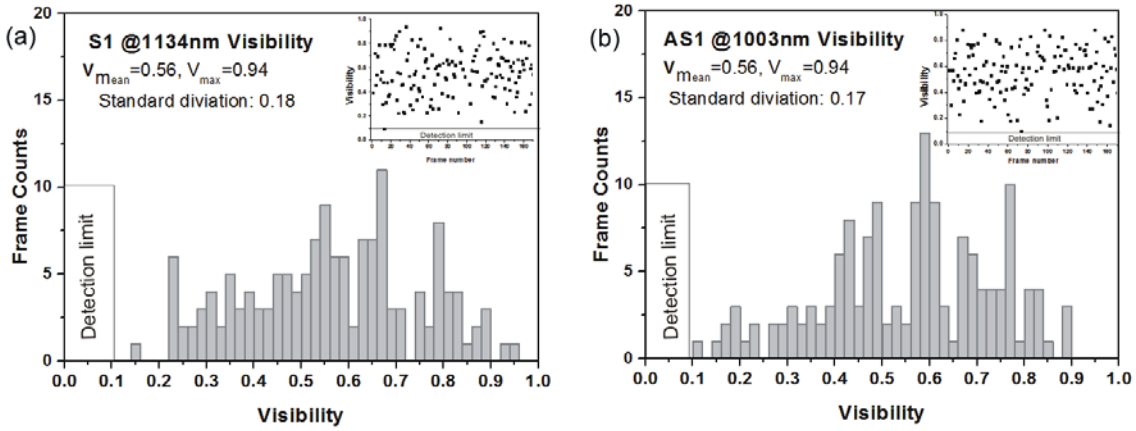

Fig. 7.7 Visibility distribution histogram for (a) S1@1134 nm (b) AS1@1003 nm. Inserts are plotted as frame number verses visibility, showing large fluctuations of the visibility.

For higher order S/AS, the statistical visibility histograms (fig. 7.8) exhibit lower values for both maximum and the average compared to the first orders. With the rotational AS2 @ 950 nm having a maximum of 0.89 and a mean value of 0.40, the rotational S1 generated by the vibrational AS1 @ 770 nm a maximum of 0.68 and a mean of 0.31, the vibrational AS1 @ 740 nm a maximum of 0.7 and a mean of 0.35 and finally the vibrational AS2 @ 570 nm having a maximum visibility of 0.82 and a mean of 0.40. Similarly to the rotational AS1/S1, the standard deviation shows rather high values of 0.178, 0.12, 0.124 and 0.176 respectively.

The decrease of the achievable visibility indicates a systematic "noise effect" during the photon conversion process such as phase mismatch due to the fibre dispersion. This effect needs, however, further investigation whereby effects such as incoherent Raman or Doppler broadening must be taken into account. Nevertheless, the large standard deviation in the visibility along with the minimum visibility reaching below our detection sensitivity level and the maximum reaching almost unity for the investigated comb lines strongly points to the scenario of a macroscopically amplified single spatio-temporal mode quantum state.

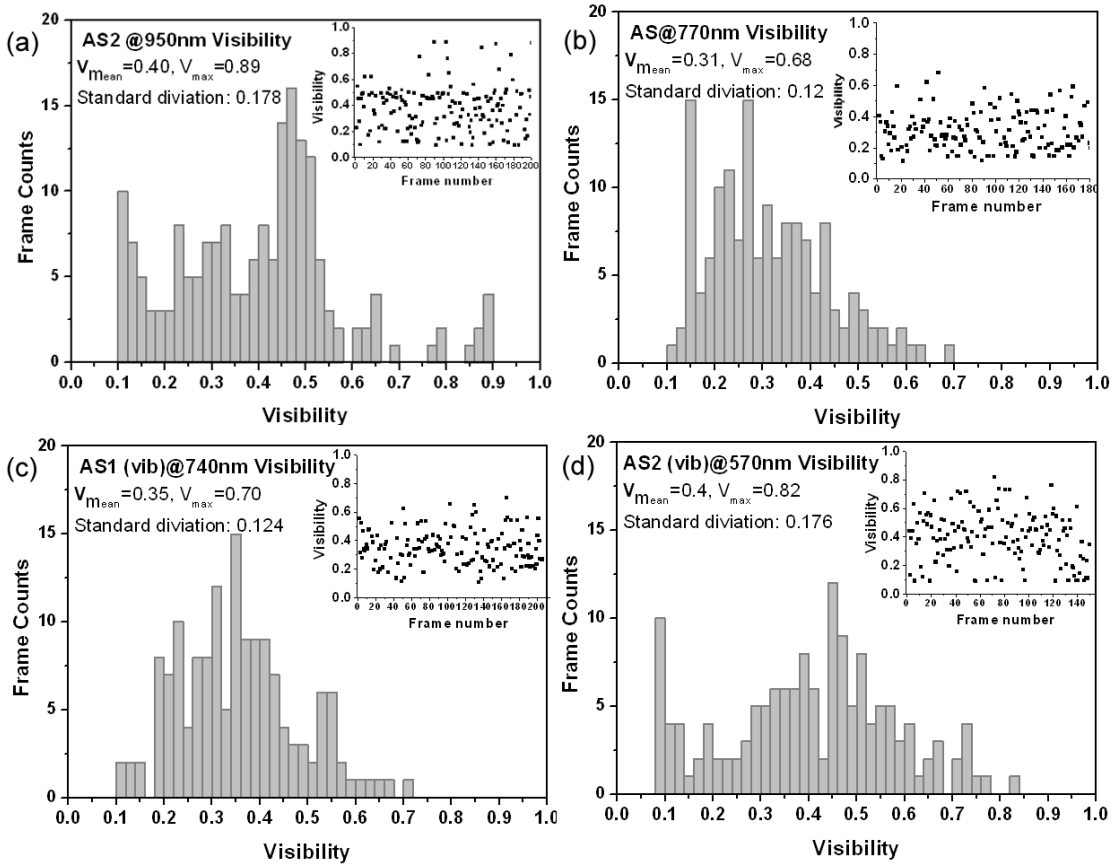

Fig. 7.8 Visibility distribution histogram at (a) rotational AS2 @ 950 nm; (b) rotational S1 @ 770 nm generated by vibrational AS1; (c) vibrational AS1 @ 740 nm; (d) vibrational AS2 @ 570 nm. Inserts are plotted as frame number versus visibility, showing large fluctuations of the visibility.

Further Investigation

To gain further empirical experimental facts about the coherence properties of the Raman comb, we carried out measurements on how the Stokes power distribution evolve with the input pump power and on how the visibility of the S1/AS1 pair change when the coupled power or the gas pressure is changed in one of the HC-PCF Raman generators. It is noteworthy, that the results obtained show a rather complex dynamics whose explanation is beyond the scope of the current work. Consequently, the results below are presented as a factual provision towards future investigations in understanding the quantum dynamics of the Raman generation in a confined geometry such as that of HC-PCF.

Firstly, in order to shed more light on the photon statistics or the energy distribution from pulse to pulse of the comb components, we carried out the measurement of the Stokes shot-to-shot power fluctuation at different pump levels. This is achieved by simply blocking one arm of the interferometer and recording on the camera the Gaussian mode profile of the Stokes line (see for example the "one beam" profile in fig. 7.4). The peak value is then taken as a representative quantity of the power of the output Stokes line. This is so because the modal profile of Stokes remains reasonably unchanged from shot to shot. Furthermore, given the slow response time of the CCD camera compared to the Stokes pulse duration, the recorded peak value is also proportional to the Stokes pulse energy. We plot the statistical histogram from 256 successive shots of this peak power distribution of the S1 line. The experiment is then repeated for different input powers (fig. 7.9).

Recording measurements performed just above Raman threshold (fig. 7.9a&b) show that the energy of the S1 pulse train obeys a negative-exponential probability distribution. This agrees with earlier theoretical and experimental results [89, 118]. These showed that in a transient regime of amplification, and in the absence of saturation and depletion of the pump or molecular population, the Stokes pulse energy distribution *P(W)* follows the following expression:

$$P(W) = \frac{1}{< W >} \exp(-\frac{W}{< W >}) \tag{7.6}$$

where <*W*> is the mean value of the Stokes pulse energy. This distribution follows the fact that the quantum noise responsible for the initiation of the spontaneous scattering obeys Gaussian statistics [118] and the spontaneously emitted field can be thought of as a Gaussian random process having zero mean. As a result, the energy emitted, proportional to the square of the field, is distributed according to equation (7.6) with a mean value <*W*> and the most probable value being zero. The same statistics also apply to a single mode thermal or blackbody field. It demonstrates a system that begins in a pure state and evolves by Hamitonian dynamics into a state with a macroscopic but strongly fluctuating value of energy. This agreement with earlier work further confirms that our configuration operates in transient regime even with very low power.

At higher pump powers, and well above threshold, the emitted Stokes photon statistics exhibit a very different probability distribution from the negative-exponential one as shown in fig. 7.9 c, d, e & f. We can distinguish two regimes. Firstly, for intermediate pump powers (5.5 mW-7 mW), the distribution shows a very large spread with a weak peak. Secondly, as the pump power is increased further, the distribution tends to exhibit a single-peak distribution centered on the average power in similar fashion to a Poissonian distribution. The limited quantum efficiency of our detection scheme doesn't allow us to have a reliable conclusion on the underlined nature of the photon statistics involved. However, the present results agree with previous experiments on S1 power fluctuation in this regime [119-121]. In particular, their results showed that the Stokes-pulse-energy fluctuations were indeed dramatically decreased as the input pump was increased, and the probability distribution changes from a clear negative-exponential to a single peaked distribution. The authors in [119-121] attributed this change to saturation effects in the Raman amplification. It is though clear that this field of research remains rather poorly explored and is worth further investigating the photon statistics of the Stokes and elucidating the contribution of the higher order Raman and saturation on one hand and the modal properties of the fibre on the other.

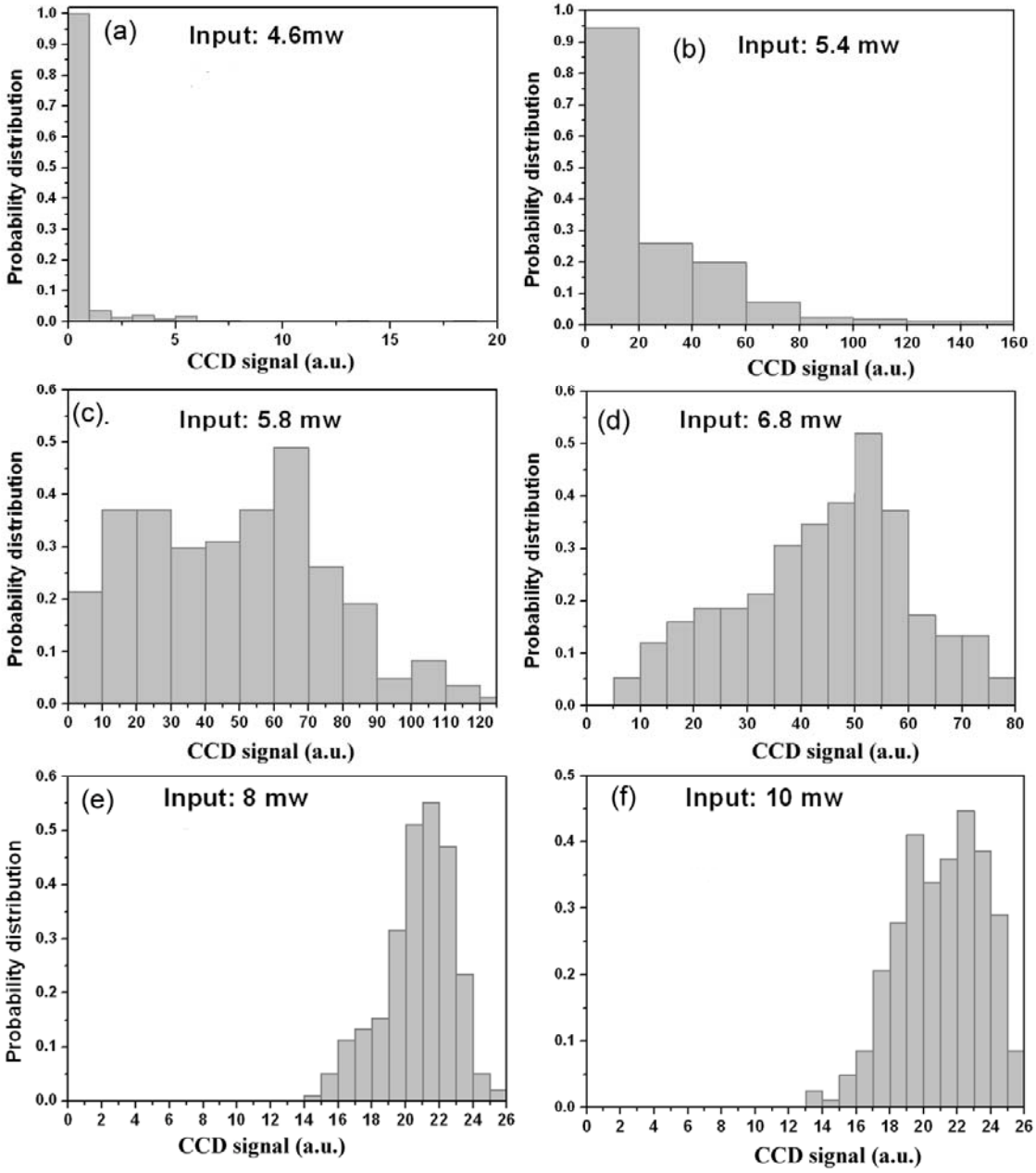

Fig7.9 Statistics histogram of S1 power (detected from the CCD camera) distribution from 256 successive shots for different input powers from (a) 4.6mW to (f) 10mW.

A further measurement was carried out to investigate the effect of pump power and pressure on the visibility. AS1 and S1 lines were selected for the measurement. It is to be noted that the fibre used in this experiment was slightly different from the one used above. Therefore, the results show a trend only and the exact value cannot be compared to previous values. The investigation was done firstly by fixing the pump power and pressure in arm 1 of the interferometer and changing those in arm 2 (fig. 7.10 a&c). This was motivated by the desire to find the optimized parameters for

coherence generation. Figure 7.10 shows the average visibility of S1 and AS1 with pump power in arm1. Here the pump power is kept fixed in arm 2. The average visibility was taken from a list of ~ 250 measured visibilities. Furthermore, in order to suppress the effect of unbalanced powers in the expression of the visibility we put an attenuator at the output of arm 1 to make the intensity equal to arm 2. The power in arm 2 was fixed at 30 mW whilst the power in arm 1 was varied from 15 mW to 40 mW. Figure 7.10a shows this visibility for both AS1 and S1 with the power in arm 1. The visibility shows a similar trend for both S1 and AS1, first an increase with power and then a decrease at power higher than 28 mW. Similarly, in fig. 7.10c when altering the pressure in arm 2 from 3 bar to 15 bar while the pressure in arm 1 is fixed at 15 bar, the visibility for both AS1 and S1 also shows an increase and a decrease with the maximum at 8 bar. This is due to the slightly varying dephasing rate for different pressures.

Fig. 7.10 b&d presents the visibility evolution when the parameters are changed simultaneously in both arms. When fixing the pressure at 15 bar and changing the power from 10 mW to 30 mW (fig. 7.10b), the visibility shows a maximum of ~0.5 at 10 mW and drops to ~0.2 at 18 mW. At higher powers, the visibility slightly increases. We speculate that the drop of the visibility is mainly caused by the conversion of AS1 and S1 to the high order Stokes. Interestingly, a linear decay is observed as the pressure is increased in both fibres. Especially, at lower pressure (3-4) bar, the visibilities for S1 and AS1 show an extremely high value of 0.65. Indeed, in this regime, no higher order Stokes is generated and there is less dephasing of the sole Raman lines generated (AS1 and S1) since the dephasing rate Γ is proportional to the pressure. This regime is of vital interest as it shows a possibility of general entanglement between S1/AS1 photons and needs to be studied in future work.

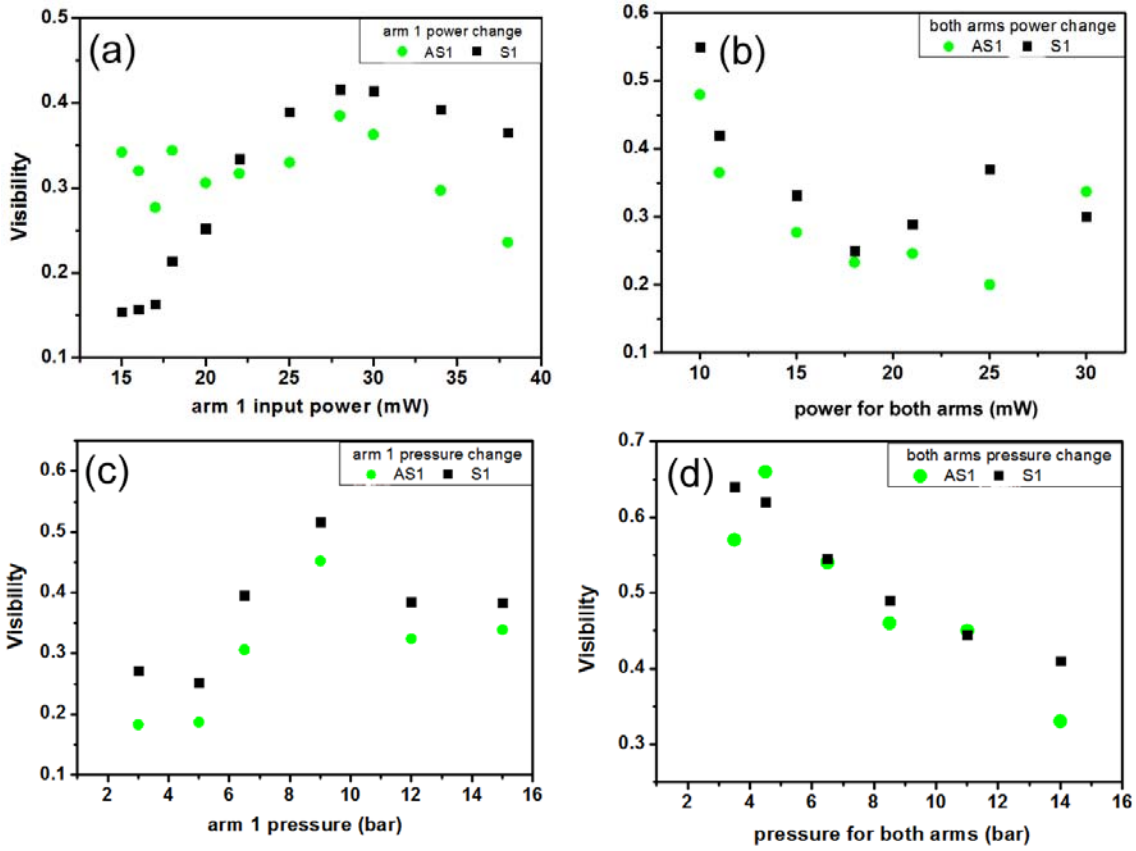

Fig. 7.10 Effect of the power and the pressure on the visibility. (a) Both pressures are fixed at 15 bar; one arm power is 30 mW, and the other arm power varies with the visibility. (b) pressure fixed at 15 bar, power change in both arms vs visibility. (c) power fixed at 30 mW, one arm pressure fixed at 15 bar, the other arm pressure vs visibility. (d) power fixed at 30 mW, two arm pressure vs visibility.

7.3.3 Shot-to-shot Phase Evolution

The quantum nature of the comb onset was also investigated by measuring the relative phase of each degenerate pair of comb lines from the two fibres. This was done by measuring the shot-to-shot phase difference between successive interferograms $\Delta\varphi^{(i)} = \varphi^{(i+1)} - \varphi^{(i)}$ for 150 shots. The superscript (i) indicates the shot number or equivalently the frame number. The extraction of relative phase information has already been shown in fig. 7.5. The histogram of the phase distribution is shown in fig. 7.11. At the input directly from the laser (fig. 7.11a), the pump shows a coherent behavior with a narrow distribution of FWHM=16.7^0 (full width at half maximum). For the transmitted pump this is broadened by the interferometer jitter and the fibre to

FWHM=45^0 (fig. 7.11b). The distribution is also presented in the inserted figure by plotting $\Delta\varphi^{(i)}$ against $\Delta\varphi^{(i+1)}$.

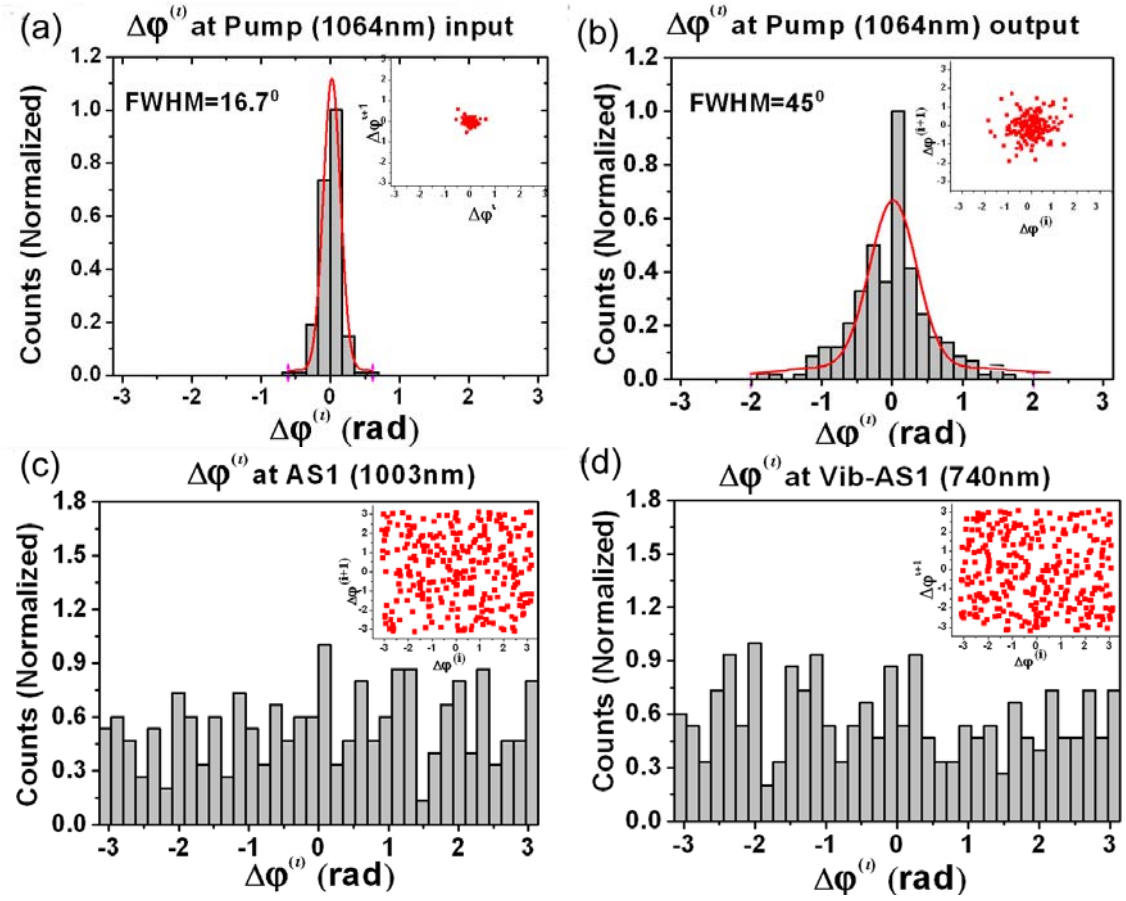

Fig. 7.11 Relative phase difference histograms for (a) pump before entering the interferometer; (b) pump at the output; (c) AS1 at 1003nm; (d) Vib-AS1 at 740nm. Inserted is the plot of $\Delta\varphi^{(i)}$ vs $\Delta\varphi^{(i+1)}$, another way of presenting the phase changing.

For all the S/AS lines, the phase distributions were found to be random. Examples are given in fig. 7.11c&d for AS1 at 1003 nm and vibrational AS1 at 740 nm. This agrees with the measurement done by Kuo [109] who studied the relative phase fluctuation for S1 only. The origin of this random fluctuation is found in the modal picture whereby for every single shot, the Raman process starts spontaneously with a large number of spatio-temporal modes, with each mode having a random $\varphi_{QF,i}$ (see section 5.3.2). The transient regime then only amplifies the dominant mode with one deterministic phase φ_{QF} which randomly evolves from shot to shot. The complete

irrelevance between $\Delta\phi^{(i)}$ and $\Delta\phi^{(i+1)}$ in fig. 7.11c&d indicates the underling quantum nature of the Raman lines.

7.4 Summary

In conclusion, by investigating the photon statistics of the individual lines in terms of visibility, power and phase, we have shown the self-coherence properties of the Raman lines within each pulse as well as the random fluctuation from shot to shot, implying the distinctive statistics of the vacuum field zero-point fluctuations. Further investigation is needed for a better explanation of the visibility data.

Chapter 8

Photon Statistics of Raman Comb: Mutual Coherence

In this chapter, we show the first experimental and theoretical demonstration of mutual coherence within each driving laser pulse among the Raman components of a multi-octave frequency comb spontaneously created by SRS in a H_2-filled HC-PCF. This coherence arises in spite of the field's initiation being from quantum zero-point fluctuations. This points to the possibility of an optical frequency comb with nonclassical correlations between all comb lines.[*]

[*] This work has been published in:

1. Y. Y. Wang, C. Wu, F. Couny, M. G. Raymer and F. Benabid. "Vacuum fluctuation-initiated coherence in multi-octave optical frequency Raman combs". Phys. Rev. Letts. 105, 123603 (2010).

2. C. Wu, M. G. Raymer, Y. Y. Wang and F. Benabid. "Quantum theory of phase correlations in optical frequency combs generated by stimulated Raman scattering." Phys. Rev. A 82, 053834 (2010).

8.1 Introduction

In this chapter, we continue a further study on the photon statistics we started in chapter 7. We will particularly be exploring the phase relationship between two different spectral components from a Raman comb. The experimental and theoretical results show that the spectral components exhibit strong correlations between them. The experimental approach consists of a phase cross-correlator, which is based on interfering independent Raman combs generated from two separate but identical Raman-scattering mediums. By comparing the fringes created simultaneously at two distinct comb frequencies, we show a strong phase cross-correlation between any two spectral lines generated from a given Raman resonance within a single medium. The theoretical results were obtained by using a rigorous solution of the quantum Maxwell-Bloch equations for the S1/AS1 pair. The results show, in corroboration with the experiment, that the S1/AS1 lines are very strongly phase anti-correlated throughout the duration of these two pulses, even in the situation where large phase-velocity dispersion is present in the medium. Finally, we show theoretically and experimentally that the intensity is also strongly correlated between the comb spectral lines. Such correlations (both in phase and intensity) would not be present in a truly thermal source; instead this indicates that they are part of a multimode squeezed state.

8.2 Experimental Demonstration of Mutual Coherence

In the previous chapter, we show that the S/AS spectral components exhibit both strong interference fringes within a single shot and thermal statistics from shot to shot. This along with the strong visibility obtained indicate that we are in a situation where the quantum seed of the amplified Stokes is a single spatio-temporal mode (wave-packet). In this chapter, we investigate experimentally the mutual coherence of the comb lines by extracting a phase relationship between two different comb lines (e.g. S1 and AS1) on each shot and investigating how it evolves from shot to shot.

Experimental Setup

We introduce a versatile cross-correlator based on interfering independent Raman combs generated from two separate but identical Raman-scattering media.

Experimentally, this is achieved by recording single-shot interferograms of several Raman pairs simultaneously within a single CCD frame (see fig. 8.6). The interferograms are obtained using the experimental set-up described in section 3.1 of chapter 7. However, unlike in section 7.3.1, where only one line is recorded on the CCD for self-coherence and visibility measurements, here, up to four interferograms from different frequency-degenerate pair of lines are registered within the CCD frame. This is achieved by dispersing the lines of the combined combs at the output of the aforementioned interferometer. Then the beams of the desired four lines are directed to the CCD camera by means of a set of beam-splitters and spectral filters (fig. 8.1). The optical length of each beam is adjusted to be the same. A CCD image of the four interferograms is then obtained (fig. 8.2.a). This is next recorded on a single shot basis over 256 shots. Finally, the data is processed using the procedure described below to extract the relative phase between two different interferograms.

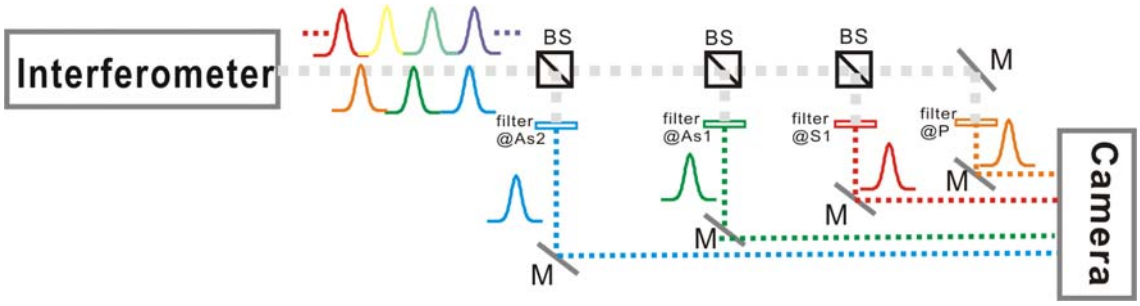

Fig. 8.1 Schematic setup of the cross-correlator for the mutual coherence measurement. The interferometer is the same as that of fig.7.2,the output of which is two Raman combs interfering with each other. It then goes through four beamsplitters and four bandpass filters and hits the camera simultaneously. BS: beam splitter, M: mirror.

Cross-phase Extraction

Figure 8.2a shows a typical single-shot frame obtained from the camera. The capture contains four interference fringes from different line-pairs. Using the method described in section 3.2 of chapter 7, we fit the envelope of each of the four fringe patterns along a fixed and arbitrary line to a Gaussian function. Then, after normalization of the fringe pattern along the reference line relative to the fitted Gaussian, we fit the obtained trace to a sine function. Figure 8.2b shows typical traces for two different line-pairs (AS2 and S1) and for two different shots (Shot *i* and shot *j*). For each

interferogram we calculate the phase difference between two different shots. Consequently, for *n*-th order of the Raman sidebands and for the *i*-th laser shot, the extracted phase can be written as:

$$\Delta\varphi_n^{(i)} = \varphi_{n,A}^{(i)} - \varphi_{n,B}^{(i)} \tag{8.1}$$

where *A* and *B* denote individual optical fibre of the interferometer. *n* denotes the *n*-th sideband. The anti-Stokes lines are indexed by $n>0$, and the Stokes orders $n<0$, $n=0$ for the pump.

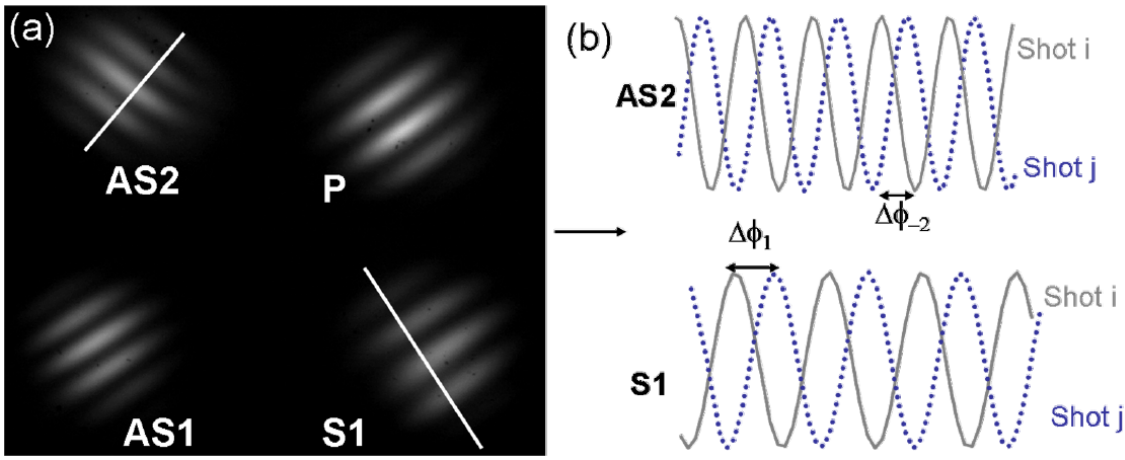

Fig. 8.2 Extraction of phase for different lines on a single shot. (a) is the picture shown on the camera in fig.8.1. It is the interferograms of four different Raman orders (AS2, P, AS1 and S1) in a single frame. (b) is the extraction of the phase difference after drawing a line on (a) and fitting a Gaussian and a sine.

As deduced in chapter 5, the theoretically expected phase between the lines follows the following relationship (Eq. (5.15)):

$$\varphi_n^{(i)} = n\varphi_{QF}^{(i)} + \delta \tag{8.2}$$

where δ is a deterministic phase shift that arises from the pump laser phase noise and any dynamical phase shifts from the amplification process, and *n* is the order of the Raman lines. $\varphi_{QF}^{(i)}$ is determined by the amplification of quantum fluctuations [86], which is constant throughout a single pulse.

Experimentally, the phase of each line cannot be extracted directly from a single comb. However, we can relate the measured phase difference mentioned above (Eq. (8.1)) with Eq. (8.2) by the following:

$$\Delta\varphi_n^{(i)} = n\varphi_{QF,A}^{(i)} + \delta_A - (n\varphi_{QF,B}^{(i)} + \delta_B) \equiv n\Delta\varphi_{QF}^{(i)} + \Delta\delta \tag{8.3}$$

Visioning beam *B* as a reference, $\Delta\varphi_n$ can be regarded as the effective phase for beam *A*.

Furthermore, in order to eliminate the deterministic phase term $\Delta\delta$, which will also remove any slow interferometer drift, we subtract the fringe phases from two successive shots, and define the phase difference $\Delta\phi_n$ (see fig. 8.2b) as the following:

$$\Delta\phi_n \equiv \Delta\varphi_n^{(i+1)} - \Delta\varphi_n^{(i)} = n\Delta\varphi_{QF}^{(i+1)} + \Delta\delta - (n\Delta\varphi_{QF}^{(i)} + \Delta\delta) = n(\Delta\varphi_{QF}^{(i+1)} - \Delta\varphi_{QF}^{(i)}) \tag{8.4}$$

Similarly, for the *m*-th sideband, the phase difference is:

$$\Delta\phi_m \equiv \Delta\varphi_m^{(i+1)} - \Delta\varphi_m^{(i)} = m(\Delta\varphi_{QF}^{(i+1)} - \Delta\varphi_{QF}^{(i)}) \tag{8.5}$$

Combining Eq. (8.4) and (8.5) gives a quantity that should be theoretically nil as long as *m*-th and *n*-th comb lines are totally correlated:

$$\Phi_{nm} = m\Delta\phi_n - n\Delta\phi_m = 0 \tag{8.6}$$

Correlation Coefficient

Experimentally, the measured $\Phi_{n,m}$ should exhibit a Gaussian distribution centred around zero and whose width could be due to either experimental uncertainty or to a possible residual incoherence factor during the comb generation process that the theory [11] didn't account for.

In order to relate this uncertainty in the value $\Phi_{n,m}$ from shot to shot to a phase and intensity correlation between the comb lines we introduce the following correlation

coefficient between the *n*-order Raman field $E_n(L,\tau)=\left|E_n(L,\tau)\right|e^{i\varphi_n}$ with the *m*-order one $E_m(L,\tau)=\left|E_m(L,\tau)\right|e^{i\varphi_m}$ by the following expression:

$$C=\frac{\left|\left\langle\left|E_n^{|m|}(L,\tau)\right|e^{im\varphi_n}\left|E_m^{|n|}(L,\tau)\right|e^{-in\varphi_m}\right\rangle\right|}{\sqrt{\left\langle E_n^{|m|}(L,\tau)E_n^{*|m|}(L,\tau)\right\rangle\left\langle E_m^{|n|}(L,\tau)E_m^{*|n|}(L,\tau)\right\rangle}} \tag{8.7}$$

Writing $I_n=\left\langle E_nE_n^*\right\rangle$ and $I_m=\left\langle E_mE_m^*\right\rangle$, and assuming that the fluctuations in intensities of *n*-th and *m*-th sidebands are independent of that of their phases, the correlation coefficient can be simplified to:

$$C=\frac{\left|\left\langle\left|E_n\right|^{|m|}\left|E_m\right|^{|n|}\right\rangle\right|}{\sqrt{I_n^{|m|}\,I_m^{|n|}}}\left|\left\langle e^{i(m\varphi_n-n\varphi_m)}\right\rangle\right| \tag{8.8}$$

This correlation coefficient consists of two parts: intensity correlation $C_I=(\left|\left\langle\left|E_n^{(-)}\right|^{|m|}\left|E_m^{(-)}\right|^{|n|}\right\rangle\right|/\sqrt{I_n^{|m|}\,I_m^{|n|}})$ and phase correlation $C_\varphi=\left|\left\langle e^{i(m\varphi_n-n\varphi_m)}\right\rangle\right|$. Note that experimentally, φ_n is replaced by $\Delta\phi_n$ (Eq. (8.4)) and therefore the phase correlation can be written as:

$$C_\phi=\left|\left\langle\exp(i(m\Delta\phi_n-n\Delta\phi_m))\right\rangle\right|=\left|\left\langle\exp(i\Phi_{n,m})\right\rangle\right| \tag{8.9}$$

This phase correlation allows the extraction of the underlying phase relationship between any two spectral components. For example, if the temporal phase of one Raman line is statistically independent of another Raman line, the C_ϕ value would be zero. In contrast, if the two Raman components are phase anti-correlated, the value $\Phi_{n,m}$ is zero and the correlation coefficient C_ϕ is equal to one. This means, even though both the two phases from the two Raman beams are fluctuating from shot-to-shot, the phase differences in two Raman lines are fluctuating in the same manner.

Experimental results

Therefore, the plot of the histograms of the variables $\Phi_{n,m}$ over a large number of shots and the average value $C_\Phi = \left|\langle \exp(i\Phi_{n,m}) \rangle\right|$ represent the degree of mutual phase coherence. The simplest case is when n=1 and m=-1. The results of the S1/AS1 pair is shown in fig. 8.3, where 256 shots were taken. The strong peak of the distribution around zero unambiguously indicates the presence of strong phase correlation. The degree of mutual phase coherence $\left|\langle \exp(i\Phi_{1,-1}) \rangle\right|$ was found to be 0.64. This quantity is smaller than the ideal value of 1. This is because when many lines are generated the comb dynamics are more complicated than the idealized model (see section 8.3) accounts for. The source of this spread is beyond the scope of this thesis and will be subject of future work.

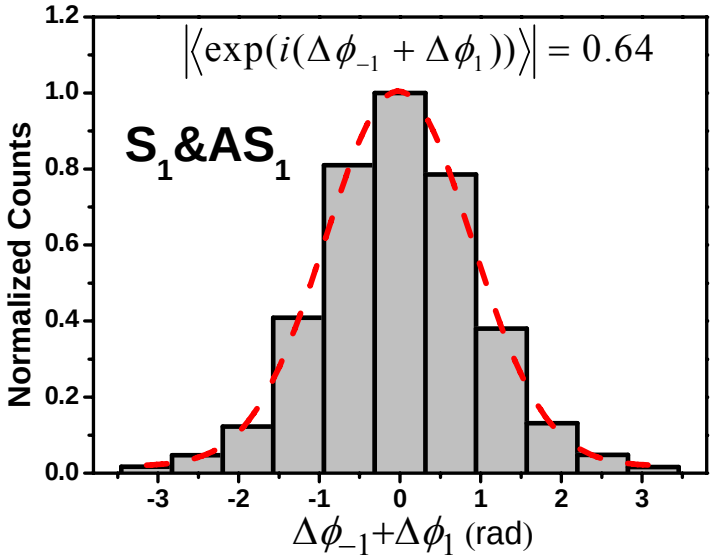

Fig. 8.3. Experimental histogram of phase-difference for AS1 and S1 pair calculated from 256 shots. The correlation coefficient is 0.64.

Furthermore, the mutual coherence is found to be present for any other spectral line pair from a given Raman resonance (not only 1 and -1), as is illustrated by the phase-correlation histograms of the pairs AS1/AS2 with the correlation coefficient $C_\Phi = \left|\langle \exp(i\Phi_{1,2}) \rangle\right| = 0.33$ (fig. 8.4a) and the vibrational AS1/AS2 pair (fig. 8.4c),

$C_{\Phi} = \left|\left\langle \exp(i\Phi_{1,2}) \right\rangle\right| = 0.23$. Even for rotational S1/AS2 pair (fig. 8.4b), with a difference of three Raman orders, the correlation coefficient still shows a relatively strong phase coherence with a phase-correlation factor of 0.35. The experiment shows a trend that the correlation coefficient decreases with increasingly higher order Raman lines. This is reasonable since more uncertainty is added every time a higher order Raman is generated.

This coherence between higher order Raman lines could be explained by the phase modulator picture [65]. During the onset of S1 and AS1, the medium polarization is driven coherently by the S1 and AS1, which in turn, modulates the field at the Raman frequency to generate the higher-order Raman sidebands. The net result is, ideally, a set of mutually phase-locked S/AS spectral components spanning from the UV to the mid-IR. Note that because of the random phase φ_{QF}, for different laser shots, the carrier envelope phase will be undetermined. This has been discussed already in chapter 5 section 5.3.2.

Finally, it is also worth mentioning that for those Raman lines with different resonances (i.e. one vibrational and one rotational), no phase correlation is obtained. The presence of two separate spontaneous seed sources implies that two random phases will enter the problem, compared to one in the pure rotational case. The additional phase is introduced by the zero-point motion of the vibrational degree of freedom. Theoretically this is straightforward to conclude. However, we currently cannot establish whether the presence of two Raman resonances that are simultaneously active has an effect on the mutual coherence degradation for either resonance induced comb. Experimentally, one could suppress the vibrational resonance with a judicious choice of pressure [99].

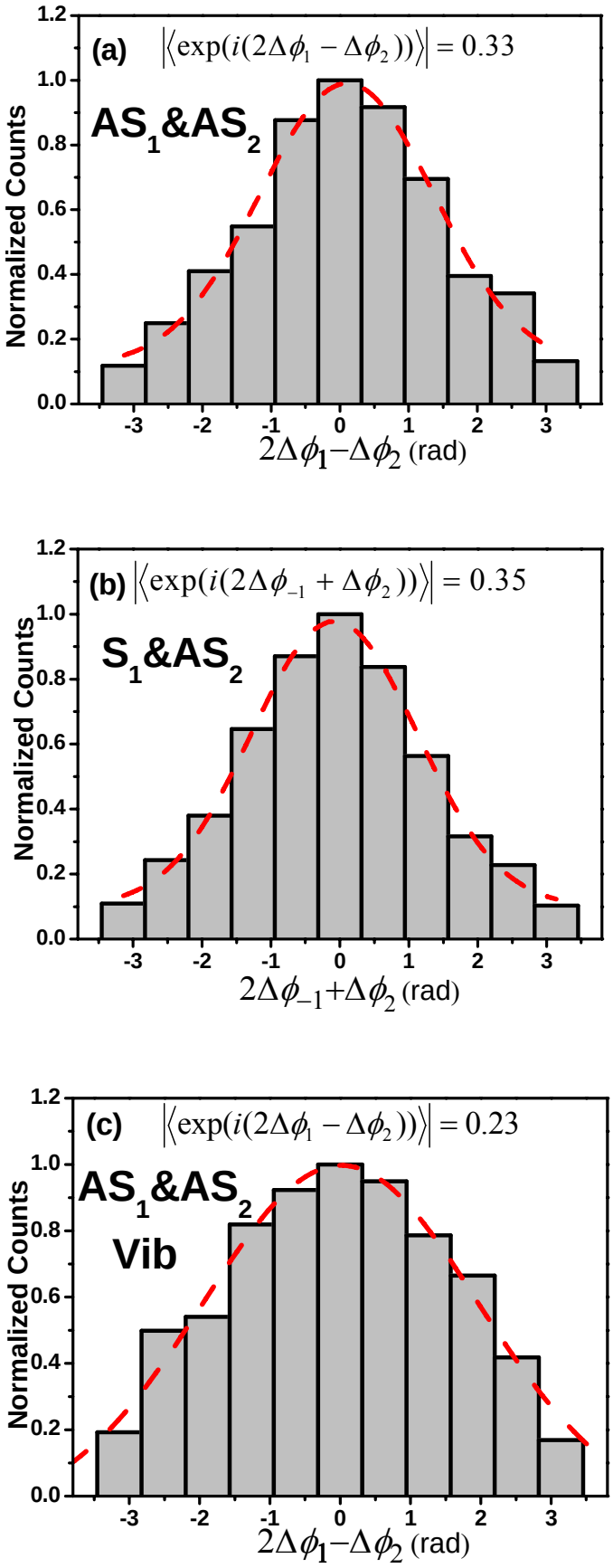

Fig. 8.4. Experimental histogram of phase-difference for different Raman pairs. (a) AS1 and AS2 pair; (b) S1 and AS2 pairs; (c) vibrational AS1 and AS2 pair.

8.3 Theoretical Study of Anti-Correlation for S1 and AS1

We have developed a rigorous quantum propagation theory* [122] based on previous work in [11, 110]. Here we limit the model to the 1st orders only; i.e. only S1 field E_{-1} and AS1 field E_{+1} are created. This is motivated by the need to extract physical insight through some analytical expressions theoretical model can provide. Also, in this model, the pump intensity is undepleted throughout the interaction. This simplified model allows us to find a complete quantum description and gain insight into the comb generation process.

Solution of coupled wave equations

In the high-gain, transient regime we can neglect the Langevin operator and damping [80]. Then the nonlinear coupled equations (5.1) are simplified to:

$$\begin{aligned}
&\partial_z \hat{E}_{-1}^{(-)}(z,\tau) = -i\kappa_{2,s} E_0(\tau)\hat{Q}^{\dagger}(z,\tau) \\
&\partial_z \hat{E}_{+1}^{(+)}(z,\tau) = i\kappa_{2,a} E_0^{*}(\tau)\hat{Q}^{\dagger}(z,\tau)\exp(-i\Delta\beta z) \\
&\partial_\tau \hat{Q}^{\dagger}(z,\tau) = i\kappa_{1,s}\hat{E}_{-1}^{(-)}(z,\tau)E_0^{*}(\tau) + i\kappa_{1,a}\hat{E}_{+1}^{(+)}(z,\tau)E_0(\tau)\exp(i\Delta\beta z)
\end{aligned} \tag{8.10}$$

where $\Delta\beta = \beta_1 + \beta_{-1} - 2\beta_0$ is the wave-vector mismatch. These coupled equations were first solved in a full quantum context by Kilin [110], who verified that a slight phase mismatch is needed to maximize the generation of S/AS sideband generation, as seen in experiments [123]. Here, we use methods in [78] to find a more general solution. Assuming that the pulses are long enough that group-velocity effects are not important, the field operators at the end of the fibre ($z = L$) and at local time τ are found to be:

$$\begin{aligned}
\begin{bmatrix} \hat{E}_{-1}^{(-)}(L,\tau) \\ \hat{E}_{+1}^{(+)}(L,\tau) \end{bmatrix} &= E_0(\tau)\int_0^{\tau} d\tau' E_0(\tau') \begin{bmatrix} \kappa_{2,s}G_{11}(L;\tau,\tau') & \kappa_{2,s}G_{12}(L;\tau,\tau') \\ -\kappa_{2,a}G_{21}(L;\tau,\tau') & -\kappa_{2,a}G_{22}(L;\tau,\tau') \end{bmatrix} \begin{bmatrix} \kappa_{1,s}\hat{E}_{-1}^{(-)}(0,\tau') \\ \kappa_{1,a}\hat{E}_{+1}^{(+)}(0,\tau') \end{bmatrix} \\
&+ E_0(\tau)\int_0^{L} dz' \begin{bmatrix} -i\kappa_{2,s}G_{13}(z';\tau,0) \\ i\kappa_{2,a}G_{23}(z';\tau,0) \end{bmatrix} \hat{Q}^{\dagger}(L-z',0) + \begin{bmatrix} \hat{E}_{-1}^{(-)}(0,\tau) \\ \hat{E}_{+1}^{(+)}(0,\tau)e^{i\Delta\beta L} \end{bmatrix}
\end{aligned} \tag{8.11a}$$

*The theoretical work is carried out by C. Wu and M. G. Raymer from University of Oregon.

$$\hat{Q}^{\dagger}(L,\tau) = i\int_0^{\tau} d\tau' \{\kappa_{1,s} E_0^{*}(\tau') G_{13}(L;\tau,\tau') \hat{E}_{-1}^{(-)}(0,\tau') + \kappa_{1,a} E_0(\tau') G_{13}(L;\tau,\tau') \hat{E}_{+1}^{(+)}(0,\tau')\} + \int_0^{L} dz' G_0(z';\tau,0) \hat{Q}^{\dagger}(L-z',0) \tag{8.11b}$$

where G_{11}, G_{22} ,G_{12} ,G_{13} ,G_{23} ,G_0 are all complex Green's functions:

$$\begin{aligned}
&G_{11}(z;\tau,\tau') = G_{12}(z;\tau,\tau') - i\Delta\beta\int_0^{z} dz' G_{12}(z';\tau,\tau');\\
&G_{22}(z;\tau,\tau') = G_{12}(z;\tau,\tau') + i\Delta\beta \exp(i\Delta\beta z) * G_{12}(z;\tau,\tau');\\
&G_{12}(z;\tau,\tau') = G_{21}(z;\tau,\tau') = I_0(2\sqrt{\xi_s(\tau,\tau')z}) * [J_0(2\sqrt{\xi_a(\tau,\tau')z}) \exp(i\Delta\beta z)];\\
&G_{13}(z;\tau,\tau') = I_0(2\sqrt{\xi_s(\tau,\tau')z}) * [\delta(z) - J_1(2\sqrt{\xi_a(\tau,\tau')z})\sqrt{\xi_a(\tau,\tau')/z} \exp(i\Delta\beta z)];\\
&G_{23}(z;\tau,\tau') = [I_1(2\sqrt{\xi_s(\tau,\tau')z})\sqrt{\xi_s(\tau,\tau')/z} + \delta(z)] * [J_0(2\sqrt{\xi_a(\tau,\tau')z}) \exp(i\Delta\beta z)];\\
&G_0(z;\tau,\tau') = [I_1(2\sqrt{\xi_s(\tau,\tau')z})\sqrt{\xi_s(\tau,\tau')/z} + \delta(z)] * [\delta(z) - J_1(2\sqrt{\xi_a(\tau,\tau')z})\sqrt{\xi_a(\tau,\tau')/z} \exp(i\Delta\beta z)].
\end{aligned} \tag{8.12}$$

where "*" denotes convolution on the variable z, and J_n, I_n are n-th order Bessel and modified Bessel functions, respectively. The time-dependent gain coefficients are:

$$\xi_{(s,a)}(\tau,\tau') = \kappa_{1,(s,a)}\kappa_{2,(s,a)}\int_{\tau'}^{\tau} dt \left|E_0(t)\right|^2 . \tag{8.13}$$

The initial conditions have already been given in Eq. (5.3) [78]:

$$\begin{aligned}
&\left\langle \hat{Q}^{\dagger}(z,0)\hat{Q}(z',0)\right\rangle = (1/AN)\delta(z-z')\\
&\left\langle \hat{Q}(z,0)\hat{Q}^{\dagger}(z',0)\right\rangle = 0\\
&\left\langle \hat{E}_S^{(+)}(0,\tau')\hat{E}_S^{(-)}(0,\tau)\right\rangle = (2\pi\hbar\omega_s/AL)\cdot\delta(\tau-\tau')\\
&\left\langle \hat{E}_S^{(-)}(0,\tau)\hat{E}_S^{(+)}(0,\tau')\right\rangle = 0
\end{aligned} \tag{8.14}$$

Equation (8.11a) represents two types of processes: The second term on the right coupling $\hat{E}_{-1}^{(-)}$ ($\hat{E}_{+1}^{(+)}$) with $\hat{Q}$ represents Stokes (anti-Stokes) scattering from pump via molecular coherence Q. The off-diagonal components in the Green's matrix (first term on the right) coupling $\hat{E}_{-1}^{(-)}$ with $\hat{E}_{+1}^{(+)}$ represent S1/AS1 four-wave mixing, in which two pump photons are annihilated and a S1/AS1 photon pair is created. Both of these processes drive the same collective molecular excitation Q. Under the high-gain transient conditions, the initial white noise is heavily filtered since the gain process is a resonant one, and the Green's propagators grow exponentially as the pulse propagates through the medium. As presented in the modal picture in chapter 7, the filtering or smoothing process eventually produces a S1/AS1 field that are determined solely by a

single spatio-temporal mode each. In this sense, these two fields resemble classical fields, that is, complex temporal envelopes with well defined carrier frequencies, although the intensities and phases of both fields dramatically fluctuate from one shot to another [89, 109, 111].

Theoretical calculation of correlation coefficient

With the solution of electric field in Eq. (8.11) and initial conditions in Eq. (8.14), we calculate the correlation coefficient *C* expressed in Eq. (8.8). In fig. 8.5 we plot *C* values and S1/AS1 intensities as functions of local time τ under the phase mismatch condition $\Delta\beta \times L = 10$, where the anti-Stokes intensity is maximized (see fig. 8.6). In all our calculations in this section we use 12 ns (FWHM) transform-limited Gaussian pump pulses (similar to what is used in the experiment), and the S1/AS 1integrated gain coefficients ($\kappa_{1,s}\kappa_{2,s}\int_{-\infty}^{\infty} dt\left|E_0(t)\right|^2 L$) are set at the values of 25 and 30, respectively.

We see in fig. 8.5 that the value of *C* nearly equals 1 throughout the duration of the generated Stokes pulses. Also note that the peak of the Stokes field is delayed by 6 ns relative to the peak of pump field, which is consistent with previously known results [80]. In fig. 8.6 we show the calculated *C* value at the peak of the Stokes-pulse intensity under various dispersion conditions, and find that its value stays close to 1. There we also show the peak S1/AS1 pulse intensities versus phase mismatch, showing the well-known minimum that occurs for perfect phase matching [110, 123].

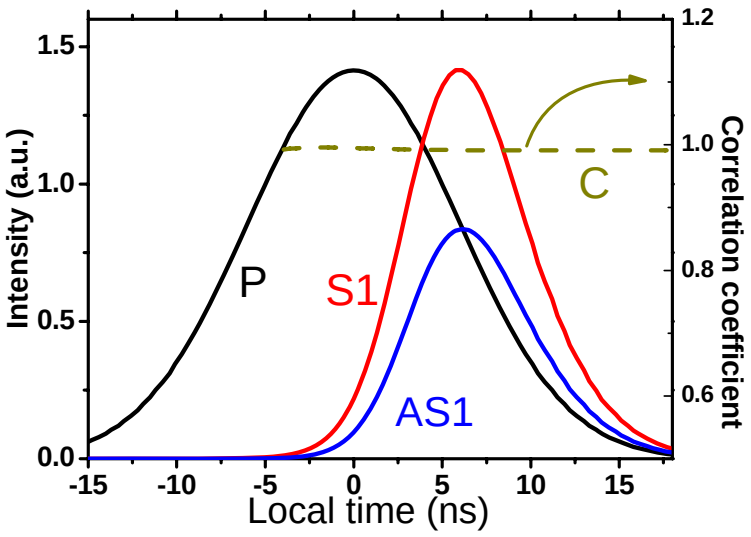

Fig. 8.5 Pump and S1/AS1 intensities, and their anti-correlation C as functions of local time. Note that S1/AS1 are scaled differently.

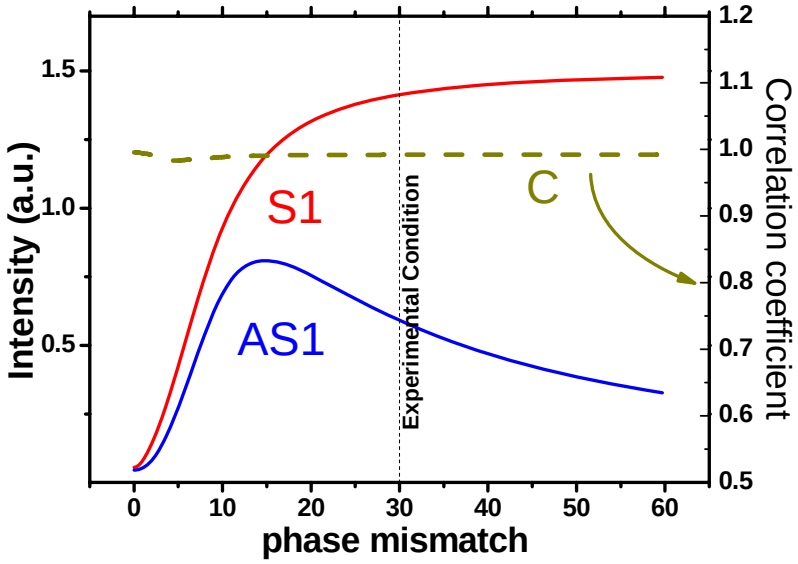

Fig. 8.6 S1/AS1 intensities, and their anti-correlation C as functions of phase mismatch. S1/AS1 are scaled differently and the scaling is also different from fig. 8.5.

The result $C \approx 1$ implies that the S1/AS1 are correlated in the following way:

$$E_{-1}^{(-)} \approx \alpha\, E_{+1}^{(+)} \tag{8.15}$$

where α is a complex constant (with magnitude less than unity). This relation shows that both the intensities and the phases of the two sidebands fluctuate in the same

manner from pulse to pulse. This confirms one of our conjectures in [11]. It indicates a tendency in this system to automatically evolve towards perfect phase anti-correlation.

In our experimental observations (section 8.2), the anti-correlation is not perfect and the *C* value for the S1/AS1 pair is 0.64. A more rigorous model including all comb lines and pump depletion is needed for explaining this discrepancy. It is noteworthy that the difference in C_{Φ} between different pairs cannot be accounted for with our simple theoretical model. One could speculate on this difference by a number of experimental environments like fibre dispersion, fibre multimode, thermal noise and fundamental to the cascade process.

8.4 Intensity correlation and speculations

As shown in the theoretical prediction, not only the phase of the two comb lines is correlated, but also the amplitude (Eq. (8.15)). This can be expressed by their intensity correlation:

$$C_I = (\left\langle \left| E_n^{(-)} \right|^{|m|} \left| E_m^{(-)} \right|^{|n|} \right\rangle / \sqrt{I_n{}^{|m|}\, I_m{}^{|n|}}) \tag{8.16}$$

To experimentally calculate the intensity correlations, we block one arm of the interferometer in fig. 7.2, leaving the other arm open. The intensity correlation can be obtained from the output pattern of the Raman comb from one arm. The output is show in fig. 8.7. With similar methods as described above, the relative intensity can be obtained for the successive 256 shots. The intensity correlation of the AS1 and S1 pair is shown in fig. 8.8a by plotting the normalized intensity of S1 versus AS1 on each CCD frame. One can see that although the normalized intensities fluctuate from shot to shot, the pair follows with a linear fit, i.e. they increase and decrease together. This corresponds to a very high correlation of C_I=0.99. This is in agreement with the above quantum theoretical model which shows that under our experimental conditions the growth of S1 and AS1 takes place simultaneously. For other Raman pairs for example the AS2 and S1 pair (fig8.7b), the intensity correlation is calculated to be C_I=0.95.

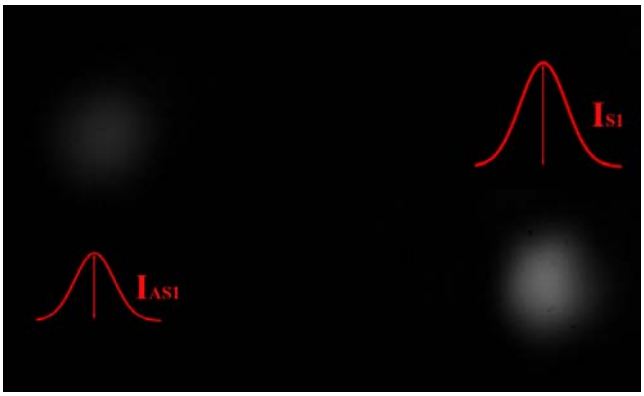

Fig. 8.7 Mode pattern of AS1 and S1 shown on the same CCD frame.

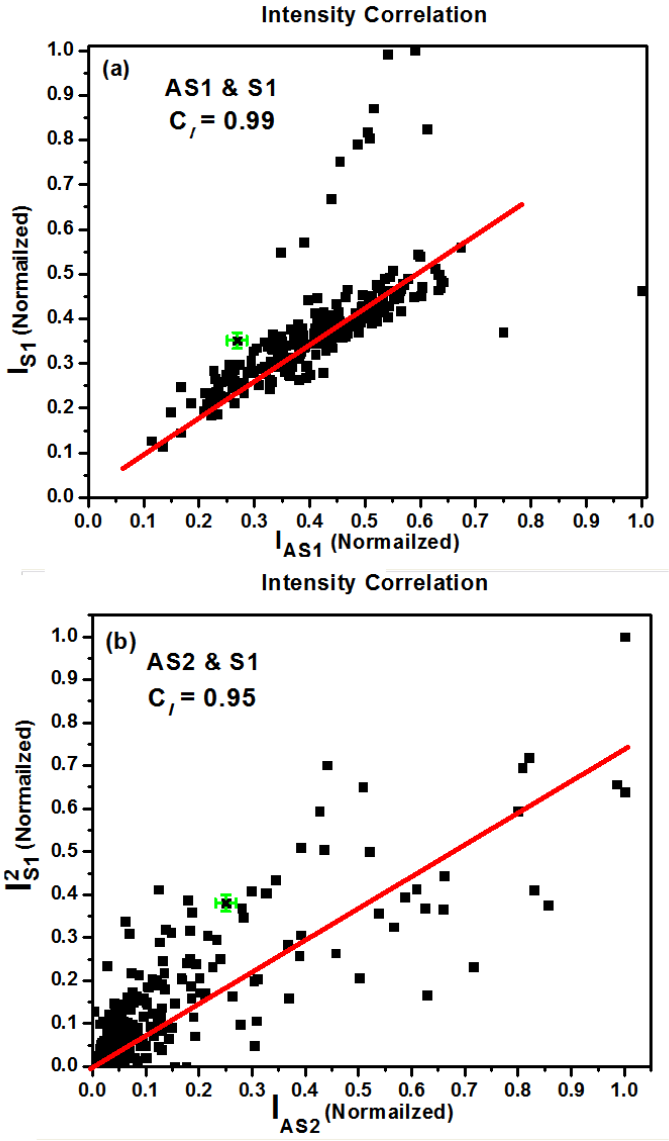

Fig. 8.8 Intensity correlations between different line pairs. Each point represents the normalized intensity of a pair on a single shot. (a) normalized intensity of AS1 vs S1; (b) normalized intensity of AS2 vs $(S1)^2$. The green symbol is the error bar.

Moreover, it is found that by measuring the visibility of different Raman lines on the same shots (fig. 8.9), they also show correlations. For example, for the AS1 and S1 pair the visibility also follows a linear fit. As the visibility is influenced by the intensity ratio between two output beams, this means the inter-beam intensity ratios for AS1 and S1 are the same in every shot.

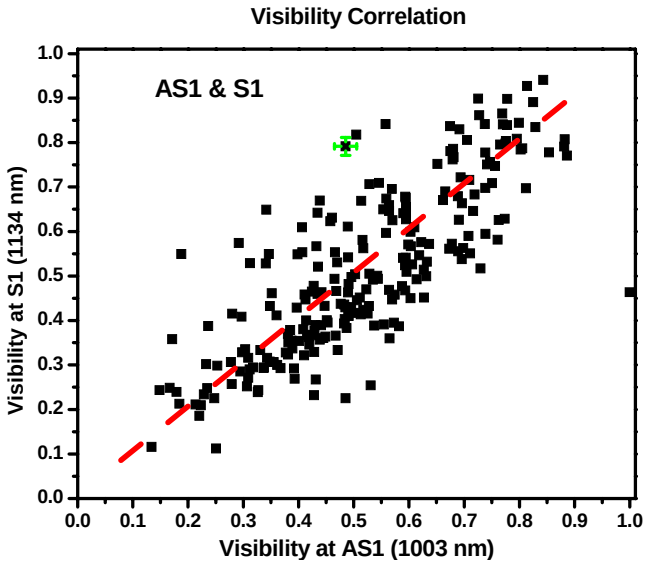

Fig. 8.9 Visibility relations between AS1/S1. Each point represents the visibility of a pair on a single shot. The green symbol is the error bar.

8.5 Note on the nature of the amplified S1/AS1

All the above work shows that complementary to earlier experiments where the 1st Stokes field was observed on its own to have thermal-like statistics [124], here we show that the growth of one Stokes line (eg. S1) is accompanied in a correlated manner with the growth of another (eg. AS1). That is, their thermal statistics follow the same trend. Such correlations would not be present in a truly thermal source; instead this shows that the S1 and AS1 vacuum fields are in fact a two-mode squeezed state [107, 125].

Furthermore, because the S1/AS1 pair acts as a pump to generate the comb through the parametric process of phase modulation, all the higher-order components should be correlated in a manner similar to the correlation of S1/AS1. Consequently, the presence of mode correlations in the absence of dephasing implies the existence of quantum entanglement among all modes. This indicates the intriguing possibility of an

optical comb spectrum with non-classical correlations (entanglement) between the amplitudes and phases of all comb lines. Ultimately, the present results set the scene for the creation of trains of isolated attosecond pulses with non-classical properties. One can speculate about achieving increased temporal resolution (at least in the sense of time differences) as a consequence of the quantum correlations in the spectrum of such pulses.

8.6 Summary

The work in chapters 7 and 8 has shown for the first time that an ultra-wide optical frequency comb can be spontaneously created containing a high degree of quantum coherence among all comb lines, without introducing any macroscopic coherence into the system from external sources. This contrasts with other demonstrations using multiple-frequency coherent laser pulses to externally "seed" the desired coherence [66, 90, 91], and with the indirect S1/AS1 phase-correlation in an experiment of Raman pulse-compression [126]. This opens the possibility to explore generating isolated pulses in the attosecond regime with non-classical properties such as reduced noise via quantum-state squeezing.

Chapter 9

Summary and Future Work

9.1 Summary

In conclusion we reported on different experimental works that show a potential route for the development of a compact and versatile optical waveform synthesiser based on the use of HC-PCF.

On the fibre design and fabrication, chapter 2 reported on how one could suppress the surface modes of PBG HC-PCF by chemical etching. This gives insights into modal properties inside the photonic bandgap and serves as a reference tool for future design of HC-PCF. In chapter 3, we reported on how one could have incremental increase in optical bandwidth of PBG HC-PCF by fabrication of double PBG HC-PCF. Toward the aim of finding out the best trade-off in wide optical bandwidth and lower transmission loss, the development of hypocycloid core Kagome fibre is reported in chapter 4. The fibre exhibits more than two times wider bandwidth than the PBG HC-PCF while sharing similar loss figures. Thus, the advantages of using PBG HC-PCF are now not as obvious as before, but they are still desirable when small core size is required or single mode propagation is preferred. Based on the above available fibres, we can conclude that for applications such as the generation of multi-octave coherent Raman comb, which require high power transportation, low dispersion and wide transmission bandwidth, the 7-cell hypocycloid core Kagome fibre or the 1-cell Kagome one are suggested. Together, these novel fibres presented in part 1 meet the ever increasing demand for high quality fibres.

On the Raman comb generation, two applications of HC-PCF have been presented in part 2. They are both based on the Raman frequency comb generation in H_2. The compact multiline Raman laser system in chapter 6 is a competitive candidate as a compact laser source for forensics and biomedicine. Chapter 7 and 8 reported on fundamental properties of the comb spectral components. Surprisingly, we have experimentally demonstrated that a vacuum-fluctuation initiated Raman frequency comb can exhibit strong self- and mutual- coherence. This opens the possibility of generating attosecond pulses and optical waveform synthesis. Furthermore, the quantum nature of the comb generation onset indicates that the formed pulses might exhibit non-classical features.

9.2 Future Work

It is noteworthy that the work which has been reported here could be improved or followed on. Firstly, the design and fabrication of tailored fibres for specific applications are always a continuous challenge; however the results obtained here represent significant milestones in future development. Secondly, the seminal nature of the work on the coherence of the Raman comb requires extensive theoretical and experimental future work. Below, we cite some of the points which could be perfected or need further investigation.

Double bandgap fibre fabrication

The fabrication of double bandgap fibre with a fundamental band centred at 1550 nm and a second order band at 1064 nm has opened up the simultaneous use of Er-doped lasers with Nd:YAG lasers inside one single hollow-core fibre. Shifting the two bands to 1064 nm and 780 nm or 780 nm and 633 nm would be desirable for dual use of Nd:YAG lasers and Ti:Sapphire lasers or Ti:Sapphire lasers and HeNe lasers. The current challenges are now in extending this fabrication technique to shorter wavelength and in reducing the effect of surface mode by independently controlling the core-surround shape and thickness.

Hypocycloid core Kagome fibre fabrication

The current fabrication of hypocycloid core Kagome fibre has achieved ultra-low loss of 40 dB/km with broadband guidance from 1100 nm to >1750 nm (limit of OSA) or 200 dB/km from 830 nm to 1350 nm. While further reducing the loss is conceivable, shifting the transmission to shorter wavelength is hard due to the deformation of the core structure when reducing the size of the structure. Future work would include improving fabrication techniques so to maintain the structure integrity for smaller pitches whilst keeping the aspect ratio between the pitch and the silica strut thickness. A future theoretical work is also required in elucidating the respective role of inhibited coupling guidance and anti-resonance guidance. This might explain the Kagome fibre bending loss spectrum and its observed sensitivity to cladding ring number. Finally, a further route of interest is the investigation of other cladding structure than that of Kagome (e.g. square lattice).

On the other hand, optical fibre for mid-IR guidance still suffers high loss due to silica absorption. Kagome fibre is believed to be a very strong competitor for this region since it guides in the hollow core and has little spatial overlap with silica (compared to PBG fibre which has a strong overlap with the surface). Current 1-cell Kagome fibre has a measured loss of 20 dB/m at 3 μm [127]. Since the hypocycloid core Kagome fibre allows even less overlap with the silica, shifting the current hypocycloid core Kagome fibre to the mid-IR region may make a good mid-IR waveguide. Furthermore no deformation of the core structure will be involved when making the structure large. Cooperation with those groups demanding 3 μm fibre is in progress.

Photon statistics of Raman frequency comb generated in H_2 filled HC-PCF

Fruitful results on the coherence properties of our Raman frequency comb has been achieved but needs further investigation since the current work shows that the dynamics of the coherence is richer and complex. For example, the visibility evolution with different power and pressure shows intriguing results and improvement in both the self-coherence and mutual-coherence are possible for future applications in attoscience and optical waveform synthesis. However, for this to materialize, a

thorough theoretical investigation that takes into account of all the relevant parameters is necessary. Furthermore, in order to corroborate the entanglement between the S/AS, a more judicious experimental set-up is required with better detection systems eg. a single photon detector and a HC-PCF with little phase-inducing noise such birefringence or a proper single mode operation.

Molecular coherence lifetime in HC-PCF

Apart from the self and mutual coherence demonstrated in chapter 7 and 8, another important aspect is the coherence lifetime, that is, how long the coherence lasts. It was previously reported that the molecular coherence lifetime can last for as long as 9 times the dephasing time [71]. Our initial results [128] have shown that in HC-PCF, 42 times the dephasing time is possible. The setup includes a strong pump pulse to excite the molecular coherence followed by a delayed weak probe pulse to measure the coherence time. However, a lot of unexpected phenomena have been observed but have not been properly explained yet. For example, the rate of the decay of coherence is much slower than the expected value, which is the molecular dephasing rate. In particular, at short delay time, the coherence is even weaker than at some longer delay time [129]. Further studies determined that this is due to the strong (not weak enough) probe injected that triggers Raman process by itself which makes the dynamics complicated. Some theoretical calculations have explained this but further studies are needed to gain a clear picture. Also, when injecting the pump and the probe from opposite positions (from two ends of the fibre), when they meet inside the HC-PCF, some surprising phenomena were found.

This future work would undoubtedly improve our understanding of the SRS and the molecular dynamics in confined geometries such that of HC-PCF.

References

1. E. Yablonovitch, *Inhibited Spontaneous Emission in Solid-State Physics and Electronics.* Physical Review Letters, 1987. **58**(20): p. 2059-2062.
2. S. John, *Strong Localization of Photons in Certain Disordered Dielectric Superlattices.* Physical Review Letters, 1987. **58**(23): p. 2486-2489.
3. P. S. J. Russell, *private papers.* 1991.
4. P. S. J. Russell, *Photonic crystal fibers.* Science, 2003. **299**(5605): p. 358-362.
5. T. A. Birks, *et al.*, *Full 2-D Photonic Bandgaps in Silica/Air Structures.* Electronics Letters, 1995. **31**(22): p. 1941-1943.
6. R. F. Cregan, *et al.*, *Single-mode photonic band gap guidance of light in air.* Science, 1999. **285**(5433): p. 1537-1539.
7. P. J. Roberts, *et al.*, *Ultimate low loss of hollow-core photonic crystal fibres.* Optics Express, 2005. **13**(1): p. 236-244.
8. F. Benabid, *et al.*, *Stimulated Raman scattering in hydrogen-filled hollow-core photonic crystal fiber.* Science, 2002. **298**(5592): p. 399-402.
9. F. Couny, F. Benabid, and P. S. Light, *Large-pitch kagome-structured hollow-core photonic crystal fiber.* Optics Letters, 2006. **31**(24): p. 3574-3576.
10. F. Couny, *et al.*, *Square-lattice large-pitch hollow-core photonic crystal fiber.* Optics Express, 2008. **16**(25): p. 20626-20636.
11. F. Couny, *et al.*, *Generation and photonic guidance of multi-octave optical-frequency combs.* Science, 2007. **318**: p. 1118-1121.
12. A. Argyros and J. Pla, *Hollow-core polymer fibres with a kagome lattice: potential for transmission in the infrared.* Optics Express, 2007. **15**(12): p. 7713-7719.
13. G. J. Pearce, *et al.*, *Models for guidance in kagome-structured hollow-core photonic crystal fibres.* Opt. Express, 2007. **15**(20): p. 12680-12685.
14. D. G. Ouzounov, *et al.*, *Generation of megawatt optical solitons in hollow-core photonic band-gap fibers.* Science, 2003. **301**(5640): p. 1702-1704.
15. C. J. S. de Matos, *et al.*, *All-fiber format compression of frequency chirped pulses in air-guiding photonic crystal fibers.* Physical Review Letters, 2004. **93**(10): p. 103901-103904.
16. S. Ghosh, *et al.*, *Resonant optical interactions with molecules confined in photonic band-gap fibers.* Physical Review Letters, 2005. **94**(9). p 093902.
17. F. Benabid, *et al.*, *Electromagnetically-induced transparency grid in acetylene-filled hollow-core PCF.* Optics Express, 2005. **13**(15): p. 5694-5703.
18. F. Luan, *et al.*, *All-solid photonic bandgap fiber.* Optics Letters, 2004. **29**(20): p. 2369-2371.

19. F. Benabid, *Hollow-core photonic bandgap fibre: new light guidance for new science and technology.* Philosophical Transactions of the Royal Society a-Mathematical Physical and Engineering Sciences, 2006. **364**(1849): p. 3439-3462.

20. T. Grujic, *et al.*, *Solid-core fiber with ultra-wide bandwidth transmission window due toinhibited coupling.* Opt. Express, 2010. **18**(25): p. 25556-25566.

21. J. D. Joannopoulos, *Photonic crystals : modeling the flow of light*. 2nd ed. 2008, Princeton: Princeton University Press.

22. N. W. Ashcroft and N. D. Mermin, *Solid state physics*. 1976, Holt, Rinehart and Winston, New York, p 826.

23. F. Couny, *et al.*, *Identification of Bloch-modes in hollow-core photonic crystal fiber cladding.* Optics Express, 2007. **15**(2): p. 325-338.

24. F. Benabid, and P. J. Roberts, *Linear and nonlinear optical properties of hollow core photonic crystal fiber.* Journal of Modern Optics, 2011. **58**(2): p. 87-124.

25. A. W. Snyder, and X. H. Zheng, *Optical Fibers of Arbitrary Cross-Sections.* Journal of the Optical Society of America a-Optics Image Science and Vision, 1986. **3**(5): p. 600-609.

26. N. W. Ashcroft and N. D. Mermin., *solid state physics*, Saunders College, Philadelphia, PA19105, 1976.

27. T. A. Birks, G. J. Pearce, and D. M. Bird, *Approximate band structure calculation for photonic bandgap fibres.* Optics Express, 2006. **14**(20): p. 9483-9490.

28. P. Yeh and A. Yariv, *Bragg Reflection Waveguides.* Optics Communications, 1976. **19**(3): p. 427-430.

29. P. Yeh, A. Yariv, and E. Marom, *Theory of Bragg Fiber.* Journal of the Optical Society of America, 1978. **68**(9): p. 1196-1201.

30. N. M. Litchinitser, *et al.*, *Antiresonant reflecting photonic crystal optical waveguides.* Optics Letters, 2002. **27**(18): p. 1592-1594.

31. S. G. Johnson and J. D. Joannopoulos, *Block-iterative frequency-domain methods for Maxwell's equations in a planewave basis.* Optics Express, 2001. **8**(3): p. 173-190.

32. P. S. Light, *et al.*, *Double photonic bandgap hollow-core photonic crystal fiber.* Optics Express, 2009. **17**(18): p. 16238-16243.

33. S. Schiller and R. L. Byer, *High-resolution spectroscopy of whispering gallery modes in large dielectric spheres.* Opt. Lett., 1991. **16**(15): p. 1138-1140.

34. H. Kogelnik, *Theory of optical waveguides*, in *Guided-wave optoelctronics*, T. Tamir, Editor. 1988, Springer-Verlag: Berlin.

35. V. Dangui, M. J. F. Digonnet and G.S. Kino, *Determination of the mode reflection coefficient in air-core photonic bandgap fibers.* Optics Express, 2007. **15**(9): p. 5342-5359.

36. P. S. Light, F. Couny and F. Benabid, *Low optical insertion-loss and vacuum-pressure all-fiber acetylene cell based on hollow-core photonic crystal fiber.* Optics Letters, 2006. **31**(17): p. 2538-2540.

37. N. V. Wheeler, *et al.*, *Large-core acetylene-filled photonic microcells made by tapering a hollow-core photonic crystal fiber.* Optics Letters, 2010. **35**(11): p. 1875-1877.

38. C. V. Raman and K. S. Krishnan. *A New Type of Secondary Radiation.* Nature, 1928. **121**(3048): p. 501.

39. Y. R. Shen and N. Bloember. *Theory of Stimulated Brillouin and Raman Scattering*. Physical Review, 1965. **1**(6A): p. 1787.

40. F. Benabid *et al.*, *Ultrahigh efficiency laser wavelength conversion in a gas-filled hollow core photonic crystal fiber by pure stimulated rotational Raman scattering in molecular hydrogen.* Physical Review Letters, 2004. **93**(12): p. 123903.

41. F. Benabid *et al.*, *Stokes amplification regimes in quasi-cw pumped hydrogen-filled hollow-core photonic crystal fiber.* Physical Review Letters, 2005. **95**(21): p. 213903.

42. F. Couny, F. Benabid and P. S. Light, *Subwatt threshold cw raman fiber-gas laser based on H-2-filled hollow-core photonic crystal fiber.* Physical Review Letters, 2007. **99**. p.143903.

43. H. Kawano, Y. Hirakawa, and T. Imasaka, *Generation of high-order rotational lines in hydrogen by four-wave Raman mixing in the femtosecond regime.* Ieee Journal of Quantum Electronics, 1998. **34**(2): p. 260-268.

44. F. Benabid, *hollow-core photonic bandgap fibres: new guidance for new science and technology.* Philosophical Transactions of the Royal Society A, 2006. **364**: p. 3439-3462.

45. J. A. West, *et al.*, *Surface modes in air-core photonic band-gap fibers.* Optics Express, 2004. **12**(8): p. 1485-1496.

46. C. M. Smith, *et al.*, *Low-loss hollow-core silica/air photonic bandgap fibre.* Nature, 2003. **424**(6949): p. 657-659.

47. F. Benabid, *et al.*, *Compact, stable and efficient all-fibre gas cells using hollow-core photonic crystal fibres.* Nature, 2005. **434**(7032): p. 488-491.

48. F. Couny, F. Benabid, and P. S. Light, *Reduction of fresnel back-reflection at splice interface between hollow core PCF and single-mode fiber.* IEEE Photonics Technology Letters, 2007. **19**(13-16): p. 1020-1022.

49. J. D. Joannopoulos, *Photonic crystals : molding the flow of light*. 2nd ed. 2008, Princeton: Princeton University Press. xiv, 286 p.61

50. F. Benabid, and P. S. J. Russell, *Hollow-core photonic crystal fiber: New regime for nonlinear optics.* Icton 2004: 6th International Conference on Transparent Optical Networks, Proceedings, Vol 2, 2004: p. 84-90

51. J. D. Joannopoulos, *Photonic crystals : modeling the flow of light*. 2nd ed. 2008, Princeton: Princeton University Press. xiv, 286 p.176.

52. R. Amezcua-Correa, *et al.*, *Optimizing the usable bandwidth and loss through core design in realistic hollow-core photonic bandgap fibers.* Optics Express, 2006. **14**(17): p. 7974-7985.

53. R. Amezcua-Correa, *et al.*, *Control of surface modes in low loss hollow-core photonic bandgap fibers.* Optics Express, 2008. **16**(2): p. 1142-1149.

54. *A complete range of useful thermal oxide etching rates.* Technical Data: Boe® Buffered Oxide Etchants, General Chemical, 2000.

55. H. H. Cui, Z. H. Silber-Li, and S. N. Zhu, *Flow characteristics of liquids in microtubes driven by a high pressure.* Physics of Fluids, 2004. **16**(5): p. 1803-1810.

56. H. Kikyuama, *et al.*, *Principles of wet chemical-processing in ulsi microfabrication*. IEEE Transactions on Semiconductor Manufacturing, 1991. **4**(1): p. 26-35.

57. B. J. Mangan, J. K. Lyngso, and P. J. Roberts, *Realization of low loss and polarization maintaining hollow core photonic crystal fibers.* 2008 Conference on Lasers and Electro-Optics & Quantum Electronics and Laser Science Conference, Vols 1-9, 2008: p. 2016-2017.

58. Y. Y. Wang, P. S. Light and F. Benabid, *Core-surround shaping of hollow-core photonic crystal fiber via HF etching.* IEEE Photonics Technology Letters, 2008. **20**(9-12): p. 1018-1020.

59. F. Poletti and D. J. Richardson, *Hollow-core photonic bandgap fibers based on a square lattice cladding.* Optics Letters, 2007. **32**(16): p. 2282-2284.

60. J. C. Knight, *et al.*, *All-silica single-mode optical fiber with photonic crystal cladding.* Optics Letters, 1996. **21**(19): p. 1547-1549.

61. T. A. Birks, *et al.*, *The Fundamental Limits to the Attenuation of Hollow-Core Photonic Crystal Fibres.* Icton 2005: 7th International Conference on Transparent Optical Networks, Proceedings, 2005: p. Mo.B2.1.

62. L. G. Cohen, *Comparison of Single-Mode Fiber Dispersion Measurement Techniques.* Journal of Lightwave Technology, 1985. **3**(5): p. 958-966.

63. E. J. Woodbury and W. K. Ng, *Ruby Laser Operation in near IR.* Proceedings of the Institute of Radio Engineers, 1962. **50**(11): p. 2367.

64. E. Garmire, C. H. Townes and F. Pandarese, *Coherently Driven Molecular Vibrations and Light Modulation.* Physical Review Letters, 1963. **11**(4): p. 160.

65. S. E. Harris and A.V. Sokolov, *Subfemtosecond pulse generation by molecular modulation.* Physical Review Letters, 1998. **81**(14): p. 2894-2897.

66. A. V. Sokolov, *et al.*, *Generation and control of femtosecond pulses by molecular modulation.* Journal of Modern Optics, 2005. **52**(2-3): p. 285-304.

67. F. L. Kien, *et al.*, *Subfemtosecond pulse generation with molecular coherence control in stimulated Raman scattering.* Physical Review A, 1999. **60**(2): p. 1562-1571.

68. A. Nazarkin, *et al*., *Generation of multiple phase-locked Stokes and anti-Stokes components in an impulsively excited Raman medium.* Physical Review Letters, 1999. **83**(13): p. 2560-2563.

69. P. J. Bustard, B. J. Sussman and I. A. Walmsley, *Amplification of Impulsively Excited Molecular Rotational Coherence.* Physical Review Letters, 2010. **104**(19): p. 193902.

70. N. Zhavoronkov and G. Korn, *Generation of single intense short optical pulses by ultrafast molecular phase modulation.* Physical Review Letters, 2002. **88**(20): p. 203901.

71. D. T. Smithey, *et al*., *Near Quantum-Limited Phase Memory in a Raman Amplifier.* Physical Review Letters, 1991. **67**(18): p. 2446-2449.

72. H. Kawano, Y. Hirakawa and T. Imasaka, *Generation of more than 40 rotational Raman lines by picosecond and femtosecond Ti:Sapphire laser for Fourier synthesis.* Applied Physics B-Lasers and Optics, 1997. **65**(1): p. 1-4.

73. E. Sali, *et al*., *High-order stimulated Raman scattering in a highly transient regime driven by a pair of ultrashort pulses.* Optics Letters, 2004. **29**(5): p. 495-497.

74. R. Loudon, , *The quantum theory of light*. 1973, Oxford,: Clarendon Press. xii, p.338

75. J. J. Wynne and P. P. Sorokin, *Optical mixing in atomic vapors.* in nonlinear infared generation. Topics in applied physics v 16, edited by Y.R.Shen. 1977, Berlin ; New York: Springer-Verlag. p.159-195

76. J. Eggleston and R. L. Byer, *Steady-State Stimulated Raman-Scattering by a Multimode Laser.* IEEE Journal of Quantum Electronics, 1980. **16**(8): p. 850-853.

77. R. L. Carman, *et al*., *Theory of Stokes Pulse Shapes in Transient Stimulated Raman Scattering.* Physical Review A, 1970. **2**(1): p. 60-72.

78. M. G. Raymer, and J. Mostowski, *Stimulated Raman-Scattering - Unified Treatment of Spontaneous Initiation and Spatial Propagation.* Physical Review A, 1981. **24**(4): p. 1980-1993.

79. J. Mostowski and M.G. Raymer, *The Buildup of Stimulated Raman-Scattering from Spontaneous Raman-Scattering.* Optics Communications, 1981. **36**(3): p. 237-240.

80. M. G. Raymer, and I. A. Walmsley, *The Quantum Coherence Properties of Stimulated Raman-Scattering.* Progress in Optics, 1990. **28**: p. 181-270.

81. M. G. Raymer, *et al*., *Quantum-Theory of Spatial and Temporal Coherence Properties of Stimulated Raman-Scattering.* Physical Review A, 1985. **32**(1): p. 332-344.

82. F. Couny and F. Benabid, *Optical frequency comb generation in gas-filled hollow core photonic crystal fibres.* Journal of Optics a-Pure and Applied Optics, 2009. **11**(10): p.103002

83. R. J. Heeman and H. P. Godfried, *Gain Reduction Measurements in Transient Stimulated Raman-Scattering.* IEEE Journal of Quantum Electronics, 1995. **31**(2): p. 358-364.

84. L. S. Meng, P. A. Roos and J. L. Carlsten, *Continuous-wave rotational Raman laser in H_2.* Optics Letters, 2002. **27**(14): p. 1226-1228.

85. J. R. Ackerhalt and P. W. Milonni, *Solitons and 4-Wave-Mixing.* Physical Review A, 1986. **33**(5): p. 3185-3198.

86. D. T. Smithey, *et al.*, *Near Quantum Limited Phase Memory in a Raman Amplifier.* Physical Review Letters, 1991. **67**: p. 2446.

87. M. Belsley, *et al.*, *Observation of Extreme Sensitivity to Induced Molecular Coherence in Stimulated Raman-Scattering.* Physical Review A, 1993. **48**(2): p. 1514-1525.

88. Z. M. Hsieh, *et al.*, *Controlling the Carrier-Envelope Phase of Raman-Generated Periodic Waveforms.* Physical Review Letters, 2009. **102**(21): p. 213902

89. I. A. Walmsley and M. G. Raymer, *Observation of Macroscopic Quantum Fluctuations in Stimulated Raman-Scattering.* Physical Review Letters, 1983. **50**(13): p. 962-965.

90. M. Y. Shverdin, *et al.*, *Generation of a single-cycle optical pulse.* Physical Review Letters, 2005. **94**(3): p. 033904.

91. E. Goulielmakis, *et al.*, *Single-cycle nonlinear optics.* Science, 2008. **320**(5883): p. 1614-1617.

92. O. Pfister, *et al.*, *Multipartite continuous-variable entanglement from concurrent nonlinearities.* Physical Review A, 2004. **70**(2): p. 020302.

93. J. Jing, *et al.*, *Experimental continuous-variable entanglement from a phase-difference-locked optical parametric oscillator.* Physical Review A, 2006. **74**(4): p. 041804.

94. *http://www.leukos-systems.com/IMG/pdf/LEUKOS-SPuv-2.pdf.*

95. N. Panchuk-Voloshina, *et al.*, *Alexa dyes, a series of new fluorescent dyes that yield exceptionally bright, photostable conjugates.* Journal of Histochemistry & Cytochemistry, 1999. **47**(9): p. 1179-1188.

96. F. Benabid, *et al.*, *Light and gas confinement in hollow-core photonic crystal fibre based photonic microcells.* Journal of the European Optical Society-Rapid Publications, 2009. **4**.: p.09004.

97. P. H. Pioger, *et al.*, *High spectral power density supercontinuum generation in a nonlinear fiber amplifier.* Optics Express, 2007. **15**(18): p. 11358-11363.

98. J. C. Travers, S. V. Popov and J. R. Taylor, *Extended blue supercontinuum generation in cascaded holey fibers.* Optics Letters, 2005. **30**(23): p. 3132-3134.

99. F. Couny, O. Carraz and F. Benabid, *Control of transient regime of stimulated Raman scattering using hollow-core PCF.* Journal of the Optical Society of America B-Optical Physics, 2009. **26**(6): p. 1209-1215.

100. K. D. Truong, *et al.*, *Raman-Active Intramolecular Ch2 and C=C Vibrations and Microwave Surface Impedance Studies of the Organic Superconductor Kappa.* Physical Review B, 1995. **51**(22): p. 16168-16173.

101. S. Yiou, *et al.*, *Stimulated Raman scattering in an ethanol core microstructured optical fiber.* Optics Express, 2005. **13**(12): p. 4786-4791.

102. S. Lebrun, *et al.*, *High-efficiency single-mode Raman generation in a liquid-filled photonic bandgap fiber.* Optics Letters, 2007. **32**(4): p. 337-339.

103. G. Antonopoulos, *et al.*, *Experimental demonstration of the frequency shift of bandgaps in photonic crystal fibers due to refractive index scaling.* Optics Express, 2006. **14**: p. 3000-3006.

104. *http://en.wikipedia.org/wiki/Near_infrared_spectroscopy*.

105. S. Haroche, and J. M. Raimond, *Exploring the Quantum, Atoms, Cavities, and Photons* 2006, Oxford: Oxfors University Press.

106. C. K. Hong, Z. Y. Ou and L. Mandel, *Measurement of subpicosecond time intervals between two photons by interference.* Physical Review Letters, 1987. **59**(18): p. 2044.

107. A. Zeilinger, *et al.*, *Happy centenary, photon.* Nature, 2007. **446**(7133): p. 342-342.

108. M. Hentschel, *et al.*, *Attosecond metrology.* Nature, 2001. **414**: p. 509-513.

109. S. J. Kuo, D. T. Smithey and M. G. Raymer, *Spatial Interference of Macroscopic Light Fields from Independent Raman Sources.* Physical Review A, 1991. **43**(7): p. 4083-4086.

110. S. Y. Kilin, *Transient Anti-Stokes Stimulated Raman-Scattering - the Possibility of Observing Quantum Macroscopic Fluctuations.* Europhysics Letters, 1988. **5**(5): p. 419-424.

111. M. G. Raymer, *Quantum state entanglement and readout of collective atomic-ensemble modes and optical wave packets by stimulated Raman scattering.* Journal of Modern Optics, 2004. **51**(12): p. 1739-1759.

112. B. E. A. Saleh, *Photoelectron statistics, with applications to spectroscopy and optical communication*. Springer series in optical sciences v 6. 1978, Berlin; New York: Springer-Verlag. section 4.13.

113. M. G. Raymer, I. A. Walmsley and Z. W. Li, *Temporal Quantum Fluctuations in Stimulated Raman-Scattering.* Coherence and Quantum Optics Vi, 1989: p. 977-980

114. M. D. Duncan, *et al.*, *Control of Transverse Spatial Modes in Transient Stimulated Raman Amplification.* Journal of the Optical Society of America B-Optical Physics, 1990. **7**(7): p. 1336-1345.

115. I. A. Walmsley and M. G. Raymer, *Experimental-Study of the Macroscopic Quantum Fluctuations of Partially Coherent Stimulated Raman-Scattering.* Physical Review A, 1986. **33**(1): p. 382-390.

116. T. A. Birks, J. C. Knight and P. S. Russell, *Endlessly single-mode photonic crystal fiber.* Optics Letters, 1997. **22**(13): p. 961-963.

117. M. Hennrich, *et al.*, *Vacuum-stimulated Raman scattering based on adiabatic passage in a high-finesse optical cavity.* Physical Review Letters, 2000. **85**(23): p. 4872-4875.

118. M. G. Raymer, K. Rzazewski, and J. Mostowski, *Pulse-Energy Statistics in Stimulated Raman-Scattering.* Optics Letters, 1982. **7**(2): p. 71-73.

119. I. A. Walmsley, *et al.*, *Stabilization of Stokes Pulse Energies in the Nonlinear Regime of Stimulated Raman-Scattering.* Optics Communications, 1985. **53**(2): p. 137-140.

120. M. Lewenstein, *Fluctuations in the Nonlinear Regime of Stimulated Raman-Scattering.* Zeitschrift Fur Physik B-Condensed Matter, 1984. **56**(1): p. 69-75.

121. A. S. Grabchikov, *et al.*, *Statistics of the Energy Fluctuations of Stokes Pulses in Stimulated Raman-Scattering in Various Situations.* Jetp Letters, 1986. **43**(3): p. 151-156.

122. C. Wu, *et al.*, *Quantum theory of phase correlations in optical frequency combs generated by stimulated Raman scattering.* Physical Review A, 2010. **82**(5): p. 053834.

123. M. D. Duncan, *et al.*, *Parametric Raman Gain Suppression in D-2 and H-2.* Optics Letters, 1986. **11**(12): p. 803-805.

124. I. A. Walmsley and M. G. Raymer, *Observation of Macroscopic Quantum Fluctuations in Stimulated Raman Scattering.* Physical Review Letters, 1983. **50**(13): p. 962.

125. M. Selvadoray and M. S. Kumar, *Phase properties of correlated two-mode squeezed coherent states.* Optics Communications, 1997. **136**(1-2): p. 125-134.

126. H. Otsuka, T. Uchimura, and T. Imasaka, *Phase locking in four-wave Raman mixing for generation of an ultrashort laser pulse.* Optics Letters, 2004. **29**(4): p. 400-402.

127. A. M. Jones, *et al.*, *Mid-infrared gas filled photonic crystal fiber laser based on population inversion.* Optics Express, 2011. **19**(3): p. 2309-2316.

128. Y. Y. Wang, *et al.*, *Ultra-long-lived molecular coherence in hydrogen filled hollow-core photonic crystal fiber.* 2010 Conference on Lasers and Electro-Optics and Quantum Electronics and Laser Science Conference (Cleo/QELS 2010), 2010: p. QTuG1.

129. Y. Y. Wang, *et al.*, *Spatial and Temporal Dynamics of Raman Coherence in Hydrogen-filled HC-PCF.* 2011 Conference on Lasers and Electro-Optics and Quantum Electronics and Laser Science Conference (Cleo/QELS 2011), 2011: p. QTuO4.